On some implications of non-crystallographic symmetry

Andrey Alekseyevich Lebedev

A Thesis submitted for the degree of Doctor of Philosophy

The University of York
Department of Chemistry
April 2009

Abstract

The standard molecular replacement (MR) protocol involves one-by-one search for molecules composing the asymmetric unit, therefore the non-crystallographic symmetry (NCS) complicates the structure determination. However, the conservation of the oligomeric state in a series of homologues and the use of information about the NCS in the target crystal may help to solve difficult MR problems. A number of the NCS cases which have required tailor-made MR protocols for successful structure solution are presented in this thesis. The ultimate goal is to rationalise these approaches and implement them as supplementary pathways for MR pipelines.

Intermolecular contacts in a macromolecular crystal can have substantially different strengths as, for example, in crystals composed of natural oligomers, or in order-disorder (OD) structures with stronger interactions within diperiodic OD-layers and weaker interactions between the layers. Symmetry of the tightly bound assemblies is often non-crystallographic, whereas weaker interactions are adjusted to enable three-dimensional translational symmetry in the crystal. Weaker interactions can vary between different crystal forms (polymorphs) or even within one crystal to give rise to NCS by translation, twinning or crystal disorder. Several twins, structures with translational NCS and OD-structures are presented in this thesis.

In some cases, the relation between NCS and twinning gives an insight into the twin morphology. Two examples of macromolecular twins are discussed in which the NCS analysis explained the accidental lattice symmetry. In another case, the NCS defined the geometry of twinning by reticular merohedry, so an accurate detwinning was possible without precise measurements of relative orientation of the alternative lattices.

The twin axis can be aligned with an NCS axis. High relative frequency of such twinning cases in the Protein Data Bank is demonstrated and the effect of such interference between twinning and NCS on the intensity statistics is analysed to provide guidelines for interpretation of the standard twinning tests. The alignment of NCS and twin axes is typical for OD-twins by metric merohedry and one of these twins is analysed in detail.

Standard MR is easily adaptable to the case of the translational NCS without significant changes in the algorithm or protocol. However, translational NCS imposes a problem of false-origin MR solution, as is demonstrated in this work. Three cases are described, in which such problem had occurred and was resolved, and which prompted to design the program *Zanuda* that automatically handles false-origin MR solutions and also enables validation and correction of the space group assignment in pseudosymmetric twins.

Thus, the two distinct topics of this thesis are the NCS guided MR, and diagnostics of twinning and incorrect symmetry assignment. Both lines of research have a common goal, to extend the boundaries of existing methods of macromolecular structure solution.

Contents

List of Figures

List of Tables

Declaration

Several protein crystal structures are used as examples in this thesis to illustrate NCS-based approaches to the structure determination and analysis of twinning. In all these collaborative structural projects, I took part in the structure solution and, in the work on the portal protein from the phage SPP1, in the modelling of DNA translocation. Any contribution from others to a particular structural work is duly acknowledged and the citations associated with the structure are provided at the appropriate points within the text. The search for twinning cases in the PDB and preliminary analysis was performed under my (co)supervision by Nagarajan Periasamy (Mres. Bioinformatics, York, 2004) and was presented earlier in a report entitled “Analysis of PDB and identification of unusual cell-symmetry combination” as part of his coursework requirement. No part of that report has been repeated here verbatim.

Abbreviations

ATP	adenosine-5′-triphosphate
BPV-1	bovine papillomavirus-1
CC	correlation coefficient
CCM	constant correlation model
CCP4	Collaborative Computational Project Number 4
CCP4mg	CCP4 molecular graphics
CRF	cross-rotation function
DNA	deoxyribonucleic acid
ECH	enoyl-CoA hydratase
EM	electron microscopy
FFT	fast Fourier transform
HCHL	hydroxycinnamoyl-CoA hydratase-lyase
HemH	ferrochelatase-1
LRF	locked rotation function
LTF	locked translation function
MAD	multiple-wavelength anomalous diffraction
MCM	modulated correlation model
MGF	moment generating function
MIR	multiple isomorphous replacement
MR	molecular replacement
NAD+	nicotinamide adenine dinucleotide (oxidised form)
NADP+	nicotinamide adenine dinucleotide phosphate (oxidised form)
NCS	non-crystallographic symmetry
NMA	normal-mode analysis
OD	order-disorder
PC	Patterson correlation
PCNA	proliferating cell nuclear antigen
PDB	protein data bank
PF	packing function
PSSG	pseudosymmetry space group
PTF	phased translation function

RF	rotation function
RNA	ribonucleic acid
RPS	rotational pseudosymmetry
SAPTF	spherically averaged phase translation function
SRF	self-rotation function
TF	translation function
TLQS	twin-lattice quasisymmetry
TLS	translation-libration-screw
TLS	twin-lattice symmetry
TPx-B	thioredoxin peroxidase B from human erythrocytes
TRAP	tryptophan attenuation protein
YSBL	York Structural Biology Laboratory
anti-TRAP	regulator of TRAP activity
dsDNA	double-stranded DNA
pRNA	procapsid RNA
r.m.s.d.	root mean square deviation

Table of examples

Protein, citation. (i,ii) Feature of interest.	Space group	Unit cell parameters (Å, ^{o})	Resolution (Å)	Contents of asymmetric unit (t) Translational NCS (p) Pseudosymmetry (g) OD-groupoid (§1.3.2)	§§ PDB code
Thioredoxin peroxidase B from human erythrocytes (TPx-B), (Schröder *et al.*, 2000), (Isupov & Lebedev, 2008). (i) Structure solution.	$P2_1$	$a = 88.9$ $b = 107.0$ $c = 119.5$ $\beta = 110.9$	1.7	One decamer	2.1 1qmv
Anti-TRAP protein from *Bacillus licheniformis*, (Isupov & Lebedev, 2008). (i) Structure solution, (ii) false-origin MR solution.	$P2_1$	$a = 118.5$ $b = 99.9$ $c = 123.2$ $\beta = 117.6$	2.2	Four dodecamers (t) $0.50\,\mathbf{a} + 0.13\,\mathbf{b}$ (p) $P2_1, \ (\mathbf{a}+\mathbf{c})/2$	2.2 4.1
Hydroxycinnamoyl-CoA hydratase-lyase (HCHL) from *Pseudomonas fluorescens*, (Leonard *et al.*, 2006), (Lebedev *et al.*, 2008). (i) Structure solution.	$P2_12_12$	$a = 154.2$ $b = 167.5$ $c = 130.8$	1.8	Two hexamers (t) $0.66\,\mathbf{a} + 0.30\,\mathbf{b} + 0.50\,\mathbf{c}$	2.3 2j5i
E1-helicase from bovine papillomavirus-1, (Sanders *et al.*, 2007), (Lebedev *et al.*, 2008). (i) Structure solution.	$P2_12_12_1$	$a = 135.1$ $b = 180.7$ $c = 187.5$	3.0	Two hexamers (t) $0.50\,\mathbf{a} + 0.08\,\mathbf{b}$	2.4 2v9p
Hypothetical protein MTH685 from *M. thermautotrophicus*, (Lebedev *et al.*, 2008). (i) Structure solution.	$P222_1$	$a = 68.3$ $b = 72.1$ $c = 146.8$	1.8	Two monomeric molecules with three domains	2.5
Portal protein (gp6) from phage SPP1 (Hg derivative), (Lebedev *et al.*, 2007). (i) Substructure solution, (ii) oligomer asymmetry.	$C222_1$	$a = 174.3$ $b = 221.4$ $c = 421.9$	3.4	One tridecamer	2.6 2jes

(Continued on the next page)

Protein, citation. (i,ii) Feature of interest.	Space group	Unit cell parameters (Å, º)	Resolution (Å)	Contents of asymmetric unit (t) Translational NCS (p) Pseudosymmetry (g) OD-groupoid (§1.3.2)	§§ PDB code
C-terminal domain of large terminase subunit (gp2), from phage SPP1. (i) Twin by metric merohedry.	$P2_1$	$a = 69.4$ $b = 159.4$ $c = 107.7$ $\beta = 108.8$	2.6	Ten monomeric molecules	3.3
Ferrochelatase-1 (HemH) from *Bacillus anthracis*, (Au *et al.*, 2006). (i) OD-twin by metric merohedry.	$P2_1$	$a = 49.9$ $b = 109.9$ $c = 59.4$ $\beta = 90.0$	2.1	Two monomeric molecules (g) $P2_12_12 : P2_1(1)1$	3.4 2c8j
L-2-haloacid dehalogenase from *Sulfolobus tokodaii* complexed with L-lactate, (Rye *et al.*, 2007), (Rye *et al.*, 2009). (i) OD-twin by reticular merohedry, (ii) detwinning.	$C2$	$a = 127.6$ $b = 58.1$ $c = 51.2$ $\beta = 97.2$	1.9	One dimer (g) $C222 : C22(2)$	3.5 2w11
GAF (N-terminal) domain of apo CodY protein from *Bacillus subtilis*, (Levdikov *et al.*, 2009). (i) False-origin MR solution.	$P4_322$	$a = 90.2$ $c = 205.6$	1.74	Two dimers (p) $P4_222$, $\mathbf{c}/2$	4.2 2gx5
Oxidoreductase from *Thermotoga maritima*. (i) Pseudosymmetry and twinning, (ii) false-origin MR solution.	$P2_12_12_1$	$a = 141.7$ $b = 141.7$ $c = 169.5$	2.36	Four dimers (p) $P42_12$, $\mathbf{c}/2$	4.4
Human proliferating cell nuclear antigen (PCNA), (Gulbis *et al.*, 1996). (i) OD-structure with space group uncertainty.	$P3_221$	$a = 83.5$ $c = 233.9$	2.6	One trimer (p) $(\mathbf{a} + 2\,\mathbf{b} + \mathbf{c})/3$ (g) $P321 : P(3)21$	4.5 1axc

1 Introduction

The method of molecular replacement (MR) is most suitable for crystal structure solution of complexes, mutants and close homologues of a macromolecule with known structure. Sometimes the structure of a distant homologue can be solved, but even in apparently easy cases a straightforward structure solution may be prevented by non-trivial organisation of a given crystal. A general overview of MR (§1.1) is therefore followed by discussion of twinning (§1.2), which frequently obscures a correct MR-solution. Finally, the theory of OD-structures and several examples of OD-twins are presented (§1.3).

1.1 Molecular replacement

1.1.1 Original meaning of the term

In current understanding, the term MR relates to a series of Patterson function superposition techniques and auxiliary methods targeting at the positioning of known molecular fragments in unknown crystal structure. When implemented for the first time (Nordman & Nakatsu, 1963), the method was not referred to as MR; instead, the term MR was initially assigned to a method, which was thought to be suitable for determination of entirely unknown molecular structure given (non-anomalous) diffraction data for two polymorphs or for a single crystal but containing more than one molecule in the asymmetric unit. Rossmann & Blow (1962; 1963) referred to Shannon's theorem and pointed out that diffraction data contained sufficient information to estimate phases provided that there were two or more copies of an unknown molecule in the asymmetric unit or diffraction data were available for two or more different crystal forms. A series of proof-of-principle works outlined the procedure involving the following three steps: (i) the search for relative orientations of identical (but unknown) electron density fragments (Rossmann & Blow, 1962; Tollin & Rossmann, 1966); (ii) the search for the position of these fragments in the crystal(s) (Rossmann *et al.*, 1964); (iii) solution of "molecular replacement equations" (Rossmann & Blow, 1963, 1964; Main & Rossmann, 1966) that restores phases. Several macromolecular polymorphs and several cases of non-crystallographic symmetry (NCS) in protein crystals were already known (*e.g.* Scouloudi, 1960 and references in Rossmann & Blow 1962; 1963) and the new method seemed to be very promising, also because of rapidly increasing computer power.

1.1.2 NCS averaging

The molecular replacement equations are reciprocal space formulations of the identity of the electron density in two or more non-equivalent positions. It was demonstrated practically (Muirhead *et al.*, 1967, and references in Bricogne, 1974) and theoretically (Bricogne, 1974) that these equations can be solved by averaging of the electron density in the real space provided reasonable starting phases are available.

Therefore the third step of the originally assumed scenario of MR evolved in what is presently termed as NCS averaging (Cowtan & Main, 1993), although the term MR was for a while applied to this procedure (Argos *et al.*, 1975).

The phasing of viral structures starting from the spherical envelope is the closest method to the originally assumed MR scenario (Chapman *et al.*, 1992, and references therein). However, such method of structure determination was only possible because of up to 60-fold averaging. Even in these very favourable cases the "MR" *ab initio* phasing required precise estimation of starting model parameters, the spherical shell radii. Therefore the prerequisites of the procedure are either good X-ray measurements at very low resolution or experimental data obtained by other methods such as low angle X-ray scattering or electron microscopy.

1.1.3 MR with known search model

The first two steps of the original MR scenario have clear counterparts in contemporary MR using a template structure.

The rotation function (RF) is typically used for two purposes, as the self-rotation function (SRF) to find NCS operations and as the cross-rotation function (CRF) to find the orientation of the template best matching the orientation of the molecule(s) in the crystal. The two functions differ in the objects to which they are applied, but both of them are conceptually identical to the RF by Rossmann & Blow (1962), which is an overlap function between spherical domains of a fixed Patterson map and a rotated copy of the same or another Patterson map. The SRF is used in the preliminary analysis of the diffraction data and the CRF accomplishes the first step of contemporary MR to define the orientation of the search model. The algorithms that are used for calculation of the RF are discussed below.

The translation function proposed by Rossmann *et al.* (1964) was intended to find the relative positions of the centres of two copies of an entirely unknown molecule given their orientations. The proposed method is in practice only applicable to molecules related by two-fold rotation in a crystal with low crystallographic symmetry and NCS (ideally, two molecules per unit cell). An extension of the method to structures with many molecules per unit cell would apparently require precise information on the molecular shape, and relations other than exact two-fold rotation between two molecules in question would require knowledge of the internal organisation of the molecule, essentially the search model. On the other hand, the improvement of phases is only possible with high-order NCS.

The translation function (TF) in the problem with known search model is conceptually different from the initially proposed translation function; it uses the complete Patterson map and the molecular envelope need not be defined explicitly, it is equally applicable to any two orientations of the search model and in later versions it accounts for all symmetry related molecules in a single run. The theory of the contemporary version of the TF is briefly discussed below; it is used in the second step of the standard MR protocol, the positioning of the model in the unit cell of the target crystal.

1.1.4 Rotation function

Given two Patterson functions P_1 and P_2 and a spherical domain U centred at the origin, the RF is defined as

$$R(o) = \iiint\limits_U P_1(r)\, P_2(o^{-1}\, r)\, \mathrm{d}r^3, \tag{1}$$

where o is a variable rotation matrix. Two widely used parameterisations of the rotation space are Euler angles α, β and γ and polar angles ϕ, ψ, χ. The first set of angles is convenient for computations, whereas the second set can be more suitable for representations. If P_1 and P_2 represent the same experimental Patterson map, equation (1) defines the SRF; if P_1 is an experimental Patterson map and P_2 the Patterson computed from the search model (atomic model or electron density map), then (1) defines the CRF. The function for two different experimental Patterson maps can also be of practical interest to verify that two crystals contain identical molecules or identical oligomers.

The RF is targeted at determining the relative orientations of the molecules but not their relative positions. Therefore, the interatomic intramolecular vectors (self-vectors) contribute to the useful signal in the RF, whereas all the interatomic intermolecular vectors (cross-vectors) contribute to the noise. Fortunately for the RF performance, all self-vectors from a spherical molecule but less than half of the cross-vectors are shorter than the diameter of the molecule. Therefore, the radius of the spherical domain U is chosen to be approximately equal to the diameter of a search model (CRF) or to the expected diameter of the unknown molecule (SRF). In practice the search model is not spherical and, moreover, its largest dimension can exceed the length of one of the cell edges. Therefore, either twice the radius of gyration of the molecule or half-length of the shortest crystallographic translation, the smaller of the two magnitudes, is substituted for the integration radius. If twice the radius of gyration is used, then most of the meaningful information from self-vectors is preserved and contributes to the signal, whereas most of the noise owing to cross-vectors is suppressed. The limit imposed by cell parameters prevents accounting for the translational equivalents of the Patterson vectors, and, in particular, prevents including any translational equivalent of the origin peak into the integration domain.

The contribution from the Patterson origin peak to the RF is almost constant for all rotations for isotropic data, but this may not be so if the data are anisotropic, and it may disguise correct RF peaks. The removal of a smaller sphere embracing the origin peak from the integration sphere U in (1) or removal or downweighting of the low harmonics in the fast RF helps resolve this problem (*e.g.* Navaza, 1987). Non-spherical integration domains were also discussed, but this generalisation seems to be sensible only in the special case of a strong prior knowledge of the orientation.

1.1.5 RF: reciprocal space formulation

Direct calculation of the RF according to (1) for reasonably fine sampling of both Patterson map and rotation space requires huge computer resources. Rossmann & Blow (1962) expressed the RF in terms of intensities and the interference function $G(\mathbf{h},\mathbf{k})$, the Fourier transform of the integration domain,

$$R(o) = \sum_{\mathbf{h}} \sum_{\mathbf{h}'} |F_1(\mathbf{h})|^2 \, |F_2(\mathbf{h}')|^2 \, G(\mathbf{h}, o^{-1}\,\mathbf{h}'). \tag{2}$$

to allow the following approximations. Firstly, only the “strong terms”, i.e. the strong intensities are preserved in one of the two sets of intensities. Secondly, all but the first nodes of $G(\mathbf{h},\mathbf{k})$ are ignored to retain only close pairs of reflections in the double summation in (2). The approximation was shown to be sufficiently accurate for practical purposes. The algorithm was later enhanced by including more nodes of $G(\mathbf{h},\mathbf{k})$ in the summation and by more efficient sampling of $G(\mathbf{h},\mathbf{k})$ (Tollin & Rossmann, 1966; Tong & Rossmann, 1990). This algorithm is rarely used now because of the introduction of the fast RF algorithm. However, the algorithms using the reciprocal space formulations of the real space problems and adequate approximations for $G(\mathbf{h},\mathbf{k})$ remain of interest. In particular, such an approach is applicable to NCS averaging to offer iterative phase extension without re-calculation of the electron density map at each cycle (Chapman *et al.*, 1992; Tsao *et al.*, 1992).

1.1.6 Fast RF

The idea of the fast RF algorithm (Crowther, 1972) is that the Patterson function in a spherical domain around the origin is expanded in series, in which the angular dependence is represented by spherical harmonics Y_{lm},

$$P(\mathbf{r}) = \sum_{l=0}^{\infty} \sum_{m=-l}^{l} c_{lm}(r) Y_{lm}(\mathbf{n}) \tag{3}$$

In this equation c_{lm} are radial functions, which only depend on r, the length of $\mathbf{r}$, and $\mathbf{n} = \mathbf{r}/r$ is a unit vector along $\mathbf{r}$. Substitution of (3) into (1) and the orthogonality of spherical harmonics result in the following expression for the RF,

$$R(o) = \sum_{l=0}^{\infty} \sum_{m=-l}^{l} \sum_{m'=-l}^{l} C^{l}_{mm'} \, D^{l}_{mm'}(o), \tag{4}$$

where $D^{l}_{mm'}$ are the Wigner matrices representing the rotation o in terms of linear transformations of spherical functions and $C^{l}_{mm'}$ depend on the data,

$$C^{l}_{mm'} = \int_{0}^{a} c^{*}_{(1)lm}(r) c_{(2)lm'}(r) r^2 \mathrm{d}r, \tag{5}$$

a is the radius of the spherical integration domain, and the indices 1 and 2 in brackets correspond to fixed and rotated Patterson functions, respectively. The Wigner matrices $D^l_{mm'}$ are computed using recursion relations. How the coefficients $C^l_{mm'}$ are handled depends on the particular implementation. Crowther approximated the radial functions $c_{lm}(r)$ by truncated Bessel-Fourier series, expressed the coefficients c_{lmn} of these series in terms of structure amplitudes and summed the products of $c_{(1)lmn}$ and $c_{(2)lm'n}$ over n to evaluate the coefficients $C^l_{mm'}$.

There were several improvements in the fast RF since it was first introduced by Crowther. Navaza (1987) proposed using Gaussian quadrature for integration in (5) instead of summation of the products of Bessel-Fourier coefficients. This simplified the code and substantially improved the accuracy without requiring extra computational time. “Linear” recursion instead of “triangular” one (Navaza, 1990) improved the accuracy of Wigner function calculation. The stability of the new recursion was especially important for calculation of Wigner functions with large l and made fine details of the rotation function available if necessary. Further improvement of radial integration (5) was achieved using expansion of the radial integral into a series of products of spherical Bessel-functions (different from Crowther’s series) allowing 30% higher efficiency and on-the-fly accuracy control (Navaza, 1993).

The calculation of the coefficients c_{lmn} (Crowther, 1972) or the coefficients e_{lmn} (Navaza, 1993) factorising the integral (5) is the most time consuming procedure in the standard MR protocol with one model and one data set. However, if several data sets and several models are available and the coefficients are pre-computed for them, the summation of the Wigner function series (4) will be required for each combination of data set and model and will in total take most of the computational time. The use of the three-dimensional fast Fourier transform instead of a two-dimensional one (Kovacs & Wriggers, 2002; Trapani & Navaza, 2006) accelerates this step by about an order of magnitude in a typical MR problem. In addition, such an approach resolves singularities that occur in the recursion for Wigner functions at special values of β. Alternatively, the RF can be sampled on sparser grids if these are defined specifically for each β-section according to the angular resolution limit (Trapani *et al.*, 2007).

1.1.7 Real space RF and direct RF

In the real-space RF (Huber, 1965) the RF is computed directly according to definition (1), but the integration is approximated by summation over only the strongest grid points of the model Patterson function. This approach is very similar to that by (Nordman & Nakatsu, 1963). Alternatively, the orientations can be scored according to the match between the coordinates of strongest peaks in the rotated and fixed Patterson maps (*OVIONE*; Álvarez-Rúa *et al.*, 2000; Borge *et al.*, 2000).

In the direct RF (Brünger, 1992) the model in each of the tested orientations is placed in a $P1$ unit cell with the same dimensions as the unit cell of the target crystal. The Patterson function of the model structure can therefore be directly compared with the observed Patterson without restricting the integration domain. This is especially important if the unit cell dimensions are very different or the shape of the model is far from spherical. It is also important that the correspondence between two sets of intensities is clearly defined and therefore a more adequate target function than the simple overlap function can be used. In particular, the target function in the direct RF is the "Patterson correlation" (PC), the linear correlation coefficient between two sets of normalised intensities. The use of all self-vectors, the PC-target and absence of any approximations are the factors enabling very high contrast in the direct RF compared to other variations of the RF (DeLano & Brünger, 1995; Grosse-Kunstleve & Adams, 2001), which compensates for the high computational cost in difficult MR problems.

1.1.8 Translation function

The "modified minimum-function" by Nordman & Nakatsu (1963), which was an equivalent of the TF with the atomic search model, was expressed in terms of a sum over all expected cross-vectors. A similar algorithm was proposed by Tollin (1966), in which the TF was considered as a modification of the sum function by Buerger (1959). Crowther & Blow (1967) presented an algorithm where summation over cross-vectors was avoided and the Fourier coefficients of the TF were expressed in terms of calculated intensities (T-function). Such formulation made the TF suitable for the solution of macromolecular structures. It was also shown that the removal of the expected self-vectors from the experimental Patterson function enhances the contrast ($T1$-function). Symmetrised versions of T- and $T1$-functions were proposed ($T2$-function), which revealed peaks from all pairs of symmetry related molecules, but in different positions and therefore without increase in contrast.

Later, several improvements of TF were proposed (*e.g.* Langs, 1975; Litvin, 1977). Major improvements were independently introduced by Harada *et al.* (1981) and Vagin (1983) to render TF essentially in its present appearance. In the new version of TF all pairs of symmetry related molecules act in accord and peak at the same point of three-dimensional TF-space to increase the signal-to-noise ratio in higher symmetry space groups.

The TF by Harada *et al.* (1981) is computed using the fast Fourier transform (FFT) and approximates the correlation coefficient. In the program *BRUTE*, Fujinaga & Read (1987) use exact centred correlation coefficient of intensities. This function is computed for each sample point in the TF-space. FFT formulation of such correlation search results in a considerable saving in computation time (Navaza & Vernoslova, 1995).

Another overlap function, although based on a quite different physical approach, is the full-symmetry phased translation function (Cygler & Desrochers, 1989). Its reciprocal-space version (Bentley & Houdusse, 1992) is computationally similar to the TF, although the TF is quadratic in the intensities, whereas the phased translation function (PTF) is quadratic in the amplitudes. In the case of two molecules in the unit cell this function is equivalent to the search of one orientation in the difference map calculated from the other orientation. However, a more important application of the PTF is to locate a model given external phases. Such combination of MR and experimental phasing proved to be successful in the cases of low homology models and poor experimental phases, when none of the methods alone succeeded (Strokopytov *et al.*, 2005).

1.1.9 Packing function

The TF defined as the overlap of two Patterson functions (*e.g.* *TO*-function by Harada et al., 1981) linearly depends on the density overlap between the symmetry related copies of the search model and quadratically on the signal, the overlap between search and target densities. Given a search model with low similarity the top peaks of such a TF are most likely to correspond to the overlap of the symmetry related copies of the search model, but not to the correct solution.

There are several ways of correcting the TF to eliminate or downweight these false peaks. Both the sum of calculated intensities and the sum of calculated intensities squared depend on the model overlap. The first magnitude and the square root of the second magnitude enter the denominators of the modified TF by Harada *et al.* (1981) and the TF defined as the correlation coefficient between observed and calculated intensities (Navaza & Vernoslova, 1995), respectively, to downweight the translation vectors corresponding to the interpenetration of the symmetry-related copies of the search model (Zhang & Matthews, 1994). The sum of calculated intensities is the height of the origin peak of the Patterson function. Thus, one of the subtraction strategies in the MR is the removal of the origin peak of the observed Patterson function, which simultaneously eliminates contribution to the TF from the origin peak of the model Patterson map and therefore substantially reduces the effect of the model overlap. The intensity-correlation search appears to be the most efficient among the FFT-based translation searches, but it is about one order of magnitude slower than others. It is therefore a common practice to avoid the global correlation search but to calculate the correlation coefficient for the top peaks of a faster version of the TF, as is done, for example, in *AMoRe* and *MOLREP*.

None of the discussed modifications of the TF is guaranteed to remove the false peaks owing to the overlaps in the model. The packing function (PF; Vagin, 1983; Stubbs & Huber, 1991; Vagin & Teplyakov, 1997) provides a straightforward way of discarding such false peaks. In this method, the density overlap in the model is computed as a function of the translation vector and then inverted and truncated to give the PF, which equals one for the position of the reference search molecule giving no overlaps between symmetry equivalents and equals zero for maximal overlap of two symmetry equivalents. The overlap function accounts for all symmetry equivalents and is computed using FFT. An empirical scaling coefficient and threshold are required for the conversion of the overlap function into the PF. The TF is multiplied by the PF to generate a modified TF, in which the false peaks owing to overlaps in the model are suppressed.

Usually, residues on the surface of biomolecules are less conserved than those buried inside it. Moreover, the conformations of exposed loops not only can be different in homologues, but can vary in different crystal forms of the same protein, especially in the areas of intermolecular contacts. Therefore it is necessary to allow some overlap between neighbouring molecules in an MR solution. In *MOLREP* this is achieved by using two different models, one for calculation of RF and TF and another for the packing function (Lebedev *et al.*, 2008). In the latter the atoms with non-zero accessible surface are removed.

1.1.10 Combination of MR and experimental phasing

Multiple-wavelength anomalous diffraction (MAD) or multiple isomorphous replacement (MIR) data are frequently used for validation of the MR solution and phase improvement. Anomalous/isomorphous substructures with multiple or partially occupied sites are difficult to solve, but they can easily be found in difference Fourier synthesis using MR phases, thus confirming the correctness of the MR solution. Experimental phases can be further used to improve poor estimates of phases provided by MR (Czjzek *et al.*, 2001). Schuermann & Tanner (2003) proposed that anomalous differences from S atoms should routinely be collected and used in MR structure determination. An interesting method is described by Grininger *et al.* (2004), in which the correctness of the MR solution was verified by identifying radiation-damage-induced structural changes.

Moreover, there are several formulations of the TF which utilise the difference data during the TF search. For example, the experimental phases can be directly used in the PTF, or the difference electron density can be monitored at known heavy/anomalous atom sites (Zhang & Matthews, 1994). In addition, the Patterson search for heavy atoms can itself be reformulated in terms of the TF (Vagin & Teplyakov, 1998). In special cases of high symmetry oligomers the MR approach to substructure determination is superior over the otherwise more powerful direct methods (§2.6; Antson *et al.*, 1995).

1.1.11 Improvement of the search model

More attention is recently paid to search model design because of rapid growth of structural databases and better understanding of the nature of structural variability. In addition, modern computers make it possible to test many search models or their ensembles and an effective ranking of these models becomes a priority (*Phaser*; McCoy *et al.*, 2007).

Model preparation typically includes searching for homologous structures in the protein data bank (PDB; Berman *et al.*, 2002), their analysis and modification. The information important for MR includes the presence and conservation of the oligomeric state and domain structure in the family of homologous proteins. Data on oligomers can be obtained from *PISA* (Krissinel & Henrick, 2005) and domain descriptions are given, for example, by *SCOP* (Murzin *et al.*, 1995), which is linked to the PDB web resources. This information, combined with analysis of the SRF, Patterson map, unit-cell parameters and symmetry of the crystal, allows the generation of a search model or a series of search models, including oligomers, single subunits or domains. There is a wide range of tools available for modification of the selected model(s). Schwarzenbacher *et al.* (2004) showed that the side-chain modelling according to target sequence has a significant impact on MR success rates. Such a model modification was implemented in the *CHAINSAW* program, written by Norman Stein and included in the CCP4 suite (Collaborative Computational Project, Number 4, 1994). A three-dimensional superposition of homologous structures using, for example, *SSM* (Krissinel & Henrick, 2004) integrated in *Coot* (Emsley & Cowtan, 2004) allows the identification of polypeptide segments that are variable within the given family of proteins. The removal of such segments from the search model can often prove critical for the MR search. More extensive modifications sometimes help to solve difficult MR cases. These include homology modelling (Schwede *et al.*, 2003; Fiser & Sali, 2003) and scanning the possible conformations of the unknown protein using normal-mode analysis (NMA; Suhre & Sanejouand, 2004).

Some of the advanced MR protocols cannot be clearly subdivided into a model preparation stage and a purely crystallographic stage (Patterson search), as a partial structure is improved using X-ray data and a better search model for subsequent rounds of Patterson search is produced.

For example, if there are many identical molecules in the asymmetric unit, it is not necessarily the case that all of them produce an equally good contrast in the RF and TF. The molecules with lower *B*-values, or those in favourable positions (e.g. making close contacts with their symmetry mates) give higher contrast than others. Therefore it frequently happens that the first few subunits are found easily, but the rest of the structure remains unidentified. In the example described by Shan *et al.* (2005), the dimer formed by the first two subunits found was used to find the remaining two dimers. A similar approach was used in (Zhou & Gong, 2004). This strategy is implemented in *MOLREP*, which outputs the coordinates of a dimer once it is generated by previously placed search models. In addition, the relative positions of located subunits or domains can be refined in *P*1 prior to the translation search (Yeates & Rini, 1990, see also §2.4). In some cases, especially with high-resolution data available, the restrained refinement of a partial structure can lead to determination of the complete structure (§2.5).

The failure of the first MR attempt can be due to conformational differences between the search model and the target molecule. These differences can frequently be described by domain mobility. In such cases the crystal structure can be solved using separate domains as search models. Also, prediction of conformational changes using NMA has been shown to be successful (Suhre & Sanejouand, 2004). An interesting application of NMA to the solution of a multidomain structure was reported by Jeong *et al.* (2006). In this work the modification of the search model using NMA was guided by CRF peaks from individual domains.

Contemporary automated MR programs offer several built-in model-preparation functionalities. The integration of model-preparation and Patterson superposition techniques in one program has several advantages. Apart from convenience, such integration allows specific adjustment of the model-modification parameters for an efficient Patterson search. Moreover, the weighting parameters for the RF and TF are more reliable if they are derived from the original sequence and atomic coordinates of the homologous protein. *MOLREP* was the first program implementing such an integrated approach, which had proven to be efficient and has recently been implemented in several MR pipelines including *BALBES* (Long *et al.*, 2008), *MrBUMP* (Keegan & Winn, 2008) and *JSCG* (Schwarzenbacher *et al.*, 2008).

1.1.12 The use of NCS in MR

Although the expectation of the 1960's of directly using NCS for phasing was not fulfilled, the methods utilising the NCS are an important ingredient of contemporary crystallographic software. In many cases the orders and directions of NCS axes can be determined from diffraction data using the SRF. Translational NCS can be detected using the native Patterson synthesis. A comparison of experimental functions and functions generated from MR solutions is a good validation tool. Two of many examples are given by Makino *et al.* (2005*b*) and Keillor *et al.* (2003).

The locked rotation function (LRF) and locked translation function (LTF) were developed to build an oligomer from subunits in accordance with the SRF (Tong, 2001). The resulting oligomer is used in a conventional TF search. NCS analysis has to be performed with special care when NCS is used directly for structure determination (as in the LRF/LTF method). An example of misleading SRF was, for example, reported by Asojo *et al.* (2003).

The point-group symmetry of an oligomer is an approximate symmetry and its deviation from the exact symmetry may be too large for methods based on averaging of the Patterson function (LRF/LTF) to be successful. The selection of the CRF peaks obeying NCS (*CRANS*; Lilien *et al.*, 2004) is free of this disadvantage. An interesting example, in which selection criterion was based on the electron-microscopy reconstruction of a trimer was presented by Trapani *et al.* (2006). A technique in which no restrictions are imposed on the organisation of the oligomer is the multi-copy search (Vagin & Teplyakov, 2000) implemented in *MOLREP*.

1.1.13 Exhaustive search

Conventional three-dimensional implementations of Patterson superposition methods suffer from a low signal-to-noise ratio at the rotation-search step. An exhaustive six-dimensional search at low resolution enhanced by multi-start local optimisation against all data (*SOMoRe*; Jamrog *et al.*, 2003) or six-dimensional stochastic optimisation employing, for example, evolutionary programming (*EPMR*; Kissinger *et al.*, 1999) partially overcome this problem. Moreover, a stochastic approach proved to be successful in solving a 23-dimensional MR problem (*Queen of Spades*; Glykos & Kokkinidis, 2003). These methods are especially relevant in cases of low solvent content (Nakai *et al.*, 2003).

As a variation of a six-dimensional search, the TF search can be conducted for a comprehensive sample of orientations of the search model (Sheriff *et al.*, 1999). In general, an exhaustive search over some parameters of the model can be combined with conventional MR. For example, a one-parameter family of hexamers generated from a homologous trimer was tested by conventional MR (Leonard *et al.*, 2006, §2.3); all possible orientations of the idealised transmembrane helices forming symmetric helical bundles were generated and used in an MR search (Strop *et al.*, 2007).

In general, in the presence of NCS in the target crystal, the availability of a related oligomeric search model makes it possible to reduce the number of dimensions of the search space. As a result, the orientations (and in some cases the internal parameters) of the oligomer can be scanned by a systematic exhaustive search using a TF and the CRF step can therefore be omitted. Three examples of successful structure solution using an NCS-constrained exhaustive search were reported in Isupov & Lebedev (2008).

1.1.14 Related methods

There are several other lines along which model-based phasing develops. Envelopes derived from electron microscopy (EM) reconstruction or small angle scattering can be in principle located in the unknown crystal structure and phases from the envelope can be extended to higher resolution (Hao, 2006). Note that the MR search at low resolution is fast and thus an exhaustive six dimensional search becomes possible (Liu *et al.*, 2003). Phased rotation, conformation and translation function was designed for automatic interpretation of electron density utilising molecular fragments with some conformational freedom (*NUT*; Pavelcik, 2006).

1.1.15 MR and translational NCS

Crystal structures containing many independent molecules in the asymmetric unit are, in general, difficult to solve using a sequence of MR searches, as there is a significant decrease in signal-to-noise ratio for an incomplete model. Even in a solvable case, a correct solution does not necessarily show as the top score in each of the consecutive one-body searches and therefore sophisticated combinatorial algorithms and extensive calculations may be required (*Phaser*; McCoy *et al.*, 2007).

The use of LRF/LTF (§1.1.12) for oligomers with known point group symmetry substantially reduces the number of required searches and correspondingly increases the signal-to-noise ratio in each search. Another special case, in which a reduction in the number of searches is possible, is translational NCS. The structure factors from a single molecule and from several molecules in the same orientation differ by a coefficient that only depends on the relative positions of the molecules and the reflection indices. The relative positions can be determined from strong non-origin peaks in the Patterson map. Therefore, a minor modification of the TF allows simultaneous search for two or more molecules (Navaza *et al.*, 1998). The efficiency of this method is affected by small differences in the orientations of the NCS-related molecules. However, the dispersion of the orientations can be estimated prior to the TF search and accounted for in the weighting scheme during the TF search, as implemented in *Phaser*.

An even more specialised case is that of translational pseudosymmetry where the NCS translations are near simple fractions of the crystallographic translations. In these cases some zones of reciprocal space are much weaker than others, and the crystal structure is very close to one with a smaller unit cell. These structures are customarily solved in the smaller cell and then the solution is expanded to the true cell. Navaza *et al.* (1998) discuss several examples, including the crystal structure of ribonuclease Barnase from *Bacillus amyloliquefaciens* (Guillet *et al.*, 1993) with eight-fold translational pseudosymmetry. It was demonstrated that such structures are solvable by either of the two techniques, the simultaneous search for translational-pseudosymmetry related molecules or the search in the smaller cell. The former method may seem more attractive as it uses in the TF search the whole data set including the sublattices of weak reflections. However, the multi-model is unlikely to be sufficiently precise to reasonably match the weak intensities because of both inaccuracy of the NCS-translation vector derived from the Patterson function and the small differences in the orientations of the pseudotranslation-related molecules.

In both structure determination strategies, the adjustment of the model to fit the weak reflections is in effect postponed till the refinement stage. An efficient approach to refinement in the presence of translational pseudosymmetry is presented by Oksanen *et al.* (2006). The first step of the procedure includes rigid body refinements against the sublattice of weak intensities alternated with restrained refinements against the sublattice of strong intensities. The second step is restrained refinement against all data. In such a way the problem with relative weighting of weak and strong intensities is avoided to accelerate the convergence.

The presence of translational pseudosymmetry not only requires specific search and refinement protocols, but also imposes additional problems with the space group assignment. It was likely that the $P2_1$ solution found by Oksanen *et al.* (2006) was a false origin solution (§4) and therefore did not refine. As a result the correct $P2_1$ symmetry was disregarded and incorrect $P1$ symmetry was assigned to the structure. Another kind of mistake, made and corrected, was reported by Makino *et al.* (2007). The *c*-dimension of the unit cell in two trigonal polymorphs of Bence Jones protein differed by a factor of two and belonged to the space groups $P3_221$ ($c = 47$ Å) and $P3_121$ ($c = 94$ Å). The large-*c* structure was solved first and the same space group was erroneously assumed for the small-*c* structure, which led the authors to report the likelihood of twinning in the small-*c* form (Makino *et al.*, 2005*a*). Note that in this case the pseudosymmetry space group also included the six-fold rotation complicating the analysis of twinning. A method and a program for validation and correction of the space group assignment for general cases of pseudosymmetry and twinning were developed and are presented in this thesis (§4.3).

1.2 NCS and twinning

1.2.1 Geometrical classification of twins

The ordered intergrowth of crystals is a phenomenon abundant in nature and widely used in industry. The mutual orientation of the individual crystals is defined by structural similarity and, in particular, dimensional similarity of the unit cells of the intergrown crystals. In such edifices, the composition plane, an interface between individual crystals has two-dimensional translational symmetry that ensures larger energy gain compared to a random interface. In this context, the terms reticular control or lattice control of orientation are used. Distinction is typically made between two- and three-dimensional lattice controls. If the intergrown crystals belong to different species (phases), the phenomenon of their definite mutual orientation with two- and three dimensional control is called epitaxy and syntaxy, respectively (Bailey *et al.*, 1977). In syntacic intergrowth, the composition surface can in principle be formed by any pair of corresponding planes of the two individual crystals. However, the structural nature of the three-dimensional control is still two-dimensional, as the mutual orientation of individual crystals is unambiguously defined by any one of possible interface types and, in practice, one type of interface prevails and define the joint growth of the adjacent individual crystals in the respective orientations (Bonev, 1972).

A special case of oriented crystal intergrowth, twinning, is an association of individual crystals of the same phase in different relative orientations. Any two individual crystals of a twin are internally identical and symmetry related (by the twin operation) and it is therefore natural that emphasis is put on symmetry relations in the description of twins. The dimensional similarity is now the similarity between the lattice and its rotated or mirror copy, and the reticular control of the orientation translates into the law of Mallard stating that the twin axis in a rotation twin exactly coincides with the direction of a certain lattice row or is exactly perpendicular to a lattice plane, and the twin plane in a mirror twin is exactly parallel to a lattice plane (Le Page, 2002).

The importance of symmetry in the description of twins is underlined by the high frequency of twins with merohedry-holohedry relation between the point symmetry of the crystal and that of the crystal lattice. A symmetry operation missing in the merohedral point group of the crystal but present in corresponding holohedral group (of the lattice) is a potential twinning operation. For twins generated by such an operation the lattices of individual crystals in their twin orientations exactly coincide.

For twins by pseudomerohedry the twin operation does not belong to the holohedral group of the crystal and, in general, the symmetry relation between the individual lattices is approximate. The mismatch between the lattice and its transformed copy is characterised by an obliquity angle, ω. In the case of a rotation twin the obliquity angle is defined as the angle between the plane perpendicular to the twin axis, which is in general non-rational, and the closest crystallographic plane. In the case of a mirror twin the obliquity angle is the angle between (non-rational) axis perpendicular to the twin plane and the crystallographic direction closest to it.

In the more general case, twinning by reticular (pseudo)merohedry, the twin operation (approximately) matches a sublattice of an individual crystal and its rotated or mirror copy, but not the whole lattice. An additional parameter characterising such a twin is the twin index n. This integer number equals the number of all lattice nodes divided by the number of nodes overlapping under the action of twin operation. The particular case of case $n = 1$ is not included, as it corresponds to twinning by (pseudo)merohedry.

Two macromolecular twins by reticular pseudomerohedry are discussed in this thesis. These are the PDB entries 1lbs (sixth example in §1.3.4; see also the end of 3.2.5) and 2w11. The latter case is discussed in detail in 3.5 and, in particular, the calculation of twin index and obliquity angle for this twin are given in 3.5.4.

The only physical constraint on the twin lattice (an approximately invariant sublattice of the individual lattice) is that imposed by dimensional similarity of the lattices at the composition plane. This condition alone does not impose any requirement on the three-dimensional symmetry of the twin lattice, exact or approximate. The use of lattice-pseudosymmetry-based description of twinning might therefore seem unnatural, were it not for an empirical observation of statistical nature that a large obliquity angle and twin index are unfavourable for the occurrence of a twin. Le Page (2002) suggests an upper limit of six for the twin index and of six degrees for obliquity angle, although twins with exceptionally high index are known (Hahn & Klapper, 2003, see also §3.5).

The effect of twin lattice symmetry on the diffraction pattern of twinned crystals is emphasised in a coarser classification (Giacovazzo *et al.*, 1992), in which TLS-twins are opposed to TLQS-twins, and TLS and TLQS stand for twin-lattice symmetry and twin-lattice quasisymmetry, respectively. Accordingly, TLS twins include twins by merohedry and twins by reticular merohedry, in which the reflections from two individual crystals overlap exactly in every n-th plane of the reciprocal space (n is the twin index) and TLQS twins include twins by pseudomerohedry and reticular pseudomerohedry, in which the overlap in every n-th plane is partial. However, it makes sense to distinguish between $n = 1$ and $n > 1$ as the former case entails more problems for structure solution and refinement and therefore the previously described classification by Friedel (1926) is typically used in macromolecular crystallography.

A finer symmetry-based classification is proposed by Nespolo & Ferraris (2004). In particular, the distinction is made between twins by pseudomerohedry with zero and non-zero obliquity angle. The former case is characterised by an exact (within experimental error) accidental metric symmetry and is therefore termed as twinning by metric merohedry (see also Flack, 1987).

In fact, this definition is structurally justified as it applies to a special morphology of twinned crystals in which the very presence of twinning implies exact lattice symmetry relative to a twin operation, which does not belong to the holohedry of the crystal (§3.3, §3.4). Of course, the constraints on unit cell parameters are not a consequence of twinning, but of certain structural features of individual crystals, which are only emphasised by the presence of twinning by metric merohedry.

The geometrical (twin-lattice symmetry) classification of twins emphasises the most general features of a given twin and imposes restrictions on its possible morphology. However the definition of twinning becomes vague in special cases of single-phase morphologies. Millward *et al.* (1983) describe an oriented intergrowth of two individual crystals of the same phase related by 90^o rotation, in which the composition plane is parallel to the (010)-plane of one individual crystal and to the (001)-plane of the other, the two crystallographic planes being independent relative to the crystal symmetry. This intergrowth is a twin from the point of view of lattice symmetry, but it was not recognised as a true twin from the point of view of its morphology owing to the lack of chemical integrity at the composition plane. In this case the composition plane is not symmetric relative to any of the potential twin operations and this might be another argument for avoiding the term twin.

1.2.2 Determination of approximate lattice symmetries

The geometrical analysis of the lattice is nevertheless sufficient for the majority of structural studies, in which the structure of an individual crystal is of interest and twinning is an unwanted factor which must be taken into account to avoid gross errors in the structure determination and refinement. In such studies no distinction is needed between twinning and, for example, the intergrowth of two individual crystals in twin orientations as in the above example by Millward *et al.* (1983).

Given the X-ray data for a single lattice, the detection of twinning starts from prediction of possible twin operations from the unit cell parameters and the point symmetry of the data. Le Page (2002) proposed an algorithm applicable for a general case of twinning by (reticular) (pseudo)merohedry. A more specialised technique for identifying data sets where the unit-cell parameters and space group can allow twinning by (pseudo)merohedry and finding the possible twin operations is described by Flack (1987).

Twinning by reticular (pseudo)merohedry can usually be handled in the later stages of the structure refinement. It can be deduced from the presence of non-origin peaks in the Patterson map, which are not accounted for by translational NCS (§3.5). In a more regular approach, possible twinning laws and associated peaks in the Patterson map (or modulation of intensities) owing to partial overlap of reflections can be predicted from the unit cell parameters, and the hypothesised twinning laws can be accepted or rejected based on their presence in the experimental data.

Twinning by merohedry, metric merohedry or pseudomerohedry with small obliquity angle is the most unfavourable case for structure determination. In the first two cases a complete overlap of twin related reflections occurs, and in the third case the intensities of partially overlapped reflections are likely to be jointly integrated during the processing of diffraction images. In a frequent case of approximately equal volumes of individual crystals (perfect twinning), the apparent symmetry of the data is higher than the true point group symmetry of the individual crystals and therefore wrong symmetry assignment is possible that results in problems with the structure determination. Similarly to twinning by reticular (pseudo)merohedry, the detection of twinning by (pseudo)merohedry includes lattice symmetry analysis to predict possible twin operation(s) and data analysis to test the predictions. In contrast to twinning by reticular (pseudo)merohedry, twinning by (pseudo)merohedry does not produce an alternative lattice(s) and does not cause the modulation of intensities, which could be detected based on the mean values of intensities in a series of parallel planes in reciprocal space. Therefore several twin tests were developed that utilise statistics that are finer than mean intensity.

1.2.3 Perfect twinning test

For the rest of this section, the term twinning means twinning by (pseudo)merohedry with two individual crystals (twinning by hemihedry) and the crystal structure is assumed to be non-centrosymmetric, the case relevant to macromolecular crystallography.

Given an X-ray data set, the three following questions related to twinning are to be answered. (i) Are the X-ray data twinned? If so, (ii) what is the twinning fraction α, the relative size of smaller twin domain, and (iii) what is the true symmetry of an individual crystal?

Let assume that the data are “ideal”, that is, the experimental error can be neglected and the structure factors of the twin-related reflections are not correlated. In this case, the first two questions and, provisionally, the third question may be answered using the method proposed by Rees (1980), in which the experimental distributions of normalised intensities are compared with the theoretical distributions derived from the Wilson distribution (Wilson, 1949).

Rees derived a simple analytical expression for the cumulative distribution of the normalised intensity Z for acentric reflections and variable twinning fraction α,

$$P(Z) = 1 - \frac{(1-\alpha)\exp\left(-\dfrac{Z}{1-\alpha}\right) - \alpha\exp\left(-\dfrac{Z}{\alpha}\right)}{1-2\alpha}, \tag{6}$$

and used numerical integration to tabulate such a distribution for centric reflections. (The latter distribution can be expressed in terms of a hypergeometric function.)

Acentric intensities constitute a majority of macromolecular X-ray data. Comparison of experimental and theoretical acentric distributions provide an answer to questions (i) and (ii). Rees underlines that determination of the twinning fraction does not require knowledge of the active twin operation. However, in a robust implementation of the test, all the potential twin operations still need to be known, as all the reflections that would have special distribution, if any of the potential twin operations were active, need special treatment.

For answering only question (i), it is sufficient to compare the experimental curve with limiting cases of the distributions, for $\alpha = 0$ and $\alpha = 1/2$. In these limiting cases, there are simple analytical expressions for both kinds of reflection, centric,

$$\begin{aligned} &P(Z|\alpha = 0) = \operatorname{erf}\left(\sqrt{\tfrac{Z}{2}}\right) = \sqrt{\tfrac{2}{\pi}} \int\limits_0^{\sqrt{Z}} \exp\left(-\tfrac{\zeta^2}{2}\right) \mathrm{d}\zeta \\ &P(Z|\alpha = \tfrac{1}{2}) = 1 - \exp(-Z) \end{aligned} \tag{7}$$

and acentric,

$$\begin{aligned} &P(Z|\alpha = 0) = 1 - \exp(-Z) \\ &P(Z|\alpha = \tfrac{1}{2}) = 1 - (1 + 2\,Z)\exp(-2\,Z) \end{aligned} \;. \tag{8}$$

Rees notes that the distributions for twinned centric reflections and for untwinned acentric reflections coincide. The nature of this coincidence becomes clear if the distributions (7) and (8) are rewritten in terms of chi-squared distributions. For centric reflections

$$\begin{aligned} &Z \sim \chi^2_1 \qquad (\alpha = 0) \\ &Z \sim \tfrac{1}{2}\chi^2_2 \qquad (\alpha = \tfrac{1}{2}) \end{aligned} \tag{9}$$

and for acentric reflections

$$\begin{aligned} &Z \sim \tfrac{1}{2}\chi^2_2 \qquad (\alpha = 0) \\ &Z \sim \tfrac{1}{4}\chi^2_4 \qquad (\alpha = \tfrac{1}{2}) \end{aligned} \;. \tag{10}$$

These equations become obvious after the following consideration. The real and imaginary parts of the acentric structure factor, A and B, as well as the centric structure factor without the phase multiplier, C are normally distributed with zero mean. Therefore, the untwinned centric intensity, C^2 is the square of the normally distributed random variable. A perfectly twinned centric intensity is a sum of intensities of two individual crystals, $C_1^2 + C_2^2$ and an untwinned acentric intensity is the sum of the real and imaginary parts squared, $A^2 + B^2$, both intensities being sums of squares of two normally distributed independent random variables. Finally, the twinned acentric intensity is the sum of four normal variables squared, $A_1^2 + B_1^2 + A_2^2 + B_2^2$. Thus, normalised intensities in untwinned and twinned centric cases and in untwinned and twinned acentric cases are distributed as chi-squared with one, two, two and four degrees of freedom divided by the number of degrees of freedom. This consideration can be continued to assign a chi-squared distribution with three and six degrees of freedom, $\chi^2_3/3$ and $\chi^2_6/6$ to perfectly twinned centric and acentric reflections of ternary twin, *etc*.

In addition, there are "apparent" centric reflections located in the plane orthogonal to a twin two-fold axis (Lunin *et al.*, 2007). If the twin axis were crystallographic, these reflections would be centric. Intensities of the twin mates located in such a plane are equal, therefore independent of twinning fraction and distributed as χ^2_2, as if they were perfectly twinned centric intensities. On the other hand, the distribution of the true centric intensities in a partial twin is intermediate between χ^2_1 and χ^2_2. Therefore, given, for example, a partial twin with *P*121 individual crystals, *Pmmm* lattice and twin two-fold axes along *a* and *c*, the true point group can in principle be identified through the analysis of intensity distributions in three planes, 0*kl*, *h*0*l* and *hk*0. This method should however be avoided, as only a small fraction of all reflections is analysed. Moreover, this method is invalid in the case of OD-twins (§1.3), which represent a significant fraction of macromolecular twins and in which the distribution of untwinned intensities in the planes of interest may differ from χ^2_2.

The similarity of the perfectly twinned distributions for true centric reflections and "apparent" centric reflections gives a technical advantage in the case of using intensity statistics for answering question (i) only, for detection of twinning. The perfectly twinned data are generated from partially twinned data by averaging the intensities of twin mates and rejecting reflections, for which any one of the twin mates is not measured. Reflections are subdivided into acentric and centric relative to the point group of the averaged data and corresponding cumulative intensity distributions are compared with the reference distributions for $\alpha = 0$ and $\alpha = 1/2$ only. This version of the perfect twinning test treats the centric reflections in a robust manner. However, it nullifies one of the advantages of the original implementation, which uses all measurements regardless of whether all twin mates of a given reflection are measured or not.

The second moments of the normalised intensities are also used for detection of twinning and estimation of twinning fraction (Giacovazzo *et al.*, 1992). Under the same assumptions as above, the second moments equal 3.0 and 2.0 for untwinned and perfectly twinned centric reflections, respectively, and 2.0 and 1.5 for untwinned and perfectly twinned acentric reflections. These values can be directly obtained from (7) and (8) or from the corresponding normal distributions. The second moments may be significantly distorted by outliers and experimental errors and therefore they are typically represented as a function of resolution. The second moment is mainly defined by the right tail of the intensity distribution (strong intensities). In this context, the cumulative intensity distribution is typically examined for relatively weak reflections to provide complementary information to the moment test. Another important use of the plot of second moments (for acentric reflection) *vs.* resolution is to find the resolution range where the second moment is approximately constant and therefore the cumulative distribution test is justified.

Rees emphasises that the distributions for twinned intensities are valid only if structure factors related by twin operation are not correlated. He provides an example in which the twin axis is approximately parallel to the NCS axis (such cases are further referred to as interference between NCS and twinning) and shows that the use of only higher resolution shells for the twinning test restores the theoretical distributions. This effect is explained by some asymmetry of NCS-related molecules relative to the twin operation. This asymmetry decreases the correlation between twin-related structure factors with increase of resolution. In contrast, the relative experimental errors are higher at higher resolution, where they introduce larger systematic distortions into the theoretical distributions. Even if there were no systematic errors from the detector or data integration, the distribution of observed intensities would deviate from the distribution of “exact” intensities because of the Poisson distribution of quantum counts. The resolution range in which the experimental distributions well match the theoretical distributions can therefore be very narrow or even absent.

The following numerical experiment illustrates the effect of interfering NCS on the perfect twinning test. The 1i1j X-ray data set represents an untwinned crystal with pseudosymmetry. The space group and pseudosymmetry space group are $P2_12_12_1$ and $P4_32_12$, respectively. The r.m.s.d. between the true structure and its symmetrised copy is about 0.25 Å. A data set with perfect twinning was simulated from the original untwinned data. The experimental second moment of Z against resolution and the cumulative distribution of Z are shown in Fig. 1.1. The experimental curves for the original untwinned data set match theoretical predictions (Figs. 1.1*a* and 1.1*b*); however, this is not so for the simulated data set, where the deviation from the theoretical curves for untwinned data is much less than expected and does not match the theoretical predictions for a perfect twin (Figs. 1.1*c* and 1.1*d*). In twins with as strong pseudosymmetry as in this example, the effect of NCS on the cumulative distribution extends to very high resolutions. It can be expected that the closer the NCS operation is to an operation of higher point group, the less contrast there is between the results of perfect twinning tests with untwinned and twinned data. In the limit, the NCS becomes crystallographic symmetry, the twin operation becomes an element of the point group symmetry of the untwinned crystal and untwinned cumulative distributions of intensities are restored. This lack of contrast creates difficulties for diagnostics. Fortunately, crystal structures with strong pseudosymmetry can frequently be solved and refined as a first approximation in a higher symmetry space group, so the structure can be resolved later and further refined in the correct space group (§4.4). In this scenario the determination of the exact space group is postponed and there could be a problem with the completeness of data if it would become necessary to reprocess them later in a lower symmetry point group.

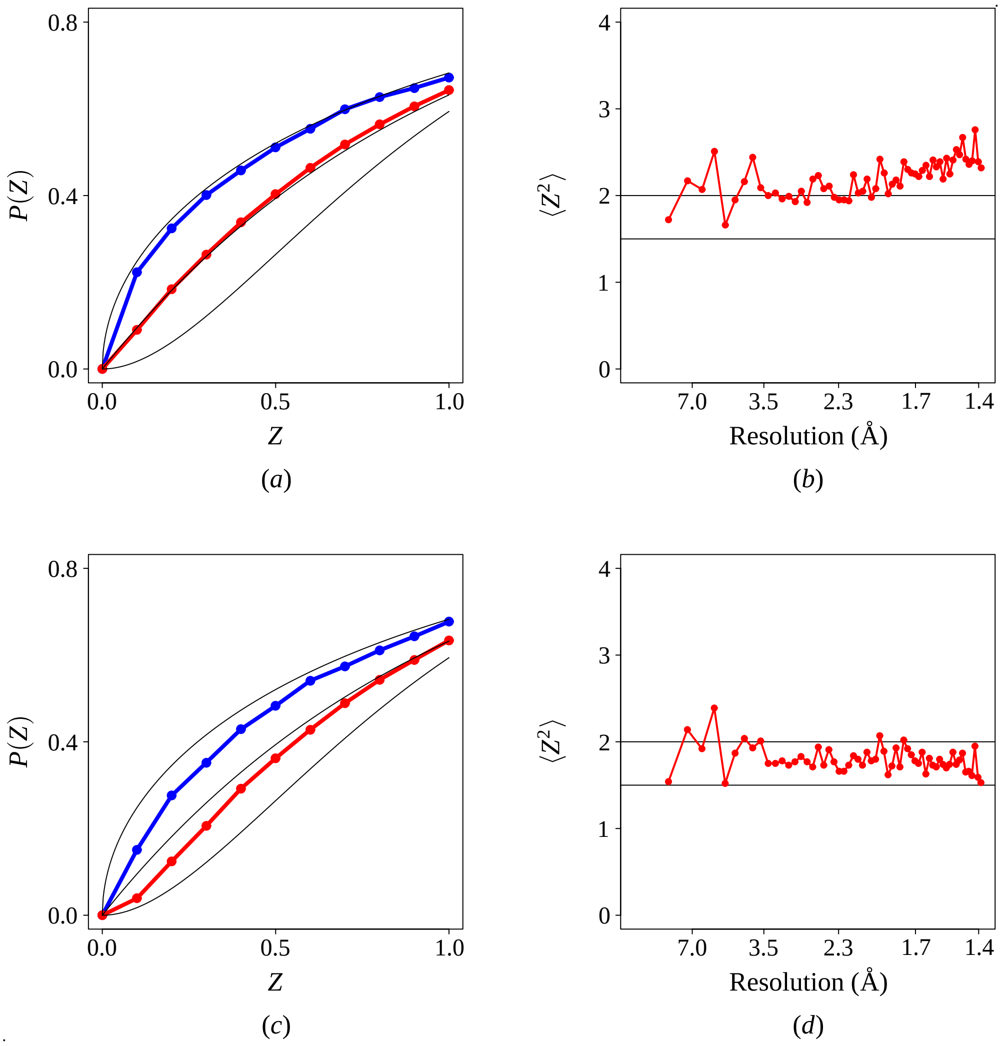

Figure 1.1. Effect of NCS on perfect twinning tests if the NCS and twin axes are approximately parallel. The plots were drawn using X-ray data from PDB entry 1i1j (Lougheed *et al.*, 2001).

Plots (*a*) and (*b*) are for the original data; (*c*) and (*d*) for data with simulated hemihedral twinning.
Plots (*a*) and (*c*) show the cumulative distributions of *Z*, and (*b*) and (*d*) show the second moment of *Z* for acentric reflections against resolution.

The cumulative distribution plots show
(i) The top thin black line is the theoretical distribution for centric untwinned data; the central line is the distribution for both acentric untwinned data, and centric perfectly hemihedrally twinned data; and the bottom line shows the theoretical distribution for acentric perfectly hemihedrally twinned data.
(ii) The thick blue and red lines present observed or simulated data and show distributions for centric and acentric reflections, respectively.

The second moment plots show
(iii) The thin black lines show theoretical moments for untwinned acentric reflections (top line) and perfectly hemihedrally twinned acentric reflections (bottom)
(iv) The red line corresponds to the observed or simulated acentric data.

The effect of experimental errors on the cumulative distribution is hard to predict. In the first example (Fig. 1.2) the experimental cumulative distribution of Z for acentric reflections clearly indicates twinning with a high-resolution cut-off at 1.7 Å. In contrast, the same test but with all data is misleading and the experimental curves are close to the theoretical curves for untwinned crystals. The high-resolution limit of 1.7 Å was chosen because R-standard $=\langle\sigma(F)\rangle/\langle F\rangle$ started growing and the second moment of Z for acentric reflections started changing at about this resolution. (The required plots of R-standard and second moment of Z against resolution were obtained using *SFCHECK* and *TRUNCATE*, respectively.) The two criteria correlate demonstrating that the misleading behaviour of the cumulative distribution test is caused by the experimental errors or during the merging of weak intensities. However, these “visual” rules are quite subjective. The use of an upper limit for R-standard is another option. In this particular example R-standard was approximately 0.07 at the cut-off resolution. According to my experience this threshold value works in most cases. However, the low resolution cut-off, which was applied to keep high completeness in the tested range, was not critical in this case.

The second example (Fig. 1.3) is the untwinned data set for a crystal of human deoxycytidine kinase belonging to $P4_32_12$ space group (Elisabetta Sabini, personal communication). The behaviour of the cumulative distribution test is just opposite to that in the first example; the test with all data (resolution 1.77 Å) indicates twinning, whereas the correct untwinned statistics are observed with the high-resolution cut-off at 3.0 Å, chosen using the same criteria as in the first example. Again, the correct result was only obtained with truncated data. It is important to emphasise that the high-resolution reflections do contain useful information about the structure and the resolution cut-off is only needed for some statistical applications including cumulative distribution tests.

Thus, it is possible to identify the resolution range for which it is correct to neglect experimental errors and to assume that all normalised intensities are sampled from only two distributions specific for centric and acentric reflections. On the contrary, it is not easy and not always possible to find the resolution range in which both experimental errors and correlations between twin related structure factors can be neglected. The effect of these correlations is analysed below in more detail (§3) to assist in interpretation of perfect twinning tests.

1.2.4 Partial twinning test

The reason why the cumulative intensity distribution is mainly used only for detection of twinning is that a more efficient way of estimating twinning fraction exists, the examination of H-statistics (Yeates, 1988). This method can also be used for point group assignment in the case of partial twinning by examining H-statistics for all rotations allowed by unit cell parameters.

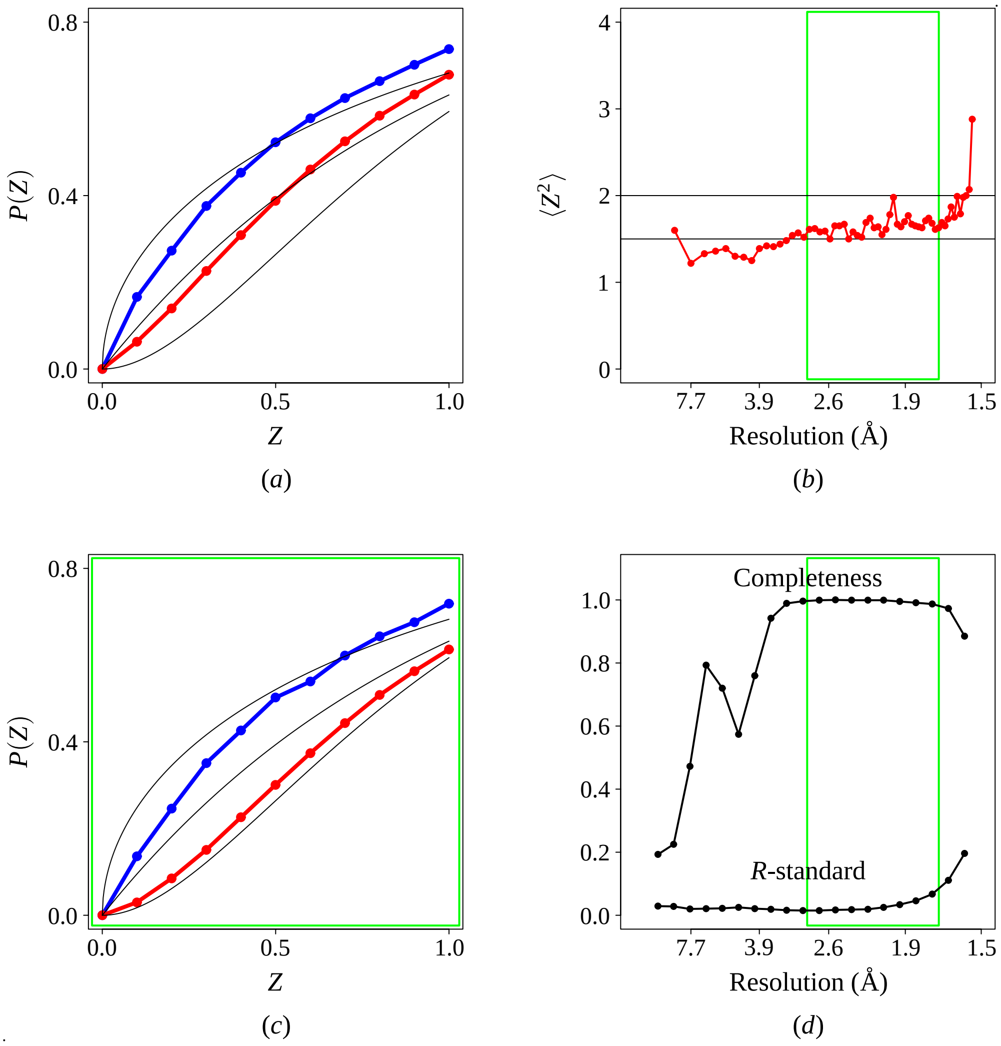

Figure 1.2. Effect of resolution cut-off on perfect twinning tests. Example 1: twinned crystal of mutant interleukin 1-beta (PDB code 1l2h; Rudolph *et al.*, 2003).

The resolution range used in (*c*) is outlined by green boxes in (*b*) and (*d*).
The colour legend for (*a*), (*b*) and (*c*) is the same as for similar plots in Fig. 1.1.

(*a*) Cumulative distributions of Z for all the data, resolution range 18.6–1.54 Å,

(*b*) Second moment of Z for acentric reflections against resolution,

(*c*) Cumulative distributions of Z in the resolution range 18.6–2.2 Å,

(*d*) Completeness and R-standard against resolution. R-standard $= \langle \sigma(F) \rangle / \langle F \rangle$

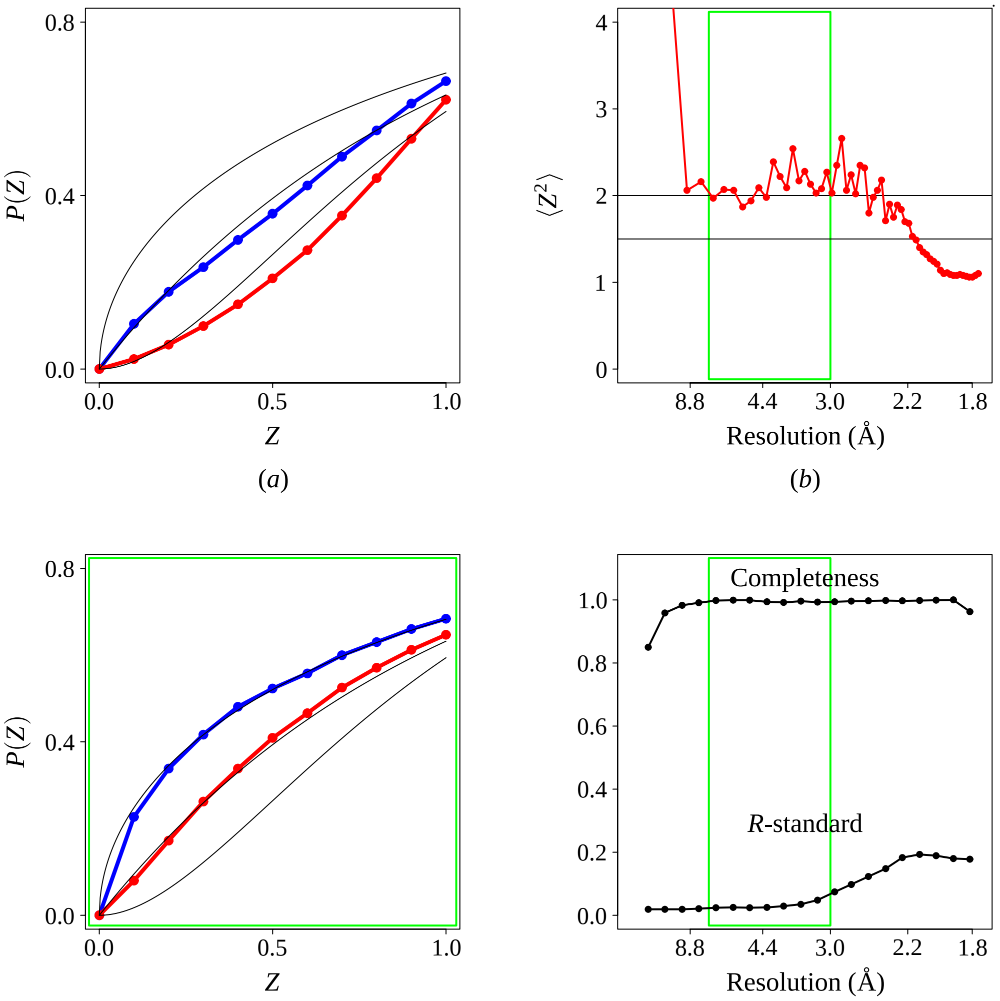

(*a*) (*b*)

(*c*) (*d*)

Figure 1.3. Effect of resolution cut-off on perfect twinning tests. Example 2: untwinned crystal of human deoxycytidine kinase (Elisabetta Sabini, personal communication).

The resolution range used in (*c*) is outlined by green boxes in (*b*) and (*d*).
The colour legend for (*a*), (*b*) and (*c*) is the same as for similar plots in Fig. 1.1.

(*a*) Cumulative distributions of Z for all the data, resolution range 29.0–1.77 Å,

(*b*) Second moment of Z for acentric reflections against resolution,

(*c*) Cumulative distributions of Z in the resolution range 7.0–3.0 Å,

(*d*) Completeness and R-standard against resolution. R-standard $= \langle\sigma(F)\rangle / \langle F\rangle$

Assuming “ideal” conditions, *viz.* negligible experimental errors and uncorrelated structure factors of the twin mates, consider the joint probability distribution of normalised intensities of two twin-related acentric reflections,

$$\mathrm{d}P(I_1, I_2) = \exp(-I_1 - I_2)\,\mathrm{d}I_1\,\mathrm{d}I_2, \qquad 0 < I_1,\, I_2 < \infty. \tag{11}$$

The intensities I_1 and I_2 are independent random variables, but this is not so for twinned intensities

$$\begin{aligned} J_1 &= (1-\alpha)I_1 + \alpha I_2 \\ J_2 &= (1-\alpha)I_2 + \alpha I_1 \end{aligned} \tag{12}$$

unless the twinning fraction α is zero.

The transformation of random variables

$$\begin{aligned} &H = |J_1 - J_2|/(J_1 + J_2), && 0 < H < 1 - 2\alpha \\ &Z = (J_1 + J_2)/2, && 0 < Z < \infty \\ &S = \mathrm{sign}(J_1 - J_2), && S \in \{-1,\, 1\} \end{aligned} \tag{13}$$

can be inverted and therefore the random variables H, Z, S completely describe the probabilistic model. The distribution of these variables immediately follows from the distribution of I_1 and I_2,

$$\mathrm{d}P(H, Z, S) = \frac{2}{1-2\alpha}\exp(-2Z)\,Z\,\mathrm{d}Z\,\mathrm{d}H. \tag{14}$$

The random variables S, H and Z are independent. Realisations $S = -1$ and $S = 1$ are equally possible, Z is distributed as $\chi^2_4/4$ according to (10) and H is distributed uniformly from 0 to $1 - 2\alpha$,

$$\mathrm{d}P(H) = (1-2\alpha)^{-1}\,\mathrm{d}H. \tag{15}$$

The dependence on α only enters the distribution of random variable H, which is therefore a sufficient statistic (Stuart *et al.*, 1999) for the twinning fraction α. Formally, the condition of sufficiency of H for α can be written as $P(J_1, J_2|H, \alpha) = P(J_1, J_2|H)$ and follows from the independence of Z, S and H and (15). This means that the random variable H contains all the information about α.

Experimental data can be transformed similarly and represented in terms of the mean intensities of twin mates and their absolute differences. The experimental distribution of normalised mean intensities is suitable for answering question (i), for detection of twinning. In turn, the distribution of H is most suitable for estimation of the twinning fraction, question (ii). In addition, the latter can be used for point group assignment, question (iii) provided that the twinning is not perfect, as the distribution of H does not distinguish between perfect twinning operation and crystal symmetry operation.

The random variable H is no longer a sufficient statistic for α in the presence of experimental errors or correlation between twin-related structure factors. It is reasonable to assume that it nevertheless remains a “good” statistics containing most of the information about the twinning fraction in practical cases of moderate correlation and experimental errors. The actual problem is not that some of the information is lost, but that interpretation of the H-test becomes complicated if the distribution of H is affected by various factors.

The “ideal” cumulative distribution $P(H)$ of the random variable H is a straight line over the whole range of possible H (Eqn. 15). In theory, which does not account for the correlation between the twin-related intensities and experimental errors, the linearity holds for both twinned and untwinned data and the slope of the plot $P(H)$ against H depends on the twinning fraction (blue lines in Fig. 1.4*a*).

In the original version of the H-test (Yeates, 1988) the linearity is essential, as the twinning fraction is estimated from the mean value of H. However, the linearity breaks if there are theoretically impossible differences between experimental intensities related by the twin operation. Such differences may appear as a result of radiation damage to the crystal, if there is a long time interval between recording two related reflections. Large differences could also occur, if the X-ray beam was focused at different parts of the crystal during these two measurements, as these parts can have different values of the twinning fraction or even belong to different individual crystals. Moreover, a certain number of large relative differences between weak reflections could arise for purely statistical reasons. The presence of such outliers distorts the experimental distribution of H at larger H and causes non-linearity as in Fig. 1.4(*a*). Such cases can be treated by a modified H-test in which the twinning fraction is estimated using the slope of the plot at the origin (Yeates & Fam, 1999).

If twin axis is approximately parallel to an NCS-axis, then the pairs of intensities involved in the H-test correlate and the cumulative distribution of H becomes non-linear over the whole range of the argument (Fig. 1.4*b*) and both versions of H-test fail to give a correct estimate of the twinning fraction. In cases similar to that in Fig. 1.4(*b*), however, the twinning fraction can be estimated from the value of H at the point where the experimental curve approaches the line $P(H) = 1$. In this formulation the H-test is equivalent to the Britton test (Britton, 1972). A disadvantage of such a formulation is that the estimate of twinning fraction is based on the right tail of the distribution, which can be seriously corrupted by the presence of outliers as mentioned above (Fig. 1.4*c*). Thus, further improvement of the test can only be achieved by accurate modelling of the effect of NCS interfering with twinning (§3.1) and by accounting for outliers, while keeping the advantage of the original version of the H-test, in which the whole data set is utilised.

An accurate interpretation of the H-test is further complicated by the effect of the experimental uncertainties of the intensities. Lunin *et al.* (2007) generated reference distributions of H in the presence of experimental uncertainties using stochastic methods. It was shown that experimental distributions match the predictions, in which both the linearity of $P(H)$ and the tangent of the $P(H)$ at low H are affected compared to the case of exact measurements. Visually, the effect is very similar to that owing to the presence of interfering NCS.

These data suggest that, similarly to the perfect twinning test, the H-test should rather be treated as a qualitative test except for the cases of essentially linear $P(H)$. However, a good

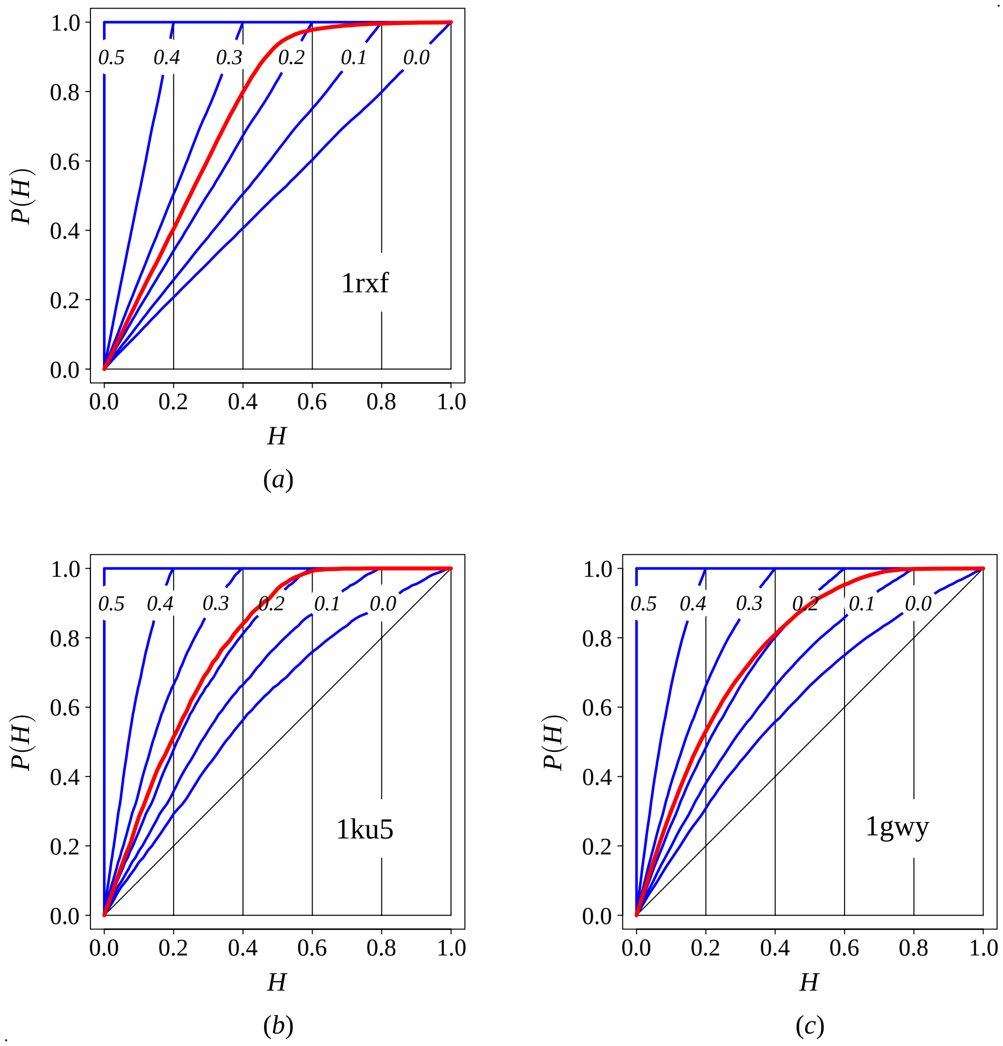

(*a*)

(*b*)

(*c*)

Figure 1.4. Effect of NCS and experimental errors on partial twinning test (H-test).

Plots present cumulative distributions of H for three twins: (*a*) PDB entry 1rxf (Morgan *et al.*, 1994), (*b*) PDB entry 1ku5 (Li *et al.*, 2002) and (*c*) PDB entry 1gwy (Mancheno *et al.*, 2003). In 1ku5 and 1gwy, NCS and twin axes are approximately parallel. Experimental distributions are represented by red lines. The intensities derived from atomic models were used to simulate cumulative distributions of H (blue lines) for different twinning fractions (the numbers in front of the blue lines).

estimate of the twinning fraction is only important for experimental phasing, which requires an accurate detwinning. For MR structure solution detwinning is not needed and the twinning fraction is estimated along with atomic parameters during refinement. However, understanding of various peculiarities in the behaviour of $P(H)$ can be important for correct point group assignment.

1.2.5 Refinement using twinned data

The perfect twinning test and partial twinning tests discussed above are important tools in the preliminary analysis of the X-ray data. These help avoid errors in space group assignment and guide detwinning, which is less relevant for MR but is important for experimental phasing using twinned data. However, joint refinement of atomic model and twinning fraction remains the ultimate twinning test (Herbst-Irmer & Sheldrick, 1998). In addition, the refinement of twinning fraction for racemic twins (Flack, 1983) in the presence of anomalous signal is a tool for establishing the true enantiomorph in small molecule structures.

The program *SHELXL* (Sheldrick, 2008) provides all necessary facilities for such refinements and handles both twins by (pseudo)merohedry and by reticular merohedry (Herbst-Irmer & Sheldrick, 1998) including obverse/reverse twins (Herbst-Irmer & Sheldrick, 2002). Its flexibility in defining restraints and constraints allows an accurate refinement of pseudosymmetric twins (Müller *et al.*, 2006).

Specialised macromolecular refinements in CNS (Brünger *et al.*, 1998) and *phenix.refine* (Afonine *et al.*, 2005) implementing the FFT (Ten Eyck, 1977) are faster and therefore more suitable than *SHELXL* for twinned macromolecular crystals with very large asymmetric units. In the case of twinned data, all these programs use least squares refinement against intensity target. The twin refinement has recently been implemented in *REFMAC* (Murshudov *et al.*, 1997) which strictly follows the Bayesian paradigm and therefore uses a marginal likelihood target (Garib Murshudov, personal communication). In addition, the internal representation of X-ray data in *REFMAC* makes it possible to handle twins by reticular merohedry.

1.3 OD structures

Partially disordered structures (including twins) and series of polymorphs are frequently composed of geometrically and chemically equivalent layers; Dornberger-Schiff (1956) introduced the term OD-structure (OD stands for “order-disorder” to indicate either actual or potential disorder) to describe this important particular set of crystal structures.

It must be underlined that a single crystal can be an OD-structure. In such crystals there is nothing special about the diffraction of X-rays or structure solution. The concept of OD-family and corresponding formalism is used in the X-ray analysis of a series of polymorphs given the structure of one of them. Such an application is not very important for macromolecular crystallography, where the structure of a biomolecule is of interest but not its crystallographic environment. What is interesting about OD-structures from the point of view of macromolecular crystallography is the description and prediction of crystal disorder including twinning. In any OD-structure there is a potential for a well-defined type of one-dimensional disorder. Thus, on one hand, one can expect a higher frequency of twinning in OD-structures than in fully ordered structures (defined below in §1.3.1), but on the other hand, the morphology of twinning becomes evident from the structure of an individual crystal. Another specific feature of an OD-twin is that the twin operations belong to the point group symmetry of the OD-layer and therefore there is a strong correlation between complex structure factors of reflections related by the potential twin operation. As this was previously discussed in §1.2.3 and §1.2.4, such a correlation complicates the detection of twinning and therefore the analysis of OD-structures from this point of view is quite important (§3.4 and §3.5).

A partially disordered OD structure can be considered as a limiting case of an OD-twin with small sizes of individual crystals. Thus the above remarks on OD-twins are also relevant to partially disordered OD-structures. In addition, the small sizes of the ordered domains result in a significant diffuse scattering of X-rays and, as the disorder in OD-structures is one-dimensional, the reflections have streaks along one direction, in which translational symmetry is only local. In practical terms, the one-dimensional partial disorder leaves more chances for structure solution compared to two- or three-dimensional disorder. Moreover, partially disordered OD-structures can be considered in the first approximation as twinned structures and diffuse features in the images can be ignored, as automatically happens during standard data processing. More accurate modelling of the crystal diffraction requires an analysis of the interference between adjacent ordered domains, but in practice this is only done when it is absolutely necessary for interpretation of the diffraction data (Examples 3 and 5 in §1.3.4). It seems therefore likely that the partial disorder occurs more frequently than is thought and is unnoticed or ignored in most cases.

1.3.1 Definition and classification

A set of structures built of equivalent layers is called an OD-family and the members of the family are called OD-structures provided that all pairs of adjacent layers in all members of the family are equivalent but there are non-equivalent triplets of contacting layers. The layers in different orientations (if present) are assumed to have the same two-dimensional translational symmetry. This defines OD-structures of types I and II (Dornberger-Schiff & Grell-Niemann, 1961). The difference between the two types is illustrated in Fig. 1.5; if the surfaces of layers are equivalent, then the OD-structure is of type I, otherwise of type II. An earlier classification (Dornberger-Schiff, 1956) distinguishes between type A with all layers in the same orientation (Figs. 1.5*c* and 1.5*b*) and type B with at least two different orientations of layers present (Figs. 1.5*h* and 1.5*f*). Combination of the two classifications is used in this thesis to distinguish types I/A, I/B, II/A and II/B (Fig. 1.5). The translation vectors relating adjacent layers in types I/A and II/A are called stacking vectors. At least two different non-equivalent stacking vectors are possible; otherwise the structure is not OD.

OD-structures of type II correspond to “head-to-tail” packing of layers with two different surfaces. The definition of OD-structures needs to be generalised to cover types I and II as well as type III OD-structures with “head-to-head” and “tail-to-tail” packing (type III is always III/B). The structure composed of equivalent layers is OD if (i) translational symmetries of all layers regardless of their orientations are equal, (ii) equivalent surfaces of layers form equivalent contacts with adjacent layers, (iii) at least some of the operations relating the layer L_1 to the layer L_2 do not relate L_2 to L_1 and (iv) at least some of the symmetry element of the layer L_1 are not the symmetry elements of the layer L_2. Statements (i, ii) and (iii, iv) deliver a brief formulations of the vicinity condition and the maximum layer condition, respectively (Dornberger-Schiff & Grell-Niemann, 1961). For example, the condition (iii) ensures that the structure in Fig. 1.5(*c*) is of type I unlike the structure in Fig. 1.5(*d*), which is of type III, while the condition (iv) ensures that the structure in Fig. 1.5(*b*) is OD but that in Fig. 1.5(*a*) is not. The latter is called a fully ordered structure. Were it not for (iii), this structure would be the only member of an OD-family with ambiguous choice of the OD-layers.

The vicinity condition means that there exists a strong energy minimum corresponding to a given packing of adjacent layers and only this packing occurs. The local interactions are therefore the same in all members of an OD family, although the global organisation is different in different members owing to asymmetric packing. Therefore, any representative of the OD family gives full information on the covalent bonding and intermolecular contacts in all other members. Furthermore, given one OD-structure (say a structure of a single crystal) the potential disorder and polymorphism can be predicted. These important properties of OD-structures justify the

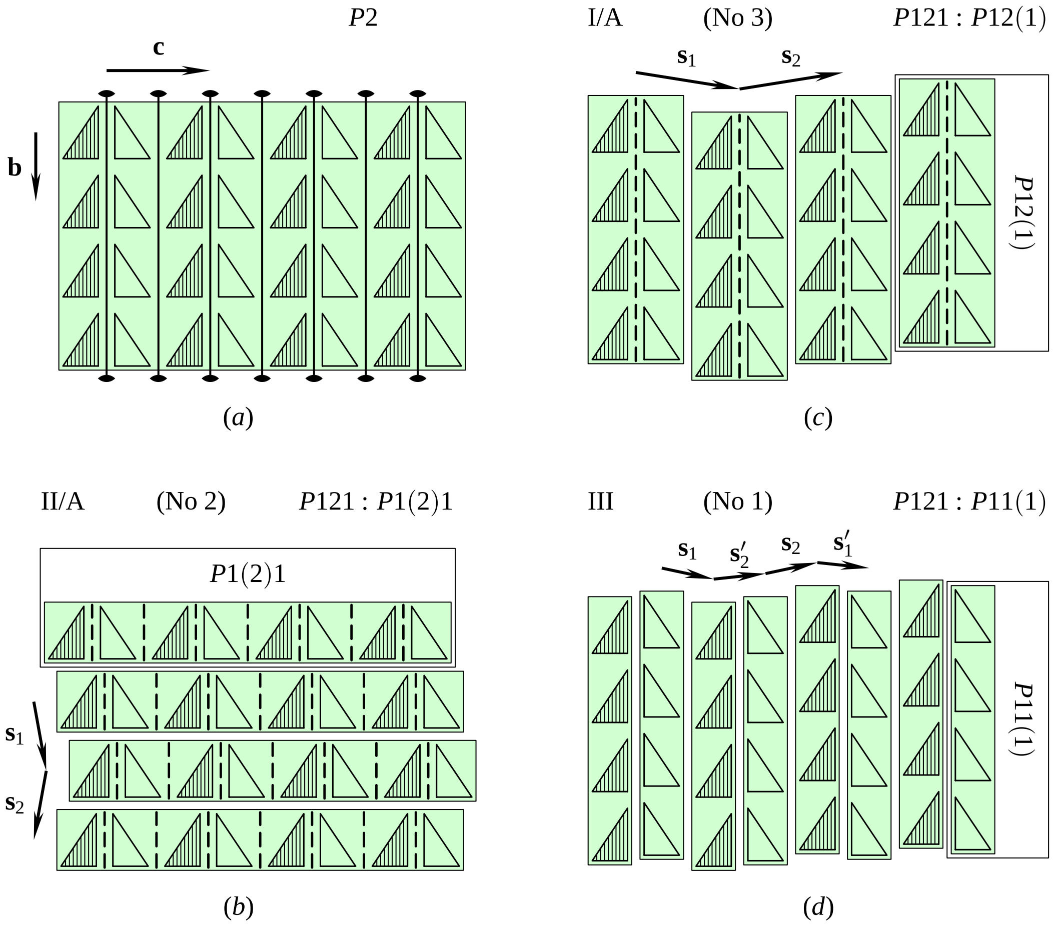

Figure 1.5. Types of OD-structures.

This classification applies to OD-structures composed of identical OD-layers and accounts for three general characteristics: (i) geometrical identity of two surfaces of a single layer; (ii) geometrical identity of contacting surfaces of adjacent layers; (iii) identical orientations of all layers.

Drawings (*b*), (*c*), (*d*), (*f*) and (*h*) present OD-structures of five possible types. The type code is shown in the top left corner of the drawing; each code includes one or two indices which have the following meanings:
(I) two surfaces of a single layer are identical;
(II) both two surfaces of a single layer and two contacting surfaces are different;
(III) two surfaces of a single layer are different but the contacts are between identical surfaces;
(A) all layers have the same orientation and;
(B) there are layers having different orientations.

Drawings (*a*), (*e*) and (*g*) present fully ordered structures which can be divided into layers identical to OD-layers of related OD-structures; (*a*) relates to (*b*), (*c*) and (*d*); (*e*) relates to (*f*); and (*g*) relates to (*h*).

The structures are composed of identical asymmetric molecules shown by triangles. OD-layers are indicated by green bands in the background. Fully ordered structures have continuous background.

(Continued on the next page.)

introduction of special terms and nomenclature. Extension of the definition to include structures composed of layers with different chemical composition (Grell & Dornberger-Schiff, 1982) is also justified, as long as the generalised vicinity condition is obeyed. The term OD-structure is sometimes applied to structures composed of blocks with one-dimensional translational symmetry. There also exist structures composed of finite blocks. A general term, modular structure (Nespolo & Ferraris, 2004) is applicable to all these cases.

1.3.2 Symmetry of OD-structures

The OD-layer is a three-dimensional object with two-dimensional translational symmetry. The total symmetry of the layer is therefore described by one of 80 plane space groups (Dornberger-Schiff, 1956). An OD-family contains both structures with space group symmetry and globally

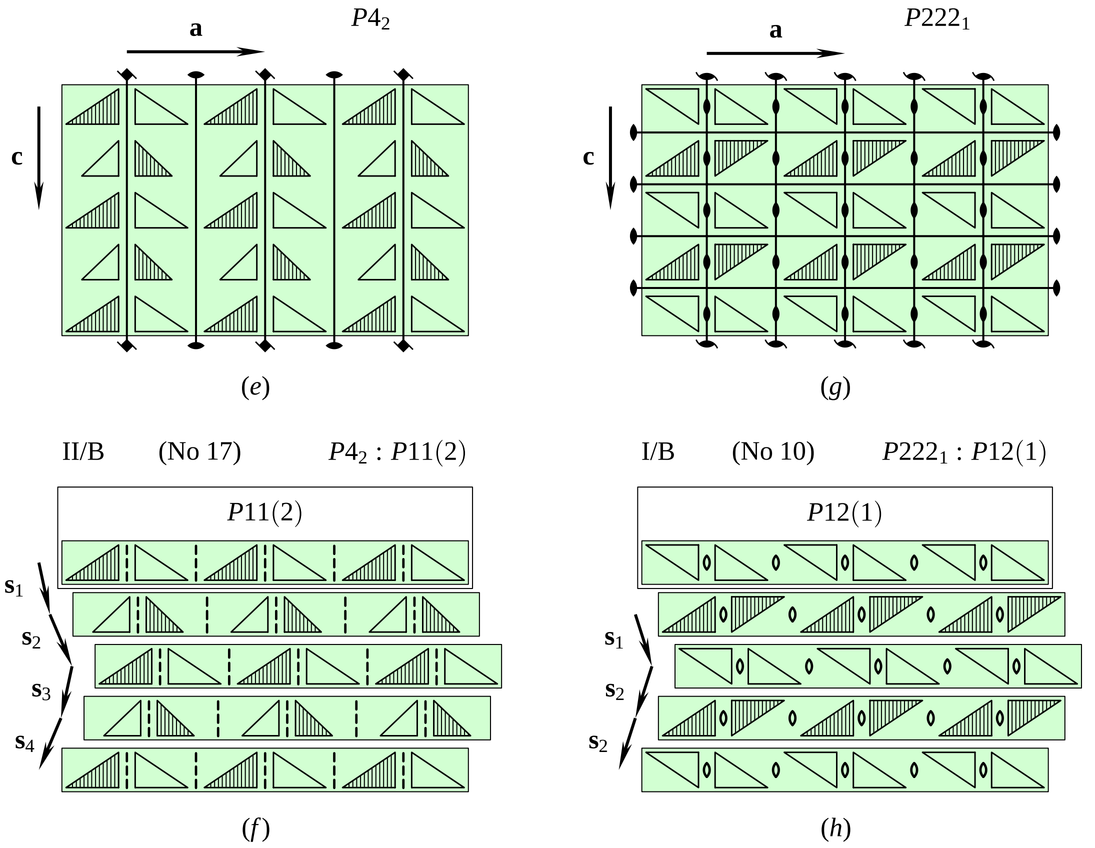

(*e*) (*g*)

(*f*) (*h*)

Figure 1.5. Types of OD-structures (continued).

The plane space group of OD-layer is shown in the frame embracing one of the layers; the groupoid symmetry of OD-structure or the space group symmetry of fully ordered structure is indicated in the top right corner of each drawing. The number in brackets is a reference to Table 1.1.

Stacking vectors $\mathbf{s}_i$ are defined using related fully ordered structure as a reference. In type A OD-structure these are the translations relating adjacent OD-layers.

asymmetric structures. Therefore the symmetry of an OD-family is described in terms of one of 333 possible groupoids, (Dornberger-Schiff & Grell-Niemann, 1961).

Notation for the layer symmetry (Table 1.1, column *c*) resembles the notation for the space group symmetry except for the index corresponding to the direction with no translational symmetry being put in brackets. Explicit notation for the groupoid symmetry (Table 1.1*b*) also resembles the notation for the space group symmetry but specifies separately the symmetry of the layer and relations between adjacent layers. One of the advantages of this rather complicated scheme is that it can be expanded to the structures with several non-equivalent layers (Grell & Dornberger-Schiff, 1982).

Table 1.1 presents “biological” groupoids (no inversion centres or reflection planes) with oblique, rectangular and square lattices. Explicit specification is shown in column (*a*) and includes two or three lines of indices. The first line defines the plane space group symmetry of the OD-layer. The second line defines symmetry operations relating the layer L_n to the layer L_{n+1} in internal coordinate system of the layer L_n. The third line is only needed for the type III. It defines the relation L_n to L_{n-1} in the coordinate system of L_n. Each line contains three, five or seven integer indices for oblique, square and hexagonal lattices of the OD-layer, respectively. These indices show rotation axes along the following directions. The index in brackets correspond to the direction orthogonal to the layer; the indices on the left to the brackets correspond to the coordinate directions of the layer lattice, $\mathbf{a}_L$ and $\mathbf{b}_L$ and, in addition, $(-\mathbf{a}_L - \mathbf{b}_L)$ for hexagonal lattice; and the indices to the right of the brackets correspond to the diagonal directions of the layer lattice, $(\mathbf{a}_L + \mathbf{b}_L)$ and $(\mathbf{b}_L - \mathbf{a}_L)$ or, for hexagonal lattice, $(2\mathbf{a}_L + \mathbf{b}_L)$, $(\mathbf{b}_L - \mathbf{a}_L)$ and $(-\mathbf{a}_L - 2\mathbf{b}_L)$.

The subscripts define translations along corresponding directions. Convention is similar to that for the space group notations, a subscript of 2 expresses the translation in halves of the unit translation and so on. The unit translation across the layers, $\mathbf{c}_N$ relates equivalent planes of adjacent layers, therefore 2_2, 4_4 and 4_{12} in the second and third lines in brackets. Other subscripts in the second and third lines are variable and can be either integer or fractional numbers, but if all of them are integers, the groupoid is a space group. The variable subscripts in the second and third lines are independent parameters; if there are more than two variable subscripts in a particular line, only two of them are independent. While the formula with variable subscripts defines an abstract groupoid, the specification of all independent subscripts define all geometrical dimensions of a particular groupoid, including all possible distances between the axes. Thus the number of independent geometrical parameters for a particular groupoid can be picked up from corresponding explicit formula, for example, four parameters for (No 22) and one for (No 23). The ambiguity in packing can also be expressed in terms of the variable subscripts, for example, u in (No 23) can be $\pm u_0$ and the sequence $+u_0$, $-u_0$, $+u_0$ defines a particular packing of three consecutive layers.

(a)	$(b):(c)$	(d)	(e)
$P\ 1\ 1\ (\ 1\ )$ $\{\ 2_p 1\ (\ 1\ )\}$ $\{\ 2_{p'} 1\ (\ 1\ )\}$	$P211 : P11(1)$	III	(1)
$P\ 1\ 1\ (\ 2\ )$ $\{\ 1_p 1_q (\ 2_2)\}$	$P112 : P11(2)$	II/A	(2)
$P\ 2\ 1\ (\ 1\ )$ $\{\ 2_p 1\ (\ 1\ )\}$	$P211 : P21(1)$	I/A	(3)
$P\ 2_1 1\ (\ 1\ )$ $\{\ 2_p 1\ (\ 1\ )\}$	$P2_111 : P2_11(1)$	I/A	(4)
$C\ 2\ 1\ (\ 1\ )$ $\{\ 2_p 1\ (\ 1\ )\}$	$C211 : C21(1)$	I/A	(5)
$P\ 1\ 1\ (\ 1\ )$ $\{\ 2_p 1\ (\ 1\ )\}$ $\{\ 1\ 2_{q'}(\ 1\ )\}$	$P222_1 : P11(1)$	III	(6)
$C\ 1\ 1\ (\ 1\ )$ $\{\ 2_p 1\ (\ 1\ )\}$ $\{\ 1\ 2_{q'}(\ 1\ )\}$	$C222_1 : C11(1)$	III	(7)
$P\ 1\ 1\ (\ 2\ )$ $\{\ 2_p 2_q(\ 1\ )\}$ $\{\ 2_{p'} 2_{q'}(\ 1\ )\}$	$P222 : P11(2)$	III	(8)
$C\ 1\ 1\ (\ 2\ )$ $\{\ 2_p 2_q(\ 1\ )\}$ $\{\ 2_{p'} 2_{q'}(\ 1\ )\}$	$C222 : C11(2)$	III	(9)
$P\ 2\ 1\ (\ 1\ )$ $\{\ 1\ 2_q(\ 2_2)\}$	$P222_1 : P21(1)$	I/B	(10)
$P\ 2_1 1\ (\ 1\ )$ $\{\ 1\ 2_q(\ 2_2)\}$	$P2_122_1 : P2_11(1)$	I/B	(11)
$C\ 2\ 1\ (\ 1\ )$ $\{\ 1\ 2_q(\ 2_2)\}$	$C222_1 : C21(1)$	I/B	(12)
$P\ 2\ 2\ (\ 2\ )$ $\{\ 2_p 2_q(\ 2_2)\}$	$P222 : P22(2)$	I/A	(13)
$P\ 2_1 2\ (\ 2\ )$ $\{\ 2_p 2_q(\ 2_2)\}$	$P2_122 : P_122(2)$	I/A	(14)
$P\ 2_1 2_1(\ 2\ )$ $\{\ 2_p 2_q(\ 2_2)\}$	$P2_12_12 : P2_12_1(2)$	I/A	(15)
$C\ 2\ 2\ (\ 2\ )$ $\{\ 2_p 2_q(\ 2_2)\}$	$C222 : C22(2)$	I/A	(16)
$P\ 1\ 1\ (\ 2\ )\ 1\ 1$ $\{\ 1_p 1_q(\ 4_4)\ 1_u 1_v\}$	$P4_2 : P11(2)$	II/B	(17)
$P\ 1\ 1\ (\ 4\ )\ 1\ 1$ $\{\ 1_p 1_q(\ 4_4)\ 1_u 1_v\}$	$P4 : P(4)$	II/A	(18)
$P\ 1\ 1\ (\ 1\ )\ 1\ 1$ $\{\ 2_p 1\ (\ 1\ )\ 1\ 1\ \}$ $\{\ 1\ 1\ (\ 1\ )\ 1\ 2_{v'}\}$	$P4_122 : P11(1)$	III	(19)
$P\ 1\ 1\ (\ 1\ )\ 1\ 1$ $\{\ 2_p 1\ (\ 1\ )\ 1\ 1\ \}$ $\{\ 1\ 1\ (\ 1\ )\ 2_{u'}1\ \}$	$P4_322 : P11(1)$	III	(20)
$P\ 1\ 1\ (\ 2\ )\ 1\ 1$ $\{\ 2_p 2_q(\ 1\ )\ 1\ 1\ \}$ $\{\ 1\ 1\ (\ 1\ )\ 2_{u'}2_{v'}\}$	$P4_222 : P11(2)$	III	(21)
$P\ 1\ 1\ (\ 4\ )\ 1\ 1$ $\{\ 2_p 2_q(\ 1\ )\ 2_u 2_v\}$ $\{\ 2_{p'}2_{q'}(\ 1\ )\ 2_{u'}2_{v'}\}$	$P422 : P(4)$	III	(22)
$P\ 2\ 1\ (\ 1\ )\ 1\ 1$ $\{\ 1\ 1\ (\ 4_4)\ 2_u 1\ \}$	$P4_122 : P21(1)$	I/B	(23)
$P\ 2_1 1\ (\ 1\ )\ 1\ 1$ $\{\ 1\ 1\ (\ 4_4)\ 2_u 1\ \}$	$P4_12_12 : P2_11(1)$	I/B	(24)
$C\ 2\ 1\ (\ 1\ )\ 1\ 1$ $\{\ 1\ 1\ (\ 4_4)\ 2_u 1\ \}$	$C4_122 : C21(1)$	I/B	(25)
$P\ 2\ 1\ (\ 1\ )\ 1\ 1$ $\{\ 1\ 1\ (4_{12})\ 1\ 2_v\}$	$P4_322 : P21(1)$	I/B	(26)
$P\ 2_1 1\ (\ 1\ )\ 1\ 1$ $\{\ 1\ 1\ (4_{12})\ 1\ 2_v\}$	$P4_32_12 : P2_11(1)$	I/B	(27)
$C\ 2\ 1\ (\ 1\ )\ 1\ 1$ $\{\ 1\ 1\ (4_{12})\ 1\ 2_v\}$	$C4_322 : C21(1)$	I/B	(28)
$P\ 2\ 2\ (\ 2\ )\ 1\ 1$ $\{\ 1\ 1\ (\ 4_4)\ 2_u 2_v\}$	$P422 : P22(2)$	I/B	(29)
$P\ 2_1 2_1(\ 2\ )\ 1\ 1$ $\{\ 1\ 1\ (\ 4_4)\ 2_u 2_v\}$	$P4_22_12 : P2_12_1(2)$	I/B	(30)
$C\ 2\ 2\ (\ 2\ )\ 1\ 1$ $\{\ 1\ 1\ (\ 4_4)\ 2_u 2_v\}$	$C4_222 : C22(2)$	I/B	(31)
$P\ 2\ 2\ (\ 4\ )\ 2\ 2$ $\{\ 2_p 2_q(\ 1\ )\ 2_u 2_v\}$	$P422 : P(4)22$	I/A	(32)
$P\ 2_1 2_1(\ 4\ )\ 2\ 2$ $\{\ 2_p 2_q(\ 1\ )\ 2_u 2_v\}$	$P42_12 : P(4)2_12$	I/A	(33)

Table 1.1. “Biological” generic OD-groupoids with monoclinic, rectangular, and square cells.

(*a*) Notations by Dornberger-Schiff & Grell-Niemann (1961) explained in §1.3.2.

(*b*) The space group symmetry of fully ordered structure with p, q, u, v, p', q', u' and v' all zero.

(*c*) The plain space group symmetry of the OD-layer.

(*d*) The type of the OD-family (§1.3.1 and Fig. 1.5).

(*e*) Reference number.

In the OD structures of type A, all OD layers are related by translation, and the translation vector between two adjacent layers is called a stacking vector. The notion of stacking vector can be extended to any OD-type using the “parent” fully ordered structure as a reference (Fig. 1.5). The set of all possible stacking vectors belongs to a certain plane space group in a sense that the points in three-dimensional space defined by these vectors are the entities related by symmetry operations. The plane space groups of stacking vectors and of the OD-layer are different but have common subgroup of translations with the basis vectors $\mathbf{a}_L$, $\mathbf{b}_L$. The number of stacking vectors per unit cell is further referred to as the number of stacking vectors.

There can be two or more stacking vectors. All of them are symmetry related in types I and II and there are two subsets of symmetry related stacking vectors in the type III (subsets $\{\mathbf{s}_1, \mathbf{s}_2\}$ and $\{\mathbf{s}'_1, \mathbf{s}'_2\}$ in Fig. 1.5*d*). In some cases any stacking vector is allowed to relate any two adjacent layers (Figs. 1.5*b*, 1.5*c* and 1.5*h*) and in the other cases there are subsets of stacking vectors such that the vectors from different subsets must alternate (subsets $\{\mathbf{s}_1, \mathbf{s}_2\}$ and $\{\mathbf{s}'_1, \mathbf{s}'_2\}$ in Fig. 1.5*d* and subsets $\{\mathbf{s}_1, \mathbf{s}_3\}$ and $\{\mathbf{s}_2, \mathbf{s}_4\}$ in Fig. 1.5*f*). In special cases $p = q$, $p = 0$ and so on, either the groupoid becomes a space group or there are less stacking vectors than in the general case. Strictly speaking, these special groupoids are different from the generic ones, so the Table 1.1 can be expanded to include the list of non-equivalent special cases for each particular generic groupoid.

If all variable subscripts in the formula of the OD-groupoid (Table 1.1*a*) are set to zero, then the OD-structure becomes the fully ordered reference structure (Figs. 1.5*a*, 1.5*e* and 1.5*g*). The space group symmetry of this structure (Table 1.1*b*) and the plane space group symmetry of the OD-layer (Table 1.1*c*) unambiguously specify the generic groupoid. For example, the generic groupoid (No 21) can be referred to as $P4_222 : P11(2)$. This style of notations is easier to apprehend at glance, but any specialisation needs to be detailed. This can be done by either providing the values of variable subscript in the explicit formula or indicating the special point in the plane space group of stacking vectors (see the last example in §1.3.4). The list of matching space group : plane space group pairs was generated using International Tables and reduced to non-redundant set shown in Table 1.1. The explicit formulae followed from mutual positions of axes in the reference space group.

1.3.3 Global organisation of OD-structures

The stacking vectors can be used to specify the global organisation of a particular OD-structure. Several members of an OD-family with two stacking vectors $\mathbf{s}_1$ and $\mathbf{s}_2$, and corresponding sequences of stacking vectors are shown in Fig. 1.6. The variable subscripts $p, q, \ldots$ in the explicit formula of the groupoid can also be used for this purpose, but they define the translation of a given layer in the coordinate system of the previous layer. On the contrary, the stacking vectors are defined in the global coordinate system and are therefore more suitable for graphical presentation of the structure.

The term order-disorder structure indicates the presence of or the potential for one-dimensional crystal disorder inherent for a given packing of adjacent layers. An OD-family contains OD-structures with both periodic and non-periodic arrangements of layers (periodic and non-periodic sequences of stacking vectors). The former correspond to single crystals, while the latter are classified according to the degree of disorder. In the case of the OD-structures possessing three-dimensional translational symmetry, the distinction is made between OD-structures with maximum degree of order (Figs. 1.6*a* and 1.6*b*), and the OD-structures with long repeats of the stacking vectors (Fig. 1.6*c*). The maximum degree of order means the following. If any two pairs of adjacent layers are superimposed, then the moved and fixed copies of the whole structure completely overlap. Individual crystals of all OD-twins discussed in §1.3.4 are the structures with maximum degree of order. The long repeats appear in *e.g.* crystals of ZnS, SiC and are

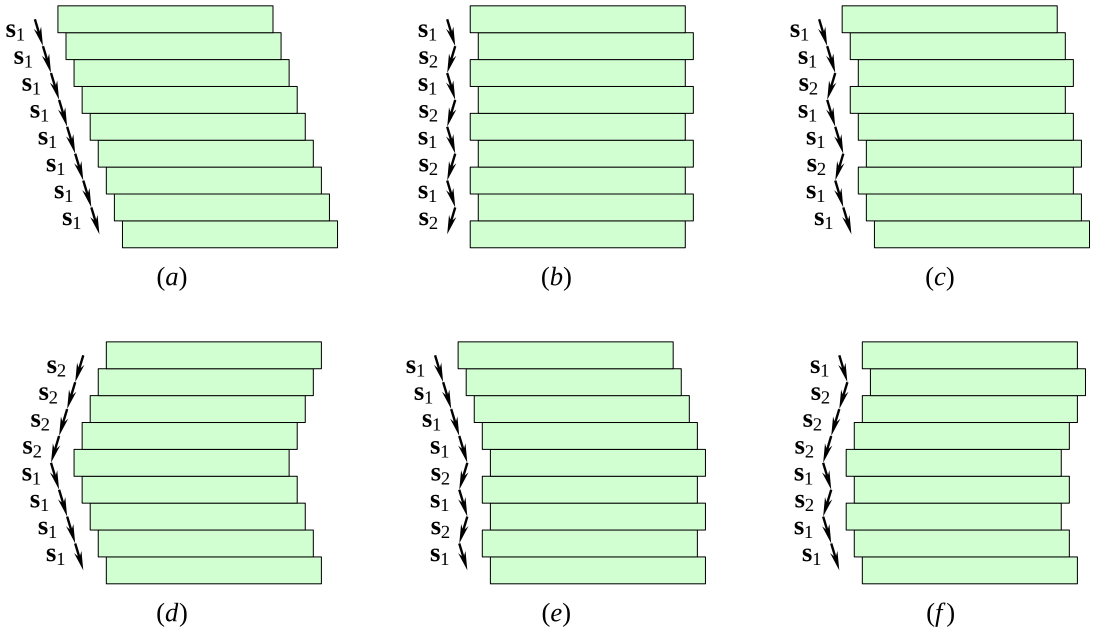

Figure 1.6. Overall organisation of OD-structures.

An OD-family with two possible stacking vectors $\mathbf{s}_1$ and $\mathbf{s}_2$ (as in Figs. 1.5*b*, 1.5*c* and 1.5*h*) is represented by six typical members:

(*a*,*b*) OD-structures with maximum degree of order, single crystals;

(*c*) OD-structure with long repeat of stacking vectors $(\ldots, \mathbf{s}_1, \mathbf{s}_1, \mathbf{s}_2, \mathbf{s}_1, \mathbf{s}_1, \mathbf{s}_2, \ldots)$, a single crystal;

(*d*) OD-twin $(\ldots, \mathbf{s}_1, \mathbf{s}_1, \mathbf{s}_1, \mathbf{s}_2, \mathbf{s}_2, \mathbf{s}_2, \ldots)$;

(*e*) allotwin $(\ldots, \mathbf{s}_1, \mathbf{s}_1, \mathbf{s}_1, \mathbf{s}_2, \mathbf{s}_1, \mathbf{s}_2, \mathbf{s}_1, \ldots)$;

(*f*) disordered OD-structure (irregular sequence of stacking vectors).

thought to be owing to the crystal growth along screw dislocations advancing several layers per turn. The global organisation of periodic OD-structures with long repeats is typically analysed using the measured intensities and the Fourier transform of a single layer (Dornberger-Schiff & Schmittler, 1971). An OD-structure without global translational symmetry can nevertheless contain ordered domains. Large domains with the same internal organisation are individual crystals of (polysynthetic) OD-twin (Fig. 1.6*d*). An allotwin (Fig. 1.6*e*) contains domains with different sequences of stacking vectors and therefore different crystallographic symmetries. If the dimensions of the ordered domains are small and comparable with the length of coherence of the X-ray beam, reflections are elongated in the direction perpendicular to the OD-layers, and the structure is referred to as partially disordered OD-structure. A structure with random sequence of stacking vectors is called disordered OD-structure (Fig. 1.6*f*).

1.3.4 Examples

(Example 1) The first case of a disordered macromolecular OD structure was reported by Bragg & Howells (1954), even before the first protein crystal structure was solved. This was a “statistically orthorhombic” crystal of imidazole methaemoglobin with apparent orthorhombic symmetry. The presence of monoclinic form of horse methaemoglobin crystal with the same a and b and two times smaller c^* indicated one-dimensional disorder with conserved structure of two-dimensional layers. The diffraction pattern was analysed in terms of equal probability of two possible relative positions of the adjacent layers (Cochran & Howells, 1954). Using the OD-terminology, the “statistically orthorhombic” crystal form can be classified as a disordered OD-structure of type I/B belonging to the OD-groupoid $C222_1 : C12(1)$ (No 12). The two crystal forms belonged to different OD-families, as in the monoclinic and “statistically orthorhombic” forms the neighbouring layers were related by crystallographic translation and two-fold screw rotation, respectively. The structure of the “statistically orthorhombic” form is unavailable, but it can be modelled using the monoclinic form (PDB code 2mhb; Ladner *et al.*, 1977).

(Example 2) Three complexes of wheat-germ agglutinin formed isomorphous crystals (PDB codes 1k7t, 1k7u, 1k7v; Muraki *et al.*, 2002) belonging to the space group $P2_1$ with equal a and c. The crystals were found to be twinned during the search for twins in the PDB (§3.2; Lebedev *et al.*, 2006). The analysis of crystal packing showed that these were OD-twins by pseudomerohedry belonging to the OD-groupoid $C222_1 : C12(1)$ (No 12) of type I/B, the same groupoid as in the previous example. A non-standard setting $B12_11$ of the individual crystal is consistent with the groupoid setting $B22_12 : B1(1)2$. The individual crystals have the same sequences of stacking vectors, $(\ldots, \mathbf{s}_1, \mathbf{s}_2, \mathbf{s}_1, \mathbf{s}_2, \ldots)$ but two possible orientations of the reference layers. Accordingly, the stacking sequences $(\ldots, \mathbf{s}_1, \mathbf{s}_2, \mathbf{s}_1, \mathbf{s}_1, \mathbf{s}_2, \mathbf{s}_1, \ldots)$ occur at the twin interfaces.

The individual crystals are therefore monoclinic with two layers spanning the *b*-dimension of the specialised *B*-centred orthorhombic unit cell. (A similar example is detailed in §3.4.) Patterson maps for 1k7t and 1k7v revealed non-origin peaks corresponding to the stacking sequences $(\mathbf{s}_1,\, \mathbf{s}_1)$ and $(\mathbf{s}_2,\, \mathbf{s}_2)$ and indicating partial disorder. There were no non-origin peaks for the twin 1k7u, which was evidently composed of larger individual crystals. The structure 1k7v with the highest non-origin peaks is likely to resemble, in terms of both order and groupoid symmetry, Bragg's "statistically orthorhombic" crystal.

(Example 3) A series of OD-structures of type I/A with $P(6)22$ OD-layers were reported by Trame & McKay (2001) for the heat-shock locus U protein from *Haemophilus influenzae* and its complexes. The layers were composed of "dodecamers" (the protomer is a hexamer). The symmetry of layers assumed the generic groupoid $P622 : P(6)22$. The native crystal was a partially disordered ternary OD-twin and belonged to a specialised groupoid with six stacking vectors, $\mathbf{s}_1 \approx \mathbf{c}_N + 0.4\mathbf{a}_L$ and $\mathbf{s}_2, \ldots, \mathbf{s}_6$ generated from $\mathbf{s}_1$ by sixfold rotation. In the proposed model of the crystal, the stacking sequences $(\ldots,\, \mathbf{s}_1,\, \mathbf{s}_4,\, \mathbf{s}_1,\, \mathbf{s}_4,\, \ldots)$, $(\ldots,\, \mathbf{s}_2,\, \mathbf{s}_5,\, \mathbf{s}_2,\, \mathbf{s}_5,\, \ldots)$ and $(\ldots,\, \mathbf{s}_3,\, \mathbf{s}_6,\, \mathbf{s}_3,\, \mathbf{s}_6,\, \ldots)$ defined three individual crystals with $P2_1$ space group symmetry and translational NCS. The asymmetric unit of an individual crystal contained two halves of the dodecamer related by NCS translation defined by a stacking vector. This model accounted for six non-origin peaks in the Patterson map. However, the authors underlined that the model was not exact, as the presence of diffuse streaks indicated partial disorder (small volumes of individual crystals). In addition, reflections corresponding to two times larger *c* were found in some of the data sets, which might be due to the presence of regular subsequences of stacking vectors with longer repeats. Because the OD-twin under study was of type A, it was possible to replace detwinning by demodulation. The corrected X-ray data corresponded to a $P622$ structure with one dodecamer per unit cell and with every second OD-layer removed.

(Example 4) An allotwin (Fig. 1.6*e*) formed by the proteolytic domain of *Archaeoglobus fulgidus* Lon protease was described by Dauter *et al.* (2005). The individual crystals belonged to $P12_11$ and $P2_12_12_1$ space groups (PDB codes 1z0v and 1z0t, respectively). The OD-layers although composed of hexamers belonged to $P2_12_1(2)$ plane space group with half of the hexamer in the asymmetric unit. There were two stacking vectors in a specialised $P2_12_12 : P2_12_1(2)$ groupoid of the type I/A (No 15), and the sequences of stacking vectors $(\ldots,\, \mathbf{s}_1,\, \mathbf{s}_1,\, \mathbf{s}_1,\, \mathbf{s}_1,\, \ldots)$ and $(\ldots,\, \mathbf{s}_1,\, \mathbf{s}_2,\, \mathbf{s}_1,\, \mathbf{s}_2,\, \ldots)$ corresponded to monoclinic and orthorhombic individual crystals, respectively. The reflections from two kinds of individual crystals were clearly separated in the diffraction images enabling processing the same set of images in two different space groups and the separate solution of the structures of the two individual crystals. Reflections with diffuse streaks were observed indicating that the volumes of individual crystals were rather small. This case should therefore be considered as allotwinning with partial disorder.

(Example 5) The crystal structure of DNA polymerase from phage ϕ29 (Wang *et al.*, 2005) is composed of identical layers. As follows from the authors' interpretation of the data, this structure is not OD, as there are present two types of non-equivalent contacts made by geometrically identical surfaces. The authors named the minority contacts translocation defects. The shape of the different subsets of reflections was shown to agree with the overall statistical model of the crystal. The data presented in the paper are however insufficient to exclude the possibility that this was a partially disordered OD-structure of type I/A with the layer symmetry $P2_11(1)$ and with predomination of $(\ldots, \mathbf{s}_1, \mathbf{s}_1, \mathbf{s}_1, \ldots)$ stacking sequences and with the sequences $(\ldots, \mathbf{s}_1, \mathbf{s}_1, \mathbf{s}_2, \mathbf{s}_1, \mathbf{s}_1, \ldots)$ at the defects. Regardless of the interpretation, the X-ray data were treated similarly to the OD case by Trame & McKay (2001). The demodulation allowed experimental phasing using MIR and MAD.

(Example 6) The monoclinic individual crystal of lipase B from *Candida antarctica* (PDB code 1lbs; 3.2.5; Uppenberg *et al.*, 1995) belonged to the space group $C2$ with unit cell parameters $a = 95.9$ Å, $b = 95.6$ Å, $c = 81.8$ Å and $\beta = 122.2^o$. The basis $\mathbf{a}' = 2\mathbf{c} - \mathbf{a}$, $\mathbf{b}' = -\mathbf{b}$, $\mathbf{c}' = \mathbf{a} + \mathbf{c}$ defined a $C2$ subgroup and an orthorhombic sublattice with $a' = 229.5$ Å, $b' = 95.6$ Å and $c' = 86.8$ Å. The twinning by reticular pseudomerohedry was generated by two equivalent twin axes along $\mathbf{a}'$ and $\mathbf{c}'$. The data were collected and processed in the large orthorhombic lattice, non-overlapping reflections from the minor twin component were removed and overlapping reflections detwinned. The modified data and the final model were deposited in the PDB in the orthorhombic coordinate system. This resulted in the apparent data completeness of 27.5% (actual completeness was 82.4%) and six molecules in the asymmetric unit (two of these were independent in the actual $C2$ space group with the smaller unit cell, the others were related by the crystallographic translations to the first two). In structural terms the crystal was an OD-twin from the OD-family $P2_12_12 : P2_12_1(2)$ of type I/A (No 15) with two-dimensional basis $\mathbf{a}_L = \mathbf{c}'$, $\mathbf{b}_L = -\mathbf{b}'$, normal component of stacking vectors $\mathbf{c}_N = \mathbf{a}'/6$, and stacking vectors $\mathbf{s}_{[12]} = \pm\mathbf{a}_L/3 + \mathbf{b}_L/2 + \mathbf{c}_N$. One possibility for its global structure is shown in Figs. 1.5(*a*), where the individual crystals lie one on top of the other. However, the exact orthorhombic symmetry of the twin lattice favours another possibility, with individual crystals one in front of the other and with each sixth OD-layer having no breaks and spanning through both individual crystals.

(Example 7) The generic groupoid $P4_22_12 : P2_12_1(2)$ (No 30) has four stacking vectors. The parallel components $s_a\mathbf{a}_L + s_b\mathbf{b}_L$ of the stacking vectors are related by operations from the plane space group $Cmm(m)$, in which $\mathbf{a}_L$ and $\mathbf{b}_L$ act as the basis translations of the primitive lattice. There are three special cases, (i) $s_a = \pm s_b$ (a special position on a mirror-reflection plane), (ii) either $s_a = 0$ and $s_b = 1/2$ or $s_a = 1/2$ and $s_b = 0$ (a special position on the intercept of glide-reflection planes) and (iii) $s_a = s_b = 0$ (a special position on the intercept of mirror-reflection planes). Accordingly, there are only two stacking vectors in the cases (i) and (ii), and the case (iii) corresponds to the reference space group $P4_22_12$. The special condition (ii) defines a single point and therefore the corresponding specialised groupoid $P2_12_1(2)/2_{\frac{1}{2}}2_{\frac{1}{2}}2$ has no variable parameters. The crystal of a domain of the splicing factor Prp8p from yeast was twinned by pseudomerohedry and belonged to this OD-groupoid (Gleb Bourenkov, personal communication). The individual crystals belonged to the space group $P2_12_12$ with $a = 77.50$ Å, $b = 77.44$ Å, $c = 97.08$ Å. The two stacking vectors and their sequence at the twin interface were $\mathbf{s}_1 = (\mathbf{a}_L/2 + \mathbf{c}_N/2)$, $\mathbf{s}_2 = (\mathbf{b}_L/2 + \mathbf{c}_N/2)$ and $(\ldots, \mathbf{s}_1, \mathbf{s}_1, \mathbf{s}_1, \mathbf{s}_1, \mathbf{s}_2, \mathbf{s}_2, \mathbf{s}_2, \ldots)$. The C$^\alpha$ r.m.s.d. from the special condition and between two molecules in the asymmetric unit were 0.48 Å and 0.21 Å, respectively. The deposited data for this protein (PDB code 2og4; Pena *et al.*, 2007) were collected from a related crystal, which was composed of the same layers as the twinned crystal, had essentially the same $a = 78.46$ Å, but belonged to the space group $P4_22_12$ and had somewhat larger $c = 122.8$ Å to accommodate less compact contacts between the layers. Hence the tetragonal crystal was a fully ordered structure which could be considered as a natural reference structure for the OD-groupoid of the twinned form.

Two OD-twins are described in this thesis, the first is a twin by metric merohedry and belongs to an OD-family of type I/B (§3.4) and the second is a twin by reticular pseudomerohedry from an OD-family of type I/A (§3.5). A case of space group uncertainty in an OD-structure of type II/A is discussed in §4.5.

2 MR protocols utilising Non Crystallographic Symmetry

MR is a multidimensional optimisation problem. In practice, the multidimensional searches are replaced by sequences of searches over subsets of parameters. In cases with many search parameters, the constraints on the parameters derived from X-ray or other data may be crucial for the success of the MR. The choice of the target function is another characteristic of an MR protocol; the target functions are typically different for rotation and translational searches although they are intended to approximate a general criterion, the likelihood of a given set of values of the parameters. Finally, the partial structure can be refined after all or specific steps of the protocol and used as a fixed partial model or a new search model. Automated MR programs implement a few “standard” protocols for which these four major characteristics (sequence of searches, constraints, target function and “refinement points”) are internally defined. A “difficult MR problem” is in fact one for which the standard protocols do not clearly indicate a solution but a case-specific protocol succeeds.

In this chapter, several difficult MR cases are presented, in which I have contributed to the structure solution. People involved in the particular projects are acknowledged and the related publications are indicated in the corresponding sections.

The structure in §2.6 was solved using experimental phasing and MR was used for substructure solution. In all other examples discussed in this chapter standard MR protocols were attempted but were not successful except for §2.5, where this resulted in a partial structure. In all these examples several search models were available including single-subunit models and either single-domain models (§2.5) or one or more oligomeric models. All the models were tried both with and without sequence correction except for §2.2, where the sequence identity was high and correction of the model seemed unnecessary. In three cases more substantial modifications of the search models were also tried, removal of low-identity segments (§2.1 and §2.3) or hybridisation of two models (§2.4). For all the structures only one MR program was used in all the trials, either *AMoRe* (§2.1 and §2.6) or *MOLREP* (all others). For each model two or more attempts at structure solution were made using all data or with high-resolution cut-offs in the range 5 to 3 Å. The initials runs were generally at low resolution for reasons of speed and efficiency. For each MR attempt, which resulted in an apparent solution with reasonable contrast, a visual analysis of the molecular packing for that solution was performed followed by rigid body and restrained refinements if the packing was reasonable. For only one structure (§2.5) was a partial solution found in this manner and confirmed by a decrease in R_{free} during refinements.

For single-subunit models of §2.2, §2.3 and §2.4, subsets of the CRF peaks approximately related by NCS were examined. A list of such relations is optionally generated by *MOLREP* using the list of the SRF peaks; this procedure is similar to that used in *CRANS* (§1.1.12). If some CRF peaks are related by NCS with a high accuracy (a threshold of 4^o was typically used) and these peaks are reproducible at different high-resolution cut-offs, they are worthy of special examination by either the standard TF or multi-copy search (§1.1.12). However such a situation did not occur in any of the examples where this analysis was done.

For oligomeric search models the CRF steps of MR were specifically validated. For each of several highest peaks of the CRF the search model was brought into the corresponding orientation and structure amplitudes from this model were computed in $P1$ with target cell parameters. If the native SRF and the SRF from the model in a tested orientation have common peaks (the native SRF contains more peaks owing to the crystallographic symmetry) then there is a high likelihood that the tested orientation of the oligomer is correct. For the E1-helicase (§2.4) this analysis, which is later referred to as an SRF test, showed that the top three equivalent CRF peaks were likely to be correct and therefore the respective orientation was used as a starting point for refinement of a hexamer. In all the other examples the oligomeric models failed the SRF test.

As the standard protocols were not successful, non-standard protocols were designed and applied to the structures under consideration. The approaches used in the first three examples can be classified as NCS-constrained exhaustive searches for the parameters defining the structures of oligomers. The selection criteria were the maximum value of the correlation coefficient (CC) in the series of the TF searches (the first and the second examples) and the maximal value of the CRF (the third example). In the fourth example, the required changes in the oligomer organisation were relatively small and therefore a local optimisation against the CRF was undertaken. In the fifth example, the restrained refinement of partial model was a key step in the structure determination. Finally, in the sixth example, an NCS-constrained exhaustive search was used for Hg-substructure determination.

2.1 NCS-constrained exhaustive search with the TF target

Thioredoxin peroxidase B from human erythrocytes (TPx-B) was studied in the group of Professor Jennifer Littlechild (University of Exeter). The protein was isolated and biochemical experiments were carried out by Dr. Ewald Schröder and Dr. Neil Errington; Dr. Michail Isupov collected the X-ray data and solved the structure. I took part in designing the protocol and scripts for the exhaustive search. The results were presented by Schröder *et al.* (2000) and structure solution is described by Isupov & Lebedev (2008).

This case is characterised by moderate similarity of the search model (30% sequence identity with the target) and a large number of molecules in the asymmetric unit (ten). However, the knowledge of the point group symmetry of the oligomer and the availability of a dimeric homologous structure enabled substantial reduction in the number of independent parameters and made an exhaustive search feasible. Our protocol is a multibody NCS-constrained version of the procedure proposed by Sheriff *et al.* (1999), §1.1.13, in which a comprehensive sample of subunit orientations was tested by conventional TF. A closely related procedure was used by Strop *et al.* (2007), §1.1.13, except that the variable search model was a single protein and the building blocks were helices in place of the oligomer and subunits in our case.

2.1.1 Background

Peroxiredoxins are ubiquitous antioxidant enzymes. TPx-B is a 2-Cys peroxiredoxin with a subunit molecular weight of 22 kDa. The protein was purified from dated blood packs and crystallised in space group $P2_1$, with unit-cell parameters a = 88.9, b = 107.0, c = 119.5 Å, $\beta = 110.9^o$. Native synchrotron data were collected to 1.7 Å.

Attempted MIR phasing did not work owing to poor native crystal isomorphism. The Se-Met MAD approach was not possible, as the protein was purified from the native source. Because of experimental uncertainties, analytical ultracentrifugation, gel-filtration chromatography and specific volume calculations were inconclusive regarding the oligomeric state of the protein, suggesting eight to twelve subunits in the oligomer. The SRF calculated with *MOLREP* revealed that TPx-B is a decamer with 52 molecular symmetry (Figs. 2.1*a* and 2.1*b*).

2.1.2 Model preparation and structure solution

The closest available homologue, dimeric hORF06 (Fig. 2.1*c*; PDB code 1prx; Choi *et al.*, 1998) shared 30% sequence identity with TPx-B. No MR solution was found for single subunit or dimeric hORF06 models.

A polyalanine model of hORF06, containing amino acids 1–189 out of 224 in order to cut off a poorly conserved domain, was used to generate all possible decamers with 52 point-group symmetry. This was done by positioning the dimeric model with its centre of mass at the origin of the coordinate system, its molecular dyad coincident with the coordinate axis *x* and the N-terminal face of the dimer pointing in the negative direction. A two-parameter family of decamers satisfying the SRF was generated by applying the following sequence of transformations to this dimer. Firstly, the dimer was translated by a distance *R* along the *x* axis and rotated by an angle ω about its molecular dyad, using 1 Å steps in *R* and 2^o steps in ω. The values of *R* and ω were the two variable parameters of the model. Each new dimer was rotated by $\pm 72^o$ and $\pm 144^o$ around *z* and the five dimers were joined to form a decamer with point-group symmetry 52 (Fig. 2.1*d*). Finally, the decamer was rotated to align its molecular dyads with the NCS dyads known from the SRF (Fig. 2.1*a*). An inspection of the possible packing of the dimers in the decamer suggested *R* to be within the ranges 32–51 Å or -51 to -32 Å. Positive and negative values of *R* corresponded to two types of packing, with the N-terminal face of the dimer pointing towards or outwards the centre of the decamer, respectively. Owing to the two-fold symmetry of

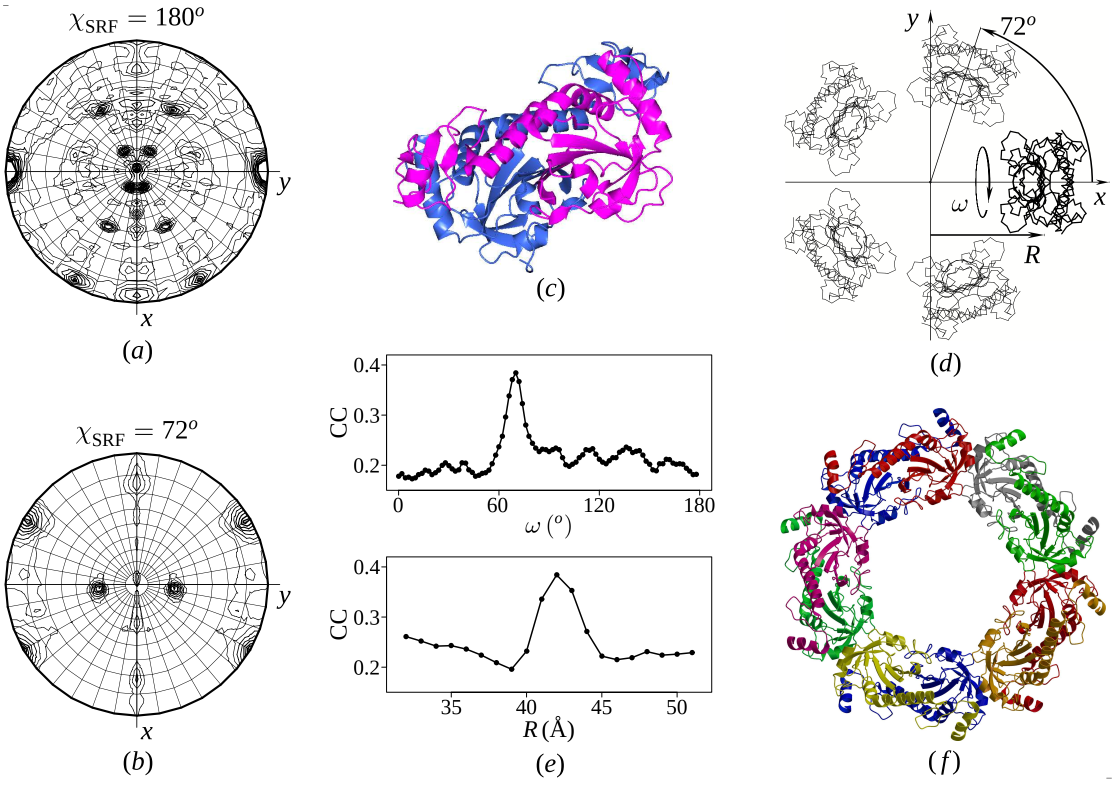

Figure 2.1. Structure solution of TPx-B. Sections of the SRF corresponding to rotations by (*a*) 180^o and (*b*) 72^o indicate the 52 point-group symmetry of the TPx-B molecule and define the orientations of NCS fivefold and two-fold axes. (*c*) The hORF06 dimer, a building block of the search model. (*d*) The search model with two variable parameters, the angle ω and the distance *R*. (*e*) Two sections of a two-dimensional search space crossing the point corresponding to the correct decamer, the point with the highest CC in the TF search against ω and *R*. (*f*) The final decameric TPx-B structure. This figure was prepared using *MOLREP*, CCP4mg, *BOBSCRIPT* and *R*.

the dimers, the ω search range was 0–180^o. A total of 3600 decamers were generated, with two types of packing. A TF search was conducted with these models using *AMoRe* and a *tcsh*-script in which one cycle included generation of a decamer and the TF with this decamer as the search model. The data with the resolution less than 5 Å were used to reduce the computational time. For each decamer the highest value of CC was stored to generate a two-dimensional plot of CC against *R* and ω (Fig. 2.1*e*). The only strong peak in this plot ($R = 42$ Å, $\omega = 70^o$) corresponded to the correct structure.

Subsequent phase improvement involved rigid-body refinement, restrained refinement (*REFMAC*), tenfold NCS averaging (*DM*) and restrained refinement with external *DM*-averaged phases (*REFMAC*). The TPx-B model was rebuilt and refined to an *R*-factor of 0.192 and an R_{free} of 0.256 (Fig. 2.1f; PDB code 1qmv; Schröder *et al.*, 2000).

2.2 Partially constrained exhaustive search with the TF target

The anti-TRAP protein from *Bacillus licheniformis* was supplied by Professor Paul Gollnick (State University of New York, Buffalo) and the structural analysis was carried out in the group of Dr. Fred Antson. Crystallisation, data collection and refinement were conducted by Mikhail Shevtsov. Dr. Mikhail Isupov (University of Exeter) and I used the available X-ray data to solve the structure (Isupov & Lebedev, 2008).

In retrospect, there were two major complications with the structure solution. Firstly, the dodecamer of anti-TRAP from *Bacillus licheniformis* turned out to be entirely different from the known dodecamer of the homologous protein and, secondly, there was four-fold translational NCS which prevented the structure solution using one-by-one RF/TF searches for single subunits or trimers. In addition, a false origin solution emerged in the first successful MR attempt (details in §4).

Assuming that the trimers were conserved gave a similar situation to that in §2.1 in which the knowledge of oligomer orientation and partial knowledge of oligomer structure were available. In the previous example all this information was used as constraints in the exhaustive search. In this case, constraints on the positions of trimers relative to the centre of the dodecamer were relaxed. This reduced the contrast but added a validation criterion, the point group symmetry of the complete oligomer. In addition, the new procedure was faster and simpler to implement. Should this approach fail, the protocol with all possible constraints would be invoked.

2.2.1 Background

Anti-TRAP is a small protein of 53 amino acids involved in regulation of tryptophan biosynthesis and transport in *Bacilli*. In particular, it regulates the activity of tryptophan attenuation protein, TRAP (Antson *et al.*, 1999). The crystal structure of anti-TRAP from *B. subtilis* was solved by Shevtsov *et al.* (2005), PDB code 2bx9. This crystal contained a dodecameric particle with cubic 23 point-group symmetry (Fig. 2.2*a*).

Anti-TRAP from *B. licheniformis* crystallised in space group $P2_1$ with unit-cell parameters $a = 118.5$ Å, $b = 99.9$ Å, $c = 123.2$ Å, $\beta = 117.6^o$. The crystal diffracted to the resolution of 2.2 Å. If there were four dodecamers in the asymmetric unit the specific volume would be 2.35 Å^{3}Da^{-1} and the solvent content 47%. The sequence identity between *B. subtilis* and *B. licheniformis* anti-TRAP was 64%.

The native Patterson synthesis of *B. licheniformis* anti-TRAP contained three strong non-origin peaks at (0.5, 0.13, 0.0), (0.5, 0.0, 0.5) and (0.0, 0.13, 0.5), with heights of 0.4, 0.4 and 0.16 relative to the origin peak, respectively (Fig. 2.2*b*). This suggested that the asymmetric unit contained four anti-TRAP particles related by translational NCS. The SRF had strong features at χ values of 180^o, 120^o (Fig. 2.2*c*) and 90^o, which correspond to the 432 symmetry. This means that the NCS axes are in special orientations with respect to the crystallographic two-fold axis (two of the four NCS triads are orthogonal to the crystallographic axis). These data may suggest that the asymmetric unit of the crystal contains either four dodecamers with 23 point-group symmetry (the high apparent symmetry of SRF in this case is the consequence of special orientations of the NCS axes) or four 24-mers with 432 symmetry. However, in the second case one of the six diagonal dyads of a 24-mer would be parallel to a crystallographic two-fold screw axis and such an arrangement would generate strong peaks in the native Patterson synthesis at $v = 0.5$, which were not observed. Moreover, four 24-mers would result in an impossible specific volume and solvent content and therefore this possibility was excluded.

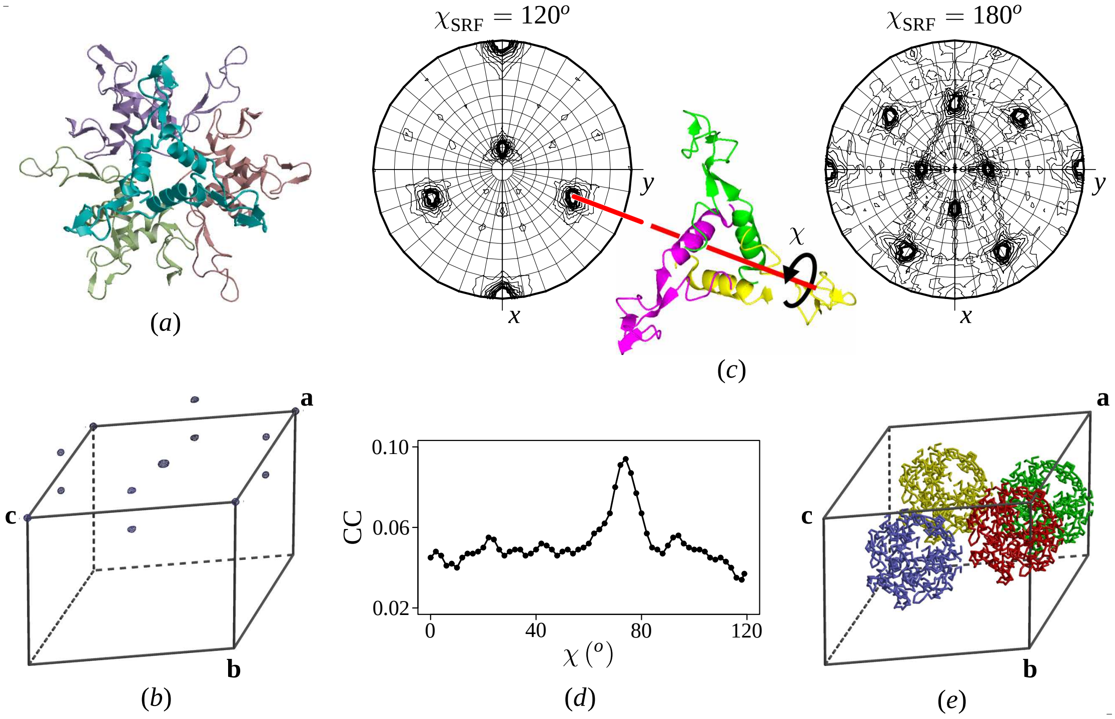

Figure 2.2. Structure solution of anti-TRAP from *B. licheniformis*. (*a*) Ribbon diagram of the dodecamer of anti-TRAP from *B. subtilis*. (*b*) Native Patterson synthesis, in which three strong non-equivalent non-origin peaks are present. (*c*) 120^o and 180^o sections of the SRF, indicating the orientations of two-fold and threefold NCS axes. The trimeric search model (centre) was oriented so that its threefold molecular axis was aligned with the NCS threefold axis (red lines). TF searches were performed for a series of orientations related to that shown by a rotation around the molecular threefold axis by the variable angle χ. (*d*) The highest CC in the TF search is plotted as a function of χ. (*e*) The MR solution with four dodecamers in the asymmetric unit, which are related by the translational NCS. This figure was prepared using *BOBSCRIPT*, *MOLREP*, CCP4mg (Potterton *et al.*, 2004) and *R*.

2.2.2 Models and preliminary MR trials

Prior to the structure determination, it seemed likely that dodecamers in the crystals of *B. licheniformis* and *B. subtilis* anti-TRAP proteins would be identical. Therefore, three models were tried in the conventional MR attempts, the dodecamer, a trimer and a single subunit. Owing to the high sequence similarity between the two proteins, the models were used without any modification, but several resolution limits were tried.

First of all, the dodecameric model was used, but without success. Moreover, the CRF did not contain strong features and its top peaks failed the SRF validation, suggesting a different organisation of the dodecamers in the anti-TRAP proteins from *B. subtilis* and *B. licheniformis*. Further attempts with the trimer and single subunit failed as well. This was not surprising, as these models represented only a small part of the asymmetric unit content.

Nevertheless, the trimeric model (Fig. 2.2*c*) appeared attractive because of the presence of a trimeric *B. licheniformis* anti-TRAP species in solution. Therefore, the next attempt at structure solution was the constrained exhaustive search with the trimeric model.

2.2.3 Structure determination

It was possible to use a two-dimensional exhaustive search similar to one described in the previous section. In this case, the variable parameters would have been the distance from the centres of trimers to the centre of the dodecamer and the angle defining the rotation of the reference trimer about its three-fold axis.

However, in order to accelerate the search and retain a validation criterion, another protocol was applied in this case. The trimeric model of *B. subtilis* anti-TRAP was positioned at the origin and rotated to align its molecular threefold axis with one of the NCS three-fold axes. The angle χ defining the rotation of the trimer about its three-fold axis was sampled with a 2^o step over the range 0–120^o, which was sufficient owing to the threefold symmetry of the model. A TF search was carried out for each of these 60 orientations using *MOLREP* and the data in the resolution range 15–4.2 Å. Fig. 2.2(*d*) shows the dependence of the highest CC in the TF search on χ, with a clear solution at $\chi = 74^o$. The CC at this global maximum is 9.4%, while the CC at the other maxima is below 6%.

In the model shown in Fig. 2.2*c*, the N-termini of the subunits point away from the origin. In the general case it would have been necessary to repeat the TF runs with the 'flipped-over' model, in which the three-fold axis has the same orientation, but the N-termini point towards the origin. However, in our particular case it was not needed, as the NCS axes were in special orientation relative to the crystallographic 2_1 axis and the 'flipped-over' trimers related to the original trimers by crystallographic rotation.

The search was repeated for the three remaining NCS threefold axes. Similarly to the conventional MR protocol, each found trimer was added to the partial model used as a fixed model in the next TF search, until one complete dodecamer was built. Visual inspection showed that the resultant dodecameric model had point group symmetry 23, as expected. This was strong evidence for the correctness of the model, as the 23 symmetry constraints were partially relaxed in the exhaustive search. Comparison of the new dodecamer with the one from *B. subtilis* showed that the two particles were entirely different and thus explained the failure of the first MR trial.

The resulting dodecamer was used as a search model for the next step of structure solution, in which four dodecamers related by translational NCS were located using conventional MR. The electron density map allowed model correction to the *B. licheniformis* sequence and the model was iteratively refined and rebuilt using *REFMAC* and *Coot*. At the early stages, the behaviour of the refinement seemed normal. However, the refinement stalled at $R = 33\%$ and $R_{\text{free}} = 43\%$. At this point, the $2F_o - F_c$ synthesis was of reasonable quality, but did not indicate ways of further model improvements. Moreover, main-chain breaks were observed in the electron density maps and the water structure was poorly defined. Therefore, one dodecamer, which had fewer main-chain breaks in the density, was used as the model for a further MR search. This time one of the correct RF peaks split. Dodecamers in slightly different orientations were positioned one by one using the TF. The new structure was easily refined to $R = 19.7\%$ and $R_{\text{free}} = 25.4\%$ (Fig. 2.2*e*). The problems with the first refinement attempt and the difference between the two models is analysed in §4.1.

2.2.4 Concluding remarks

Given a known trimer and the orientations of the NCS axes, an unknown dodecamer with point symmetry 23 is defined by two internal and three translational parameters. Four independent trimers have twelve rotational and twelve translational parameters. Therefore, there are 19 symmetry constraints available for the exhaustive search with the trimeric model. In our exhaustive search, only eight angular parameters (two for each of four trimers) were constrained. This was nevertheless sufficient to exclude the CRF from the protocol and to solve the structure. (The fact that the CRF was a weak link in the structure determination was realised during the preliminary MR trials with the trimeric model, as the orientations of the model defined by CRF did not pass the SRF validation.)

The protocol with partially relaxed NCS constraints had two major advantages compared to the fully constrained exhaustive search. Firstly, it was a variation of one-by-one search and therefore it was fast and, secondly, the relaxed constraints provided a validation criterion, the expected 23 symmetry of the dodecamer.

In addition, this protocol was easy to implement, as it required only a minimal modification to the standard protocol. Namely, *MOLREP* was instructed to switch the RF step off and to use the external list of orientations instead. So, for each of four series of translation searches, a table was manually created that contained polar angles defining the model orientations to be tested by the TF. In our case, these were 60 rotations about the three-fold NCS axes. In each table the first two polar angles were the same and the third was 0^o to 120^o with the step of 2^o. The first two angles were copied from the table of peaks of the experimental SRF.

A similar protocol was used in the structure solution of the oxygenating component of 3,6-diketocamphane monooxygenase from *Pseudomonas putida* (Isupov & Lebedev, 2008). In the latter case the homology was much lower (14%), but there was only one dimer to locate in the asymmetric unit. The automation of this protocol is straightforward and only requires a simple additional program to test the symmetry of the experimental SRF against the point group symmetry of the model.

The crystal structure solution of anti-TRAP from *B. licheniformis* underlines the importance of using a conserved protein oligomer for the MR. It was the anti-TRAP trimer that was conserved in two species, *B. subtilis* and *B. licheniformis* although both homologue proteins form dodecamers with quite rare 23 point group symmetry.

2.3 Partially constrained exhaustive search with the CRF target

The biochemical and structural studies of hydroxycinnamoyl-CoA hydratase-lyase (HCHL) from *Pseudomonas fluorescens* AN103 were carried out by Dr. Gideon Grogan's group (YSBL) in collaboration with Dr. Marek Brzozowski (YSBL), Dr. Nicholas Walton (Institute of Food Research, Norwich), Dr. Derek Smith and Dr. Chandra Verma (Bioinformatics Institute, Singapore). My role was in finding the MR solution of the crystal structure of HCHL (PDB code 2j5i). The results are presented by Leonard *et al.* (2006). The details of the structure solution are presented in a separate publication (Lebedev *et al.*, 2008).

Compared to the previously described protocols, the constraints on the orientation of the oligomer were relaxed in this case, but constraints on its internal organisation were used in full. The oligomeric models from a one-parameter family were scored by maximum value of the CRF and the consistency of the orientation of the best oligomer with the SRF was a validation criterion. This approach was adopted because it seemed essential to build a reliable model of the complete oligomer prior to any use of the TF, which was complicated by translational NCS.

2.3.1 Background

The bacterium *P. fluorescens* AN103 is able to grow on ferulic acid as the sole carbon source utilising a catabolic pathway *via* vanillin (Narbad & Gasson, 1998). An interest in the transformation of ferulic acid, an abundant natural product into a flavour agent vanillin is dictated by its industrial significance.

Ferulic acid is transformed to vanillin in a three-step reaction. Ferulic acid was first ligated to coenzyme A to form feruloyl-CoA by the action of 4-hydroxycinnamate-CoA ligase-synthetase. The acyl-CoA thioester of ferulic acid was then transformed to vanillin by the action of a single enzyme, HCHL, which first catalyses the hydration of the double bond between C_2 and C_3 to yield a hydroxyacyl-CoA and then retro-aldol cleavages the C_2-C_3 bond to give vanillin and acetyl-CoA.

The enzymatic transformation performed by HCHL represents an interesting mode of enzymatic activity that is reminiscent of the hydration of double bonds in enoyl-CoA and related substrates in fatty-acid oxidation pathways by the enzyme crotonase or enoyl-CoA hydratase (ECH). In contrast to ECH, HCHL performs a second half-reaction, a cleavage of a C-C bond. The hydration mechanism proposed for ECH by (Bahnson *et al.*, 2002) involves sin-addition in which the only source of protons is the catalytic water molecule donating all its three atoms to the product, presumably in a concerted mode. Thus, of special interest is the question whether such hydration mechanism is conserved in the two enzymes and how the active cite of HCHL is modified to be able to perform the second half-reaction.

Both ECH and HCHL are members of a low-sequence-identity superfamily of enzymes known as the crotonase or low-similarity hydratase/isomerase (LSI/H) superfamily. The enzymes of this superfamily are characterised by pronounced structural similarity, which is at odds with the divergent catalytic chemistry including the stereospecific hydration of double bonds performed by ECH and also dehalogenation (Benning *et al.*, 1996), double-bond isomerisation in fatty acids (Modis *et al.*, 1998; Mursula *et al.*, 2001), cyclisation/aromatisation reactions in the synthesis of vitamin K intermediates (Truglio *et al.*, 2003) and the retro-Dieckmann condensation (Eberhard & Gerlt, 2004). The divergent catalysis is often enabled by amino acid residues which have no counterparts in the sequences of the other superfamily members (Gerlt & Babbitt, 2001).

The majority of solved crotonase structures are homohexamers consisting of a dimer of trimers. Moreover, the trimers of the closest HCHL homologues possess an intra-trimer domain-swapping fold as defined by Hubbard *et al.* (2005), in which the trimer is stabilised by extensive interactions between the C-terminal domain of one subunit with the N-terminal domain of its neighbour. These homologues include ECH, dienoyl-CoA isomerase, 4-chlorobenzoyl dehalogenase and the human AUH protein. The major overall difference between these homologous hexamers is therefore defined by different relative orientations of trimers.

HCHL was crystallised and a native 1.8 Å resolution data set was collected at ESRF Grenoble station ID14-EH1 (Leonard *et al.*, 2004). The crystal belonged to the space group $P2_12_12$ with unit cell dimensions $a = 154.2$ Å, $b = 167.5$ Å, $c = 130.8$ Å.

Three structures of HCHL sequence homologues, rat liver ECH (24% sequence identity; PDB code 1dub; Engel *et al.*, 1996) *T. thermophilus* ECH (31% sequence identity; PDB code 1uiy) and 4-chlorobenzoyl-CoA dehalogenase from *Pseudomonas sp.* (28% sequence identity; PDB code 1nzy; Benning *et al.*, 1996) were used in the structure solution by MR as described below. These structures are further referred to by their PDB codes.

The native CRF and the Patterson map were indicative of two hexamers in the asymmetric unit related by translational NCS $0.66\,\mathbf{a} + 0.30\,\mathbf{b} + 0.50\,\mathbf{c}$ (the heights of the corresponding Patterson peaks were 23% of the origin peak at 3 Å resolution cut-off). This interpretation was in agreement with the solvent content of 46% corresponding to twelve subunits per asymmetric unit. Hexamers and trimers derived from the crystal structures of the selected homologues were used as a search models in the preliminary MR trials, along with the single subunits. Both complete models and their truncated versions were tested using *MOLREP* (Vagin & Teplyakov, 1997). The TF searches were attempted in both default mode, in which the translational NCS is automatically accounted for (§1.1.15) and with the translational NCS option turned off. No significant contrast was observed in the RF or TF for all data and for resolution cut-off 3 Å. The difficulties with the MR were attributed to different organisation of the hexamers in the target structure compared to the search models and to the presence of the translational NCS.

2.3.2 Structure solution

The RF uses only the fraction of the Patterson map within a sphere centred at the origin, which does not include the non-origin peaks. It was therefore reasonable to try a non-standard approach, in which the search hexamer is adjusted using the RF as a target function. It was expected that the subsequent TF search with two corrected hexamers related by translational NCS would be substantially assisted by the packing function, as two hexamers would constitute a complete asymmetric unit except for the truncated residues.

To achieve the best possible contrast in the MR searches and to make the MR searches with alternative models comparable, a careful search model preparation was undertaken. Firstly, the models of single hexamers were derived from PDB entries 1dub, 1uiy and 1nzy, in two of which, 1uiy and 1nzy, the asymmetric unit contained one and three molecules, respectively, and the complete hexamers were generated by crystallographic symmetry. Secondly, the single subunits from three homologues were superimposed using the secondary structure match (*SSM*; Krissinel & Henrick, 2004) implemented in *Coot* (Emsley & Cowtan, 2004) to identify segments of residues that were spatially aligned in all three homologues and had close values of the backbone torsion angles (Fig. 2.3*a*). These highly conserved segments (Fig. 2.3*b*) were kept intact in corresponding hexameric models, while all other residues were removed from all their subunits. In particular, the removed segments included the complete C-terminal domain and all loops. Figs. 2.3(*c*), 2.3(*d*) and 2.3(*e*) represent the spatial alignment of the three truncated hexameric models by one of two trimers. The fitted and free trimers are separately shown in Figs. 2.3(*c*) and 2.3(*e*), respectively. The side view of the aligned hexamers is represented in Fig. 2.3(*d*). The difference in orientations of the free trimers was measured using *LSQKAB* (Fig. 2.3*e*).

Comparison of oligomers from homologue structures (Fig. 2.3) suggests that trimers in the unknown structure are spatially similar, but the hexamers are different from those in homologues. The centres of masses of the trimers have similar spacing in homologous hexamers. Assuming similar spacing in the unknown structure, the relative rotation of the trimers around three-fold axis is the only parameter to vary in order to build a correct hexameric model. Therefore, a set of models was generated from the three truncated hexamers with the relative rotations of trimers in the range 0-120^o (sufficient range for the point group 32) and with an increment of 2^o. Smaller differences in the organisation of trimers and in the spacing between trimers might be nevertheless essential for the performance of the MR. In effect, the related parameters were roughly sampled by scanning hexameric models derived from three different homologues.

The RF (*MOLREP*) at 5 Å resolution cut-off was performed with these three sets of models using a *tcsh*-script to generate plots in Figs. 2.4(*a*), 2.4(*b*) and 2.4(*c*), in which the maximum

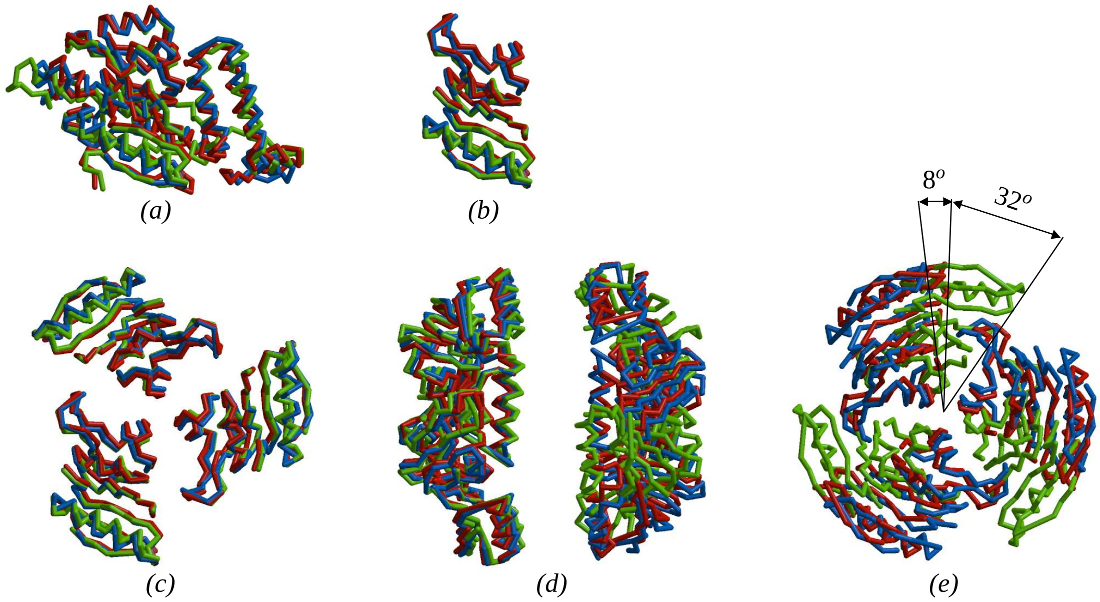

Figure 2.3. Comparison of hexamers formed by three homologues of HCHL, ECH from *T. thermophilus* (PDB code 1uiy, red), ECH from rat liver (PDB code 1dub, green) and 4-chlorobenzoyl-CoA dehalogenase from *Pseudomonas sp.* (PDB code 1nzy, blue). (*a*) Superposition of single subunits to identify spatially conserved segments. (*b*) Superposition of the conserved cores of subunits. (*c*) Superposition of truncated trimers, in which only the cores of their subunits have been preserved. (*d*, *e*) Superposition of truncated hexamers by fitting one of two trimers: (*d*) the side view showing that the distance between centres of trimers is conserved in the three homologues; and (*e*) the top view showing the relative rotation of the second trimer, which was not used in fitting of hexamers.

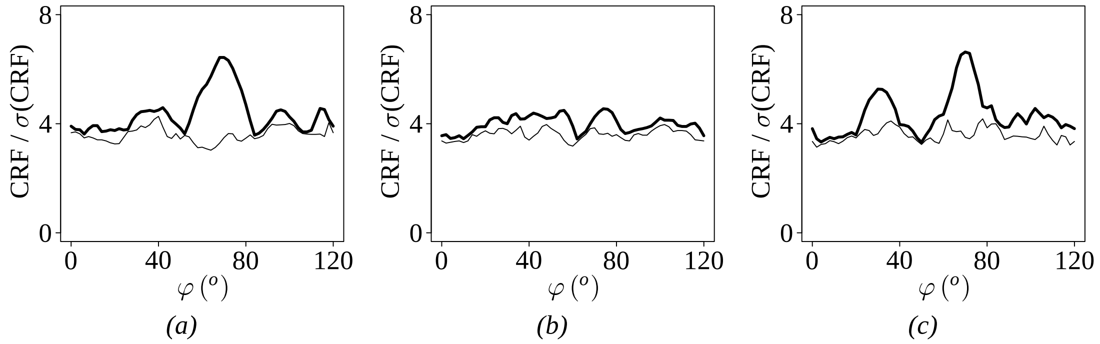

Figure 2.4. Determination of relative orientation of trimers in the HCHL hexamer using NCS-constrained exhaustive search with the CRF target. Search models were generated from the truncated hexamers shown in Fig. 2.3(*d*). In each case, the CRF was computed for a series of hexamers, in which the reference trimers were fixed and the free trimers were rotated around the molecular threefold axis by the variable angle φ. The value of CRF/σ(CRF) for the highest CRF peak (thick line) and for the 10th peak (thin line) were plotted against φ for three series of hexamers generated from (*a*) PDB entry 1uiy (*b*) PDB entry 1dub and (*c*) PDB entry 1nzy. The reference angles in the three series were consistent, so any two hexameric models with the same value of φ were spatially aligned.

value of RF/σ(RF) was plotted against the angle φ defining the relative rotation of trimers in a given model. For the consistency of the plots, the reference relative orientation ($\varphi = 0$) corresponded to spatially aligned hexamers. Two of three series of models (1uiy and 1nzy) produced strong peaks at $\varphi \approx 70^o$. In both cases, the orientation of hexamers associated with this peak was consistent with the SRF. This peak was the only strong peak in the 1uiy-based plot (Fig. 2.4*a*) and therefore the corresponding hexameric model (1uiy, $\varphi = 70^o$) was selected for the final MR search, which was performed using *MOLREP* at 3 Å resolution in the default mode, in which both hexamers related by translational NCS were accounted for in a single TF run. The results of this search are given in Table 2.1. Significant contrast is observed between the first six NCS-related RF-peaks and the seventh RF-peak in both the RF and the TF. In addition, eight relevant orthorhombic groups were tested and a significant contrast in the TF was observed between the correct space group $P2_12_12$, known from systematic absences, and incorrect groups. Rigid-body refinement of the TF solution and an initial round of restrained refinement by *REFMAC* (Murshudov *et al.*, 1997) gave an *R*-value of 0.43 and an R_{free} of 0.52.

Subsequent model building and refinement were carried out with *REFMAC* in conjunction with *ARP/wARP* (Perrakis *et al.*, 1999) in the whole (30-1.8 Å) resolution range. *Coot* was used for manual corrections to the model. The final *R* and R_{free} were 0.179 and 0.215, respectively, with 94.1% residues in the most favoured regions, 5.6% in additional allowed regions and 0.3% in generously allowed regions as indicated by *PROCHECK* (Laskowski *et al.*, 1993).

2.3.3 Structure analysis

The substrate, feruloyl-CoA, was modelled into the active site based on the structure of ECH bound to the feruloyl-CoA-like substrate 4-(N,N-dimethylamino)-cinnamoyl-CoA (PDB code 1ey3) and energy minimisation was performed using *CHARMM* (Brooks *et al.*, 1983). The model revealed certain differences between the active cites of HCHL and ECH. One of two

RF peak No	RF/σ(RF)	TF: the best CC	
		$P2_12_12$	$P22_12_1$
1-6	6.67	0.294	0.256
7-12	3.06	0.250	0.221

Table 2.1. The second step of the crystal structure solution of HCHL, in which the modified hexamer from PDB entry 1uiy was used as a search model in conventional MR (*MOLREP*). The results of the TF search are shown for two space groups, in which the highest correlation coefficients were obtained. Every 6 peaks define equivalent orientations of the hexamer, produce identical values in the RF and TF runs and are grouped in a single row.

carboxylate residues (Glu) binding the catalytic water molecule in ECH active cite is replaced by Ser123 in HCHL sequence. This serine residue is 7.7 Å away from the catalytic water and makes contact with the reactive carbon of the substrate via water molecule. The restructuring of the active site may be necessary for HCHL to catalyse the retro-aldol half-reaction, which is not performed by ECH, and may also indicate a somewhat different mechanism of the hydration step compared to ECH. In addition, the modelling showed that Tyr239, which is hydrogen bonded to the phenolic group of feruloyl-CoA missing in cinnamoyl-CoA, is an excellent candidate for the structural determinant of the HCHL specificity.

A comparison of the architecture of the trimers and hexamers of HCHL homologues is summarised in Table 2.2. These data support and explain the efficiency of *T. thermophilus* ECH (ECHTt; PDB code 1uiy) as the model in the molecular-replacement strategy. The best superposition of HCHL and ECHTt trimers requires only 1.8^o adjustment of subunits, indicative of their similar organisation. However, the assemblies of these trimers into hexamers are quite different and a rotation of ECHTt trimers by 9.6^o with respect to each other was required for the best superposition of hexameric enzymes. The combination of a wide range of rotational differences in quaternary structures of trimers (1.8-3.8^o) and hexamers (0.7-21.6^o) within the

PDB code	1dub	1nzy	1uiy
Identity (%)	28	25	31
Aligned C$^\alpha$ atoms (%)	79	80	74
Angle (1 $\leftrightarrow$ 3) (^{o})	3.84	2.42	1.84
Angle (3 $\leftrightarrow$ 6) (^{o})	0.72	14.93	4.77
R.m.s.d. (single subunit) (Å)	1.62	1.63	1.60
R.m.s.d. (trimer) (Å)	2.08	1.78	1.80
R.m.s.d. (hexamer) (Å)	2.17	6.43	2.70

Table 2.2. Comparison of molecular architecture of HCHL and its homologues used in molecular replacement. For comparison of trimers, each trimer was firstly globally superimposed with the HCHL trimer. This was the subsequent starting position for the best superposition of corresponding subunits of those trimers: it resulted in the rotation by a certain angle that is quoted here as angle (1 $\leftrightarrow$ 3). Hexamers were also initially globally superimposed and then one trimer of the relevant protein was fitted onto the corresponding trimer of HCHL, giving the rotation angle that is quoted here as angle (3 $\leftrightarrow$ 6). (The relative rotation of trimers required for the best fit of hexamers is twice as large.) R.m.s.d.s were calculated for three-dimensionally aligned C$^\alpha$ atoms. All superpositions and three-dimensional alignments were performed using the program O (Jones *et al.*, 1991). The C$^\alpha$ atoms for the spatial alignment were selected automatically, using the default threshold of 3.8 Å. The fraction of aligned C$^\alpha$ atoms is shown relative to their total number in HCHL.

crotonase superfamily illustrates the plasticity of the trimer/hexamer architecture that is adopted to support efficient catalysis of a particular type of chemical process.

2.3.4 Alternative method of the HCHL structure determination

The strategy discussed here helped to solve the MR problem complicated by translational NCS and by differences in the oligomer organisation of the target protein and its homologues. This strategy may seem quite specific and applicable only in the cases when the factors defining such differences can be derived from the known structures. It was therefore interesting to resolve this structure using a more general approach. A strategy utilising the ideas of the locked rotation and translation functions (LRF; LTF; Tong, 2001) was implemented in *tcsh*-script that cut a sphere out of the Patterson map computed with a fine grid, rotated the map and placed it in a trigonal lattice to align NCS axes with crystallographic translations. The map was averaged to produce synthetic P32 data, which would correlate with a P32 structure containing one correct hexamer per unit cell and one subunit per asymmetric unit. Such a structure was built in a single run of conventional MR to yield a correct hexamer, which was placed in the correct cell in the second round of MR against experimental data. This procedure was conceptually identical to the LRF/LTF procedure, but only required the programs available in the CCP4 suite.

2.3.5 Conclusion

This example demonstrated the efficiency of the RF-like target in optimisation of the search model prior to the translational search. In this particular case the optimisation was performed by simple one-dimensional exhaustive search, but multidimensional local optimisation is also possible (§2.4). An important characteristic of the optimisation against the RF is that the filtering of the data is accomplished in the rotational space and it is not equivalent to the filtering by additional temperature factor or by a resolution cut-off; the angular resolution is controlled by the number of terms preserved in the spherical harmonics series (Eqn. 3) approximating the Patterson function. Broad peaks in Figs. 2.4(*a*) and 2.4(*c*) indicate that there is a significant signal even for the models that differ from the target by substantial relative rotation of their internal fragments. This feature means there is a larger radius of convergence in the iterative refinement of oligomeric models against RF-like target compared to conventional rigid body refinement.

2.4 Rigid-body refinement with the CRF target

This example demonstrates how the RF target performs in multidimensional optimisation. Biochemical studies and protein production of the E1-helicase from bovine papillomavirus-1 (BPV-1) were carried out in the group of Dr. Cyril Sanders (University of Sheffield) and structural analysis was conducted in the group of Dr. Fred Antson at York (2v9p; Sanders *et al.*, 2007). Apo E1 was crystallised by Dmytro Sizov and the structure solution was conducted by Oleg Kovalevskiy using as a model the structure of E1 in complex with DNA determined at Cold Spring Harbor laboratory (PDB code 2gxa; Enemark & Joshua-Tor, 2006). Dr. Michail Isupov (University of Exeter) and I determined this structure independently, using structural data of other hexameric helicases before the E1-DNA complex structure became available. Our protocol is presented in a separate manuscript (Lebedev *et al.*, 2008).

Compared to the previous example, in which accurate although incomplete information on the oligomer organisation was available, only an approximate model of the oligomer was available in this case. Therefore an exhaustive search was replaced by rigid body refinement of four parameters. Thus, the protocol involved: the CRF search, rigid body NCS-constrained refinement of the oligomer in the best three orientations and the TF search with corrected oligomeric model in the best orientation.

Improvement of a model after the CRF step is typically performed using PC-refinement in $P1$ space group (Brünger, 1990). However, we used the CRF as a target function, which gave just the opposite effect to that achieved by PC-refinement. Namely, the use of CRF target function allowed removal of unreliable long cross-vectors and a reduction in both spatial and angular resolutions. This was necessary as we wanted to apply point group symmetry constraints to the oligomer, for which certain asymmetry was expected by analogy with other available helicase structures.

2.4.1 Structure solution

The crystal structure of BPV-1 E1 helicase (Sanders *et al.*, 2007) belongs to the space group $P2_12_12_1$ with unit-cell parameters $a = 135.1$ Å, $b = 180.7$ Å, $c = 187.5$ Å. The asymmetric unit contains two hexamers related by translational NCS $0.50\,\mathbf{a} + 0.08\,\mathbf{b}$. Each subunit is composed of an AAA+ domain ($\sim$200 amino acids) and an oligomerisation domain ($\sim$75 amino acids). The best crystal diffracted to a resolution of 3.0 Å. At the time of the structure determination, the closest homologue in the PDB was the AAA+ domain of HPV-18 helicase, which had 51% sequence identity with the AAA+ domain of the target protein (PDB code 1tue). In this structure the oligomerisation domain was absent and the AAA+ domain existed in a monomeric form. The closest homologue with a known hexameric structure was SV40 helicase (PDB code 1n25), which shared only 16% of its amino acid sequence with the full length of the target protein. Attempts to find a solution with the monomeric protein from 1tue or with the hexamer from 1n25 failed.

The structure was solved starting from a synthetic model containing six AAA+ domains from 1tue, corrected according to the target sequence and fitted to the six subunits of the hexamer from 1n25 using *SSM* (Figs. 2.5*a*, 2.5*b* and 2.5*c*).

Firstly, the synthetic model was tried as a search model for *MOLREP* using a simultaneous search for two hexamers related by translational NCS at the TF step. Use of all data to the high resolution limit of 3 Å, as well as with high-resolution cut-offs of 4 and 5 Å was tried but no TF solution was found. However, the first three peaks in the RF persistently had a small but appreciable contrast compared with other peaks (results for high-resolution cut-off of 4 Å are shown in Fig. 2.5*f*). These three peaks were equivalent and corresponded to the special orientation of the hexamer six-fold axis along **a** and along the crystallographic screw two-fold

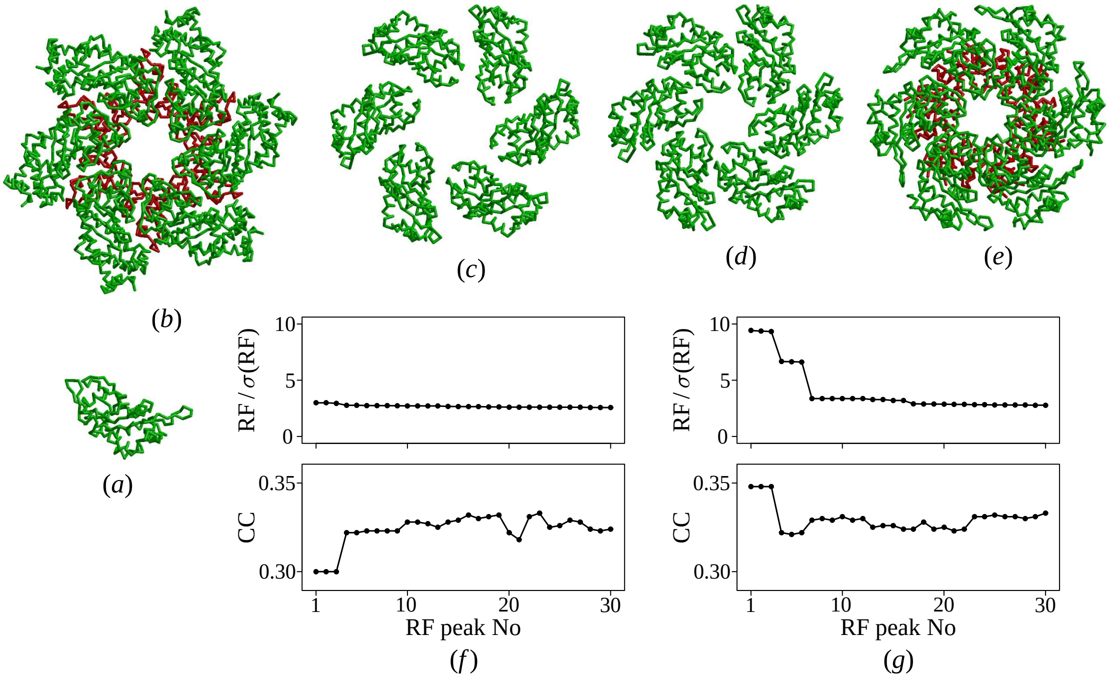

Figure 2.5. Structure solution of BPV-1 E1 helicase. (*a*) The AAA+ domain of HPV-18 helicase and (*b*) the hexamer of SV40 helicase, which were used to generate (*c*) a synthetic hexamer. (*d*) The synthetic hexamer after refinement against the CRF. (*e*) A hexamer from the final structure of BPV-1 E1 helicase. Colours indicate (red) oligomerisation and (green) AAA+ domains. The r.m.s.d. for C$^{\alpha}$ atoms between the last three models were 5.6 Å (synthetic and final models), 4.5 Å (synthetic and refined models) and 2.5 Å (refined and final models). The sixfold symmetry was significantly perturbed in the final hexamer. Therefore, the r.m.s.d. between the refined and symmetrised final hexamers was only 1.2 Å. (*f*) The behaviour of MR for synthetic and (*g*) refined hexamers. The RF and TF steps are represented by plots of RF/σ(RF) and CC, respectively, against the RF peak number.

axis. Such an orientation of the hexamer was consistent with the SRF and was considered as a likely RF-solution. However, the best CC in the TF for this orientation was lower than for other orientations and it seemed likely (and confirmed later) that the correct TF solution was suppressed by the packing constraints.

Therefore we assumed that the hexamer in the unknown structure had a slightly different organisation and undertook refinement of the synthetic hexamer model. The data up to resolution of 4.5 Å were used for efficiency, but it was known from the previous RF trials that the orientation of interest had the first rank for the resolution cut-offs from 3 to 5 Å. During this procedure four parameters were refined: three angles defining the orientation of the subunit *A* and the distance between the centre of subunit *A* and the sixfold axis. The remaining five subunits were generated from subunit *A* by the sixfold symmetry. The target function was the value of RF/σ(RF) for the highest RF peak. Maximisation of the target function was performed iteratively using a *tcsh*-script. For a given current hexamer, eight new hexamers were generated, in which the distance was incremented by ± 1 Å or one of the angular parameters was incremented by $\pm 1^o$. *MOLREP* was used to compute the RF for each of new hexamers. The values of the target function, RF/σ(RF) for the first RF peaks were extracted from the log files. The new hexamer with the highest value of the target function became the current model in the next iteration. The procedure was terminated when none of the new models gave an increase in the target function compared with the current model. The refinement rotated the subunits by 10^o and translated their centres of mass by 6 Å (Fig. 2.5*d*). Using the refined hexamer, the behaviour of conventional MR improved dramatically (Fig. 2.5*g*). The refined hexamer (Fig. 2.5*d*) and the hexamer from the final structure (Fig. 2.5*e*) were very similar to each other and differed significantly from the initial synthetic hexamer (Fig. 2.5*c*).

Similar refinements were performed with the fourth and seventh peaks of the RF from the starting model. The target functions was the value of RF/σ(RF) for the RF peaks closest to the initial peak. The increase in the target function was significantly less than in the refinement with the first peak.

2.4.2 Concluding remarks

After the structure was solved it became evident why the default MR protocol with the synthetic model failed, although the correct orientation was the first in the list of the RF peaks. The large C^α r.m.s.d. of 5.6 Å between the synthetic and final hexamers (Figs. 2.5*c* and 2.5*e*) and larger size of the former prevented the TF solution and, in particular, a proper functioning of the PF. On the other hand, it is unlikely to be possible to solve a structure with translational NCS without packing constraints.

It seems likely that the success of refinement using CRF were owing to the following reasons, (i) the presence of NCS constraints in the successful refinement protocol, (ii) additional reduction in the angular resolution in the RF target (spherical harmonics with large *l* are ignored in the RF by default) and (iii) the absence in the RF target of long cross-vectors, which may result in false local minima. However, a general implementation of such refinement does not necessarily imply the use of spherical harmonics. For example, adjustment of the angular resolution can be performed by refining the TLS parameters of the rigid groups. An improved rigid body refinement program could be useful in cases similar to one described here and those in which the adjustment of a multi-domain model is needed, as in the next example.

2.5 MR with feedback from the refined partial model

Structural studies of the hypothetical protein MTH685 from the archaeon *Methanothermobacteria thermautotrophicus* was part of a mini structural genomics project on RNA-binding proteins carried out in the group of Dr. Fred Antson (YSBL) in collaboration with several other groups. The protein was produced, characterised, crystallised and the X-ray data were collected by Dr. Chyan Leong Ng. Dr. Michail Isupov (University of Exeter) and I used the available X-ray data and solved the structure (Lebedev *et al.*, 2008). A manuscript describing the structure is being prepared by Dr. Chyan Leong Ng.

There are two three-domain molecules in the asymmetric unit of the crystal. Flexibility of the molecules prevented a straightforward structure determination despite the availability of a closely homologous structure. A domain-by-domain search was therefore performed alternated with restrained refinements of partial structures, as proposed by Brünger (1990). Furthermore, the refined domains were the search models in the subsequent steps of the MR. In effect, the restrained refinements allowed utilisation of higher-resolution data, which otherwise would not contribute to the MR searches with less similar models.

2.5.1 Structure solution

The symmetry relations between structural elements (subunits or domains) forming the asymmetric unit are not necessarily obvious from the SRF or other methods. Moreover, there can be several different types of structural elements. In such cases, the NCS-based protocols are not applicable and the structure solution requires a standard one-by-one search with very incomplete search models. Two problems are usually encountered in this approach. Firstly, a minor problem is the lack of contrast in the TF when positioning the last few structural elements. The major problem is that the RF is calculated only once for each search model, each representing only a small fraction of the asymmetric unit (Fig. 2.6*a*). Even if the search model is adequately modified, some of the correct RF peaks may remain weak owing to the specific configuration of the interatomic vectors in the actual crystal structure. Such peaks are therefore absent in the list of top RF peaks provided for the further TF search. As a result, the corresponding elements of the asymmetric unit are not positioned at all. If, however, a partial MR solution is found, restrained refinement of the partial structure allows an update of the search model(s) and the list of RF peaks (Fig. 2.6*b*).

This technique was instrumental in the determination of the crystal structure of the hypothetical protein MTH685 from the archaeon *Methanothermobacteria thermautotrophicus*. The crystal with unit-cell parameters $a = 68.3$, $b = 72.1$, $c = 146.8$ Å belonged to the space group $P222_1$. X-ray data were collected to a resolution of 1.8 Å. The asymmetric unit contained two monomeric protein molecules with identical sequences, which, however, were not related by any point group NCS and, moreover, were in different conformations (Fig. 2.6*c*). Each molecule contained three domains. To the date of structure determination, the PDB contained a structure of a homologous protein from *Archaeoglobus fulgidus* with a sequence identity of 50%, PDB code 1p9q. Because of the domain mobility (Fig. 2.6*c*), the target structure could not be solved using the complete molecule as a search model. Thus, the problem turned out to be not a simple MR problem despite the high sequence identity. None of the possible search models were perfect, the complete molecule because the three-dimensional similarity was too low and the single domains because the completeness was too low.

The protocol presented in Fig. 2.6(*a*) allowed *MOLREP* to find the correct MR solutions for domain 1 from chain *A* and domain 2 from chain *B* (steps 1 and 2 in Table 2.3). However, it was not obvious whether this partial model was correct, as the orientation of domain *B*2 corresponded to only the 24th highest peak in the RF and the search for the remaining domains was unsuccessful. Moreover, this model could not be validated on the basis of connectivity considerations, as the two found domains belonged to different polypeptide chains.

In contrast to the standard protocol, the protocol including refinement of partial structures (*REFMAC*) produced the complete model (steps 3–6 in Table 2.3). Although the partial model after step 2, $A1 + B2$ was only about 30% complete, restrained refinement of this model per-

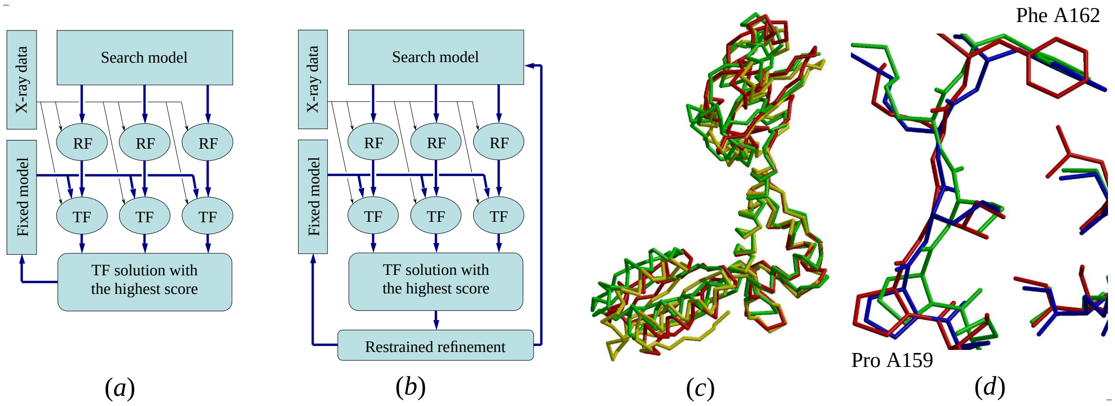

Figure 2.6. Structure solution of the MTH685 protein. (*a*) The one-by-one MR protocol in which the RF is computed only once for each single-domain search model. (*b*) The successful MR protocol with two feedbacks, in which each new partial model is refined and therefore search models and lists of their possible orientations are updated at each step, along with the partial structure. (*c*) Superposition of (red, yellow) two molecules of MTH685 protein forming the asymmetric unit and (green) the homologous protein Af0491 (PDB code 1p9q) fitted onto the second domain, showing that the MR structure solution using the whole molecule as a search model is impossible. (*d*) Enlarged superposition of the second domains; red from chain *A* of the final structure, blue from a refined partial structure containing two of six domains and green from the homologue corrected according to the target sequence.

formed quite efficiently: most of the atoms moved closer to their final positions (Fig. 2.6*d*) and the r.m.s.d. for C^{α} atoms between domains *A*1 in the partial and final structures decreased from 1.42 to 0.98 Å. This improvement completely changed the behaviour of the RF. It turned out that the correct orientation of domain *A*2 was not in the list of 200 highest RF peaks until the corresponding search model was updated. The impact of the search-model improvement on the TF was not so significant. Additional tests showed that if the correct orientation of *A*2 were known, the improvement of the search model would only cause a 15% increase in contrast. Nevertheless, step 3, in which the refined *A*1 was used to find *A*2, was critical for structure determination. Starting from step 3, the models were validated by the connectivity between neighbouring domains and by the decrease in R_{free} (Table 2.3). It is likely that after step 3, when 50% of the complete structure had been defined, it was already possible to switch to searching for the remaining domains in the electron density using, for example, SAPTF (Vagin & Isupov, 2001) implemented in *MOLREP*.

Step	1	2	3	4	5	6
Composition of fixed model						
Chain A	-	1	1	1,2	1,2	1,2
Chain B	-	-	2	2	1,2	1,2,3
Search model that gave						
the best TF score	1	2	2[†]	1[†]	3	3[†]
Refinement of partial structure						
R	0.526	0.495	0.459	0.447	0.404	0.358
R_{free}	0.548	0.534	0.503	0.486	0.445	0.425

Table 2.3. The sequence of MR searches that led to the solution of the MTH685 protein crystal structure. The composition of the models is given in terms of domains comprising residues 1–89 (domain 1), 90–162 (domain 2) and 163–232 (domain 3).

[†] The search model was taken from the refined partial structure from the previous step

2.6 Substructure solution using NCS-constrained exhaustive search

The structure and function of the portal protein from the phage SPP1 was studied in the group of Dr. Fred Antson (YSBL) in collaboration with several other groups and researchers (PDB code 2jes; Lebedev *et al.*, 2007). Dr. Margaret Krause (Max-Planck Institut für Molekulare Genetik, Berlin, Germany), Professor Eleanor Dodson (YSBL), Dr. Fred Antson and I were involved in the crystal structure solution and analysis. My contribution was the solution of the phase problem by MR and analysis of the results and model.

The crystal structure was determined using a Hg-derivative and native data. The Hg substructure was solved using an NCS-constrained exhaustive search with a CRF-target against the anomalous differences. This method was first used by Dr. Fred Antson to solve the structure of the TRAP protein (Antson *et al.*, 1995) and was invoked for this case because of the failure of direct methods, probably owing to a low signal-to-noise ratio in the isomorphous differences. Essentially the same approach was used for the structure solution of HCHL (§2.3), except that in this case it was applied to substructure determination.

The X-ray study of the isolated 13-mer form of the portal protein revealed the structure of the tunnel loops, which interact with the DNA during the DNA translocation. The asymmetry of the tunnel loops in the functional dodecameric form of the portal protein was established and the model of the DNA translocation was proposed based on a combination of various data including the results of the X-ray model fitting into the electron microscopy (EM) reconstruction of the connector.

2.6.1 Background

The assembly of tailed bacteriophages and herpesviruses (Fig. 2.8*a*) starts from the formation of a procapsid with a portal protein embedded in one of the twelve five-fold icosahedral symmetric vertices of the shell. At a later stage, a complex composed of the multisubunit terminase assembly and concatameric phage dsDNA binds to the portal vertex to form a DNA translocating molecular motor, which packages DNA into the capsid. Finally, after concatameric DNA cleavage and terminase dissociation a few other proteins are attached to the portal to form the tail of infective phage.

In bacteriophage SPP1, the molecular motor consists of three proteins (Fig. 2.8*a*) – gp1, gp2 (small and large terminase subunits, respectively) and gp6 (portal protein) – and powers translocation of the 45.9 kbp phage chromosome (Camacho *et al.*, 2003; Oliveira *et al.*, 2005). DNA translocation is fuelled by ATP hydrolysis; ATPase activity is associated with the large terminase subunit gp2. However, it is still not clear if the power stroke generated by gp2 protein applies directly to the DNA or to the portal protein, causing its structural rearrangement and DNA translocation. All components of the DNA-translocating motor possess distinct symmetries. For example, the capsid's vertex and the backbone of the B-form DNA have five-fold and screw ten-fold symmetry axes, respectively. In common with the herpesvirus portal protein (Trus *et al.*, 2004), the portal protein of bacteriophage SPP1 can exist as a circular assembly with varying number of subunits (Lurz *et al.*, 2001; Orlova *et al.*, 2003): it was found as a 13-subunit assembly in its isolated form and as a 12-subunit assembly when integrated into the functional viral capsid. According to the latest results, the small terminase subunit gp1 forms decamers with ten-fold rotational symmetry (Maria Chechik and Fred Antson, personal communication). The large terminase subunit gp2 exist in a monomeric form in solution, but the number of gp2 subunits and their orientations in the functional motor assembly is unknown.

High-resolution EM reconstructions of the SPP1 portal protein were available both for the isolated 13-subunit oligomer (9 Å resolution) and for the connector (10 Å resolution), an assembly purified from the viral capsids consisting of the 12-mer portal protein in a coaxial complex with two other viral components gp15 and gp16 (Orlova *et al.*, 2003).

Although in all species the portal protein is a central and essential component of the DNA-translocating machine, the organisation of the molecular motor varies. For example, in bacteriophage ϕ29, the motor consists of three coaxial macromolecular rings, the portal protein, the ATPase and the procapsid RNA (pRNA) acting as the substrate for ATPase binding (Simpson *et al.*, 2000), while there is no evidence for the presence of pRNA in other bacteriophages. This motor generates a force of up to 57 pN, which makes it one of the most powerful molecular motors discovered so far (Smith *et al.*, 2001). Such a force is needed to pump the viral DNA against the high internal pressure that increases as the DNA is encapsidated.

The available EM data showed that portal proteins of different phages and herpesviruses all shared a common turbine-like shape (Valpuesta & Carrascosa, 1994; Orlova *et al.*, 1999; Trus *et al.*, 2004). However, they showed no detectable similarity in amino acid sequence and exhibit large variations in their subunit molecular masses, for example 36 kDa in the case of phage ϕ29 and 57 kDa in the case of phage SPP1. Therefore, the ϕ29 portal protein, the only portal protein for which the crystal structures had been available (Simpson *et al.*, 2000; Guasch *et al.*, 2002), could not be used as a MR search model for solving the crystal structure of the SPP1 portal protein.

The operation of the DNA-translocation molecular motor has been the subject of much debate. The low-energy barriers to rotation of symmetry mismatching protein rings relative to each other led Hendrix (1978) to propose that DNA translocation is accompanied by rotation of the portal protein inside the capsid vertex. Different models of DNA translocation, all involving the rotation of the portal protein, were put forward following the EM image analysis of the SPP1 portal protein (Dube *et al.*, 1993) and the determination of the X-ray structure of the ϕ29 portal protein (Simpson *et al.*, 2000; Guasch *et al.*, 2002). These models were based mostly on symmetry considerations, as even the available X-ray data provided no atomic-scale structural information about the most constricted part of the internal tunnel that would be in close contact with the DNA during translocation: the tunnel loops in the ϕ29 portal protein (residues 229–245) were either disordered in the native structure (Simpson *et al.*, 2000) or missing in the higher-resolution structure of mutant (Guasch *et al.*, 2002).

2.6.2 Crystallisation and X-ray data analysis

Diffracting crystals were obtained for the SPP1 portal protein gp6SizA with the amino acid substitution N365K. This mutation reduced the length of encapsidated DNA but did not affect the DNA packaging process (Tavares *et al.*, 1992). The crystallisation conditions were found by Jekow *et al.* (1998) and optimised by Dr. Margaret Krause. The best crystals were obtained using hanging-drop vapour diffusion. A solution containing 8 mg/ml of protein was mixed in a 1:1 ratio with the reservoir solution containing 20% PEG 400, 100m*M* $CaCl_2$, 50m*M* HEPES pH 7.6 and 10% glycerol, which acted also as a cryoprotectant. The non-derivative crystals of this mutant and the X-ray data from these crystals are further referred to as native crystals and native data.

The presence of a single cysteine residue (C55) per subunit suggested that the mercury derivative is a good candidate for isomorphous replacement phasing. The crystals of $HgCl_2$ derivatives were obtained by cocrystallisation, in which different amounts of $HgCl_2$ were added directly to the protein solution. X-ray data from several native crystals and from several $HgCl_2$ derivative crystals were collected at 100K using synchrotron radiation at the ESRF, beamline ID14-4. The data were processed using *DENZO* and *SCALEPACK* (Otwinowski & Minor, 1997). Some characteristics of the three best crystals used in structure solution are presented in Table 2.4.

Table 2.4 shows that the increase of the concentration of $HgCl_2$ in mother liquor further improves the resolution of the diffraction data, although it causes increase of non-isomorphism. This observation suggested that the derivative crystal Hg-1 obtained with lower concentration of $HgCl_2$ was more suitable for substructure determination, but the less isomorphous derivative Hg-2 was a better candidate for model building and refinement.

The confirmation that the crystals Hg-1 and Hg-2 were true derivatives came from the SRF that was computed for the observed native structure factors, and for two sets of isomorphous differences between the derivative and the native structure factors (Fig. 2.7*a*). The SRF from the observed structure factors clearly revealed peaks accounting for thirteen-fold NCS (section $\chi = 27.7^o$) and for interaction between this NCS and crystallographic symmetry (section $\chi = 180^o$).

Similar features were expected for the SRF from isomorphous differences provided that these differences were owing to regular mercury binding and not only because of non-isomorphism and measurement errors. The differences between Hg-1 and native structure factors showed all the expected features, a clear peak in the section $\chi = 27.7^o$ and a ring of smeared peaks in the section $\chi = 180^o$. In the case of differences from the less isomorphous derivative Hg-2, the peaks in the section $\chi = 27^o$ were conserved while the ring of peaks in the section $\chi = 180^o$ partially disappeared. The latter observation can be treated as the negative control of what had been observed for the derivative Hg-1 and is therefore a further confirmation of Hg binding. Indeed, the peaks at $\chi = 27^o$ were defined by intra-oligomer self-vectors and their presence mostly depended on the similarity between oligomers and their orientations in the two crystal forms. On the other hand, the peaks in the section $\chi = 180^o$ were defined by cross-vectors between crystallographic-symmetry related oligomers and the match between such cross-vectors in two (approximately) isomorphous crystals would quickly vanish with relative changes in the unit-cell parameters (Table 2.4).

The anomalous differences were measured for both $HgCl_2$-derivatives under consideration, but showed no SRF-patterns corresponding to the 13-fold NCS axis or its interaction with crystallographic symmetry.

2.6.3 Solution of the substructure

Despite the presence of the true isomorphous differences, the substructure solution could not be obtained by automated Patterson search or direct method using *Solve* or *SHELXS*. Unsurprisingly, attempts to solve the Hg-substructure using anomalous differences failed as well. Therefore a constrained exhaustive MR search was attempted, which was earlier used by Antson *et al.* (1995) for substructure solution of the derivative crystal of the TRAP protein 11-mer.

Data set	Native	Hg-1	Hg-2
contents of $HgCl_2$ (mM)	–	0.5	2.5
Space group	$C222_1$	$C222_1$	$C222_1$
a (Å)	173.5	173.4	174.3
b (Å)	222.4	221.7	221.4
c (Å)	419.8	419.7	421.9
Resolution (Å)	100 – 4.1	40 – 3.7	40 – 3.4
R_{merge} (%)	11.0	9.6	10.4
R_{iso} (%)	–	15.3	25.1

Table 2.4. Data sets used for structure solution of SPP1 portal protein.

A series of search models was generated. Each model contained 13 Hg atoms located around a circle with a step of 27.7^o (Fig. 2.7*b*). An additional carbon atom was placed on the axis of the circle but outside of its plane for the MR program to be not confused with an ill-conditioned inertia matrix, which would occur for a flat model. The radius of the circle varied in the series of the search models from 10 to 90 Å with a step of 1 Å. Every model was submitted to a rotation

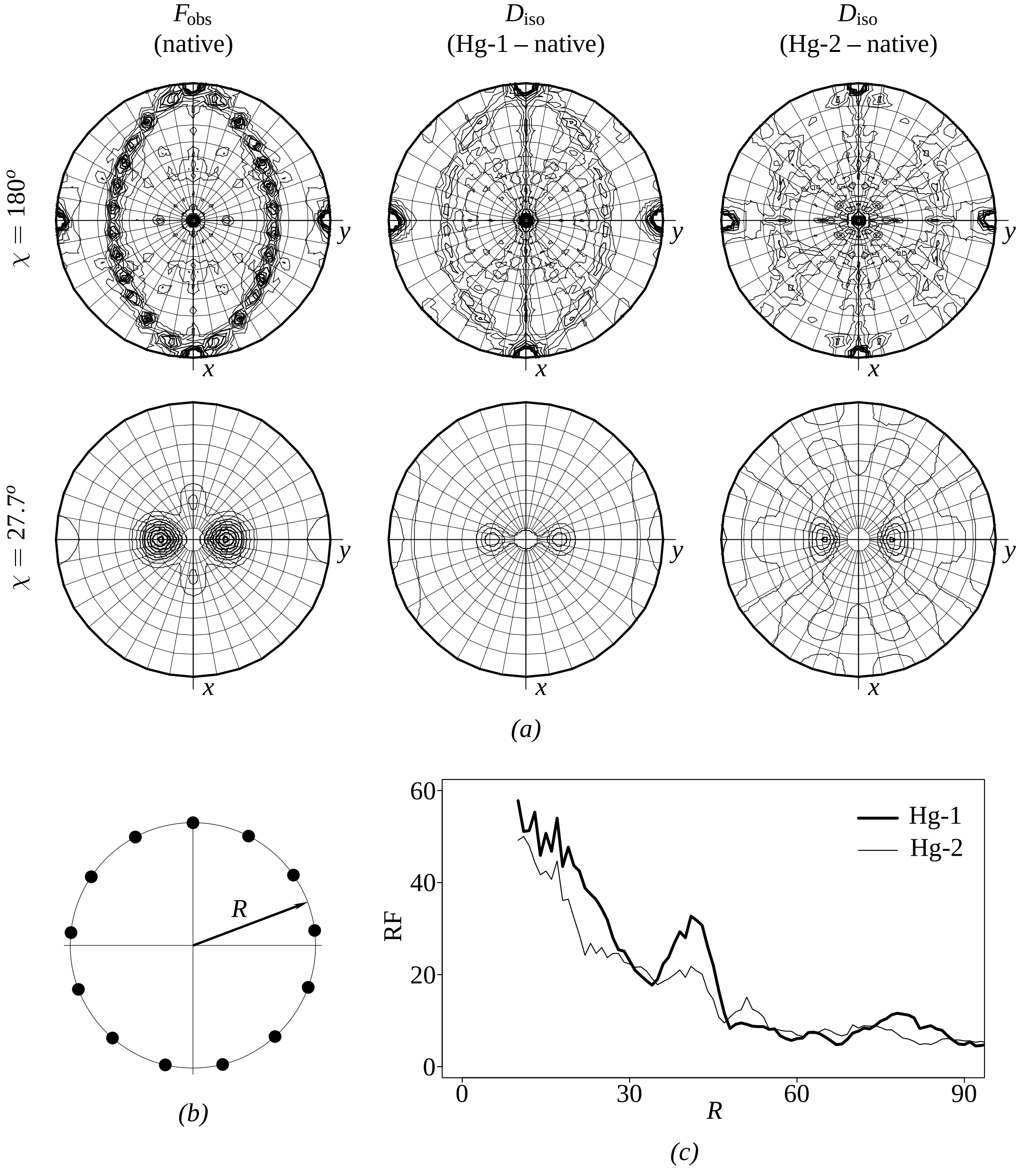

(a)

(b)

(c)

Figure 2.7. The Hg-substructure solution of the portal-protein derivative crystals. (*a*) The SRF computed for the native data (left) and for the isomorphous differences between the native data and the derivative data Hg-1 (middle) and Hg-2 (right). (*b*) The search model for exhaustive search composed of 13 mercury atoms located on the circle of variable radius *R*. (*c*) The plots of the maximal value of the CRF against *R* computed for the isomorphous differences between the native data and the derivative data Hg-1 (thick line) and Hg-2 (thin line).

run of *AMoRe* (Navaza, 2001) against isomorphous differences from the derivative Hg-1 and the best CC was plotted against the radius of the Hg-cycle (thick line in Fig. 2.7*c*). The CC peaked at 32.7% for the 41.0 Å radius model. The orientation of the Hg-ring corresponding to this peak was consistent with the SRF.

An identical search was performed against isomorphous differences between the less isomorphous derivative Hg-2 and the native data (thin lines in Fig. 2.7*c*). Again, there was a peak at $R = 41$ Å corresponding to the correct model in the correct orientation. However, the contrast in this case was much lower, so the results of this search alone would not be convincing enough.

The background of the plots in Fig. 2.7(*c*) decreases with the growth of the Hg-circle radius. This is because the radius of integration in the RF was not constant but was adjusted to be linearly dependent on the Hg-sphere radius. Thus the integration sphere included cross-vectors between Hg-atoms and their first and second neighbours only (the integration radius was about half the radius of Hg-circle). With this approach, the signals from all correct models (the case of multiple Hg binding) but not the noise would have been equalised. The protocol with large constant integration radius would be significantly slower, but would presumably result in a constant level of noise and higher level of signal coming from more cross-vectors.

The model with the Hg-circle radius 41 Å and 30 best orientations for this model found during the RF search against Hg-1 isomorphous differences were selected for the TF trials. The TF search using *AMoRe* and Hg-1 differences gave eight equivalent solutions with a CC of 13.5% (orientations 5–12). The second best CC was 9.9% (orientations 1–4). The found solutions were consistent with the SRF, had reasonable (97.5 Å) distance between symmetry equivalents and were the best among the TF peaks for the same orientation in terms of *R*-factor, CC of structure factors and the height of the TF peak. Therefore, there were no doubts that the correct substructure solution was found.

Thus the NCS-constrained exhaustive search with the CRF target proved to be successful for both the protein oligomer rebuilding (§2.3) and substructure solution. An important feature of this approach is that the orientations of the NCS axes are known, but corresponding constraints are relaxed during the search and this information is used for validation only. In the particular case under consideration, the validation of the substructure model was important, as it helped avoiding time-consuming attempts at phase improvement starting with a false substructure model.

After the portal protein structure was solved, another method of substructure solution was successfully tested, in which all possible NCS constraints were applied during the exhaustive search. Two parameters were scanned against the TF target, the Hg-circle radius and the position of the reference Hg on the circle. This was the analogue of the method used for structure solution of TPx-B (§2.1). Had only the Hg-2 derivative been available, the exhaustive search with the

RF target would not be sufficiently convincing to select the best substructure model and this two-dimensional search should have been invoked.

2.6.4 Structure determination and analysis

The phases to 3.4 Å were estimated using X-ray data from native crystal and both derivative crystals in an iterative procedure including heavy atom refinement, calculation of expected phases and 13-fold averaging. Heavy atom refinement and phase calculations were performed using my own program, which treated structure factors from the averaged map as a prior allowing implicit phase combination. The map averaging was performed using *maprot*. The model was built using *QUANTA* (Accelrys) and refined using *REFMAC* (Murshudov *et al.*, 1997). Initially, only the α-helical region around the tunnel was visible in the electron density map. This was built as polyalanine segments. The first model constituted 44.6% of the complete structure and the directions of some segments were incorrect. Several rounds of refinement with NCS restraints followed by rebuilding into the 13-fold averaged map allowed the correction and expansion of the model. Owing to the limited resolution, TLS parameters (Winn *et al.*, 2001) but not individual atomic *B* factors were refined.

The final model was refined against the 3.4 Å data set of the derivative Hg-1 to $R = 28.8\%$ and $R_{\mathrm{free}} = 31.9\%$. A complete subunit of the portal protein contained 503 residues, of which 28 N-terminal and 36 C-terminal residues were not included in the final atomic model and the segment 170–238 located in the peripheral part of the oligomer was partially modelled by a 30-residue polyalanine segment which was not docked into the sequence.

The 13 subunits of the portal protein are arranged around the central tunnel in a circular assembly with an overall diameter of $\sim$165 Å and a height of $\sim$110 Å (Fig. 2.8*b*). Helixes $\alpha 3$, $\alpha 5$ and $\alpha 6$ form the core of a single subunit (Fig. 2.8*c*). Helix $\alpha 5$ is connected to $\alpha 6$ by tunnel loop (residues 345–359) called so because it protrudes into the tunnel and the belt formed by these loops defined the most constricted area of the tunnel with the diameter of 27 Å in the 13-mer. The loops from adjacent subunits did not make any direct hydrogen-bonding interactions with each other but made extensive van der Waals contacts that stabilised their conformation and position in the tunnel. The most distinctive feature of the portal protein is that the long helix $\alpha 6$ contains a 45^o kink. This unusual conformation is stabilised by interactions with the C-terminus of helix $\alpha 5$, which is approximately perpendicular to $\alpha 6$. Two direct hydrogen bonds (A358–N421 and G360–E424) linking the tunnel loop and the N-terminus of $\alpha 6$ to the C-terminal domain of the subunit further stabilise this kinked conformation (Fig. 2.8*d*).

The three-helical core and some other features of the topology are conserved in the portal proteins of bacteriophages SPP1 and $\phi 29$. This similarity provides additional evidence for

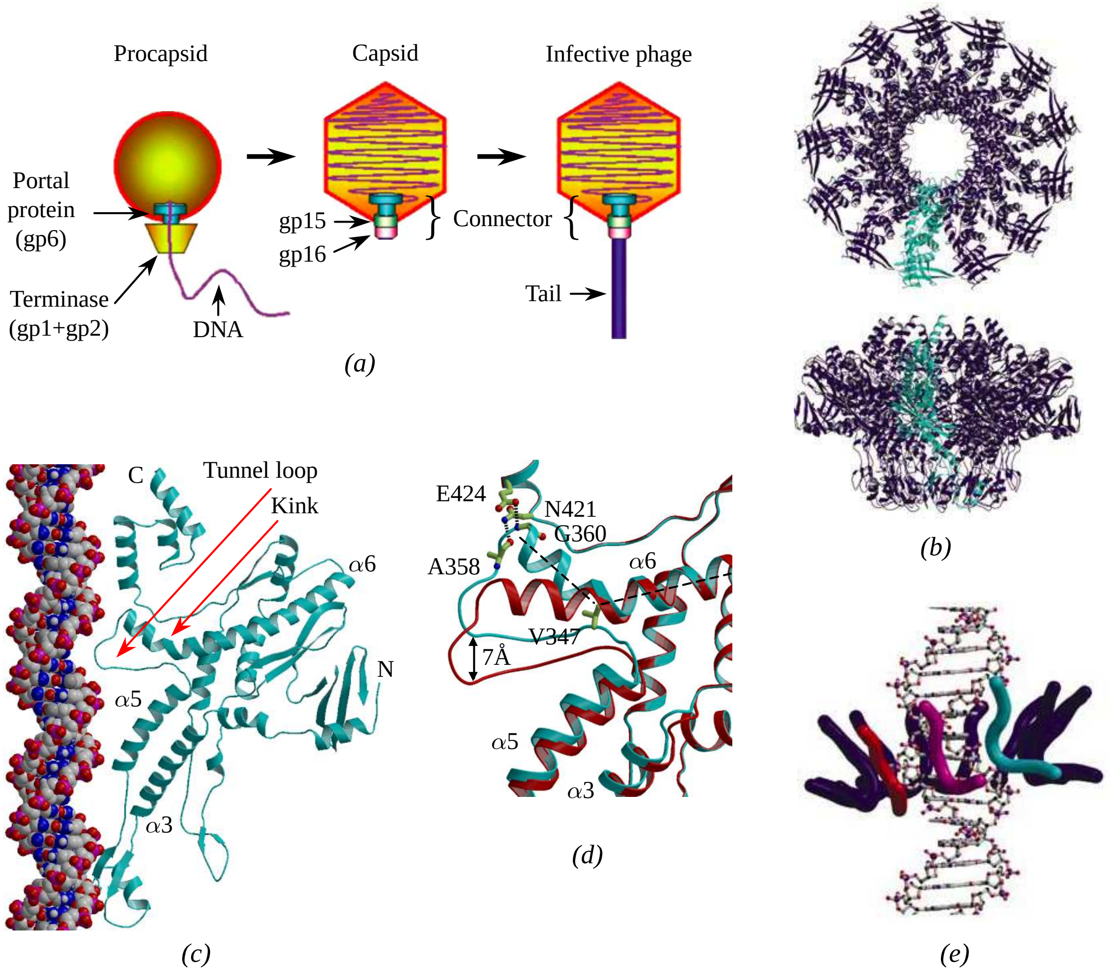

Figure 2.8. DNA translocation *via* the SPP1 portal protein. (*a*) Bacteriophage SPP1 assembly. Double-stranded DNA is translocated into the procapsid through the portal protein, which together with the terminase, forms a molecular motor. After termination of packaging, head completion proteins (gp15 and gp16) bind to the portal protein forming a head-to-tail connector. Tail attachment to the connector yields the infective phage particle. Before and after association with the procapsid the portal protein exists as 13- and 12-mer, respectively (*b*) X-ray structure of the SPP1 portal protein. Ribbon diagrams show the portal protein 13-mer along and perpendicular to its 13-fold axis. (*c*) Single subunits of the SPP1 portal protein. The B-form DNA (van der Waals model) is positioned along the tunnel to show the relative size and match between the tunnel loop and the major groove of the DNA. The relative position shown is that expected between the DNA and the “discharged” subunit 3 of the 12-mer portal protein in a functional complex. (*d*) Two extreme states of the tunnel loop: (cyan) observed in the crystal structure and (red) obtained by modelling a straightened conformation of helix α6. The residues stabilising the kinked conformation of this helix in the crystal structure are shown in ball and stick. (*e*) The proposed arrangement of the tunnel loops (ribbons drawn along the main-chain atoms of residues 350–360) in the complex of the dodecameric portal protein with the DNA (ball and stick). Loops occupying the three states inside the major groove are coloured red, magenta and cyan, while the remaining nine loops are in dark blue. The red and cyan states are the same as in (*d*).

the proposal that the dsDNA tailed bacteriophages diverged from a common ancestor, which was the root of the lineage formed by tailed phages and herpesviruses (Bamford *et al.*, 2005). Equally this conservation suggests that the mechanism of DNA translocation is similar in all these systems.

The application of normal mode analysis (NMA) to the MR structure solution was discussed in §1.1.11. In this study, the NMA-server ElNemo (Suhre & Sanejouand, 2004) was used to investigate possible conformational changes in the portal protein. One of the low-frequency modes corresponded to the movement of the loops along the tunnel axis and included the conformation in which helix $\alpha6$ was straightened and the end of the loop moved by about 7 Å down the tunnel, the distance corresponding to translocation of two base-pairs of the DNA (red ribbon in Fig. 2.8*d*). This conformation breaks the hydrogen bonds A358–N421 and G360–E424, but gains five α-helical hydrogen bonds, which are otherwise disrupted by the kink of $\alpha6$.

Further inspection of the structure showed that the structural motif comprising $\alpha5$ – tunnel loop – $\alpha6$ could function as molecular lever, in which a slight axial shift of helix $\alpha5$ is associated with a much larger axial shift of the N-terminal end of helix $\alpha6$ and the tunnel loop, the latter making shape matching interaction with the major groove of the translocated DNA (Fig. 2.8*c*). Mutagenesis and biochemical data (Isidro *et al.*, 2004; Oliveira *et al.*, 2006) suggested that the structural organisation of this motif is crucial for DNA translocation. In particular, five single amino acid substitutions in the tunnel impair DNA packaging. These include two mutations of V347 underpinning the kink in the helix $\alpha6$ with its side chain (Fig. 2.8*d*). Its mutation to alanine (smaller side chain) or methionine (larger side chain) apparently alters the kink in helix $\alpha6$ and therefore abolishes the DNA packaging. The above data, as well as the conservation of $\alpha3$, $\alpha5$ and $\alpha6$ in two known portal protein structures (phages $\phi29$ and SPP1) suggested that the signal or force exchange between ATPase and DNA could be accomplished through the structural motif $\alpha3$ – $\alpha5$ – tunnel loop – $\alpha6$.

2.6.5 Conformational asymmetry of the portal protein

During the structure solution the NCS is generally treated as an exact symmetry and the information on the NCS operations is particularly useful for reduction of the dimensionality of the search space. From the biological point of view, of interest are both the overall mode of the association of subunits into oligomers and the conformational variability of subunits. In particular, the conformational and atomic-scale asymmetry gives an insight into functioning of the motor proteins composed of several identical subunits (as in the case of E1-helicase, §2.4).

The 13-mer of the portal protein in the crystal structure was symmetric. No significant conformational differences between refined subunits were detected. Furthermore, the omit map showed no interpretable density that would not be accounted for in the model. However, the docking of twelve portal protein subunits into EM map of the dodecameric connector (§2.6.1 Orlova *et al.*, 2003) showed that the tunnel loops forming symmetric belt in the 13-mer would necessarily deviate from this symmetric arrangement in the active dodecameric assembly.

The fitting into the EM map was performed by Alexei Vagin using SAPTF (Vagin & Isupov, 2001) and NCS-constrained rigid body refinement, both implemented in *MOLREP*. The pseudoatomic model of the portal protein 12-mer revealed reasonable intersubunit contacts except for the C-terminal domain and the tunnel loops. Dissecting subunits into several rigid bodies and further refinement restored acceptable contacts between C-terminal domains, but not between loops.

The minimal diameter of the tunnel decreased by 10 Å on the transition of the portal protein from 13- to 12-mer, a substantially greater contraction than a simple scaling down by a factor 12/13. The reason for so large variation in the tunnel diameter was that the dimensions of the two oligomers were defined by inter-subunit contacts in the area separated from the tunnel axis by about 50 Å. As a result, the tunnel in the 12-mer was too narrow (van der Waals diameter $\sim$ 18 Å) to accommodate the B-form of the DNA (van der Waals diameter $\sim$ 23 Å) without clashes.

The clashes between neighbouring tunnel loops and the too narrow tunnel in the symmetric pseudoatomic model of 12-mer suggested that actual structure of dodecameric portal protein was asymmetric, at least in area of the tunnel, with flexible loop conformations. Conformational variability of the tunnel loops was supported by several other observations. These included weak electron density for the tunnel loops in the EM reconstructions of both the dodecameric SPP1 connector and the dodecameric ϕ29 portal protein embedded in the procapsid (Morais *et al.*, 2005). Similarly, in the crystal structures of the 12-subunit assembly of the ϕ29 portal protein (Simpson *et al.*, 2000; Guasch *et al.*, 2002), amino acid segments 229–245 that could form tunnel loops were not observed in the electron density.

The mutant of SPP1 portal protein with truncated C-terminal domain was found to form 14-mers and the crystal structure of this mutant has recently been solved (Joanne Turner and Fred Antson, personal communication). The extrapolation of the 14- and 13-mer structures to the 12-mer showed similar clashes and the same diameter of the tunnel as the pseudoatomic model.

The structure of the tunnel loops observed in the X-ray structure of the 13-mer and relative position of subunits in pseudoatomic model of 12-mer imposed strong constraints on possible organisation of the portal protein complex with the DNA. A model of the complex was therefore generated, in which unfavourable interatomic contacts were avoided (Fig. 2.8*e*). Subunits 1 and 3 were assigned the conformations shown in Fig. 2.8(*d*). The intermediate conformations of the remaining ten subunits were modelled by linear interpolation. The axis of the DNA was slightly shifted relative to the axis of the portal protein, so the tunnel loops of the subunits 1, 2 and 3 sank into the major groove of the DNA as shown in Fig. 2.8(*c*) for subunit 3. During the active event, tunnel loops 11 and 12, which are initially outside the major groove, are forced to slide between adjacent phosphates into the major groove and the communication between the active subunit of the ATPase and the active tunnel loops is accomplished via $\alpha3 – \alpha5$ as mentioned at the end of §2.6.4. After the active event, the system relaxes into an energy minimum, in which the individual states of subunits circularly permuted and the DNA is translocated by two base pairs. According to measurements by (Guo *et al.*, 1987; Morita *et al.*, 1993), one such transition occurs per one ATP hydrolysis event.

2.6.6 Conclusion

An NCS-constrained exhaustive search with the CRF target was used for the Hg-substructure solution in the course of determination of the SPP1 portal protein crystal structure. This method was used because the substructure could not be solved by automated direct methods.

Two structures of the bacteriophage SPP1 portal protein were determined and analysed, the X-ray structure of the isolated 13-subunit form and the pseudoatomic structure of a 12-subunit assembly derived from the EM reconstruction. The first defines the DNA-interacting segments (tunnel loops) that pack tightly against each other forming the most constricted part of the tunnel; the second shows that the functional dodecameric state must induce variability in the loop positions. Structural observations together with geometrical constraints dictate that in the portal-DNA complex, the loops form an undulating belt that fits and tightly embraces the helical DNA, suggesting that DNA translocation is accompanied by a Mexican wave of positional and conformational changes propagating sequentially along this belt.

3 Twinned structures

Geometrical classification of twins and intensity statistics in twinned crystals are discussed in the introduction (§1.2). In this chapter, the geometry of the crystal lattice and the intensity statistics in twins are studied in their relation to NCS.

It is known that if the NCS and twinning axes are aligned, then the correlations between NCS-related reflections affect the distributions of intensities and their differences used in twinning tests. For handling such data I first restate the equations for intensity statistics in a more convenient form (§3.1) and then derive theoretical distributions for two idealised cases. In the first case, the twinned structure contains an untwinned substructure with higher crystallographic symmetry (§3.1). Such a situation may, for example, occur in a crystal containing larger dimers complexed with smaller monomeric proteins. The second case under consideration is an OD-twin of type I/B (§3.4).

The second section of this chapter (§3.2) presents the analysis of the PDB, in which the cases of twinning were revealed and classified in terms of the presence or absence of interfering NCS. This section highlights the problem of incorrect space group assignment and, in particular, the problem of false-positive twins.

The last three sections present three examples of twinned structures with different relations between twinning and NCS. In the first and the second examples, attention is paid to the structural nature of the lattice constraints that make the twinning by metric merohedry possible. In the second of these two examples, the OD-nature of the crystal was shown to be responsible for both the lattice constraints and the alignment of the NCS and twin axes. In the third example, the OD-nature of the twin by reticular merohedry defines the relation between alternative lattices.

In all three cases I contributed to structure solution. People involved in the projects are acknowledged and related papers are cited in corresponding sections.

3.1 Intensity statistics in the case of correlated structure factors

In this section, the statistics that are used in twinning tests are derived for the following particular case of twinning by hemihedry. Two individual crystals represented by normalised structure factors f_1 and f_2 possess a common substructure represented by a structure factor f_0,

$$\begin{aligned} f_1 &= f_o + \Delta_1 \\ f_2 &= f_o + \Delta_2 \end{aligned} \tag{16}$$

Equation (16) assumes an agreement between the origins in the structures f_1 and f_2, so the two copies of the substructure f_0 overlap (if extended by crystallographic translations). It is also assumed that the substructures Δ_1 and Δ_2 do not contain complete translated copies of f_0.

In the hemihedral case under consideration the set of equivalent twin operations includes a twofold rotation $\hat{o}_t$. The twin operation $\hat{o}_t$ can be assigned a translational component to become a pseudosymmetry operation for f_0. The action of $\hat{o}_t$ on

$$\mathbf{f} = (f_1, f_2)^T \tag{17}$$

is written as

$$\hat{o}_t\mathbf{f} = \begin{pmatrix} 0 & 1 \\ 1 & 0 \end{pmatrix} \mathbf{f}. \tag{18}$$

Accordingly, $\hat{o}_t$ is further referred to as either NCS operation or twin operation depending on the context. When it acts on structure factors, it is an element of the pseudosymmetry space group of f_0. When it acts on intensities, its translational component is inactive and its rotational component is the twin operation.

3.1.1 Twinned intensities

Let α_1 and α_2 be relative volumes of individual crystals,

$$\alpha_1 + \alpha_2 = 1. \tag{19}$$

Typically, the smallest of α_1 and α_2 is denoted as α and is called the twinning fraction. In some equations, it is convenient to use another parameter,

$$\beta = \alpha_1 - \alpha_2. \tag{20}$$

Thus, $\alpha_1 = \alpha_2 = 1/2$ and $\beta = 0$ correspond to perfectly twinned crystal and $\beta = \pm 1$ correspond to a single crystal in one of two possible crystallographic orientations.

The squared moduli $|f_1|^2$ and $|f_2|^2$ of the two components of $\mathbf{f}$ are the intensities of the different individual crystals. Both intensities contribute to the total intensity Z,

$$Z = \alpha_1 |f_1|^2 + \alpha_2 |f_2|^2, \tag{21}$$

The operation $\hat{o}_t$ (18) permutes structure factors of twin-related reflections and, accordingly, intensities of individual crystals,

$$\hat{o}_t Z = \alpha_1 |f_2|^2 + \alpha_2 |f_1|^2. \tag{22}$$

Of particular interest are the mean of two intensities related by the twin operation, Z', and the difference between the two intensities represented here by its half value Z'',

$$\begin{aligned} Z' &= \frac{Z + \hat{o}_t Z}{2} = \frac{|f_1|^2 + |f_2|^2}{2} \\ Z'' &= \frac{Z - \hat{o}_t Z}{2} = \beta \frac{|f_1|^2 - |f_2|^2}{2} \end{aligned} \tag{23}$$

In a perfect twin $Z' = Z$ and $Z'' = 0$. Rotation of a twinned crystal by the twin operation does not change Z' and changes sign of Z''.

The random variable H,

$$H = \frac{|Z''|}{Z'} \tag{24}$$

is a more convenient representation of the difference between two intensities. Firstly, it is independent of the overall B-factor. Also, it is positive and therefore has, in general, a non-zero first moment, which is a preferable statistic compared to the second moment, as it is less sensitive to experimental errors. It is also important that H is a sufficient statistic for the twinning fraction α in the ideal model of twin (§1.2.4) and is likely to remain a "good" statistic in the presence of various factors perturbing the ideal model.

The experimental distributions and moments of random variables Z and H are used in perfect and partial twinning tests, respectively, and are compared with the theoretical predictions. The theoretical distributions of Z and H for uncorrelated structure factors were discussed in the introduction, in §1.2.3 and §1.2.4, respectively. The distribution of these variables for acentric correlated structure factors are derived and discussed in this section.

3.1.2 Examples

The PDB entries 1ewy and 1irm present examples of this type of twinning. In the first case (1ewy; Morales *et al.*, 2000), the asymmetric unit of the space group $P2_12_12_1$ contains a dimer of ferredoxin-NADP+ reductase (A) complexed with a single molecule of ferredoxin (B), so f_0 corresponds to the $P4_32_12$-substructure formed by molecules A, whereas Δ_1 and Δ_2 correspond to two different orientations of the $P2_12_12_1$-substructure formed by molecules B. In the second case (1irm; Sugishima *et al.*, 2002) the asymmetric unit of the individual crystal f_1 (or f_2) with the space group symmetry $P3_2$ contains three molecules of apo-heme oxygenase-1. Two of the three molecules are attributed to the substructure f_0 with the space group symmetry $P3_221$ and the third molecule belongs to Δ_1 (or Δ_2).

The operation $\hat{o}_t$ can be chosen as follows: any of two diagonal two-fold rotation of the $P4_32_12$ space group of f_0 (the first example), and any of two-fold rotations of the $P3_221$ space group of f_0 (the second example).

3.1.3 Joint distribution of structure factors

Let ρ, $0 < \rho < 1$, denote the correlation between normalised structure factors f_1 and f_2. This is a positive real number because of the common substructure f_0. Using vector notations (17), and $\mathcal{E}$ for the expected value, the covariance matrix for $\mathbf{f}$ is defined as follows,

$$M = \mathcal{E}(\mathbf{f}\,\mathbf{f}^{*T}) = \begin{pmatrix} 1 & \rho \\ \rho & 1 \end{pmatrix}. \tag{25}$$

It is further assumed that ρ is the same for all reflections. This corresponds to exact symmetry of f_0 relative to the NCS operation $\hat{o}_t$. In reality, the NCS is approximate and ρ decreases with increase of the resolution. Nevertheless, constant ρ is a good approximation especially because only low and medium resolution data are to be used in twinning tests to avoid the effect of experimental errors (§1.2.3, Fig. 1.2). It will be also shown in §3.4 that the model with constant ρ works even if the actual ρ is an oscillating function of l.

The assumption (25) is not always justified. For example, in the case of pseudotranslation, even the intensities from the same resolution shell should not be assumed to have the same expected values. Formal analysis of this special case is not included in this thesis, although a related example is presented below (§4.4). Also, the normal distribution of $\mathbf{f}$ is not always a good approximation for anisotropic data, although most anisotropic cases can be treated using a reduced resolution range for twinning tests.

The complex vector $\mathbf{f}$ can be represented in terms of its real and imaginary parts, $\mathbf{a}$ and $\mathbf{b}$, real vectors,

$$\mathbf{f} = \mathbf{a} + i\mathbf{b} \tag{26}$$

The joint distribution of $\mathbf{a}$ and $\mathbf{b}$ is normal with zero mean and variance-covariance matrix defined by (25),

$$p(\mathbf{a}, \mathbf{b}|\rho) = \frac{1}{\pi^2|M|} \exp\big(- \mathbf{f}^{T*} M^{-1} \mathbf{f} \big) \tag{27}$$

Because M is a real matrix,

$$p(\mathbf{a}, \mathbf{b}|\rho) = \frac{1}{\pi^2|M|} \exp\big(- \mathbf{a}^T M^{-1} \mathbf{a} - \mathbf{b}^T M^{-1} \mathbf{b} \big), \tag{28}$$

that is, the vectors $\mathbf{a}$ and $\mathbf{b}$ are identically distributed and mutually independent.

This is a standard statistical model for the structure factors f_1 and f_2 from two similar but not identical structures containing an equal number of atoms. The structure factors f_1 and f_2 are identically distributed and the correlation between them is ρ. The property $\rho \geqslant 0$ is not essential for the intensity statistics and it is ρ^2 that matters. All equations of this section are valid for $|\rho| \leqslant 1$, so they are applicable for the case of an OD-twin (§3.4), in which ρ may be considered as the cosine function of index l.

3.1.4 Moment generating function for Z' and Z''

The moment generating function (MGF; Stuart & Ord, 1994) of the random variables Z' and Z'' is defined as follows,

$$\mathcal{L}_{Z'Z''}(t', t'') = \mathcal{E}\left(e^{t'Z' + t''Z''}\right) \tag{29}$$

The calculations below are performed in terms of the random vectors **a** and **b** distributed according to (27). Equations (23) are transformed into vector form (17) and substituted into (29) to give

$$\mathcal{L}_{Z'Z''}(t', t'') = \frac{1}{\pi^2 |M|} \iint_{\mathbb{R}^2} \mathrm{d}\mathbf{a}^2 \iint_{\mathbb{R}^2} \mathrm{d}\mathbf{b}^2 \exp\left(-\mathbf{f}^{T*} A \mathbf{f} \right), \tag{30}$$

where M is defined in (25) and

$$A = M^{-1} - \frac{1}{2} \begin{pmatrix} t' + \beta t'' & 0 \\ 0 & t' - \beta t'' \end{pmatrix}. \tag{31}$$

Explicitly,

$$\mathcal{L}_{Z'Z''}(t', t'') = \frac{1}{|AM|} = \frac{1}{1 - t' + \frac{1}{4}(1-\rho^2)(t'^2 - \beta^2 t''^2)}. \tag{32}$$

The MGF (29) can be expressed in terms of joint probability distribution density of Z' and Z'',

$$\mathcal{L}_{Z'Z''}(t', t'') = \int\limits_{-\infty}^{\infty} \int\limits_{-\infty}^{\infty} p_{Z'Z''}(Z', Z'')\, e^{t'Z'} e^{t''Z''} \mathrm{d}Z' \mathrm{d}Z''. \tag{33}$$

and the probability distribution density can be restored as follows,

$$p_{Z'Z''}(Z', Z'') = \frac{1}{(2\pi i)^2} \int\limits_{-i\infty}^{i\infty} \int\limits_{-i\infty}^{i\infty} \mathcal{L}_{Z'Z''}(t', t'')\, e^{-t'Z'} e^{-t''Z''} \mathrm{d}t' \mathrm{d}t''. \tag{34}$$

In the last two equations, physically impossible pairs of Z' and Z'' are assumed to have zero probability. In (34), the integral with limits $-i\infty$ and $i\infty$ denotes an integral along the imaginary axis. Equations (33) and (34) are direct and inverse Fourier transformations in terms of parameters $\tau' = -it'$ and $\tau'' = -it''$. In the general case, the MGF is therefore defined for imaginary t' and t'' and, in special cases including the one under consideration, there exists an analytical extension of the MGF in the entire complex plane. The reason why the MGF transformation is used instead of Fourier transformation is a minor convenience of the MGF being real for real t (if defined) and n-th mixed moments of the random variables Z' and Z'' being equal to the n-th mixed derivatives of the MGF (without the coefficient i^n).

3.1.5 Moment generating function for Z' and $|Z''|$

The definition of the joint MGF of random variables Z' and $|Z''|$ and its explicit expression through the density function of random variables Z' and Z'' are as follows,

$$\mathcal{L}_{Z',|Z''|}(t',t'') = \mathcal{E}\big(e^{t'Z'+t''|Z''|}\big) \tag{35}$$

and

$$\mathcal{L}_{Z',|Z''|}(t',t'') = \int\limits_{-\infty}^{\infty}\int\limits_{-\infty}^{\infty} p_{Z'Z''}(Z',Z'')\, e^{t'Z'+t''|Z''|}\, \mathrm{d}Z'\mathrm{d}Z''. \tag{36}$$

The substitution of (34) and integration over Z' gives the following equation,

$$\mathcal{L}_{Z',|Z''|}(t',t'') = \frac{1}{2\pi i}\int\limits_{-i\infty}^{i\infty} \mathcal{L}_{Z'Z''}(t',t)\,\mathrm{d}t \int\limits_{-\infty}^{\infty} e^{t''|Z''|-t\,Z''}\mathrm{d}Z''. \tag{37}$$

To integrate over Z'', this integral is split into two integrals, over positive and negative Z''. The latter two are equal because $\mathcal{L}_{Z'Z''}(t',t)$ defined in (32) is a symmetric function of t. Therefore,

$$\mathcal{L}_{Z',|Z''|}(t',t'') = \frac{1}{\pi i}\int\limits_{-i\infty}^{i\infty} \mathcal{L}_{Z'Z''}(t',t)\,\frac{1}{t-t''}\,\mathrm{d}t. \tag{38}$$

As follows from (32), the integrand in (38) has three special points for the variable t. If $\Re(t'') < 0$, there is only one special point for $\Re(t) > 0$ and *vice versa*. The integration path is locked around this unique special point to get the following explicit expression for the MGF of interest,

$$\mathcal{L}_{Z',|Z''|}(t',t'') = \frac{1}{\sqrt{1-t'+(\mu\,t')^2}}\,\frac{1}{\sqrt{1-t'+(\mu\,t')^2}-\mu|\beta|t''}, \tag{39}$$

where

$$\mu = \frac{1}{2}\sqrt{1-\rho^2}. \tag{40}$$

As follows from (35), the joint moments of Z' and $|Z''|$ are obtained by differentiating this MGF. In particular, the first moments,

$$\mathcal{E}(Z') = 1 \tag{41}$$

and

$$\mathcal{E}(|Z''|) = \frac{1}{2}\,|\beta|\sqrt{1-\rho^2}, \tag{42}$$

and the following combination of the first and second moments,

$$\mathcal{E}\Bigg(\Big(|Z''| - Z'\mathcal{E}\big(|Z''|\big)\Big)^2\Bigg) = \frac{1}{8}\,\beta^2(1-\rho^4) \tag{43}$$

are used in the next section to estimate the R-factor between twin related intensities and the standard deviation of this estimate.

3.1.6 Perfect twinning test

The distribution of normalised intensities $P(Z)$ in the absence of the correlation between twin related structure factors is discussed in the introduction (§1.2.3). This is the case for $\rho = 0$. In this subsection, $P(Z)$ is derived and analysed for the general case of $\rho \neq 0$.

As follows from (23) and (29), the MGF of $p(Z)$ can be obtained from the MGF of $p(Z', Z'')$,

$$\mathcal{L}_Z(t) = \mathcal{E}\left(e^{tZ}\right) = \mathcal{E}\left(e^{t(Z'+Z'')}\right) = \mathcal{L}_{Z'Z''}(t,t). \tag{44}$$

From (32),

$$\mathcal{L}_Z(t) = \frac{1}{1 - t + \frac{1}{4}(1-\tilde{\beta}^2)t^2}, \tag{45}$$

where

$$1 - \tilde{\beta}^2 = (1-\rho^2)(1-\beta^2). \tag{46}$$

Equation (45) defines a one-parameter family of probability distribution functions. The normalised intensities are therefore distributed identically for all pairs of ρ and β corresponding to the same value of $\tilde{\beta}$ and neither ρ nor β can be identified from single experimental distribution.

Effective twinning fractions $\tilde{\alpha}_1$ and $\tilde{\alpha}_2$ are defined by similarity with (19) and (20),

$$\begin{aligned} \tilde{\alpha}_1 + \tilde{\alpha}_2 &= 1 \\ \tilde{\alpha}_1 - \tilde{\alpha}_2 &= \tilde{\beta}. \end{aligned} \tag{47}$$

If $\rho = 0$, then $\tilde{\beta} = \beta$. Hence $\tilde{\alpha}_1 = \alpha_1$, $\tilde{\alpha}_2 = \alpha_2$ and (6) is rewritten as follows,

$$P(Z) = 1 - \frac{\tilde{\alpha}_1 \exp(-Z/\tilde{\alpha}_1) - \tilde{\alpha}_2 \exp(-Z/\tilde{\alpha}_2)}{\tilde{\alpha}_1 - \tilde{\alpha}_2}. \tag{48}$$

Because $\mathcal{L}_Z(t)$ and, accordingly $P(Z)$, depend on a single parameter, $\tilde{\beta}$, equation (48) is valid for any value of ρ. Of course, $p(Z)$ can also be directly obtained from (44) and then integrated to give (48).

For a single crystal one of α_1 and α_2 is zero and therefore $\beta^2 = 1$. If $\hat{o}_t$ is in fact a crystallographic operation then $\rho = 1$. In both cases $|\tilde{\beta}| = 1$ and one of $\tilde{\alpha}_1$ and $\tilde{\alpha}_2$ is zero, and equation (48) reduces to

$$P(Z) = 1 - \exp(-Z). \tag{49}$$

This is a reference distribution for untwinned intensities.

The case $\tilde{\beta} = 0$ can only occur for uncorrelated structure factors ($\rho = 0$) and only if the crystal is a perfect twin ($\beta = 0$). In this case $\tilde{\alpha}_1 = \tilde{\alpha}_2$ and the singularity should be resolved in the denominator of (48) to give

$$P(Z) = 1 - (1 + 2Z)\exp(-2Z). \tag{50}$$

This distribution is used as a reference distribution for perfectly twinned intensities. This is a valid reference only for the hemihedral case without correlation.

The *n*-th moment of the distribution $P(Z)$ equals to the *n*-th derivatives of the MGF (45) at $t = 0$. In particular, the first moment equals one, as it should be for normalised intensities, and the expression for the second moment is as follows,

$$\mathcal{E}(Z^2) = \mathcal{L}''_Z(0) = \frac{3 + \tilde{\beta}^2}{2}. \tag{51}$$

It is common to plot the experimental distribution $P(Z)$ in the range of Z from 0.0 to 1.0. On the other hand, the second moment mostly depends on the distribution of large Z. Therefore, with this style of presentation, the plot of the distribution and the plot of second moments supply independent information.

Fig. 3.1(*a*) presents the family of distributions $P(Z)$ with variable $\tilde{\beta}$ defined by equation (48). Fig. 3.1(*b*) shows the second moments of these distributions according to equation (51), the assumption of constant correlation ρ being indicated by the independence of the second moments on resolution. In both plots, the limiting lines represent the limiting cases of single crystal (top blue line) and perfect twin (bottom red line), for which equations (49) and (50) are valid, respectively.

The family of the curves in Fig. 3.1(*a*) is one-parametric, so none of the distributions except for the above limiting cases of untwinned and perfectly twinned data allow an unambiguous evaluation of ρ and β. For example, the second top line in Fig. 3.1(*a*) corresponds to a partial twin with the twinning fraction $\alpha = 0.067$ ($\beta^2 = 0.75$) and uncorrelated structure factors ($\rho = 0$), or to a perfect twin with $\alpha = 0.5$ ($\beta = 0$) and partially correlated structure factors ($\rho^2 = 0.75$), or to any of the intermediate cases with $\tilde{\beta}^2 = 1 - (1 - \rho^2)(1 - \beta^2) = 0.75$.

In theory, the values of ρ and β can be restored using artificially twinned data, for which $\beta = 0$ and hence $\rho = |\tilde{\beta}|$. This procedure can be formally viewed as finding ρ using the distribution $P(Z')$ of symmetrised intensities Z' (23). Once ρ is known, β can be found from the distribution $P(Z)$ of intensities in the original data. The main disadvantage of this variation of the perfect twinning test is that the twin operation $\hat{o}_t$ must be known. This is a limitation from the original aim to provide a twinning test which does not require knowledge of the twin operation and is suitable for incomplete data.

Originally, Rees (1980) proposed to use the experimental distribution $P(Z)$ to estimate the twinning fraction. In most practical applications, this test is only necessary to establish the presence of twinning to avoid errors with the space group assignment. With such relaxed requirements to the perfect twinning test any correlation between structure factors is less critical. It is sufficient to establish a trend in the experimental distribution toward the theoretical twinned distribution. In this context, the most characteristic feature is the behaviour of $P(Z)$ at small Z.

It follows from (48) and (49) that in the untwinned case this behaviour is linear, while in twinned case it is quadratic,

$$\begin{array}{ll} P(Z) = \dfrac{2Z^2}{1-\tilde{\beta}^2} + O(Z^3) & |\tilde{\beta}| \neq 1 \\ & \qquad\qquad , \\ P(Z) = Z + O(Z^2) & |\tilde{\beta}| = 1 \end{array} \tag{52}$$

This difference is clearly seen even for quite a small effective twinning fraction $\tilde{\alpha} = 0.07$ (the second top line in Fig. 3.1*a*). Because of this quadratic behaviour at small Z, the twinned $P(Z)$ is often referred to as "sigmoidal" distribution. This feature emerges even in the presence of pseudotranslation, when the experimental $P(Z)$ may be very different from the distributions in Fig. 3.1(*a*), and when such quadratic behaviour may be the only sign of twinning in standard implementations of twinning tests. It is important that this criterion of twinning remains valid for $\rho \neq 0$. However, it needs to be underlined that although attractive because of its generality, this criterion relies on the accuracy of weak intensities and can only be used for well measured data.

Interestingly, the magnitudes ρ and β contribute to $\tilde{\beta}$ in an identical manner (46), although their meaning is exactly opposite in terms of correlation between related intensities: $\rho = \pm 1$ and $\beta = 0$ correspond to 100%-correlation, while $\rho = 0$ and $\beta = \pm 1$ result in the minimal possible

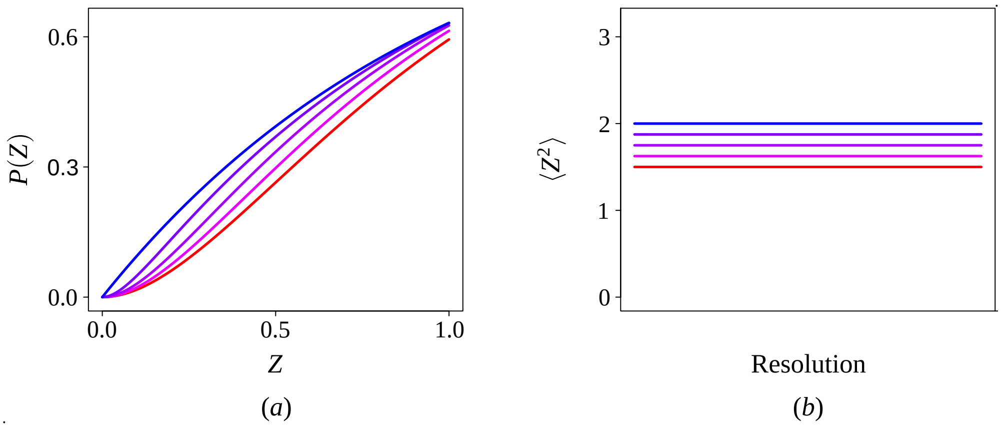

Figure 3.1. Perfect twinning tests in the case of correlated structure factors.

(*a*) The theoretical cumulative distributions of Z.

(*b*) The second moments of Z.

The colours red to blue *via* magenta correspond to $1-(1-\rho^2)(1-\beta^2)$ in the sequence 0.00, 0.25, 0.50, 0.75, 1.00; ρ is the correlation coefficient of structure factors, $\beta = 1-2\alpha$ and α is the twinning fraction. Accordingly,
(i) red line corresponds to perfect twin ($\alpha = 0.5$) and uncorrelated structure factors ($\rho = 0$),
(ii) in the intermediate cases α depends on ρ and varies in these ranges: 0.25–0.5, 0.146–0.5, 0.067–0.5.
(iii) blue line formally accounts for two cases, $\rho = 1$ (higher point group symmetry) and $\alpha = 0$, in both cases data are untwinned.

correlation. Accordingly, the correlation of structure factors and the correlation of intensities owing to twinning produce opposite effects on $P(Z)$ (Fig. 3.1). If the data are twinned, then the higher the correlation ρ, the smaller is the apparent twinning fraction if the data are assumed to be uncorrelated. In other words, any correlation between twin-related structure factors reduces the contrast of the perfect twinning test.

This property of the perfect twinning test may be confusing in some circumstances. For example, an erroneous assignment of too high crystal symmetry is quite likely in the presence of strong pseudosymmetry. Such errors result in "overmerged" data, which in theory can be identified using a perfect twinning test. However, it would be incorrect to expect the ideal statistics of perfect twin in this case because of $\rho \neq 0$.

3.1.7 Partial twinning test

The H-test, a partial twinning test is based on the experimental cumulative distribution of H defined in (24). The case of uncorrelated structure factors ($\rho = 0$) is discussed in §1.2.4. Here, $P(H)$ is derived and analysed for the general case of $\rho \neq 0$.

Let S be the following discrete random variable with possible realisations -1 and 1,

$$S = \frac{Z''}{|Z''|}. \tag{53}$$

Definitions (24) and (53) mean that $Z'' = SHZ'$ and, therefore,

$$p_{Z'Z''}(Z', Z'')\mathrm{d}Z'\mathrm{d}Z'' = p_{Z'Z''}(Z', SHZ')Z'\mathrm{d}Z'\mathrm{d}H. \tag{54}$$

The function in the right hand side of this equality is the joint probability density of S, H and Z',

$$p_{S\,H\,Z'}(S, H, Z') = p_{Z'Z''}(Z', SHZ')Z'. \tag{55}$$

As follows from (32) and (34), the probability distribution density in the right-hand side of (55) does not depend on S, the sign of the second argument. Therefore,

$$p_{H\,Z'}(H, Z') = \sum_{S\in\{-1,1\}} p_{S\,H\,Z'}(S, H, Z') = 2p_{Z'Z''}(Z', HZ')Z'. \tag{56}$$

An explicit expression for the probability distribution density $p(H)$ is derived below starting from the MGF of $p_{H\,Z'}(H, Z')$ with respect to the variable Z',

$$\mathcal{L}_{Z'}(H, t) = \int_{-\infty}^{\infty} p_{H\,Z'}(H, Z')e^{tZ'}\mathrm{d}Z'. \tag{57}$$

Substitution of (56) into (57) gives

$$\mathcal{L}_{Z'}(H, t) = 2\int_{-\infty}^{\infty} p_{Z'Z''}(Z', HZ')Z'e^{tZ'}\mathrm{d}Z' = 2\frac{\partial}{\partial t}\int_{-\infty}^{\infty} p_{Z'Z''}(Z', HZ')e^{tZ'}\mathrm{d}Z'. \tag{58}$$

Substitution of (34) and integration over Z' results in

$$\mathcal{L}_{Z'}(H,t) = \frac{1}{\pi i}\frac{\partial}{\partial t}\int_{-i\infty}^{i\infty} \mathcal{L}_{Z'Z''}(t - Ht'', t'')\,\mathrm{d}t''. \tag{59}$$

The integral in (59) is non-zero, if two special points of the integrand, r_1 and r_2 are separated by the imaginary axis, $\Re(r_1) < 0 < \Re(r_2)$. This corresponds to non-zero probability of given H. Associated boundaries of H are derived below; at the moment H is simply assumed to be within these boundaries. Therefore, the integration path can be considered as surrounding any one of two special points and integration can be performed using the following equation,

$$\frac{1}{2\pi i}\int_{-i\infty}^{i\infty} \frac{\mathrm{d}t''}{(t''-r_1)(t''-r_2)} = \frac{1}{r_1 - r_2} \tag{60}$$

to give

$$\mathcal{L}_{Z'}(H,t) = \pm 2\frac{\partial}{\partial t}\frac{1}{\sqrt{\beta^2 q(t)^2 - \beta^2\rho^2 + H^2\rho^2}}, \tag{61}$$

where

$$q(t) = 1 - \frac{1-\rho^2}{2}t. \tag{62}$$

As follows from (57), $\mathcal{L}_{Z'}(H,t)$ at $t = 0$ is the probability distribution density of H, which is a positive function suggesting the sign “+” in (61),

$$p(H) = \mathcal{L}_{Z'}(H,0) = \beta^2(1-\rho^2)\left(\beta^2(1-\rho^2) + H^2\rho^2\right)^{-\frac{3}{2}}. \tag{63}$$

The integration of $p(H)$ gives the cumulative probability distribution function of H,

$$P(H) = \frac{H}{\sqrt{\beta^2(1-\rho^2) + H^2\rho^2}}, \tag{64}$$

which reaches the value of one at $H = |\beta|$ thus defining the limits in which H varies,

$$0 \leqslant H \leqslant |\beta|. \tag{65}$$

In the case $\rho = 0$ equation (64) reduces to equation (15) validating presented calculations.

The first moment of H is derived from (63) by direct integration using the limits (65),

$$\mathcal{E}(H) = \int_0^{|\beta|} p(H)H\mathrm{d}H = |\beta|\frac{\sqrt{1-\rho^2}}{1+\sqrt{1-\rho^2}}. \tag{66}$$

Both the increase of ρ (correlation between structure factors increases) and decrease of β (correlation between intensities owing to twinning increases) cause $\mathcal{E}(H)$ to decrease. So in contrast to the behaviour of $\mathcal{E}(Z^2)$, the two sources of correlation between twin related intensities affect $\mathcal{E}(H)$ in accord.

However, the distribution of H (64) is two-parametric and the variation of the parameters ρ and β cause different changes in the function $P(H)$. The cases with different ρ differ by the curvature of the function $P(H)$ (Fig. 3.2*a*). The effect of decreasing β is shrinking of the untwinned function along H by factor β (Fig. 3.2*b*).

A low value of $\mathcal{E}(H)$ and the rapid growth of $P(H)$ similar to that represented by the blue lines in Figs. 3.2(*a*) and 3.2(*b*) occur either if the data are perfectly twinned or if the symmetry of the data is wrongly assigned and the twin operation being tested is actually a crystallographic operation. In such cases the perfect twinning test can be used to identify if there is twinning. Still a third case is possible, a strong pseudosymmetry coexisting with twinning. Any test can fail to distinguish such a case from the case of higher crystallographic symmetry. Fortunately, incorrect space group assignment in such cases is unlikely to prevent the structure solution and the symmetry can be corrected at the stage of structure refinement (related example is presented in §4.4).

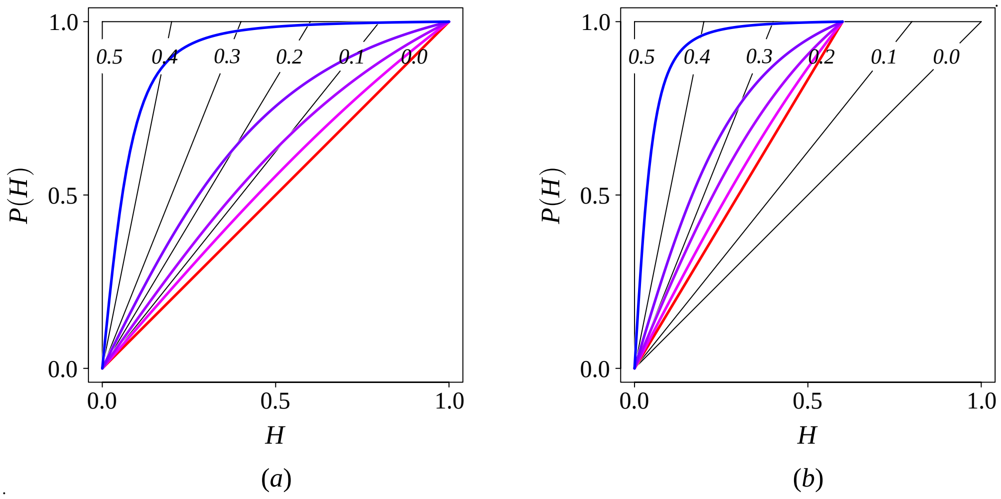

Figure 3.2. Partial twinning test in the case of correlated structure factors.

The coloured lines show theoretical cumulative distributions of H for
(*a*) untwinned data ($\alpha = 0$) and
(*b*) twinned data ($\alpha = 0.2$).
The colours red to blue *via* magenta correspond to squared correlation coefficient of structure factors ρ^2 in the sequence 0.00, 0.25, 0.50, 0.75, 0.99.

The thin black lines represent theoretical distributions for uncorrelated structure factors ($\rho = 0$) and the numbers in front of these lines indicate corresponding values of the twinning fraction α.

3.2 RvR plot

Refinement against twinned data has recently been implemented in *REFMAC* (Garib Murshudov, personal communication; §1.2.5). This work required a collection of test cases. Therefore, we undertook an investigation of all the possible twinning cases, known or undetected, for structures deposited in the PDB (Lebedev *et al.*, 2006). The goal of the work was to understand the symmetry environments most frequently accompanying twinning and to pinpoint problems with refinement of twinned structures.

The search for twins in the PDB was originally performed in terms of estimates of the twinning fraction obtained from the mean values of H (§3.1.7) for both observed and calculated intensities. I wrote a subroutine for the analysis of the lattice symmetry for Alexei Vagin to incorporate it into *SFCHECK*. A project student, Nagarajan Periasamy, under my and Garib Murshudov's supervision, wrote a *tcsh*-script for scanning the PDB and I analysed all the structures that were likely to be twinned. The estimate of twinning fraction for the calculated intensities was intended to be a negative control that could help identifying structures overfitted to the twinned data, but it was found that there are too many structures for which this value was significantly greater than zero because of the alignment of the NCS and twin axes. I later recast the scatter plot in terms of R_{twin}, as this statistic is more robust to the resolution range used compared to the above estimate of twinning fraction. This also helped avoid confusing terms such as "an estimate of twinning fraction for calculated intensities". For this thesis I have rewritten the software using the statistical package *R* (R Development Core Team, 2005) but have analysed the same set of structures. The new script used only acentric reflections which made the comparison with the theory possible. In addition, a larger area of RvR-plot was annotated and more twins found, and the detection of false-positives was more accurate as all pseudosymmetric structures selected for annotation were automatically converted into higher symmetry space group using subroutines from *Zanuda* (§4.3) and refined to check whether the pseudosymmetry and twinning were actually a misinterpretation of a higher crystallographic symmetry. The updated results are presented below in this section.

Firstly, the algorithm is described, which was used for the automatic determination of potential twin operations. Next, the expected value of the R-factor between twin related intensities is derived. Finally, analysis of the PDB is presented and the results are summarised in Fig. 3.3 (p.110) and Table 3.1 (p.114).

3.2.1 Algorithm for lattice symmetry

Several authors (Flack, 1987; Le Page, 2002; Grimmer, 2003) have already described the automatic identification of potential twin operations using unit-cell parameters and space group.

An algorithm, which is simpler to implement and more efficient in the case of twinning by (pseudo)merohedry, is described below.

A necessary step in all these algorithms is reducing the cell to a minimum primitive cell, either a Buerger or Niggli cell; see, for example, Mighell & Rodgers (1980) and references therein. In the basis associated with any minimal primitive unit-cell, the basis vectors of any other minimal primitive unit-cell have components -1, 0 or 1. Accordingly, any crystallographic point group operation is represented in this basis by a matrix with elements from $\{-1, 0, 1\}$, as it transforms a minimal primitive cell into a minimal primitive cell.

The set X of all 480 matrices with elements from $\{-1, 0, 1\}$, of finite order with respect to matrix multiplication and with determinant equal to one is generated. This set includes all matrices representing (pseudo)rotations of the lattice, but also contains irrelevant matrices. Each matrix $o \in X$ is scored according to the perturbation $\bar{\omega}$ that it causes to the metric matrix m derived from the primitive unit-cell parameters,

$$8\,(\tan\tilde{\omega})^2 = \mathrm{trace}\Big(\big(\,\delta - o\,m^{-1}o^T m\,\big)^2\Big). \tag{67}$$

In the case of two-fold rotations, the perturbation $\bar{\omega}$ converges to the obliquity angle ω as the obliquity angle decreases. The reason for using $\bar{\omega}$ as a score instead of ω is that the obliquity angle is not a good measure of lattice perturbation for the rotations of higher order.

The operations of the crystal point group are transformed to the primitive cell to give G, a group of 3×3 matrices with elements from $\{-1, 0, 1\}$. The matrices from X are used sequentially, in order of increasing $\bar{\omega}$, to expand G to the point group of the lattice (pseudo)rotations H. At each step, the current H is replaced by its external product with the next $o \in X$. The procedure is terminated and the last step cancelled, if the new H is an infinite group (25th element is generated).

Finally, the coset decomposition of H relative to G is found and one representative from each coset is selected to be further used as a potential twin operation. The lattice perturbation $\bar{\omega}$ is invariant relative to the exact rotations from G and the same value of $\bar{\omega}$ is therefore associated with all members of the same coset. This is an additional advantage of $\bar{\omega}$ as compared with the obliquity angle ω.

The twin is a twin by merohedry if the twin operation belongs to the hemihedry of a merohedral point group and the twin is a twin by pseudomerohedry otherwise. To draw Fig. 3.3(*b*), the type of twinning associated with given potential twin operation was automatically analysed using the following method. Let G be a point group and m be a metric matrix represented as a set of 6×6 matrices and as a 6-vector, respectively. Let m be invariant with respect to G,

$$g\,m = m, \quad g \in G. \tag{68}$$

Consequently, the projector

$$\pi = |G|^{-1} \sum_{g \in G} g$$

is such that $\pi m = m$. Let o be a 6×6 matrix representing a potential twin operation. If

$$o\pi = \pi, \tag{69}$$

then

$$om = o\pi m = \pi m = m$$

and no constraints are needed for m to be invariant with respect to o in addition to those imposed by (68). Therefore, if (69) holds, then o generates twinning by merohedry. This test requires no tables and can be performed in integers if the 6×6 matrix representation of G corresponds to its 3×3 matrix representation in fractional coordinates.

These two algorithms were implemented in a *FORTRAN* program used for the analysis of twins in the PDB. A modified version of my algorithm for determination of twin operations was later implemented in *cctbx* (Ralf W. Grosse-Kunstleve, personal communication)

3.2.2 *R*-factor between twin-related intensities

Let R_{twin} denote the intensity-based R factor between reflections related by potential twin operation S_{twin},

$$R_{\text{twin}} = \frac{\sum_{\mathbf{h}} |I_{\mathbf{h}} - I_{\mathbf{h}'}|}{\sum_{\mathbf{h}} (I_{\mathbf{h}} + I_{\mathbf{h}'})}. \tag{70}$$

Summation in (70) is over all unique reflections $\mathbf{h}$, such that intensities for both $\mathbf{h}$ and $\mathbf{h}' = S_{\text{twin}}\mathbf{h}$ have been measured and $\mathbf{h} \neq \mathbf{h}'$. The definition (70) coincides with the definition of R_{sym} in the case of two symmetry operations. Therefore, R_{twin} can be directly compared with R_{sym} estimated during data processing.

In terms of the normalised sum, Z' and difference, Z'' of twin-related intensities defined in (23),

$$R_{\text{twin}} = \frac{\sum_{\mathbf{h}} \chi_{\mathbf{h}} |Z''_{\mathbf{h}}|}{\sum_{\mathbf{h}} \chi_{\mathbf{h}} Z'_{\mathbf{h}}}. \tag{71}$$

In this equation, $\chi_{\mathbf{h}}$ is the normalisation coefficient, which depends on the resolution of a given reflection.

The expected value of R_{twin} is approximated by the ratio of the expected values of the numerator and denominator. Under assumption of constant correlation between twin-related structure factors, as in §3.1, the expected values of Z' and $|Z''|$ are independent of $\mathbf{h}$ and sums of normalisation coefficients are cancelled,

$$\mathcal{E}\big(R_{\text{twin}}\big) \approx \frac{\mathcal{E}\Big(\sum\limits_{\mathbf{h}} \chi_{\mathbf{h}} |Z''_{\mathbf{h}}|\Big)}{\mathcal{E}\Big(\sum\limits_{\mathbf{h}} \chi_{\mathbf{h}} Z'_{\mathbf{h}}\Big)} \approx \frac{\mathcal{E}\big(|Z''|\big)}{\mathcal{E}(Z')}. \tag{72}$$

The expression in terms of the correlation coefficient between twin-related structure factor ρ and relative volume of smaller individual crystal α follows from (20), (41) and (42),

$$\mathcal{E}\big(R_{\text{twin}}\big) \approx \mathcal{E}\big(|Z''|\big) = \frac{1}{2}\,(1-2\alpha)\,\sqrt{1-\rho^2}. \tag{73}$$

The standard deviation,

$$\sigma^2(R_{\text{twin}}) = \mathcal{E}\bigg(\Big(R_{\text{twin}} - \mathcal{E}\big(R_{\text{twin}}\big)\Big)^2\bigg) \tag{74}$$

is expressed through the ratio of the expected values,

$$\sigma^2(R_{\text{twin}}) \approx \frac{\mathcal{E}\bigg(\Big(\sum\limits_{\mathbf{h}} \chi_{\mathbf{h}} |Z''_{\mathbf{h}}| - \mathcal{E}\big(|Z''|\big) \sum\limits_{\mathbf{h}} \chi_{\mathbf{h}} Z'_{\mathbf{h}}\Big)^2\bigg)}{\mathcal{E}\bigg(\Big(\sum\limits_{\mathbf{h}} \chi_{\mathbf{h}} Z'_{\mathbf{h}}\Big)^2\bigg)}. \tag{75}$$

The expected value of the square in the denominator in (75) is approximated by the square of the expected value, the expected values of Z' and $|Z''|$ are assumed to be independent of $\mathbf{h}$, and equations (41) and (43) are used to obtain the following approximation,

$$\sigma^2(R_{\text{twin}}) \approx \frac{1}{8}(1-2\alpha)^2(1-\rho^4)\Big(\sum_{\mathbf{h}} \chi_{\mathbf{h}}\Big)^{-2} \sum_{\mathbf{h}} \chi^2_{\mathbf{h}}. \tag{76}$$

The dependence of the normalisation coefficient χ on $s = |\mathbf{h}|$, on the overall scale factor a and the temperature factor b is approximated by the following Gaussian,

$$\chi(s) \approx a\,e^{-\frac{1}{2}bs^2} \tag{77}$$

and summation is replaced by integration to evaluate the two sums in (76),

$$\begin{aligned} \sum_{\mathbf{h}} \chi_{\mathbf{h}} &\approx \frac{3N}{\bar{s}^3} \int\limits_0^{\bar{s}} a\,e^{-\frac{1}{2}bs^2} s^2 \mathrm{d}s \approx \frac{3\sqrt{\pi}}{\sqrt{2}}\,\frac{Na}{(\bar{s}\sqrt{b})^3}, \\ \sum_{\mathbf{h}} \chi^2_{\mathbf{h}} &\approx \frac{3N}{\bar{s}^3} \int\limits_0^{\bar{s}} \big(a\,e^{-\frac{1}{2}bs^2}\big)^2 s^2 \mathrm{d}s \approx \frac{3\sqrt{\pi}}{4}\,\frac{Na^2}{(\bar{s}\sqrt{b})^3}. \end{aligned} \tag{78}$$

In these approximations, N is the number of reflections including all symmetry equivalents, the intensities of the reflections beyond the upper resolution limit $\bar{s}$ are assumed to be negligible and therefore the upper integration limits are replaced by infinity. Finally, the combination of (73), (76) and (78) gives the following approximation for the relative error of the estimate (73),

$$\frac{\sigma(R_{\text{twin}})}{\mathcal{E}(R_{\text{twin}})} \approx \sqrt{\frac{(\bar{s}\sqrt{b})^3\,(1+\rho^2)}{12\sqrt{\pi}\,N}}. \tag{79}$$

In the rather unfavourable case of high temperature factor, $b = 50\text{Å}^2$, inadequately high upper resolution limit $\bar{s} = 0.5\text{Å}^{-1}$, moderate number of reflections, $N = 10000$ and $\rho = 1$, the relative error is 0.02. The absolute error of the estimate of ρ^2 from R_{twin} is of the same order of magnitude and is much less than the variation of ρ^2 with resolution.

Let $R_{\text{twin}}^{\text{obs}}$ and $R_{\text{twin}}^{\text{calc}}$ denote R_{twin} calculated using observed intensities and intensities derived from the atomic model, respectively. The calculated intensities, which represent a single individual crystal, are untwinned. Therefore,

$$\begin{aligned} R_{\text{twin}}^{\text{calc}} &\approx \frac{1}{2}\sqrt{1-\rho^2}, \\ R_{\text{twin}}^{\text{obs}} &\approx (1-2\alpha)\, R_{\text{twin}}^{\text{calc}}. \end{aligned} \tag{80}$$

Given twinned data and an atomic model of the crystal, the mean squared correlation between twin-related structure factors, ρ^2 and the twinning fraction, α can be estimated from the first and the second equations in (80), respectively.

If the unit cell parameters and space group of a given structure allow twinning, then the structure can be represented by a point in the plot of $R_{\text{twin}}^{\text{obs}}$ against $R_{\text{twin}}^{\text{calc}}$ (RvR-plot, Fig. 3.3). The value of ρ^2 is in the range 0 to 1 and the value of α is in the range 0 to 1/2. Therefore, as long as the approximation (25) is valid, the point is located in the triangle defined by the following inequalities,

$$\begin{aligned} 0 \leqslant R_{\text{twin}}^{\text{calc}} &\leqslant \frac{1}{2}, \\ 0 \leqslant R_{\text{twin}}^{\text{obs}} &\leqslant R_{\text{twin}}^{\text{calc}}. \end{aligned} \tag{81}$$

Fig. 3.3(*a*) provides a qualitative characterisation of possible cases. The points with $R_{\text{twin}}^{\text{calc}} \approx 1/2$ represent the cases, in which the twin-related structure factors do not correlate (these may be twinned or untwinned). If the space group assignment is incorrect and the potential twin operation is in fact the operation of the crystal point group, then $R_{\text{twin}}^{\text{calc}} \approx 0$. The abbreviation RPS stands for rotational pseudosymmetry and denotes the intermediate cases, in which the orientations of some molecules are related by the potential twin operation.

Any single-value intensity statistic can be used in a similar manner to estimate α and ρ and to characterise the relation between NCS and twinning. A good candidate is the mean value of H defined in (24). In the case of uncorrelated structure factors, H is a sufficient statistic for α and, similarly to R_{twin}, the expected value of this statistic (66) linearly depends on α. However, R_{twin} has several minor advantages: it is directly comparable with R_{sym}; there is no singularity in the denominator for small intensities, in contrast to H; and the contribution from high-resolution shells with high experimental errors is downweighted. In addition, the nonlinearity on ρ^2 is less in the case of R_{twin}.

The RvR-plot or similar plot for another single-value statistic can be useful for structure validation. In this project, it was used for detection of twinned cases in the PDB.

3.2.3 Scatter RvR plot based on PDB-data

The simplest possible way to select twinning cases from the PDB would be to extract the relevant information from the PDB headers or related papers. However, this approach is not sufficient because the researchers depositing data or writing papers may have not noticed or not discussed twinning (false negatives), or may have misinterpreted higher crystal symmetry as twinning (false positive). Therefore, it was decided to analyse PDB entries directly. This direct approach may also lead to a better understanding of the problems with the detection of twinning.

The PDB February 2004 release containing about 22 000 structures was screened and the entries in which both coordinates and structures factors were available and readable by CCP4 software (11 367 entries) were used in the analysis. The unit-cell parameters and space group of these entries were analysed using the technique described above (§3.2.1). In this analysis, a lattice perturbation (67) less than 3.5^o was allowed. This threshold was about two times less than the Mallard's limit of 6^o for the obliquity angle §1.2.1. If twinning by (pseudo)merohedry was possible then this data set was selected for further analysis (4010 entries). If observed intensities were present they were used directly for the *R*-factor calculations, and if only observed structure amplitudes were available, they were squared to approximate corresponding intensities.

For each of the selected PDB-entries, potential twin operations were selected, one from each coset of equivalent operations, and the associated $R_{\text{twin}}^{\text{obs}}$ and $R_{\text{twin}}^{\text{calc}}$ were calculated. If there were more than one non-equivalent operations (as, for example, in *P*3), the one with the lowest value of $R_{\text{twin}}^{\text{obs}}$ was selected. Thus, each selected entry was characterised by two quantities, $R_{\text{twin}}^{\text{obs}}$ and $R_{\text{twin}}^{\text{calc}}$, and the corresponding point was drawn on the scatter RvR plot (Fig. 3.3*b*). In addition, the method described in §3.2.1 was used to decide whether any twinning for the selected twin operation could be by merohedry or pseudomerohedry. The points in Fig. 3.3(*b*) are coloured according to the results of this analysis. The specific areas and some peculiarities of the RvR plot are discussed below.

Calculation of $R_{\text{twin}}^{\text{obs}}$ and $R_{\text{twin}}^{\text{calc}}$ were performed for all data and for the resolution range 10 to 3 Å and revealed only a marginal difference between two sets of R-factors for most examples. Only for six structures from the annotated area of the RvR-plot was this difference for any of $R_{\text{twin}}^{\text{obs}}$ and $R_{\text{twin}}^{\text{calc}}$ greater that 0.05 and only in one case could lead to misinterpretation of the results. However the latter structure was annotated manually as untwinned. Fig. 3.3 shows the results with the resolution cut-off applied, as it was done for the previous versions of the RvR plot discussed in the beginning of this section (§3.2).

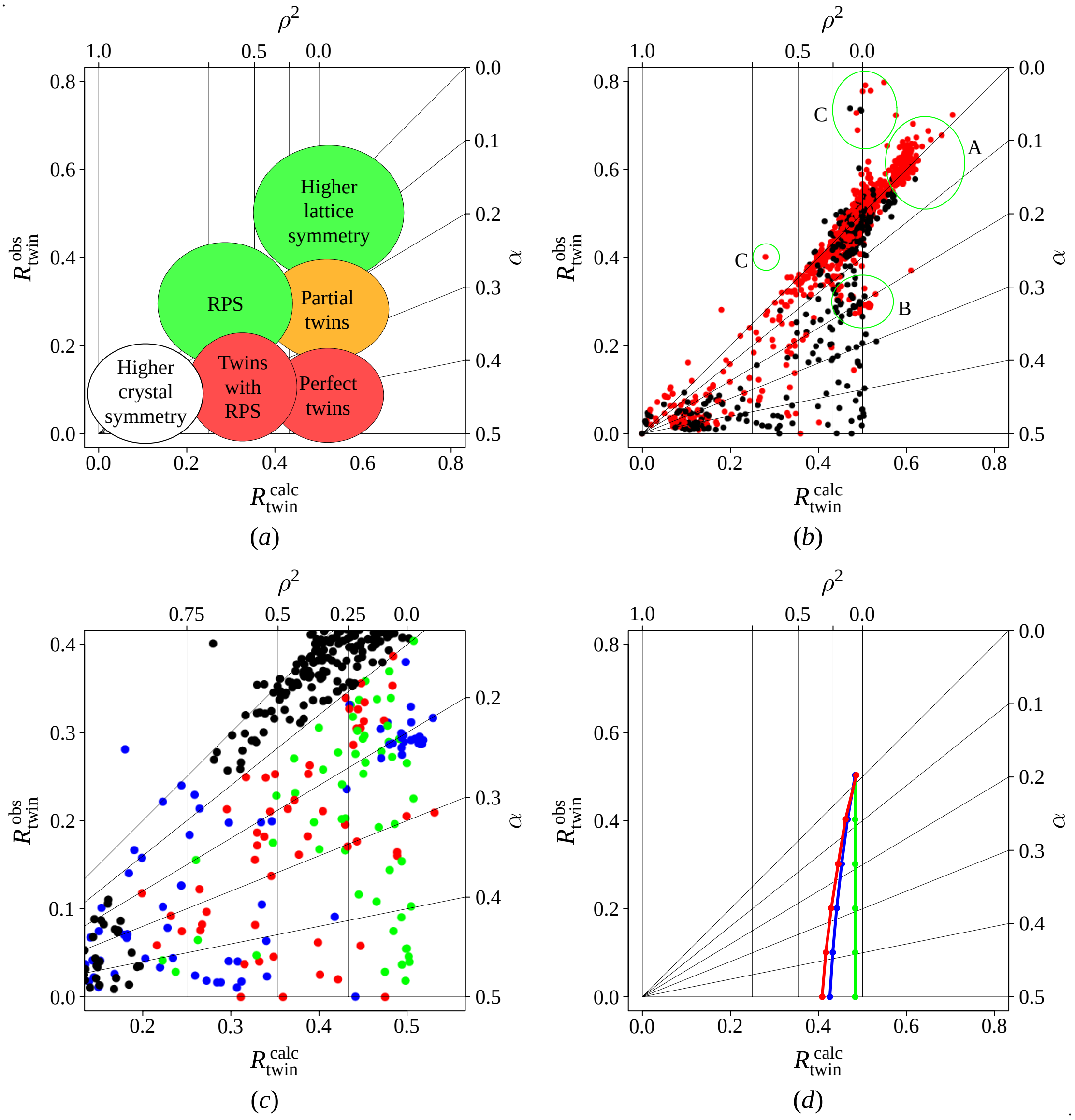

Figure 3.3. RvR scatter plot. (*a*) Schematic view of RvR scatter plot: expected locations of points corresponding to different combinations of twinning and RPS. (*b*) Observed RvR scatter plot: red, (potential) twins by merohedry; black, (potential) twins by pseudomerohedry. Green ovals show the area populated by cases with translational NCS (labelled *A*) and the areas corresponding to experimental data incorrectly deposited in the PDB with structure amplitudes marked as intensities and *vice versa* (labelled *B* and *C*, respectively). (*c*) Observed RvR scatter plot, enlargement of (*b*): black, known to be untwinned and not analysed; blue, found to be untwinned after further analysis; green, twins without RPS; red, twins with some degree of RPS. (*d*) Middle blue curve, results after refinement of PDB entry 1nqh, performed without taking twinning into consideration, against simulated data sets with the twinning fractions in the range 0–0.5 with default restraints on temperature factors. Left red curve, the same calculations with relaxed restraints on the temperature factors. Right green curve, results before refinement, $R^{\rm calc}_{\rm twin} \approx 0.5$. It is expected that proper twin refinement would preserve this value.

3.2.4 Untwinned cases

A large cluster around (0.5, 0.5) includes the points corresponding to untwinned crystals without RPS and, in particular, to untwinned crystals belonging to merohedral point groups 4, 3, 32, 6, 23. In addition, some of the points from this cluster are likely to represent detwinned data sets. The latter cases of twinning could be found by scanning the headers of the coordinate files, but could not be validated. This analysis has not been performed.

The points on and close to the diagonal, with $R^{\text{calc}}_{\text{twin}} \approx R^{\text{obs}}_{\text{twin}}$ in the range 0.3–0.4 form the lower tail of the main cluster and correspond to untwinned crystals with RPS. This tail extends down the diagonal to about 0.2, where one can find an extreme example of pseudosymmetry (1i1j; Lougheed *et al.*, 2001). In this high-resolution structure, the r.m.s.d. of C^{α} atoms from the positions corresponding to higher crystal symmetry is about 0.25 Å.

The main cluster also has an upper diagonal tail around (0.6, 0.6) corresponding to structures with translational NCS, in which the set of NCS vectors is not invariant with respect to S_{twin}. In these structures, S_{twin} maps weak reflections into strong reflections and the assumption that the expected values of twin-related intensities are equal (25) is violated. The numerator in (71) increases and therefore R_{twin} becomes greater than expected. Twinning seems unlikely in such structures, note the empty area in the RvR plot below the area under consideration.

The cluster at the origin corresponds to the structures in which the crystal symmetry is incorrectly assigned and is actually higher than that used in the refinement and reported in the PDB entry. In 42 cases randomly chosen from this cluster refinements in the original and higher symmetry space groups were performed starting from symmetrised models without solvent and gave differences in R_{free} in the range -0.02 to 0.02. (Inclusion of solvent would break the higher symmetry.) I deemed this to represent successful refinement. In all these cases the intensity statistics either favour the higher symmetry or are inconclusive. It seems therefore impossible to reject the null hypothesis of higher symmetry with the experimental data available in the PDB, although it cannot be excluded that analysis of unmerged intensities and merging statistics could reveal pseudosymmetry and twinning in some of these structures.

There are extra features in the RvR-plot, which arise from errors in deposition. These are two small clusters located above and below the main cluster and highlighted by green ovals in Fig. 3.3(*b*). In the first one, at about (0.5, 0.3), the structure amplitudes are labelled as intensities, and in the second one, at about (0.5, 0.7), the intensities are labelled as the structure amplitudes. Such mistakes can in principle be automatically identified if necessary. However, if additional factors, such as twinning, pseudosymmetry or anisotropy affect the data, or several deposition inaccuracies (for example, deposition of the detwinned data instead of the measured data) are present simultaneously, then such an analysis becomes complicated, if at all possible.

For example, the manual analysis of the "twinned" area of the RvR-plot revealed several data sets with unusual intensity statistics, which could not be unambiguously attributed to twinning, NCS or a combination of these two.

3.2.5 Cases of twinning

The cases with $R^{\text{obs}}_{\text{twin}} < 0.4 R^{\text{calc}}_{\text{twin}}$ and $R^{\text{calc}}_{\text{twin}} > 0.2$, as well as some randomly chosen cases from other areas of the RvR plot, were further investigated (coloured circles in Fig. 3.3*c*) to validate the presence or absence of twinning and to characterise the NCS if present. It was assumed that this area contained all twinned cases with significant twinning fraction ($\alpha > 0.1$) except for the PDB entries with detwinned data. However, some of the twins with $\alpha \gtrapprox 0.1$ could have been overlooked, and actual α in identified twins could be greater than expected from the RvR plot. This is because refinement against twinned data but with twinning ignored leads to underestimated value of $R^{\text{calc}}_{\text{twin}}$ and consequently underestimated α (§3.2.6; Fig. 3.3*c*).

The protocol of analysis included validation of the model (*SFCHECK*; Vaguine *et al.*, 1999), visual analysis of the structure (*Coot*; Emsley & Cowtan, 2004), analysis of the SRF (*MOLREP*; Vagin & Teplyakov, 1997), perfect twinning tests (cumulative distribution of normalised intensity and the second moments of acentric reflections; *TRUNCATE*; Collaborative Computational Project, Number 4, 1994) and partial twinning test (*H*-tests; *SFCHECK*). The analysis of the SRF and twinning tests were performed for both observed and calculated intensities with different resolution cut-offs. In problematic cases the statistics of calculated intensities were examined for different models, original and refined with strong restraints, with and without solvent atoms. The NCS operations if present were compared with potential twin operations to identify RPS. If pseudosymmetry was present, an attempt was made to transform and refine the structure in the corresponding higher symmetry space group using subroutines form *Zanuda* (§4.3) and *REFMAC*, in order to validate the reported space group.

Twinning has been identified with a high degree of confidence in 110 cases shown by red and green circles in Fig. 3.3(*c*); red and green indicating the cases with and without RPS, respectively. The remaining cases analysed (blue circles) split into three groups, untwinned structures, untwinned structures with incorrect space group assignment and pathological cases, in which the model is incomplete or corrupted, or intensity statistics could not be unambiguously interpreted. The minimal value of $R^{\text{calc}}_{\text{twin}}$ for twinned structures was 0.2. At the same time, there were several cases with incorrect space groups, in which $R^{\text{calc}}_{\text{twin}}$ was more than 0.2, up to 0.4. These models were strongly overfitted towards twinned data and there were significant differences between independently refined molecules which were symmetry-related in the actual crystal structure.

In general, only one third of the cases identified as twins were reported as such in the PDB submission (32 out of 110), although in some of the remaining twinned cases the analysis of intensities derived from atomic models shows that the twinning was actually taken into account during refinement. Nevertheless, in a significant number of cases this was not done (false negatives). In two certainly untwinned cases twinning was reported in the PDB file and, accordingly, the structures were refined in lower symmetry space groups (false positives).

Table 3.1 contains symmetry and NCS information for the identified cases of twinning and demonstrates that twins by pseudomerohedry are not unusual and that RPS is present in half of all twins. The nature of additional lattice symmetry in macromolecular twins by pseudomerohedry is analysed for two examples in §3.3 and §3.4. The second example also demonstrates that RPS is necessarily present in OD-twins by pseudomerohedry.

Four orthorhombic twins by pseudomerohedry with a specialised tetragonal lattice have been identified (Table 3.1). In these cases, the lattice symmetry also allows twin by merohedry with tetragonal crystal symmetry. These examples therefore highlight the importance of an exhaustive analysis of possible twin laws and show that the attempts at structure solution should not be limited by consideration of twinning by merohedry despite its higher probability, if both types of twins are allowed by the lattice symmetry.

The blue point in the RvR plot with $R_{\text{twin}}^{\text{calc}} = 0.18$ and $R_{\text{twin}}^{\text{obs}} = 0.28$ corresponds to detwinned data of an OD-twin be reticular pseudomerohedry (PDB code 1lbs) discussed in §1.3.4.

3.2.6 Effect of refinement on $R_{\text{twin}}^{\text{calc}}$

The cases with RPS (red points in Fig. 3.3*c*) were defined from the analyses of the atomic models. The similarity between NCS related molecules and the alignment of NCS and twin axes (a discrepancy of up to 6^o was tolerated) could be insufficiently precise to cause any significant correlation between twin related structure factors. It is therefore unsurprising that $R_{\text{twin}}^{\text{calc}}$ for some of the cases with RPS is large, up to 0.5.

On the contrary, the assignment of cases without RPS was strict (green points in Fig. 3.3*c*); there was only one molecule per asymmetric unit in many of these, and the relation between symmetry independent molecules was clearly irrelevant to twin rotation in others. The low values of $R_{\text{twin}}^{\text{calc}}$ for some of these cases can only be explained by either pathologies in the experimental data, or, more likely, by overfitting of the model toward twinned data.

The decrease in $R_{\text{twin}}^{\text{calc}}$ owing to untwinned refinement against twinned data was examined using a simulated experiment. The 3.1 Å data from an untwinned crystal (PDB entry 1nqh, space group $P3_121$) were artificially twinned to produce six data sets with twinning fractions of 0.0, 0.1, 0.2, 0.3, 0.4, 0.5. The model from the PDB was refined against all these data sets following the same protocol, without model rebuilding and ignoring twinning. The values of

	No. of twins			
Crystal symmetry or type of twinning	Total	RPS total	TNCS total	RPS + TNCS
$P1$	2	–	–	–
$P2_1$	26	25	4	4
$C2$	2	2	1	1
$P2_12_12$	1	1	–	–
$P2_12_12_1$	2	2	1	1
$C222_1$	1	1	1	1
twins by pseudomerohedry, total	34	31	7	7
$P4_1$	4	1	2	1
$P4_2$	1	1	1	1
$P4_3$	6	4	1	1
$I4$	3	2	–	–
$I4_1$	1	–	–	–
$P3$	2	2	2	2
$P3_1$	10	4	2	2
$P3_2$	8	3	2	2
$H3$	18	–	–	–
$P321$	3	3	1	1
$P3_121$	3	–	–	–
$P3_212$	1	–	–	–
$P3_221$	1	–	–	–
$P6_1$	1	–	–	–
$P6_5$	6	3	1	1
$P6_4$	1	–	–	–
$P6_3$	6	1	1	1
$I2_13$	1	–	–	–
twins by merohedry, total	76	24	13	12
total	110	55	20	19

Table 3.1. Frequency of twinning in different symmetry environments.
TNCS stands for translational NCS.

$R_{\text{twin}}^{\text{obs}}$ and $R_{\text{twin}}^{\text{calc}}$ were calculated for the simulated data sets and corresponding "refined" models. The result is shown as the central blue curve in Fig. 3.3(*d*).

If twinning had been properly taken into account during refinement then $R_{\text{twin}}^{\text{calc}}$ would remain constant throughout all these refinements (vertical green line on the right in Fig. 3.3*d*). With this reference curve the decrease in $R_{\text{twin}}^{\text{calc}}$ owing to incorrect refinement is clearly seen. To analyse this trend further "refinements" were carried out with more relaxed restraints on temperature factors. The results are plotted in red in Fig. 3.3(*d*) and show further reduction of $R_{\text{twin}}^{\text{calc}}$. The plots in Fig. 3.3(*d*) show that there is a significant bias of $R_{\text{twin}}^{\text{calc}}$ owing to untwinned refinement but this is still too small to explain green points with $R_{\text{twin}}^{\text{calc}} < 0.3$.

The "incorrect refinements" have been carried out starting from the correct model. Since real-life crystal structure solution requires many cycles of refinement alternated with model building, it is anticipated that in some cases the drift of the points to the left of the plot might be more serious than in the simulation. To check this, the PDB entry 1qth represented by the green point at (0.260, 0.155) in Fig. 3.3(*c*) was inspected in more detail. This was a crystal structure of T4 lysozyme belonging to the space group $P3_1$ with $a = 53.6$ and $b = 101.9$ Å and with one dimer per asymmetric unit. The axis of the dimer deviated from the closest twin axis by 65^o. Firstly, the PDB model, which is further referred to as Model 1, was refined using untwinned restrained refinement with reasonably strong restraints (using *REFMAC* option "weight matrix 0.03") to generate Model 2. As a result the $R_{\text{twin}}^{\text{calc}}$ increased from 0.260 in Model 1 to 0.393 in Model 2. Nevertheless, the new value of $R_{\text{twin}}^{\text{calc}}$ was significantly less than the expected value of 0.5, indicating that the atomic parameters in Model 2 remained biased toward those in the corrupted Model 1. To exclude the bias Model 2 was corrected as follows. The subunit A of the dimer was fitted to B and *vice versa*, the model with exchanged subunits was refined, corrected manually using *Coot* and refined again, untwinned restrained refinement being used in both instances. The resultant Model 3 had $R_{\text{twin}}^{\text{calc}}$ of 0.442, which was in agreement with the results of the simulated experiment in Fig. 3.3(*d*). Finally, Model 3 was subjected to twinned restrained refinement with the new version of *REFMAC* to generate Model 4 with a reasonable value of 0.475 for $R_{\text{twin}}^{\text{calc}}$. Fig. 3.4(*a*) shows Models 1, 2, 3 and 4 as points in the RvR plot.

Further comparison of the four models is presented in Figs. 3.4(*b*) and 3.4(*c*) and in Table 3.2. An increase in $R_{\text{twin}}^{\text{calc}}$ can equivalently be expressed as a decrease in the CC between twin related intensities. In tern, SRF peaks represent rotations associated with high correlation of intensities, so such rotations can be seen from the SRF plots (Fig. 3.4*c*). The 180^o section of the SRF for Model 4 showed only the peaks corresponding to three NCS axes, which were equivalent in the space group $P3_1$. The same section of the experimental SRF revealed additional peaks from three equivalent twin axes and from interactions between twinning and NCS. All these additional peaks were not relevant to the structure of an individual crystal and could not be present in the SRF calculated from a correct model but all of them were present in the SRF from corrupted Model 1. Such a feature of Model 1 was associated with a quite large r.m.s.d. of C$^{\alpha}$ atoms from their positions in the reference Model 4, small correlation of *B*-factors in Models 1 and 4 and a huge *R*-factor of 30% between structure amplitudes calculated from the two models

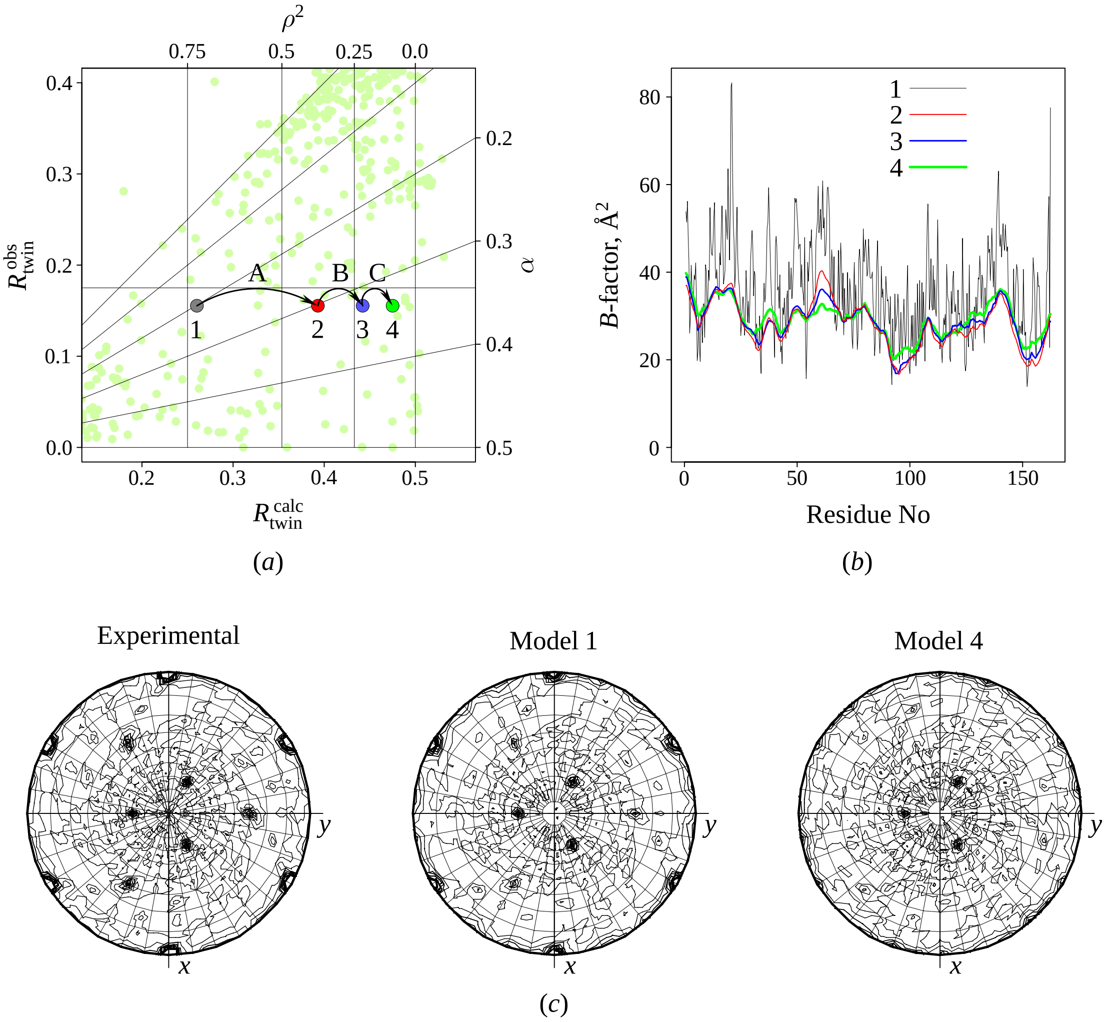

(*a*)

(*b*)

(*c*)

Figure 3.4. Overfitting of models to twinned data.

(*a*) Relation between Models 1, 2, 3 and 4 is shown: Model 1 was from the PDB (1qth), untwinned refinement of this model (the arrow labelled A) resulted in Model 2, further untwinned refinement alternated with rebuilding (the arrow labelled B) resulted in Model 3, which converged to Model 4 after twinned refinement (the arrow labelled C). Green points in the background are from Fig. 3.3(*c*).

(*b*) *B*-factors of the main chain atoms N, CA and C of chain A in the four models; the lines in (*b*) and corresponding points in (*a*) are shown in the same.

(*c*) the 180^o section of the SRF from experimental data (left) and from structure factors calculated using Models 1 (centre) and 4 (right) with strong peaks corresponding to three equivalent twin axes ($\psi = 90^o$), three equivalent NCS axes ($\psi \approx 30^o$) and interactions between NCS and twin axes ($\psi \approx 60^o$).

(Table 3.2). Model 1 also revealed impossible in a correct model fluctuations of *B*-factors along the main chain (Fig. 3.4*b*). Comparison of Model 2 with the reference Model 4 showed better behaviour of the above indicators, and Model 3 seemed to be very reasonable in that sense. It was therefore concluded that the main role of twinned refinement is not a model improvement, but avoiding overfitting towards twinned data in the course of model building and refinement. In particular, twinned refinement of a correct model produces correct low values of reliability factors signalling that the model needs no further "improvement". All these may be especially important for novices at crystallography and for automated model building.

3.2.7 Concluding remarks

The detection of twinning should ideally be performed at the stage of data acquisition before the crystal structure is known. This task is not always trivial; for example, perfect twinning ($\alpha = 0.5$) cannot be detected from merging statistics. In some instances, even the twinning tests (distributions of Z and H) are too ambiguous for assignment of crystal symmetry and detection of twinning prior to the structure determination; this can be for several reasons including pseudosymmetry, radiation damage or rejection of week intensities.

The analysis of the RvR scatter plot with the PDB-data demonstrated the importance of pre-deposition symmetry validation. Both false-positives and false-negatives in detection of twinning were found in the PDB. Twinning was frequently overlooked in the examples with low twinning fraction and in the cases with RPS. There were also cases with incorrect space group assignment, in which the higher point group symmetry of the data had been modelled as

Model No	1	2	3	4
Refinement:				
Twinned	n/a[†]	no	no	yes
R	0.189[†]	0.255	0.250	0.187
R_{free}	n/a[†]	0.309	0.289	0.218
Comparison with Model 4:				
R-factor between calculated amplitudes	0.298	0.243	0.133	
R.m.s.d. over C^{α} atoms	0.354	0.234	0.112	
Correlation coefficient for *B*-factors	0.539	0.913	0.954	

Table 3.2. Overfitting of models to twinned data.

Four models of the same crystal structure are compared.
Relations between the models are explained in Fig. 3.4.

[†] Values from the PDB entry 1qth

twinning. However, these false-positives constituted only a minor fraction of the whole set of structures modelled and deposited in a lower symmetry space group.

The program *Zanuda* was therefore developed for validation and, if necessary, automatic correction of the space group assignment for pre-refined models. This program is described in §4.3 in the discussion on false origin MR solutions, yet another reason for incorrect identification of symmetry in the presence of NCS.

In addition, the identified twinned data were used as test cases for the new version of *REFMAC*, which performs twinned refinement against a marginal likelihood target.

3.3 Example of twin by metric merohedry

Proteins from the phage SPP1 involved in DNA translocation are studied in the group of Dr. Fred Antson (YSBL). Two crystal forms of the C-terminal domain of the large terminase protein (gp2) were obtained by Dr. Maria Chechik, anomalous diffraction data (Se-Met) were collected by Mikhail Shevtsov and the structure of a non-twinned form determined by Oleg Kovalevskiy. I solved and analysed the structure of the twinned crystal form.

This is an example of a crystal in which several NCS operations are present but none of them has its axis aligned with the twin axis. Therefore the theoretical intensity distribution (§1.2.3) holds despite the high-order NCS. Accordingly, the point in the RvR plot (§3.2) corresponding to this structure is located in the area of "simple" twins (Fig. 3.5). A remarkable feature of this example is that the analysis of NCS clearly reveals the structural nature of constraints on cell dimensions required for twinning.

3.3.1 Background

The diffraction data from a twinned crystal of the gp2 C-terminal domain were initially processed in $C222_1$ space group. Perfect twinning tests clearly revealed twinning by hemihedry (Fig. 3.6). With these data, the space group can be unambiguously determined. There are four subgroups, $P1$, $P2_1$ and two non-equivalent $C2$ in the apparent $C222_1$ space group. Only one of them, $P2_1$ accounts for observed systematic absences. The data were therefore reprocessed in $P2_1$ with $a = 69.4$ Å, $b = 159.4$ Å, $c = 107.7$ Å and $\beta = 108.8^o$. The partial twinning test in $P2_1$ (H-test for the twin operation $h, -k, -h-l$) is shown in Fig. 3.7. Similar behaviour was

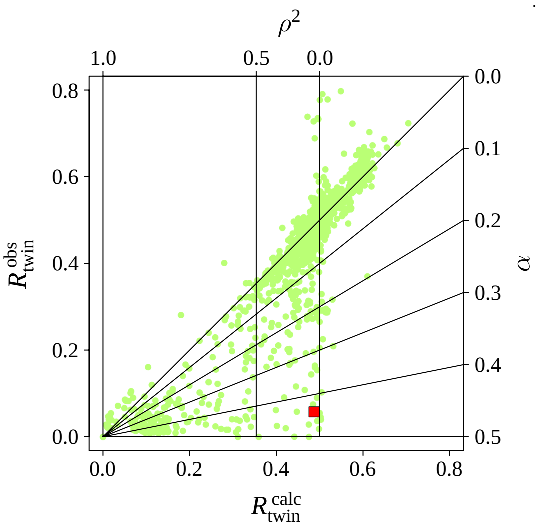

Figure 3.5. Twinned crystal of C-terminal domain of gp2 protein from phage SPP1. The red point in the RvR plot (§3.2) corresponds to the $P2_1$ crystal structure and X-ray data collected from twinned crystal. Green points in the background present scatter plot derived from the PDB (Fig. 3.3b).

observed in both $C2$ subgroups. Such behaviour means that the crystal is an almost perfect twin and that the partial twinning tests provide no additional evidence for space group assignment.

The SRF calculated using the twinned data revealed peaks for twofold (Fig. 3.8*a*), fourfold, fivefold and tenfold rotations. The SRF-peak at (0^o, 0^o, 180^o) is a crystallographic peak and the peaks at (90^o, 0^o, 180^o) and (90^o, 90^o, 180^o) are due to two equivalent twin operations (the angular coordinates of the SRF peaks are given relative to the view in Fig. 3.8*a*). Two interpretations of the remaining peaks seemed likely. In the first interpretation, the asymmetric unit contains a decamer and the tenfold axis of the decamer makes angles of about 45^o with **a** and **c** and 90^o with **b**. In this case, the SRF-peak at (90^o, $\pm 45^o$, 180^o) corresponds to the twofold axis of the decamer and the peaks at ($18n^o$, $\mp 45^o$, 180^o) are generated by the tenfold axis of the decamer and the crystallographic two-fold axis, peaks with "$+$" and "$-$" coming from two different individual crystals. In the second interpretation, the asymmetric unit comprises two pentamers related by NCS fourfold rotation about **b**. Then, the peaks at ($36n^o$, $\pm 45^o$, 180^o) are generated by fivefold symmetry of the pentamer and crystallographic symmetry, whereas peaks at ($18+36n^o$, $\pm 45^o$, 180^o) can be considered as generated by fivefold symmetry of the pentamer and rotations (90^o, $\pm 45^o$, 180^o), which, in turn, are generated by NCS fourfold axis and twin operations. The first set of peaks would be present in the SRF of the single crystal, whereas the second set is owing to twinning. In both interpretations the asymmetric unit contains ten molecules, in agreement with sizes of molecules and the unit cell.

With this data, it was reasonable to expect that the C-terminal domain of gp2 forms oligomers with point group symmetry 5 or 10. This is of considerable biological interest. If such an oligomeric state had been confirmed, it would be reasonable to extrapolate it on the whole gp2 molecule, whose second (N-terminal) domain has the ATPase activity and is involved in processive packaging of DNA into the viral capsid. In turn, the symmetry of the biomolecule with the ATPase function is important for understanding the mechanism of the DNA packaging. This symmetry is currently debated. For example, the fivefold symmetry of the ATPase in the phage ϕ29 was concluded from the EM-reconstruction of the phage particle by Simpson *et al.* (2000) and was a key feature in the mechanism of the DNA packaging that they proposed. The fivefold symmetry of the ATPase from a different phage would be strong evidence for this mechanism and for its variation discussed in §2.6.

Interestingly the small terminase subunit (gp1), another protein from SPP1 interacting with the DNA and the portal protein (gp16), also shows a fivefold axis in the SRF (Fig. 3.8*b*). The three proteins are likely to form a complex at the stage of DNA packaging initiation. Two observations of fivefold symmetry in the related proteins were suggestive of its biological significance. This was one reason why the twinned crystal form of gp2 was still of interest even though a different crystal form of gp2 had already been solved.

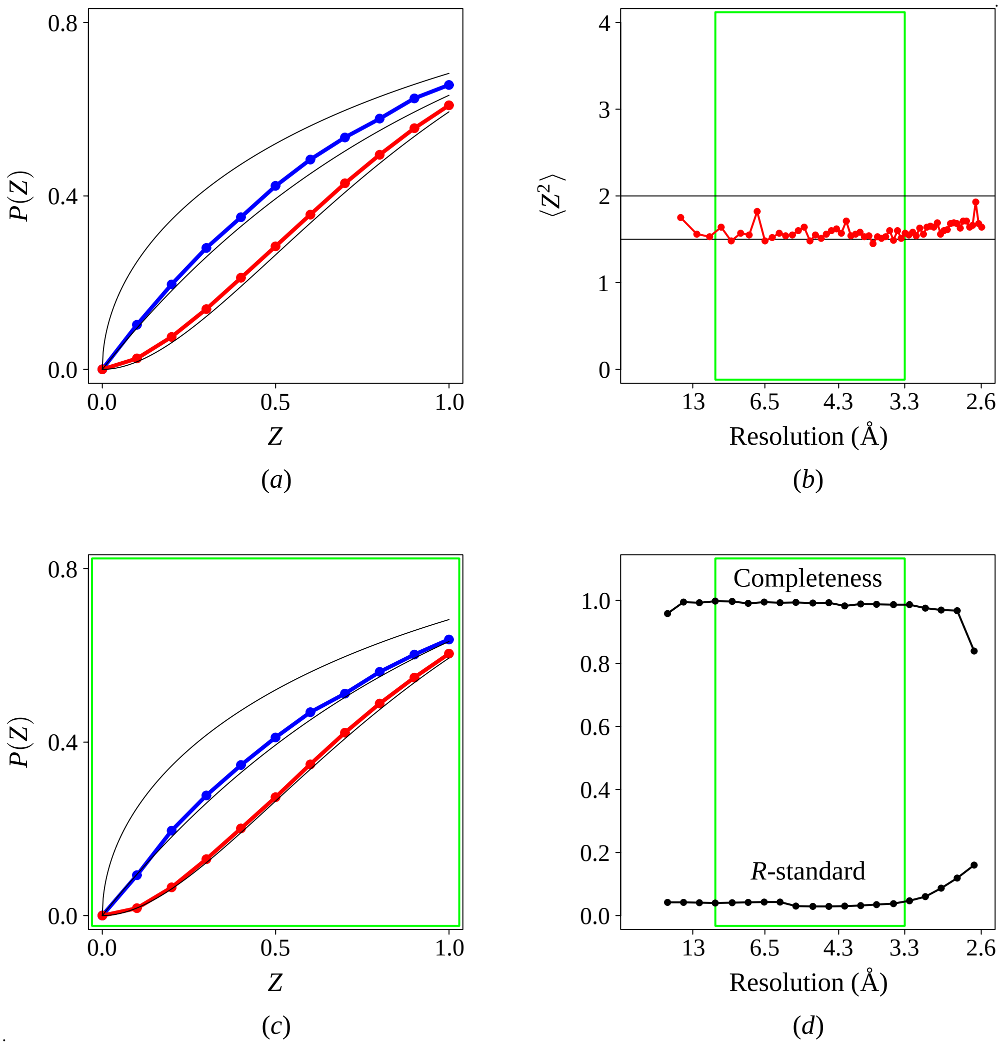

Figure 3.6. Perfect twinning test for twinned monoclinic crystal of C-terminal domain of gp2 protein from phage SPP1.

The colour legend for (*a*), (*b*) and (*c*) is the same as for similar plots in Fig. 1.1.
The resolution range used in (*c*) is outlined by green boxes in (*b*) and (*d*).

(*a*) Cumulative distributions of *Z* for all the data, resolution range 24.6–2.60 Å.
(*b*) Second moment of *Z* for acentric reflections against resolution.
(*c*) Cumulative distributions of *Z* in the resolution range 9.90–3.30 Å.
(*d*) Completeness and *R*-standard against resolution.

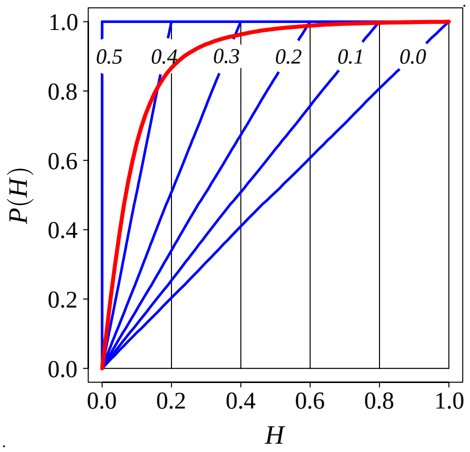

Figure 3.7. Partial twinning test for twinned monoclinic crystal of C-terminal domain of gp2 protein from phage SPP1. Experimental distribution of H is presented by red dotted line. The intensities derived from the atomic model were used to simulate the cumulative distribution of H (blue lines) for different twinning fractions (the numbers in front of the blue lines).

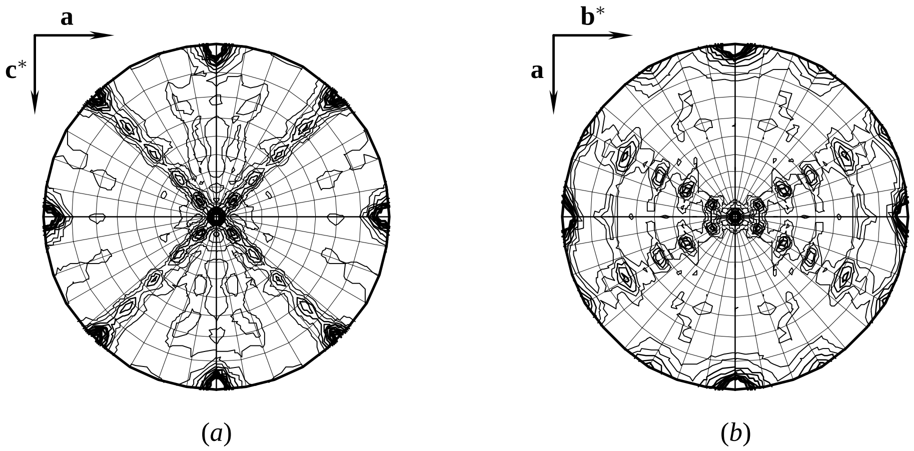

Figure 3.8. The SRF sections $\chi = 180^o$ for crystals of two proteins from SPP1 phage showing 10-2-2 symmetry. (*a*) Twinned $P2_1$ crystal of gp2 C-terminal domain and (*b*) single $P2_12_12_1$ crystal of gp1 C-terminal domain. Orientation in (*a*) is the same as in Figs. 3.9*a*, 3.9*c*, and 3.9*d*. This figure was generated using *MOLREP*.

3.3.2 Structure solution

Several data sets were collected for the twinned crystal form, including KBr derivative data sets. The crystals were diffracting to 2.6 Å at best. All of the crystals were twins and attempts to solve the structure with experimental phasing failed.

The Se-Met mutant of the gp2 C-terminal domain was thereafter obtained and crystallised. These crystals belonged to space group $P3_221$ with $a = 69.9$ Å, $c = 72.7$ Å, had one molecule in the asymmetric unit and diffracted to 1.9 Å. These crystals were not twinned. X-ray diffraction data were collected at ESRF at three wavelengths, 0.94213 Å (remote), 0.97873 Å (peak), 0.97891 Å (inflection). An initial set of phases was obtained using *SHELXD* and *SHELXE* and a partial model was built using *SOLVE*. The complete model was built manually using *Coot* and refined using *REFMAC* and the data from the remote wavelength.

The twinned crystal form was solved by MR. Eight of ten molecules constituting the asymmetric unit were found using the default mode of *MOLREP*. The remaining two molecules were placed using *LSQKAB* by interpolating NCS symmetry. The MR was repeated in $P1$ to validate the assumption of $P2_1$ symmetry. The model was refined using *REFMAC*, the first chain was corrected manually using *Coot* and changes were propagated to NCS-related molecules. The next round of refinement, *REFMAC* with TLS parameters gave $R = 31.5\%$, $R_{\text{free}} = 33.9\%$ and further twinned refinement with CNS resulted in $R = 21.6\%$, $R_{\text{free}} = 23.3\%$.

3.3.3 NCS and orthorhombic cell

The organisation of the crystal is shown in (Fig. 3.9). The expectation of an oligomer with point group symmetry 5 was not fulfilled. On the contrary, the molecules form filaments with 5_3 screw symmetry, in which neighbouring molecules are approximately related by a rotation of 144^o about the axis of the filament and by translation along it. The molecules are polar and neighbouring molecules make contacts by oppositely charged faces.

Parallel filaments form layers with much weaker contacts. The layers are stacked across each other in the **b**-direction to generate NCS fourfold symmetry and crystallographic symmetry $P2_1$ with four layers spanning the length of **b** (Fig. 3.9*a* and 3.9*b*). That is, the neighbouring layers shown in Figs. 3.9(*c*) and 3.9(*d*) are approximately related by a NCS screw fourfold rotation and every first and third layers are related by the crystallographic two-fold screw rotation.

The most significant conformational differences between the two crystal forms occur in the interfaces forming filaments. The (electrostatic) intermolecular interactions within the filaments appear to be the strongest in the crystals, and a filament appears to be the most stable substructure. Thus, external interactions have little effect on the internal structure of filaments. In particular, this means that base vectors of crystallographic translations along filaments, $\mathbf{e}_1$ and $\mathbf{e}_2$

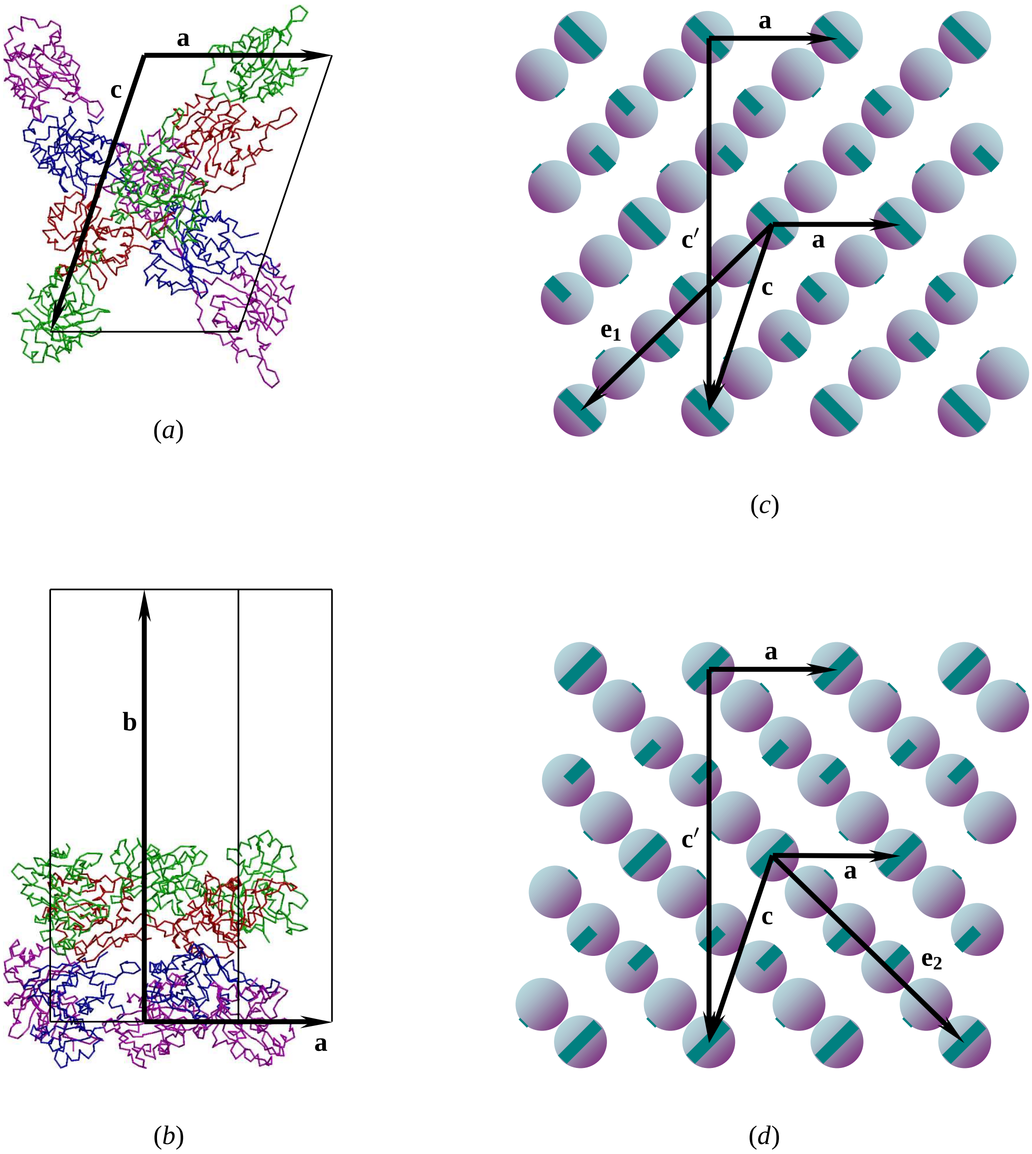

(*a*)

(*c*)

(*b*)

(*d*)

Figure 3.9. Organisation of the crystal of the C-terminal domain of gp2 protein from phage SPP1. (*a*, *b*) C$^{\alpha}$ representation of ten molecules constituting the asymmetric unit of the crystal. Different molecules are shown by different colours. The “legs” of the “X”-shaped asymmetric unit are extended by crystallographic translations into infinite filaments and repeated to form layers in (010)-plane. (*c*, *d*) Schematic views of (010) layers, in which individual molecules are shown by spheres coloured according to the dominating surface charge. The green bands on the surfaces of the spheres span 144^{o} and show the approximate 5_3-symmetry of the filaments. The black arrows show the basis translations of the primitive lattice, **a** and **c**, the basis translations of the *B*-centred lattice, **a** and $\mathbf{c}'$, and the basis crystallographic translations along filaments, $\mathbf{e}_1$ and $\mathbf{e}_2$.

in Figs. 3.9(*d*) and 3.9(*e*) have equal length,

$$|\mathbf{e}_1| = |\mathbf{e}_2|. \tag{82}$$

It is reasonable to assume that the contacts of given filament with its neighbours are mainly accommodated by shifts perpendicular to the filament axis. It is therefore clear that equation (82) holds with much higher accuracy than the accuracy of 5_3 filament symmetry. Relations between $\mathbf{e}_2$ and $\mathbf{e}_1$ and crystallographic base vectors **a** and **c** are shown in (Fig. 3.9*b*). These are substituted in (82) to get

$$|\mathbf{c} + 2\mathbf{a}|^2 = |\mathbf{c} - \mathbf{a}|^2 \tag{83}$$

and

$$2(\mathbf{c}, \mathbf{a}) + |\mathbf{a}|^2 = 0. \tag{84}$$

This extra constraint on the unit-cell parameters is conveniently written in terms of the basis vectors

$$\mathbf{c}' = 2\mathbf{c} + \mathbf{a} \tag{85}$$

and **a** of a centred lattice (Figs. 3.9*d* and 3.9*e*). These vectors are orthogonal because of (84) and (85),

$$(\mathbf{c}', \mathbf{a}) = 0. \tag{86}$$

Thus our structure belongs to a monoclinic space group but possesses a *B*-centred pseudoorthorhombic lattice, in which the diffraction data were initially processed ($C222_1$, different setting). The question remains, whether the equation (86) should be treated as an exact equation. Note that in the general case of monoclinic twins by hemihedry, the constraint $\beta = 90^o$ (in either primitive or centred cell) is not strict. The deviation of β from 90^o translates into non-zero obliquity angle and partial overlap of diffraction spots.

3.3.4 Twin axis and composition plane

Mallard's law for rotation twins states that the twin axis exactly coincides with the direction of a certain lattice row with small indices (§1.2.1). The twin axis is a purely geometrical notion and the Mallard's law is an empirical law.

The structural reason for Mallard's law can be the presence of an interface between individual crystals (composition plane) that has an exact two-dimensional translational symmetry, such that the associated two-dimensional lattice (or its sublattice) is exactly invariant with respect to the twin operation. In such an interface, optimal interactions between two individual crystals are repeated in all two-dimensional unit cells to increase dramatically the energy gain on its formation compared to a "random" interface.

Two cases are possible in monoclinic twins (Fig. 3.10), the crystallographic twofold axes can be either parallel to the composition plane (Figs. 3.10*a* and 3.10*b*) or orthogonal to it (Figs. 3.10*c* and 3.10*d*).

No extra constraints on β are implied in the first case. In general, this is a twinning by reticular merohedry, in which the twin index and obliquity angle depend on β and a partial overlap of a fraction of all spots takes place (§1.2.1). A particular case with $\beta \approx 90^o$ (Fig. 3.10*a*) or $\beta' \approx 90^o$ (the angle between **a** and **c**$'$, Fig. 3.10*b*) is classified as twinning by pseudomerohedry (non-zero obliquity angle). In such a twin, the twin-related reflections from different individual crystals are separated for sufficiently large indices *h* or *l*.

In the second case, the presence of translational symmetry in the twin interface and the invariance of associated two-dimensional lattice relative to the twin two-fold rotation implies that $\beta = 90^o$ (Fig. 3.10*c*) or $\beta' = 90^o$ (Fig. 3.10*d*). This is a particular case of twinning by pseudomerohedry, in which the obliquity angle is exactly zero, and which is also known as twinning by metric merohedry. Nespolo & Ferraris (2004) refer to several monoclinic cases of small-molecule twins, in which $\beta = 90^o$ within the measurement errors. Without structural analysis indicating the orientation of the composition plane, it might seem surprising that such a situation had occurred.

In this geometrical analysis, the constraints on the two-dimensional lattice at the twin interface were extrapolated onto the three-dimensional crystal lattice. That is, an approximation was used, in which all unit cell repeats of the crystal were exactly identical. This approximation is in fact assumed in both data processing and refinement. If these constraints are largely disobeyed in the three-dimensional lattice, then large strains are required at the twin interface, especially at its peripheral part, to restore the translational and rotational symmetries of its two-dimensional lattice. Such a situation can occur in twins formed by small dendrite crystals, but not in macroscopic twins.

An individual crystal of our twin is analysed in Fig. 3.9. The twin interface is unlikely to cut the filaments, in which the strongest intermolecular interactions occur. This means that the vectors along the filament axes, $\mathbf{e}_1$ and $\mathbf{e}_2$ (Figs. 3.9*c* and 3.9*d*) are both parallel to the twin interface. The twin interface is therefore parallel to the plane (010). Hence the second of the above cases takes place, the twinning by metric merohedry explained in Fig. 3.10*d*.

Thus, given the (010) orientation of the twin interface, the presence of twinning in our example means that the constraints (86) should be treated as exact (as long as the model of the crystal with identical unit cell repeats is assumed). The precision of (86) is demonstrated by the low penalty for indexing in $C222_1$ and by the absence of split or partially overlapping spots in the diffraction images.

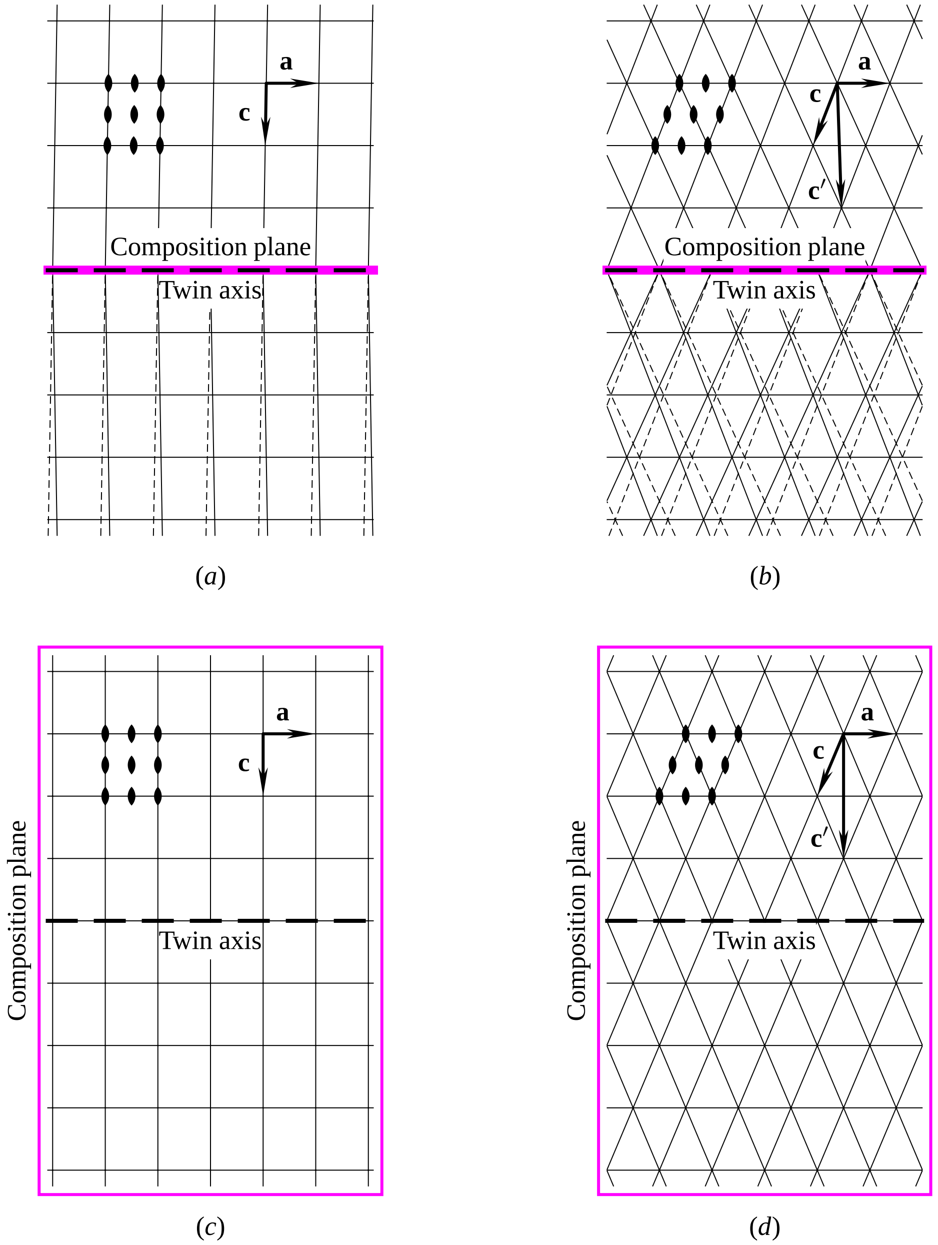

(*a*) (*b*)

(*c*) (*d*)

Figure 3.10. Possible orientations of composition plane in monoclinic twins.

The crystallographic twofold axes are perpendicular to the plane of figure and shown by black ovals. The composition planes and twin axes are shown by magenta and thick dashed black lines, respectively. Individual crystals of the twin are (*a*,*b*) above and below, and (*c*,*d*) in front of and behind the composition plane. Thin solid black lines show lattices. Thin dashed black lines in (*a*,*b*) show an extension of the first individual lattice.

(*a*,*b*) Twinning by (reticular) pseudomerohedry, in which the crystallographic axes are parallel to the composition plane. There are no constraints on β.

(*c*,*d*) Twinning by metric merohedry, in which the crystallographic axes are orthogonal to the composition plane and therefore (*c*) $\beta = 90^o$ or (*d*) $\beta' = 90^o$ (β' is the angle between **a** and **c**′).

3.3.5 Concluding remarks

Macromolecular structures allow convenient visual analysis of the intermolecular interactions involved in formation of twinned crystals. In particular, the twinned crystal of C-terminal domain of gp2 protein from phage SPP1 is composed of one-dimensional arrays of molecules, in which the strongest intermolecular interactions occur and which span the whole crystal. The presence of such filaments explains both (i) the presence of molecular layers, which make relatively weak contacts with each other and which can therefore form boundaries of individual crystals and (ii) the constraint (86) that makes the translational symmetry of two individual crystals consistent at such boundary. The next section represents the more common case, in which the symmetry of a two-dimensional array of molecules is the reason for the “accidental” symmetry of the lattice.

3.4 Example of OD-twin by metric merohedry

Ferrochelatase-1 (HemH) from *Bacillus anthracis* was one of the targets of SPINE (Au *et al.*, 2006). A diffracting crystal was obtained and the crystal structure was solved by Dr. Elena Blagova, Dr. Olga Moroz, Dr. Vladimir Levdikov and Dr. Axel Müller (PDB code 2c8j). I took part in the structure refinement. The crystal was twinned but the time constraints imposed by the genomics project did not allow a scan for another crystal form.

The crystal of HemH was an OD-twin belonging to an OD-family of type I/B (§1.3). This example is presented to demonstrate a typical morphology and the effect of NCS on the intensity statistics for this type of twin.

The internal symmetry of the OD-layers is shown to impose additional constraints on the lattice parameters. In terms of geometrical classification, the twin under consideration is therefore a twin by metric merohedry (*i.e.* by pseudomerohedry with zero obliquity angle, §1.2.1).

The NCS and twin axes are necessarily aligned and structure factors related by the twin operation correlate in this type of twins. The theoretical model of an ideal OD-twin is analysed, in which the symmetry of the OD-layers is exact and correlation between structure factors is modulated. The experimental distributions of Z and H and these distributions for simulated data sets are compared with the theoretical distributions for a constant correlation model (§3.1) and for a modulated correlation model.

3.4.1 Structure solution

Ferrochelatase-1 (HemH) from *Bacillus anthracis* was crystallised using Mosquito robot and mother liquor containing 0.2M $MgCl_2$, 0.1M Tris-Cl pH 8.5, 30% PEG 30K to yield diffracting crystals with unit-cell parameters $a = 49.9$, $b = 109.9$, $c = 59.4$ Å and $\alpha = \beta = \gamma = 90^o$. The diffraction data were collected at SRS Daresbury PX9.6 beamline to 2.1 Å resolution and initially processed in the point group 222 using *MOSFLM* (Leslie, 1992; Leslie, 2006) and *SCALA* (Evans, 1997; Evans, 2006).

The MR was carried out using Ferrochelatase from *Bacillus subtilis* as a search model (PDB code 1ak1), a homologue with a sequence identity of 73%. The MR trials and preliminary refinements were later repeated in a consistent manner to generate Table 3.3 showing the three best solutions in both orthorhombic and monoclinic systems. In this Table the space group settings are such that the unit cell parameters are the same in all six presented space groups but the directions of the (unique) crystallographic axes vary.

Initially, eight "biological" orthorhombic space groups were tested. The best CC was obtained in space group $P2_12_12$ and the second best in $P2_12_12_1$. In addition, unlike the other six orthorhombic groups tested, these two showed substantial contrast in terms of the CC between the best and the second best orientations (Table 3.3). Analysis of intensities along coordinate axes (Fig. 3.11) clearly excluded $P2_12_12_1$, but the highest CC space group $P2_12_12$ could neither be confirmed or excluded with certainty. Therefore it was only the preliminary refinement that caused doubts in the original point group assignment. Although R_{free} was decreasing during the first cycles in both $P2_12_12_1$ and $P2_12_12$, the final values of R and R_{free} were too high given the highly similar search model (Table 3.3). It was also suspicious that refinement in the incorrect $P2_12_12_1$ performed better and, with weaker restraints, resulted in $R = 0.197$ but $R_{\text{free}} = 0.394$. At this point twinning tests had been performed with the high resolution cut-off of 3 Å to reveal features characteristic for perfect twinning interfering with NCS: the cumulative intensity

Space group	$P2_12_12$	$P2_12_12_1$	$P22_12_1$	$P12_11$ (true)	$P2_111$	$P112_1$
Highest CC in the TF for						
correct orientation	0.510	0.493	0.466	0.566	0.530	0.505
incorrect orientations	0.376	0.384	0.435	0.422	0.445	0.473
Refinement						
R	0.403	0.397	0.452	0.312	0.369	0.420
R_{free}	0.465	0.451	0.496	0.364	0.411	0.497

Table 3.3. Structure solution of HemH from *Bacillus anthracis*.

The MR trials in alternative space groups are presented by the highest correlation coefficients (CC) for correct and incorrect orientations. The data for the monoclinic space groups are for the second molecule found. Three monoclinic and three orthorhombic space groups with highest CC are shown. Preliminary refinements of corresponding models are presented by R-factors.

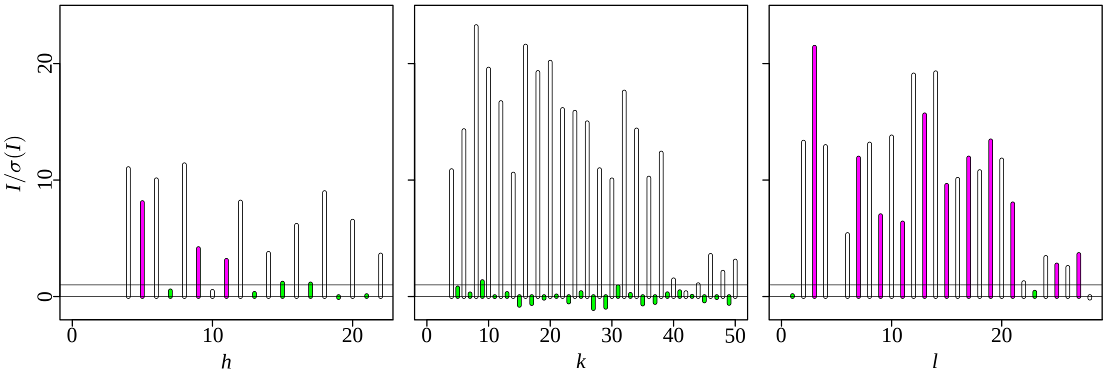

Figure 3.11. Analysis of screw axes in the crystal structure of HemH.

Three histogram-like plots show the ratios $I/\sigma(I)$ for reflections $h00$ (left), $0k0$ (middle) and $00l$ (right). Reflections with odd h, k or l are shown in green if $I/\sigma(I) < 2$ and in magenta otherwise. Horizontal thin black lines are drawn at $I = 0$ and $I = \sigma(I)$.

distribution curve was lower than the reference curve for untwinned data, but higher than the reference for the perfect twin without an additional effect of NCS (Fig. 3.14*d*, p.139).

Therefore the data were reprocessed using *MOSFLM* and *SCALA* in three possible monoclinic point groups (with two-fold axes along different coordinated axes) and the MR trials were performed in six possible space groups of types $P2$ or $P2_1$. The results of the MR and preliminary refinements for three best space groups are shown in Table 3.3. In contrast to the MR attempts in the orthorhombic space groups, the monoclinic MR model with the highest CC refined to reasonable *R*-factors substantially lower than those for other monoclinic space groups. This model was rebuilt, refined to $R = 0.234$ and $R_{\text{free}} = 0.281$ and deposited (PDB code 2c8j). Because of the initially unnoticed twinning the completeness of the data in the true $P12_11$ space group was only 82% (Fig. 3.13*b*, p.138). The assignment of $P12_11$ was further supported by the systematic absences for $k = 2n + 1$ (Fig. 3.11) and by the partial twinning test (Fig. 3.15*b*, p.141) showing a twinning fraction of only 0.2, whereas it would have been 0.5 if the assignment were wrong.

The final round of refinement included TLS parameters and was completed using *REFMAC* which had no twinned refinement implemented at the time of structure solution but anyway produced lower *R*-factors and better electron density than twinned refinement with *SHELXL*. This was apparently because the twinning fraction was only 0.2 but the molecules in the crystal had significant TLS mobility that needed to be accounted for.

An exactly orthorhombic cell was one reason of the late detection of twinning and initially erroneous space group assignment. Another reason was that interfering NCS reduced the contrast of the perfect twinning test, and the use of all data including very noisy 2.5 to 2.1 resolution range caused further decrease of contrast and made the test misleading. Therefore this example underlines the importance of at least an awareness of the above phenomena while a better solution would be a twinning test taking into account both experimental errors and interfering NCS. Further confusion with the symmetry assignment was at the stage of the MR and was caused by pseudo-absences at $h = 2n + 1$ which were likely to be due to the $P2_1(1)1$ symmetry of the OD-layers (Figs. 3.12*a* and 3.12*c*). In the rest of this section the symmetry of the OD-structure of HemH is discussed in relation to the lattice symmetry and twinning tests.

3.4.2 Twin morphology

An individual crystal of the HemH twin belongs to the space group $P12_11$ with $a = 49.9$, $b = 109.9$, $c = 59.4$ Å and $\beta = 90^o$. It is composed of two-dimensional layers in the plane (010). Fig. 3.12(*a*) presents a top view of a single layer and Fig. 3.12(*b*) is a side view of three adjacent layers. The asymmetric unit contains two molecules related by a NCS two-fold screw rotation. If the two independent molecules are assigned to the same layer, the NCS axis

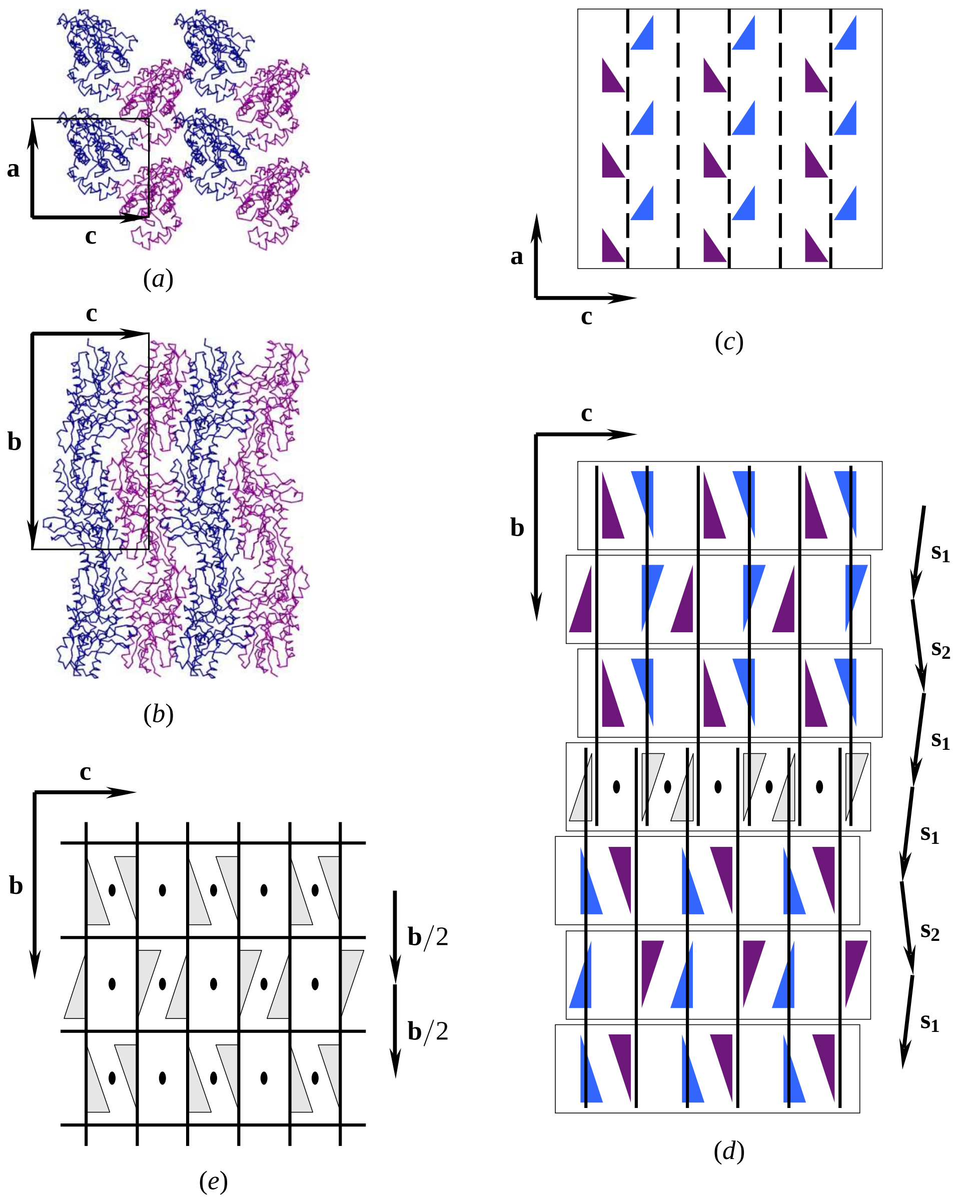

Figure 3.12. OD-twin of HemH.

(*a*, *b*) An individual $P12_11$-crystal of the twin: (*a*) a single OD-layer and (*b*) three adjacent OD-layers shown as C^{α} traces with symmetry related molecules in the same colour.

(*c*) Schematic view of a single OD-layer with $P2_1(1)1$ plane space group pseudosymmetry. The pseudosymmetry axes of the OD-layer are shown by dashed black lines.

(*d*) Schematic view of the OD-twin with two $P12_11$ individual crystals at the top and bottom and with the interface OD-layer in the middle. Crystallographic axes are shown by black lines, the pseudosymmetry axes of the interface OD-layer are shown by black ovals and the molecules related by these symmetry elements are shown in the same colour. The stacking vectors $\mathbf{s}_1$ and $\mathbf{s}_2$ relating the origins of the adjacent layers are shown by black arrows at the right margin.

(*e*) The symmetrised $P2_12_12_1$-structure that would occur if $\mathbf{s}_1$ and $\mathbf{s}_2$ in (*d*) were equal to $\mathbf{b}/2$.

relating them is an element of the approximate $P2_1(1)1$ plane space group symmetry of the layer (§1.3.2). The adjacent layers are related by the crystallographic two-fold screw rotation.

Accordingly, the crystal belongs to an OD family of type I/B (Fig. 1.5*h*) with the groupoid symmetry $P2_12_12 : P2_1(1)1$ (No 11 in Table 1.1). In contrast to the types I/A or II/A, the monoclinic member of this family with maximum degree of order does not have translational NCS, but instead is prone to twinning by pseudomerohedry (by metric merohedry, as will be shown below). Figs. 3.12(*c*) and 3.12(*d*) are schematic representations of a single OD-layer and of the OD-twin belonging to the OD-family under consideration. It is characteristic for OD-twins in general that the interface OD-layer can be attributed to any of the two connected individual crystals. The internal symmetry operations of this interface layer not only relate its own molecules, but also molecules from adjacent individual crystals (Fig. 3.12*d*). Thus the NCS and twin axes are necessarily aligned in such a twin.

There are two (imaginary) fully ordered structures composed of the same OD-layers as the OD-twin under consideration. These belong to the space groups $P2_12_12$ and $P2_12_12_1$. The second one (Fig. 3.12*e*) is closer to the actual structure and is used as a reference. The origins of individual layers in the reference structure are set to be related by $\mathbf{b}/2$. Accordingly, the stacking vectors $\mathbf{s}_1$ and $\mathbf{s}_2$ relating the origins of the adjacent layers in the actual OD-structure (Fig. 3.12*d*) are parameterised as follows,

$$\begin{array}{c} \mathbf{s}_1 = \mathbf{b}/2 + \varepsilon\,\mathbf{c} \\ \mathbf{s}_2 = \mathbf{b}/2 - \varepsilon\,\mathbf{c} \end{array} . \tag{87}$$

In this approximation, the components of the vector $\mathbf{s}_1$ along $\mathbf{b}$ and $\mathbf{c}$ in the basis $(\mathbf{a}, \mathbf{b}, \mathbf{c})$ are 1/2 and ε, respectively, and the small component along $\mathbf{a}$ is neglected. The regular sequences $(\ldots\ \mathbf{s}_1\ \mathbf{s}_2\ \mathbf{s}_1\ \mathbf{s}_2\ \ldots)$ occur inside the individual crystals, whereas the sequence $(\ldots\ \mathbf{s}_2\ \mathbf{s}_1\ \mathbf{s}_1\ \mathbf{s}_2\ \ldots)$ occurs at the interface, as shown in Fig. 3.12(*d*).

The symmetry $P2_1(1)1$ of the layer is not exact. The coefficient ε in (87) and the asymmetry of the OD-layer were estimated as follows. The asymmetric unit of the refined HemH structure was transformed by the two-fold screw rotation about an axis, which was parallel to $\mathbf{a}$ and displaced from the origin by $\mathbf{c}/4$. A rotated copy of the whole OD-layer would relate to its fixed copy by translation. To find this translation, the asymmetric unit was further transformed, molecules A and B were renamed to B and A, respectively, and B was translated by $-\mathbf{a}$. The transformed copy was then shifted to the position of the best match with the fixed copy. The projection of this shift on $\mathbf{c}$ was 5.14 Å, so

$$\varepsilon = \frac{\varepsilon c}{c} \approx \frac{5.14\ \text{Å}}{59.4\ \text{Å}} \approx 0.086. \tag{88}$$

The r.m.s.d. over C^α atoms between fixed copy and shifted copy in its final position was 0.24 Å. This value characterises the asymmetry of the OD-layer.

3.4.3 Lattice constraints

The symmetry of an OD-layer can be significantly perturbed and, in general, for an OD-layer with approximate symmetry $P2_1(1)1$, the angle between **a** and **c** is not necessarily exactly equal to 90^o.

However, as in the previous example (§3.3), the very ability of the crystal to form an OD-twin requires that **a** is orthogonal to **c** to the same accuracy to which the individual crystal has translational symmetry. Rotation about a symmetry axis of the interface OD-layer shows that the basis vectors **a** and **c** in the layer below the interface correspond to the basis vectors **a** and $-$**c** in the layer above the interface. The translation bases in the two layers have to be in exact agreement to form the twin interface, so the angles between **a**, **c** and **a**, $-$**c** are equal and thus 90^o.

Hence, the lattice of the individual monoclinic crystal in question possesses specialised orthorhombic symmetry, the twinned crystal has zero obliquity angle and can be classified as a twin by metric merohedry (§1.2.1). From the geometric point of view, the situation is exactly the same as in the previous example, *i.e.* the twin axis is parallel to the composition plane (Fig. 3.10*c*).

3.4.4 Idealised model of the OD-twin of HemH

In the idealised model of the OD-twin, the OD-layers have exact plane space group symmetry. The cumulative distribution of normalised intensities $P(Z)$ for a perfect twin and the cumulative distribution of relative differences between twin-related reflections $P(H)$ are derived below and compared with the corresponding distributions for a twin with constant correlation of structure factors, as discussed in §3.1.

The idealised model is built starting from the symmetrised structure in Fig. 3.12(*e*). Let structure factors p_1 and p_2 represent two parts of this structure containing odd- and even-numbered layers, respectively, so all the layers in a given partial structure have the same orientation. The vector notations are used similarly to (17),

$$\mathbf{p} = (p_1\ p_2)^T. \tag{89}$$

Let $\hat{o}_x$, $\hat{o}_y$ and $\hat{o}_z$ be symmetry operations of the space group $P2_12_12_1$ of the symmetrised structure. Both p_1 and p_2 are symmetric relative to $\hat{o}_x$, whereas $\hat{o}_y$ and $\hat{o}_z$ transform them one into another,

$$\begin{aligned} &\hat{o}_x\mathbf{p} = \mathbf{p} \\ &\hat{o}_y\mathbf{p} = \hat{o}_z\mathbf{p} = \begin{pmatrix} 0 & 1 \\ 1 & 0 \end{pmatrix} \mathbf{p} \end{aligned} \quad . \tag{90}$$

The individual crystals of the OD-twin f_1 and f_2 are assembled as follows. The substructures p_1 and p_2 are shifted by $+\varepsilon\mathbf{c}/2$ and $-\varepsilon\mathbf{c}/2$, respectively, and merged into f_1. In the individual crystal f_2 the shifts are applied with opposite signs.

Let ω be the phase angle corresponding to the shift $\varepsilon\mathbf{c}$,

$$\omega = 2\pi\varepsilon l \tag{91}$$

and t be the phase multiplier corresponding to the two times smaller shift,

$$t = e^{i\omega/2}. \tag{92}$$

Then, in vector notations (17) and (89), the relation between **f** and **p** is as follows,

$$\mathbf{f} = \begin{pmatrix} t & t^* \\ t^* & t \end{pmatrix} \mathbf{p}. \tag{93}$$

Examination of the symmetry of the vector **f** validates the above procedure. The shifts that had been applied to the substructures were along **c**. Therefore, the rotation $\hat{o}_z$ does not change the shift, $\hat{o}_z\, t = t\, \hat{o}_z$, whereas the rotations $\hat{o}_x$ and $\hat{o}_y$ change its direction, $\hat{o}_x\, t = t^*\, \hat{o}_x$ and $\hat{o}_y\, t = t^*\, \hat{o}_y$. Thus, because of (90), the actions of these rotations on (93) are written as

$$\begin{aligned} \hat{o}_x\mathbf{f} = \hat{o}_z\mathbf{f} &= \begin{pmatrix} 0 & 1 \\ 1 & 0 \end{pmatrix} \mathbf{f} \\ \hat{o}_y\mathbf{f} &= \mathbf{f} \end{aligned} . \tag{94}$$

As it should be, $\hat{o}_y$ is now a crystallographic symmetry operation, while $\hat{o}_x$ and $\hat{o}_z$ relate individual crystals and are therefore twin operations. (It is correct to call these operations twin operations, as their translational components become inactive when they are applied to intensities.)

The individual crystals represented by **f** are shifted by $\pm\varepsilon\mathbf{c}/2$ compared to Fig. 3.12(*d*). These overall shifts simplify the equations and, of course, are cancelled out as soon as structure factors are converted into intensities.

3.4.5 Covariance model

The biomolecules forming the crystal under consideration have no internal symmetry and therefore the structures p_1 and p_2 do not contain fragments related by non-crystallographic translation and do not correlate,

$$\mathcal{E}\mathbf{p}\mathbf{p}^{*T} = \begin{pmatrix} \frac{1}{2} & 0 \\ 0 & \frac{1}{2} \end{pmatrix}. \tag{95}$$

Here, the partial structures are normalised by one half to make the complete structure normalised by one.

Because of (93) and (95),

$$\mathcal{E}\mathbf{f}\mathbf{f}^{*T} = \begin{pmatrix} 1 & \cos\omega \\ \cos\omega & 1 \end{pmatrix}. \tag{96}$$

Equation (25) is restored by letting

$$\rho = \cos\omega. \tag{97}$$

With this notation, all the results of §3.1 are applicable but only for the section of the data with a fixed index l, on which ω linearly depends. However, the goal is to derive distributions for the whole data set, not for each l-section individually.

The parameter ρ enters the probability distributions $P(Z)$ and $P(H)$ (§3.1) as $\rho^2 = \cos^2\omega$. The period of this function is $\Delta\omega = \pi$. The period of this function in terms of l follows from (88) and (91),

$$\Delta l = \frac{\Delta\omega}{2\pi\varepsilon} = \frac{1}{2\varepsilon} \approx 5.8. \tag{98}$$

In particular, $l \approx 11.6n$ and $l \approx 5.8 + 11.6n$ for integer n correspond to complete correlation and anti-correlation of structure factors of the two individual crystals, respectively ($\rho = \pm 1$), and the intensities of reflections with these l are symmetric relative to the twin operation and do not contribute to the "twin-like" behaviour of intensity statistics. In contrast, the structure factors for $l \approx 2.9 + 5.8n$ do not correlate ($\rho = 0$), so the intensity statistics of this fraction of the reflections is purely "twin-like". The overall intensity statistics are therefore a mixture of different distributions.

In the 2.1 Å data set from the HemH twinned crystal, the range of l is 0 to 28 (0 to 19 for 3 Å resolution cut-off). This includes 4.8 (3.3) periods (98) of the correlation squared $\rho^2 = \cos^2\omega$. The distributions for such a case of modulated correlation can be derived from the corresponding distributions for the case of constant correlation by averaging over a period of l. Equivalently, the averaging can be over ω, which linearly depends on l. The range for averaging over ω can be from 0 to $\pi/2$, the half-period of the function $\cos^2\omega$, as the latter is symmetric. The moment generating function (MGF) is a linear transformation of the probability distribution function and therefore the former can be averaged instead of the latter.

Formally, the averaging over ω means that ω is considered as a uniformly distributed random variable, a nuisance variable to be integrated out.

Two theoretical models, one with constant ρ as in §3.1, and one, in which ρ is the cosine of a continuous random variable as in (97), are further referred to as the constant correlation model (CCM) and modulated correlation model (MCM), respectively.

3.4.6 Second moment of normalised intensities

The MGF of the random variable Z in the case of MCM is the average of the MGF (45) over ω. Substitutions (46) and (97) give

$$\mathcal{L}_Z(t) = \frac{2}{\pi}\int_0^{\frac{\pi}{2}} \frac{\mathrm{d}\omega}{1 - t + \frac{1}{4}(1-\beta^2)t^2\sin^2\omega}. \tag{99}$$

The integration is performed using substitution

$$\cot\omega = \sqrt{1 + \frac{1-\beta^2}{4}\frac{t^2}{1-t}}\cot\omega' \tag{100}$$

to give

$$\mathcal{L}_Z(t) = \frac{1}{\sqrt{1-t}\sqrt{1 - t + \frac{1}{4}(1-\beta^2)t^2}}. \tag{101}$$

The second derivative of this function is the second moment of Z for the MCM,

$$\mathcal{E}(Z^2) = \frac{7+\beta^2}{4}. \tag{102}$$

This equation can also be obtained by substitution of mean value, $\mathcal{E}(\rho^2) = 0.5$ for ρ^2 in the expression for $\mathcal{E}(Z^2|\rho)$, as the latter is a linear function of ρ^2, equations (46) and (51).

In other words, the second moments of Z in the MCM and in the CCM with $\rho^2 = 0.5$ coincide. Accordingly, the experimental and simulated distributions were compared with both references, see below.

In particular, the second moment of Z for a perfect twin in both models equals 7/4. This is an intermediate value between the standard references for untwinned and perfectly twinned data, 2 and 3/2, respectively.

The resolution range suitable for twinning tests was chosen to be 9.0 to 3.0 Å using the plots in Fig. 3.13 and following the protocol described in §1.2.3. Note that the plot in Figs. 3.13(*a*) is not indicative of twinning. This is because (i) the twinning fraction is only 0.2 and (ii) the difference between the twinned and untwinned second moment of Z is twice less in the MCM-twin compared to a twin in which the effect of NCS is absent.

Both the set of experimental intensities and the sets of intensities calculated using the refined model of HemH (PDB code 2c8j) were averaged relative to the twin operation to generate perfectly twinned data sets. Corresponding plots of the second moment of Z against resolution are shown in Figs. 3.14(*a*) and 3.14(*b*). Both curves reasonably well match the theoretical prediction of 7/4.

3.4.7 Cumulative distribution of normalised intensities

In the untwinned case ($\beta = \pm 1$), the MGF (101) equals $(1-t)^{-1}$ and corresponds to the general reference for untwinned cases (49).

For perfect twinning ($\beta = 0$), the MGF

$$\mathcal{L}_Z(t) = \frac{2}{\sqrt{1-t(2-t)}} \tag{103}$$

corresponds to the probability distribution density

$$p(Z) = \frac{4e^{-Z}\sqrt{Z}}{\sqrt{\pi}} F(1, \tfrac{3}{2}, -Z) \tag{104}$$

and cumulative distribution function

$$P(Z) = \frac{2e^{-Z}\sqrt{Z}}{\sqrt{\pi}} \left(F(1, \tfrac{3}{2}, Z) - F(1, \tfrac{3}{2}, -Z)\right). \tag{105}$$

The latter function is non-linear at small Z,

$$P(Z) = \frac{8}{3\sqrt{\pi}} Z^{\frac{3}{2}} + O(Z^{\frac{7}{2}}). \tag{106}$$

Although the first term of this expansion differs from Z^2, the first term of the twinned distribution for the CCM (52), the qualitative criterion of non-linearity of twinned $P(Z)$ for small Z remains valid in the case of the MCM.

The function (105) was calculated using a power series of Z and is shown by dotted lines in Figs. 3.14(c) and 3.14(d). In addition, these figures present cumulative distributions of Z for perfectly twinned observed and calculated intensities in the resolution range 9.0 to 3.0 Å. These were the same data sets used in Figs. 3.14(a) and 3.14(b); the perfect twinning was simulated by averaging related intensities.

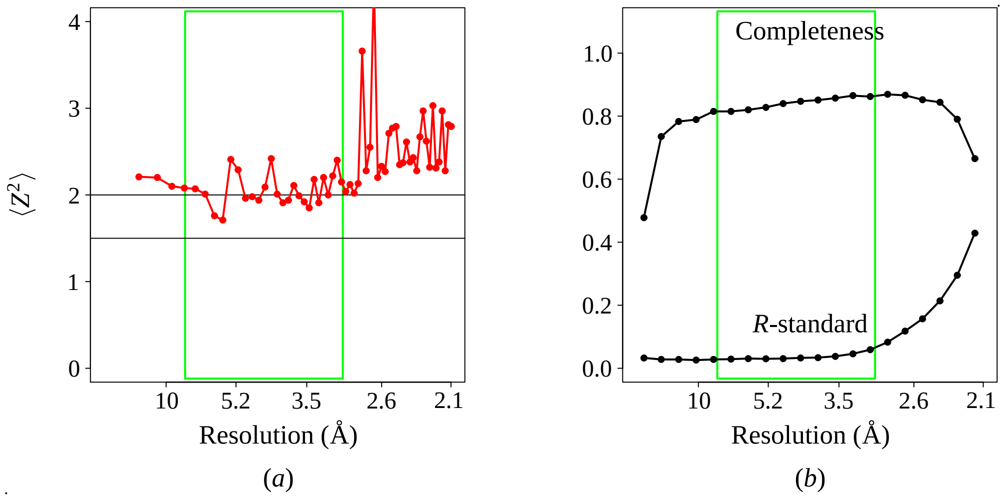

Figure 3.13. Resolution cut-off for twinning tests.

(a) The experimental second moment of Z for acentric reflections against resolution.
(b) Completeness and R-standard against resolution.

The resolution range used for twinning tests in Fig. 3.14 is shown by green boxes.

As discussed above, the two simulated distributions, the MCM-distribution and the CCM-distribution with $\rho^2 = 0.5$ have the same second moments. In addition, all four distributions are very similar in the range of Z from 0 to 1 used for perfect twinning test; both essential qualitative signs of twinning are present, a non-linearity at the origin ("sigmoidal" shape) and location of the plot below the reference distribution for untwinned data. Small differences between the four distributions are not essential for the qualitative analysis.

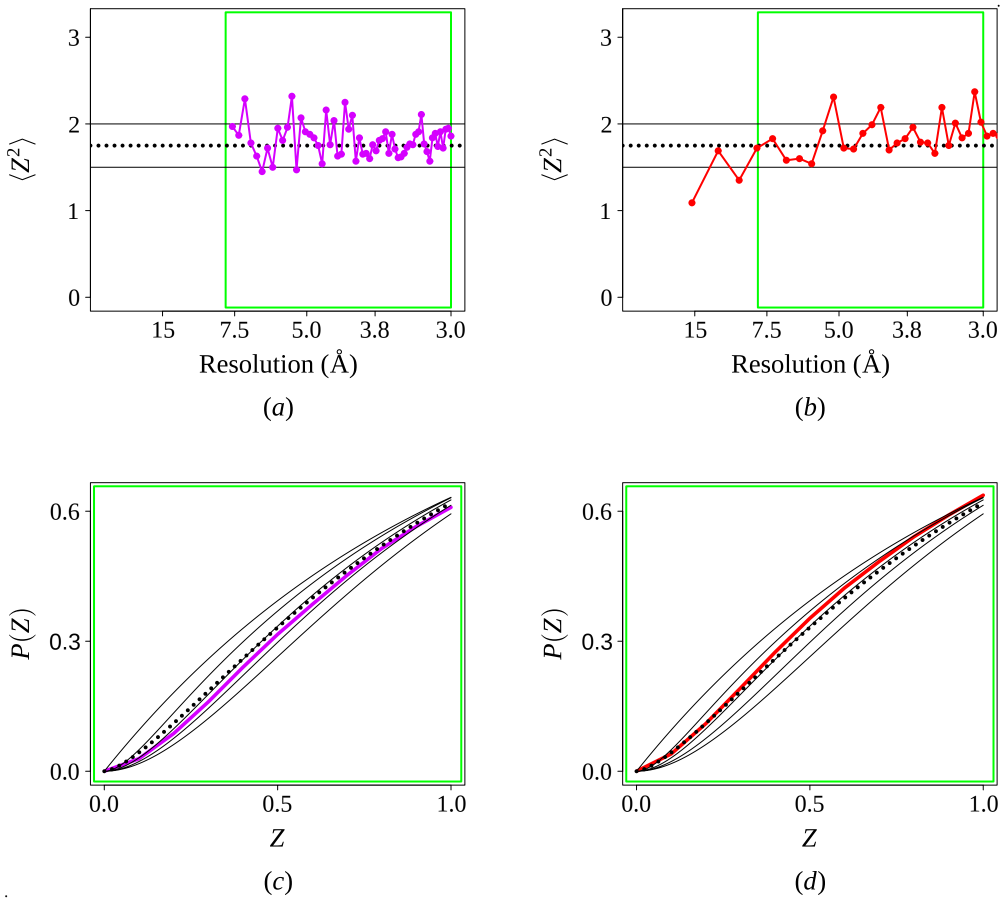

(*a*) (*b*)

(*c*) (*d*)

Figure 3.14. Perfect twinning tests in the case of OD-twin of type I/B.

(*a*,*b*) The second moments of *Z*.

(*c*,*d*) Cumulative distribution of *Z*.

The data were averaged relative to the twin operation to generate perfectly twinned data. The coloured lines show results for twinned intensities generated from

(*a*,*c*) intensities calculated from the refined model of HemH and

(*b*,*d*) experimental intensities.

The solid black lines have the same meaning as corresponding lines in Fig. 3.1. The dotted lines represent the modulated correlation model, the theoretical model of an ideal OD-twin of type I/B.

3.4.8 Partial twinning test

The series expansion for $P(H)$ is performed starting directly from the probability distribution for the uncorrelated case (64). In the current context, the latter equation represents the conditional probability distribution function $P(H|\omega)$. Substitution (97) and averaging over uniformly distributed ω give the probability distribution function of H,

$$P(H) = \frac{2}{\pi} \int_0^{\frac{\pi}{2}} \frac{H \, \mathrm{d}\omega}{\sqrt{\beta^2 \sin^2\omega + H^2 \cos^2\omega}}. \tag{107}$$

Expansion into power series of $\cos\omega$ and separate integration of each term give

$$P(H) = \frac{H}{\beta} \sum_{n=0}^{\infty} \left(\frac{\Gamma(n+\frac{1}{2})}{\Gamma(\frac{1}{2})\, n!} \right)^2 \left(1 - \frac{H^2}{\beta^2} \right)^n. \tag{108}$$

This series is identified as the following hypergeometric function,

$$P(H) = {}_2F_1(\tfrac{1}{2}, \tfrac{1}{2}, 1, 1 - H^2\beta^{-2})\, H\beta^{-1}. \tag{109}$$

The special point of this function at $H = 0$ is not removable and the first derivative of $P(H)$ at this point is infinite.

Dotted lines in Figs. 3.15(a) and 3.15(b) are the plots of this function for $\beta = 1$ ($\alpha = 0$) and $\beta = 0.6$ ($\alpha = 0.2$). The function was evaluated using expansion (108).

Two approximations were made in the derivations of the MCM-distributions, the $P2_1(1)1$ symmetry of the OD-layers was assumed to be exact, and summation over reflections was replaced by integration. The effect of these approximations was evaluated using untwinned ($\beta = 0$) distributions of H for three atomic models, including the refined structure of HemH (PDB code 2c8j) and two modifications of the latter. These distributions were compared with the theoretical distribution for MCM and with the theoretical distributions for CCM with variable ρ^2 (Figs. 3.15a).

One of the modified atomic models was generated following the procedure of §3.4.4 and represented an ideal OD-twin, in which the layers have exact $P2_1(1)1$ symmetry. The symmetrised $P2_12_12_1$ model was generated from the PDB model using one of subroutines of the program *Zanuda* (§4.3) and the layers were translated using *LSQKAB*. The distribution of H for this model (green line in Fig. 3.15a) matches the theoretical distribution for MCM well and justifies the replacement of summation over reflections by integration. The small difference between the two distributions is explained by the infinite first derivative of the MCM-distribution at $H = 0$, which is impossible in any distribution obtained from discrete set of intensities.

A copy of the molecule A of the refined model of HemH was fitted to the molecule B using *LSQKAB* and substituted for B to generate the second modified model, in which the $P2_1(1)1$ symmetry of the OD-layers was not exact but was less perturbed than in the refined model, as the contributions from conformational and temperature factor differences between A and B to the asymmetry of the OD-layer were excluded. The distribution of H for this model (blue line in Fig. 3.15*a*) significantly deviates from the MCM distribution toward the CCM distribution for $\rho^2 = 0.5$.

Finally, the distribution of H for the refined model (magenta line in Fig. 3.15*a*) matches well the CCM-distribution for $\rho^2 = 0.5$, the mean value of ρ^2 in the OD-twin under consideration. This suggests that MCM model is not a valid reference for non-ideal OD-twin, and, moreover, the modulation of ρ^2 can be ignored and CCM-model with mean ρ^2 is a proper reference.

The experimental distribution of H was computed for partially twinned unmodified HemH data. In accordance with the results of simulated experiments, the experimental distribution was compared with a series of distributions for CCM with $\rho^2 = 0.5$ and variable twinning fraction (Fig. 3.15*b*). The experimental curve matched the CCM-reference for twinning fraction 0.2. The latter estimate for twinning fraction coincided with the estimate obtained from the RvR plot, a

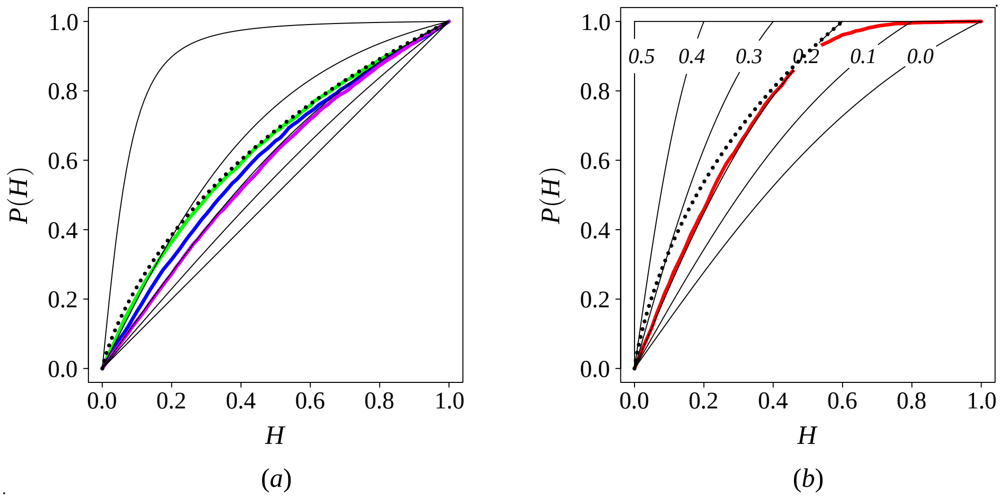

Figure 3.15. Partial twinning test in the case of OD-twin of type I/B.

(*a*) Coloured lines show cumulative distribution of H for untwinned intensities generated from
(magenta) refined model of HemH,
(blue) the model with two exactly identical molecules in the asymmetric unit and
(green) the model with exactly symmetric OD-layers.
The solid black lines correspond to the constant correlation model for zero twinning fraction and ρ^2 in the sequence 0.00, 0.25, 0.50, 0.75, 0.99 (same as coloured lines in Fig. 3.2*a*).

(*b*) Red line shows cumulative distribution of H for experimental intensities from partially twinned crystal of HemH.
The solid black lines correspond to the constant correlation model for variable twinning fraction (numbers in front of the lines) and $\rho^2 = 0.5$.

The dotted lines represent the modulated correlation model for twinning fraction 0 in (*a*) and 0.2 in (*b*) robust estimate based on both experimental and calculated intensities (Fig. 3.16). Accordingly, the experimental distribution of H was quite different from the MCM-distribution for twinning fraction 0.2 (dotted line in Fig. 3.15*b*), although the latter seemed more adequate given the large-scale organisation of the OD-twin.

3.4.9 Concluding remarks

The assumption (97) entails the presence of sections $l = l_0$ in reciprocal space in which twin related intensities exactly coincide. In addition, the differences between twin related intensities in the domains $l_0 - \delta l < l < l_0 + \delta l$ are small and quadratically depend on δl. The presence of such domains cause, in particular, the presence of an irremovable special point in $P(H)$ at $H = 0$ with infinite first derivative. Exactly symmetric sections as well as the singularity at $H = 0$ would disappear, if the assumption $\rho = \varkappa \cos \omega$ with $0 < \varkappa < 1$ were used in place of (97). In the new model, $\varkappa < 1$ would account for the perturbation of symmetry in the OD-layers.

In reality, the exact symmetry of the OD-layers never occurs in the macromolecular OD-structures. The asymmetry of the OD-layers can be characterised by the r.m.s.d. over C$^\alpha$-atoms between the OD-layer in the refined crystal structure and the symmetrised OD-layer. This magnitude equals 0.24 Å for the OD-structure of HemH. The tests with experimental and simulated data showed that the effect of modulated correlations should be completely disregarded even with this small asymmetry. Accordingly, the distributions of Z and H derived for the constant correlation model (Figs. 3.1 and 3.2) were sufficiently good references for the corresponding distributions in the case of non-ideal macromolecular OD-twin. Further tuning of the modulated correlation model was therefore unnecessary.

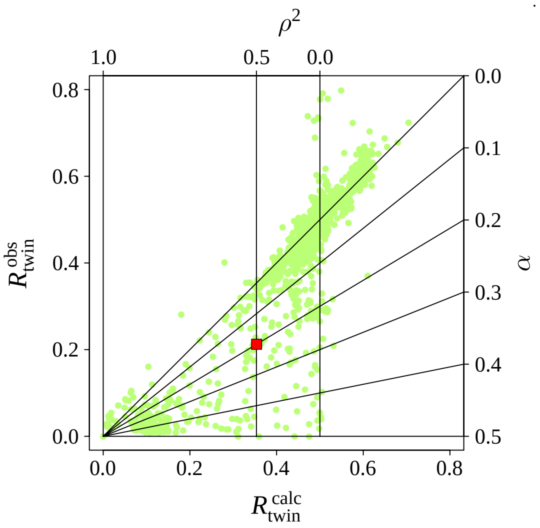

Figure 3.16. Effect of interfering NCS on R_{twin}. Red square on the RvR plot corresponds to OD-twin of HemH. Green points in the background present scatter plot derived from the PDB (Fig. 3.3*b*).

Another parameter of the OD-structure under consideration, ε defines the relative positions of the OD-layers and the period of ρ as a function of the index l. In the actual crystal structure of HemH, $\varepsilon = 0.086$ and the whole range of index l accommodates five periods of the function ρ. In an imaginary structure with more than ten times smaller ε, the function ρ would be a decreasing function of resolution in the whole range of l. The latter structure should be considered as the structure with $P2_12_12_1$ space group pseudosymmetry. Exact crystallographic symmetry $P2_12_12_1$ would occur in the limiting cases of $\varepsilon = 0$ (Fig. 3.12*e*) and $\varepsilon = 1/2$ (different fully ordered structure). The pseudosymmetric case would be characterised by a narrower range of ρ and it would be reasonable to expect that the constant correlation model would remain applicable. The "constant correlation statistics" of the actual HemH data are restored for a different reason, owing to asymmetry of the OD-layers (Fig. 3.15*a*).

The analysis of twins in the PDB showed that the alignment of NCS and twin axes and consequent correlation of twin-related intensities are characteristic for a large fraction of protein twins (§3.2.5). An OD-twin can be considered as a limiting case of such twins, as the correlation between twin-related structure factors in the ideal OD-twin varies in the range from -1 to 1 with the majority of values close to limits. The distributions of Z and H derived from the constant correlation model proved to be good references for an OD-twin and therefore are likely to be good references for the general case of twin with interfering NCS.

Both the twin of the C-terminal domain of gp2-protein (§3.3) and the twin of HemH are twins by metric merohedry. These structures present two different mechanisms through which an orthorhombic lattice is restored in a monoclinic structure. In the first example, the structural elements controlling the lattice symmetry are NCS-related one-dimensional filaments spanning the crystal in two different directions. In the second example, these are two-dimensional OD-layers. A common feature of the two cases is that strongly bound "infinite" associations of molecules dictate the lattice symmetry, which is higher than the holohedry of the point group of the individual crystals.

3.5 Example of OD-twin by reticular pseudomerohedry

The L-2-haloacid dehalogenase from *Sulfolobus tokodaii* was studied in the group of Professor Jennifer Littlechild (University of Exeter). The biochemical and crystallisation experiments were performed by Dr. Carrie Rye. Diffraction data were collected and crystal structure was solved by Dr. Carrie Rye and Dr. Michail Isupov (PDB code 2w11). I designed a program for detwinning and completed refinement. The results were presented by Rye *et al.* (2007; 2009).

This crystal of L-2-haloacid dehalogenase was an OD-twin belonging to an OD-family of type I/A (§1.3). In terms of geometrical classification (§1.2.1), it was a twin by reticular pseudomerohedry, the type of twinning typical for OD-families of type I/A. Twinning by reticular pseudomerohedry cannot be predicted from the lattice parameters alone (§1.2.2) and in this example it was only detected during integration of images since there were more spots than predicted. Despite a non-zero obliquity angle and because of the symmetry of the OD-layers, it was possible to accurately detwin the data without precise measurements of the operation relating two lattices. This section gives a brief introduction to the project and describes the morphology of the twin, and the process of structure solution and detwinning.

3.5.1 Background

The 2-haloacid dehalogenases (EC 3.8.1.2; halidohydrolases) catalyse the hydrolytic dehalogenation of 2-haloalkanoic acids to produce 2-hydroxyalkanoic acids. They are only active on compounds in which the halogen is attached at the C2 position. The 2-haloacid dehalogenases have important implications in the biodegradation of toxic halogenated compounds from the environment. Many of these compounds are produced synthetically for use as herbicides and growth regulators (Allpress & Gowland, 1998) and over 60% of herbicides contain at least one Cl atom (Slater, 1982). Owing to the importance of removing halogenated compounds from the environment, there has been much interest in dehalogenase enzymes.

Based on substrate specificity, three different types of haloacid dehalogenase have been identified. DL-haloacid dehalogenases work equally well on both enantiomers of the haloacid, with either retention or inversion of the stereochemistry at the C2 atom position. D- and L-2-haloacid dehalogenases are specific to only one enantiomer and cause an inversion in the C2 configuration of the product (Slater *et al.*, 1997). 2-haloacid dehalogenases can be subdivided into two evolutionary unrelated groups (Hill *et al.*, 1999). Group I contains the D- and DL-haloacid dehalogenases and group II contains the L-haloacid dehalogenases. L-2-haloacid dehalogenases belong to the HAD superfamily (Pfam PF00702), which also includes some ATPases, epoxide hydrolases and a number of different phosphatases.

X-ray structures are available for two mesophilic L-2-haloacid dehalogenases: L-DEX YL from *Pseudomonas* sp. YL (Hisano *et al.*, 1996) and DhlB from *Xanthobacter autotrophicus* GJ10 (Franken *et al.*, 1991). Both of these enzymes are homodimers, with each subunit having a core domain of a Rossmann-fold-like six-stranded parallel β-sheets flanked by five α-helices and a four-helix-bundle subdomain. The monomeric structure of a putative haloacid dehalogenase (PH0459) from the thermophilic archaeon *Pyrococcus horikoshii* OT3 has also recently been reported (Arai *et al.*, 2006).

The dehalogenase enzyme under consideration is from *Sulfolobus tokodaii* strain 7, which was isolated from Beppu hot springs in Kyushu, Japan in 1983. *S. tokodaii* is able to convert hydrogen sulphide to sulphate and grows optimally at 353 K in an aerobic acidic sulphur-rich environment. The genome has been sequenced using the whole-genome shotgun method (Kawarabayasi *et al.*, 2001). The putative L-2-haloacid dehalogenase sequence has been identified from the genome sequence and has 31% sequence identity to L-DEX YL, 28% to DhlB and 29% to PH0459. The *S. tokodaii* dehalogenase has been cloned, overexpressed, purified and shown to have haloacid dehalogenase activity. Crystals of two complexes, with inorganic phosphate (orthorhombic form) and L-lactate (monoclinic form) have been obtained and analysed (Rye *et al.*, 2009). The structure solution and refinement of the monoclinic crystal (Rye *et al.*, 2007), a twin by reticular pseudomerohedry, is described below.

3.5.2 Structure solution

The monoclinic crystals belonged to the space group $C2$ with unit-cell parameters $a = 127.59$, $b = 58.08$, $c = 51.19$ Å and $\beta = 97.23^o$. The solvent content of the crystals, which contain two subunits in the asymmetric unit, has been estimated at 37%; $V_M = 1.96$ Å^{3}Da^{-1} (Matthews, 1968). The X-ray diffraction data were collected at 100 K at Daresbury SRS station 10.1 (Cianci *et al.*, 2005) using wavelength 1.729 Å and a MAR 225 CCD detector and processed using the programs *DENZO* and *SCALEPACK* (Otwinowski & Minor, 1997) to give $R_{\text{sym}} = 9.6\%$ and completeness 97.6% in the resolution range 25 to 1.9 Å.

The MR was carried out with the program *MOLREP* using the haloacid dehalogenase from *X. autotrophicus* (PDB code 1qq5), which has 28% sequence identity to the *S. tokodaii* dehalogenase. The MR solution could only be found when the search model was trimmed according to its sequence alignment to the target protein. This was carried out using the model modification option of *MOLREP* (Lebedev *et al.*, 2007). The structure was refined using *REFMAC* 5.2 and the model was rebuilt using the program *Coot* (Emsley & Cowtan, 2004). Initial refinement gave $R = 0.42$ and $R_{\text{free}} = 0.48$. After several cycles of manual model rebuilding/refinement, the model was subjected to the *ARP/wARP* protocol (Perrakis *et al.*, 1999). The resulting model was refined to a crystallographic *R*-factor of 0.21 and an R_{free} of 0.27. These still appeared to be high as all main-chain atoms of the model were clearly defined in electron density. Moreover, the solvent structure appeared to be poorly defined and addition of solvent molecules failed to significantly lower the *R*-factors. Inspection of the native Patterson synthesis revealed a number of strong non-origin peaks on the *u* axis (Fig. 3.17*a*). The highest of them had a height of ~ 0.2 of the origin peak. At the same time, there was no translational NCS in the structure and therefore no such peaks were present in the Patterson map calculated from the model.

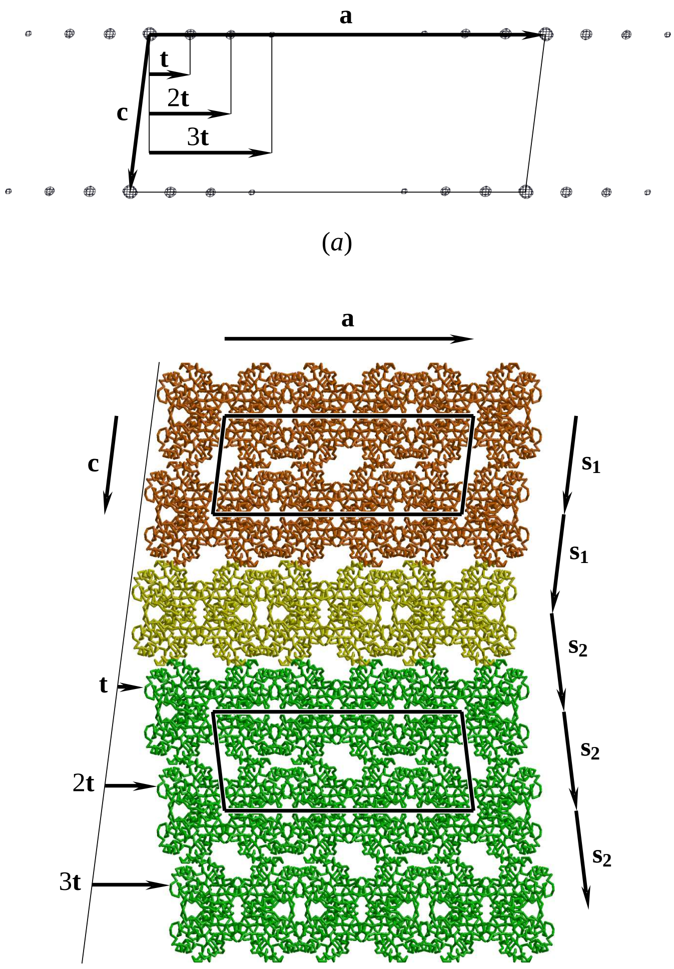

(*a*)

(*b*)

Figure 3.17. Organisation of an OD-twin of L-2-haloacid dehalogenase.
(*a*) A section $v = 0$ of the native Patterson synthesis contoured at 4.5σ (blue). Vectors $\mathbf{t}$, $2\mathbf{t}$ and $3\mathbf{t}$ define the positions of non-origin peaks. This figure was prepared using *Coot* (Emsley & Cowtan, 2004).
(*b*) Possible organisation of a crystal fragment including two adjacent individual crystals with local *C*2 symmetry, in which OD-layers are related by stacking vectors $\mathbf{s}_1$ (orange) and $\mathbf{s}_2$ (green). The intermediate layer (yellow) can be assigned to either of the two connected individual crystals. Vectors $\mathbf{t}$, $2\mathbf{t}$ and $3\mathbf{t}$ define the offsets of three consecutive layers from their positions in a single crystal. This figure was prepared using *BOBSCRIPT* (Esnouf, 1999).

3.5.3 Analysis of twinning

An analysis of molecular packing shows that the crystal structure under consideration is an OD-structure of type I/A (§1.3; Dornberger-Schiff, 1956; Nespolo *et al.*, 2004). It is arranged as a stack of layers which are parallel to the crystallographic plane (001). The layers are related by translations; the plane space group of a layer is $C22(2)$ (Fig. 3.17*b*). As a consequence of this layer arrangement, there is the potential for formation of (polysynthetic) OD twins and disordered OD structures (Dornberger-Schiff & Dunitz, 1965). A switch from stacking vector $\mathbf{s}_1 = \mathbf{c}$ to $\mathbf{s}_2 \approx \mathbf{c} + 0.1\mathbf{a}$ within one crystal forms a twin interface separating two internally identical individual crystals (Fig. 3.17*b*). Layers from different individual crystals are related by translations, which are in agreement with the observed non-origin peaks in the Patterson map. The lattices of individual crystals partially overlap in such an OD-twin, and therefore the presence of twinning can be validated directly by a more careful inspection of the diffraction data. Therefore the data processing was repeated to observe that some of the diffraction images clearly revealed two lattices. Dependent on the starting image the autoindexing was peaking up one or another lattice. This made it possible to confirm that alternative lattices have identical cell parameters.

Fig. 3.18 shows an image, in which alternative lattices are clearly seen. This is not so for some other images (Fig. 3.19). In particular, the presence of the second lattice was not quite obvious in several starting images and therefore it was initially overlooked. Because of this and because of the presence of streaky reflections (Fig. 3.19) the crystal was initially identified as a disordered OD-structure with predomination of one of the two possible domain orientations, but this hypothesis was abandoned when the second lattice was observed. Fig. 3.20 helps explaining why some images are less indicative of the second lattice than others. If the incident beam is along **a** then only (partially) overlapped reflections intersect the Ewald sphere, whereas incident beam along $\mathbf{c}^*$ results in an image with most of the spots belonging to only one of the two lattices, as in Fig. 3.18. Finally, the observation of both second lattice and diffuse streaks (Fig. 3.19) suggested that the crystal was partially disordered OD-twin, that is a polysynthetic OD-twin with small volumes of individual crystals.

3.5.4 Real space lattice geometry and classification of the twin

Because of $C2$ symmetry of individual crystals, the twin under consideration has two equivalent twin elements. These are the two-fold twin axes parallel to $\mathbf{c}^*$ and **a**, as can be seen from Fig. 3.17(*b*). These can be classified as an irrational twofold twin axis normal to a rational lattice plane, and a rational twofold twin axis normal to an irrational plane, respectively (Hahn & Klapper, 2003, p.396, types ii and iii). The individual crystals of such a twin have one common

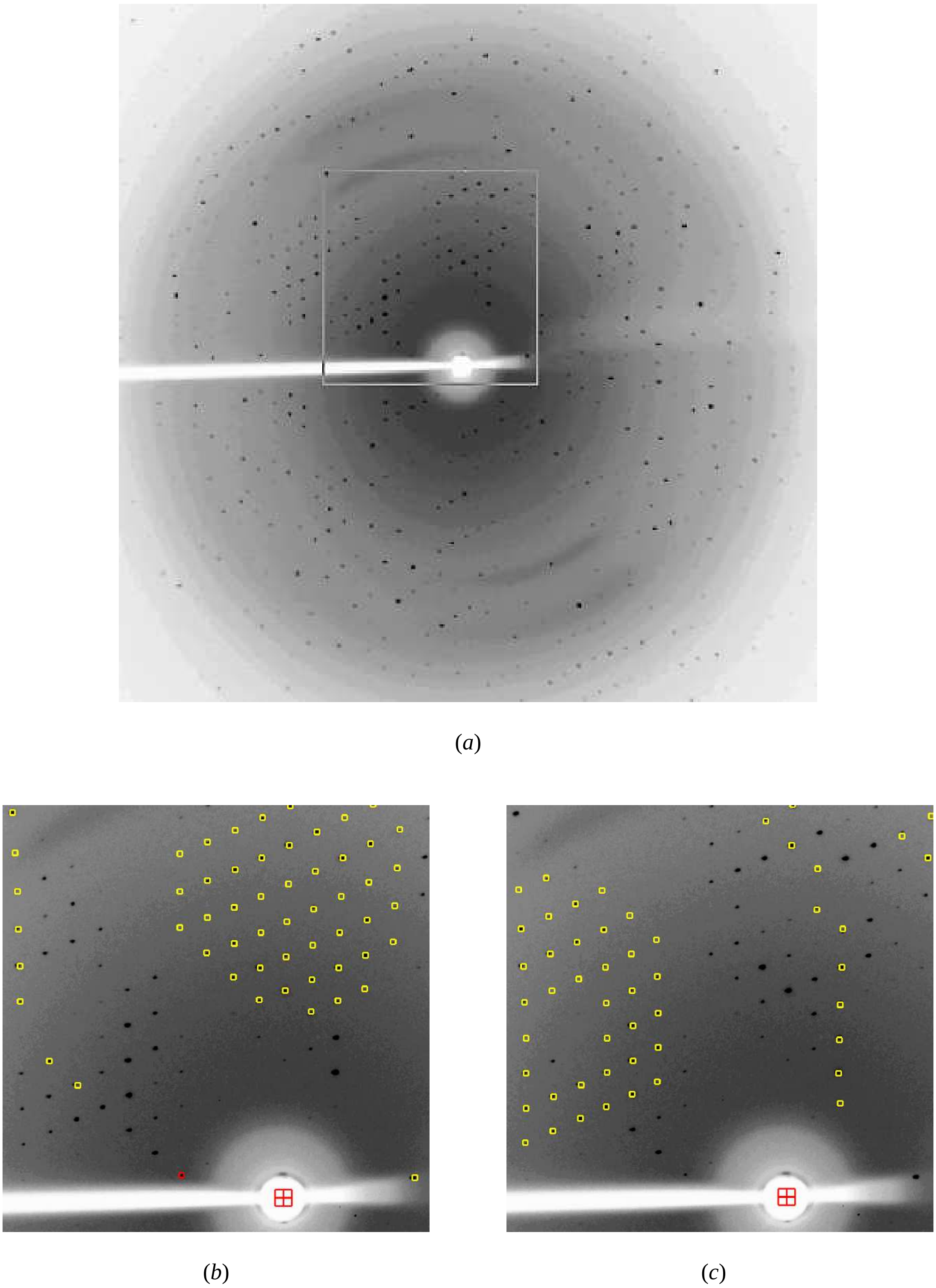

(*a*)

(*b*)

(*c*)

Figure 3.18. Diffraction image of an OD-twin of L-2-haloacid dehalogenase showing alternative lattices. (*a*) The whole image with the enlarged area shown by a white box. (*b*, *c*) Enlarged images with the predictions corresponding to alternative lattices. This figure was prepared using *DENZO* (Otwinowski & Minor, 1997).

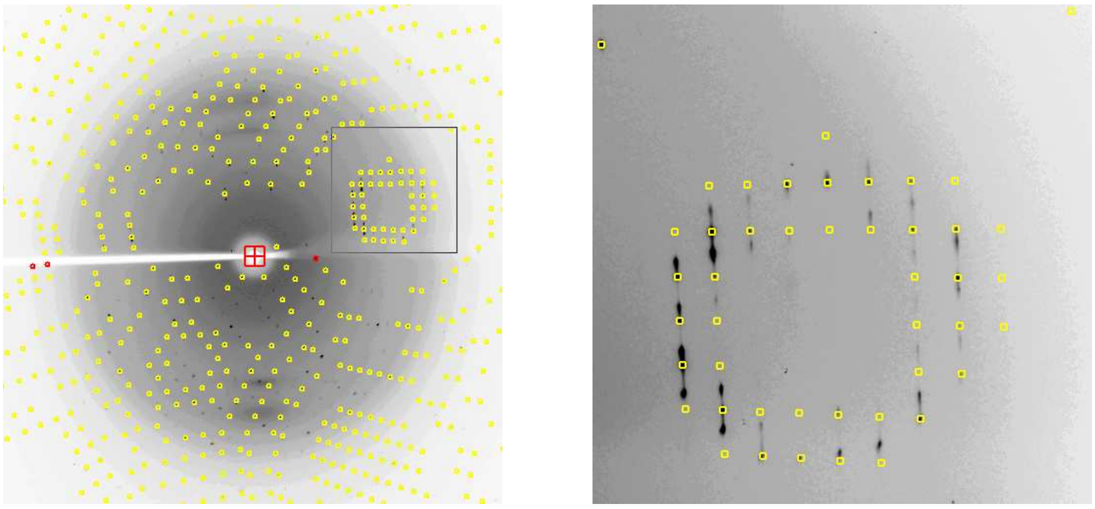

(*a*) (*b*)

Figure 3.19. Diffraction image of an OD-twin of L-2-haloacid dehalogenase showing streaky reflections. (*a*) The whole image with the enlarged area shown by a black box. (*b*) Enlarged image with clearly seen diffuse streaks indicating partial disorder.

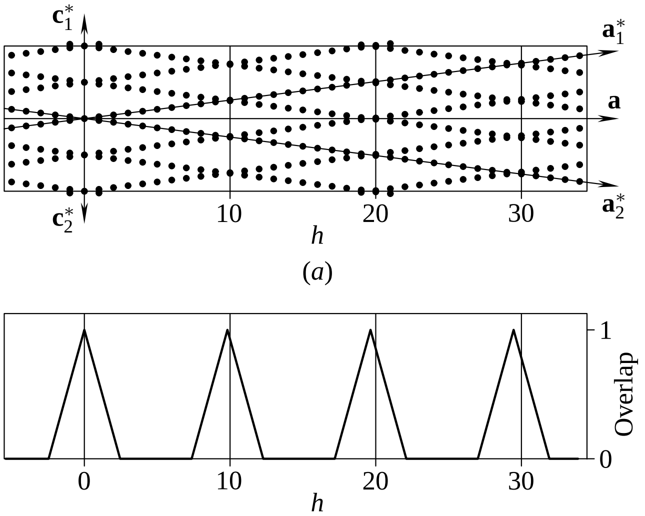

(*a*)

(*b*)

Figure 3.20. Arrangement of spots in the reciprocal space. (*a*) The reciprocal-space, a view along **b**. The series of close spots parallel to axes $\mathbf{a}_1^*$ and $\mathbf{a}_2^*$ belong to two alternative lattices corresponding to two different orientations of individual crystals forming a polysynthetic OD twin by reticular pseudomerohedry with twin index 10 and with obliquity angle 0.1^o. Owing to systematic absences in $C2$, reflections with even and odd h will only appear in sections with even and odd k, respectively. The axes of the two equivalent twin operations coincide with the axes $\mathbf{c}^*$ and $\mathbf{a}$. The overlap between reflections from alternative lattices occurs only if the two reflections have the same index h and $h \approx 10n$. Because of non-zero obliquity angle, spots with $h = 10n$ do not overlap exactly except for $h = 0$. (*b*) If the reflections have the same size, the overlap is a periodical function of h and does not depend on k and l.

rational plane in the real space (and also one common rational plane in the reciprocal space), but there is no three-dimensional coincidence lattice. However, it is common practice to use the term twinning by reticular pseudomerohedry and to classify such twins in terms of approximate lattice coincidence, *i.e.* to assign twin index and obliquity (§1.2.1; Hahn & Klapper, 2003, p.420). The latter classification is useful for X-ray data analysis, as it characterises in standard general terms the mode in which the spots from alternative reciprocal lattices overlap.

The twin lattice is a sublattice of the individual crystal lattice, which is (approximately) invariant relative to the twin operation. The twin lattice is completely specified by its (approximately) invariant subsets, the crystallographic direction (approximately) parallel to the twin axis or orthogonal to the twin plane, and the crystallographic plane (approximately) orthogonal to the twin axis or parallel to the twin plane. Let $\mathbf{u}$ and $\mathbf{v}^*$ be the shortest real and reciprocal lattice vectors, respectively, corresponding to the above crystallographic direction and plane[1], and let n' be the scalar product of these vectors, an integer number,

$$n' = (\mathbf{v}^*, \mathbf{u}).$$

If the twin lattice is exactly invariant relative to the twin operation, then $\mathbf{u}$ and $\mathbf{v}^*$ are exactly parallel. Therefore the departure from the exact invariance is characterised by the angle between these vectors, the obliquity angle ω,

$$\cos\omega = \frac{n'}{|\mathbf{v}^*||\mathbf{u}|}.$$

Another characteristics of the twin lattice is the twin lattice index n, which is the ratio of the unit-cell volumes of the twin lattice and the individual crystal lattice. This value can be calculated a follows (Hahn & Klapper, 2003, p.418),

$$n = \begin{cases} n' & \text{if} \quad n' \quad \text{is odd} \\ n'/2 & \text{if} \quad n' \quad \text{is even} \end{cases}.$$

Two pairs of lattice vectors can be used in our particular case,

$$\mathbf{u}_1 = \mathbf{a} + 20\mathbf{c}, \qquad \mathbf{v}_1^* = \mathbf{c}^*$$

and

$$\mathbf{u}_2 = \mathbf{a}, \qquad \mathbf{v}_2^* = 20\mathbf{a}^* - \mathbf{c}^*,$$

which are associated with the two twin axes along $\mathbf{c}^*$ and $\mathbf{a}$, respectively. The vector $\mathbf{u}_1$ can be found graphically, if the two unit cells in Fig. 3.17(*b*) are expanded into two lattices containing

[1] The vectors $\mathbf{u}$ and $\mathbf{v}^*$ have integer coprime components in the primitive bases associated with the real and reciprocal lattices, respectively, but may have fractional components or components with a common divider greater than 1, respectively, if the basis corresponds to a centred lattice.

a sufficient number of unit-cell repeats. The vector $\mathbf{v}_2^*$ is the axis of the zone containing $\mathbf{u}_1$ and $\mathbf{b}$. Because $\mathbf{u}_1$ and $\mathbf{v}_1^*$ are orthogonal to $\mathbf{v}_2^*$ and $\mathbf{u}_2$, respectively, both pairs result in the same value for the twin lattice index, $n = 10$ and obliquity angle, $\omega = 0.071^o$. The last angle was the result for the unit cell parameters from §3.5.2 and the PDB entry 2w11. Variation of the data processing parameters resulted in a small variation in the unit cell parameters. Corresponding values of ω were 0.067^o and 0.152^o. The mean of the three measurements is approximately 0.1^o. A more precise estimation of ω was not needed as a related parameter t was refined with the demodulation program (§3.5.5).

Thus the analysis of the unit-cell parameters suggests that we are dealing with an OD-twin by reticular pseudomerohedry with twinning index $n = 10$ and the obliquity angle $\omega \approx 0.1^o$. This means that every tenth reflection strongly overlap with a reflection of alternative lattice (Fig. 3.20*a*).

The twin index of our twin equals ten and is higher than Mallard's empirical limit of six (Le Page, 2002). However this is not a surprise. Small values of twin index and obliquity angle may have structural reasons in, for example, transformation and mechanical twins, in which a three-dimensional pseudosymmetry of the twin lattice may be associated with a pseudosymmetry of individual crystal. In our case the twinning is due to a two-dimensional symmetry of OD-layer, so the three-dimensional twin lattice is only a formal entity, and its parameters, the twin index and obliquity angle, are standard but formal parameters. Our data are in agreement with the analysis by Hahn & Klapper (2003, p.421) showing that in the general case Mallard's limits have little prediction power.

3.5.5 Demodulation

The geometry of the reciprocal space is shown in Fig. 3.20(*a*). Under the assumption of identical three-dimensional profiles of reflections (disregarding the geometry of data collection), the overlap q is a periodic function of index h and does not depend on indices k and l (Fig. 3.20*b*). Owing to the non-zero obliquity, reflections with $h = 10n$, $n \neq 0$ do not overlap exactly. On the other hand, reflections with indices h close to $10n$ partially overlap owing to the non-zero size of the reflections and the small angle between $\mathbf{a}_1^*$ and $\mathbf{a}_2^*$ (Fig. 3.20*b*). Contributions from the alternative lattice affect the intensities of the reflections with h close to $10n$ and cause modulation of the intensities (Fig. 3.21*b*), which results in non-origin peaks in the Patterson map (Figs. 3.17*a* and 3.21*d*). The effect of twinning by reticular pseudomerohedry on the intensities can be modelled similarly to the case of twinning by merohedry. In our particular case, in which overlapping reflections have the same index h and the overlap does not depend on k and l, the equations below can be used, where $I_{T1} = I_T(h, k_1, l_1)$ and $I_{T2} = I_T(h, k_2, l_2)$ are the measured

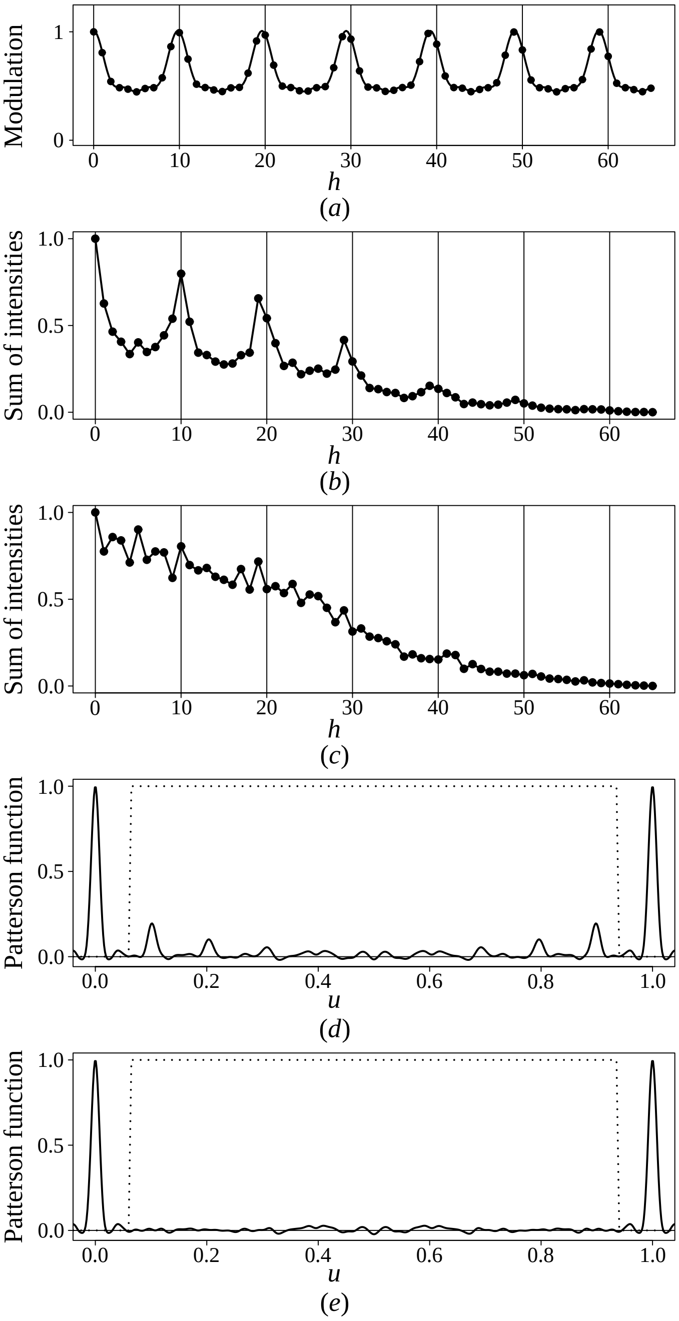

Figure 3.21. Demodulation of the diffraction data.

(*a*) Periodic modulation function (Eqn. 113) with three harmonics and optimised parameters.

(*b*) The sum of the measured intensities with given h.

(*c*) The sum of the demodulated intensities with given h.

(*d*) Patterson function calculated using measured intensities on the line $v = w = 0$.

(*e*) Patterson function calculated using demodulated intensities on the line $v = w = 0$.

All functions are shown in relative scale.

Relations between the plotted functions are as follows. The discrete function shown by points in (*a*) is the ratio of the discrete functions in (*b*) and (*c*). The latter two are Fourier series of the Patterson functions in (*d*) and (*e*), respectively. Optimisation of the modulation function (*a*) was performed by minimising the dispersion of the Patterson function along u within the mask shown by the dotted line in (*d*) and (*e*).

(twinned) intensities and $I_1 = I(h, k_1, l_1)$ and $I_2 = I(h, k_2, l_2)$ are the detwinned intensities of two overlapping reflections from the alternative lattices,

$$\begin{cases} I_{T\,1} = (1-\alpha)\, I_1 + \alpha\, q(h)\, I_2 \\ I_{T\,2} = (1-\alpha)\, I_2 + \alpha\, q(h)\, I_1 \end{cases} . \tag{110}$$

The difference from the case of twinning by merohedry is that the contribution from the alternative lattice depends on both the twinning fraction α and the overlap $q(h)$.

A good estimate of the twinning fraction α can be obtained by comparing the intensities of non-overlapping reflections from the alternative lattices provided that the two sets of intensities are on the same scale. Although less accurate, an estimate of α can also be obtained using intensities from a single lattice. For example, the reflections with $h = 10$ overlap with the reflections from the second lattice, while the reflections with $h = 15$ do not overlap. The mean intensity for $h = 10$ is about twice larger than the mean intensity for $h = 15$, as follows from Fig. 3.20(*a*). Consequently, the contributions from the two lattices into $h = 10$ are approximately the same and therefore the twinning fraction α is approximately $1/2$ (the mean untwinned intensities for the two values of *h* are assumed to be approximately equal).

Our twinned crystal appears to be a polysynthetic twin with many twin interfaces, as suggested by the lack of well-defined edges. Therefore the individual crystals of this twin appear to be too small to be cut out for data collection. Deconvolution of partially overlapped reflections during data processing is not yet possible with standard software for protein crystallography. Therefore, the improvement of integrated data was required, a detwinning procedure taking into account the non-uniform overlap of the reflections from the two lattices. In principle, this can be performed using the system of equations (110). However, it was found that α is close to 1/2. Thus, as in the case of perfect twinning by merohedry, detwinning would not work for reflections with $q(h)$ close to 1. Fortunately, detwinning becomes feasible owing to the internal symmetry of a single OD layer. The Fourier transform amplitude of the layer's electron density has point-group symmetry that includes twin operations. This means that overlapping reflections from the two lattices have very similar intensities. Moreover, the higher the overlap the closer the intensities are (indeed, R_{sym} with respect to the twin operation for the subset of reflections with $h = 10n$ is 4.1% for observed and 11.9% for calculated intensities). Also, the less the overlap the less the contribution is from the alternative lattice and therefore less accurate estimates for intensities from the alternative lattice are required in (110). Thus, for the pairs of reflections related by (110), we assume that

$$I_1 = I_2 \tag{111}$$

and (110) can be rewritten as

$$I_T = [1 - \alpha + \alpha\, q(h)]\, I = \tilde{q}(h)\, I. \tag{112}$$

This means that detwinning can be performed by pure demodulation, where the detwinned intensity is derived solely from the original intensity multiplied by a coefficient dependent on h. Similarly to $q(h)$ in (110), the coefficient $\tilde{q}(h)$ in (112) can be modelled by a periodic function of h, where t approximately equals 1/10 and its exact value depends on the obliquity angle,

$$\tilde{q}(h) = c_0 + c_1 \cos(2\pi th) + c_2 \cos(4\pi th) + \ldots \tag{113}$$

Thus, the detwinning procedure must involve refinement of t, on which the overlap strongly depends. The coefficient c_0 is defined by the equation $\tilde{q}(0) = 1$, which follows from $q(0) = 1$ and (112).

The demodulation was performed using a specially written *FORTRAN* program. Firstly, optimisation of the parameters t, c_1, c_2, ... (113) was performed by minimising the dispersion of the Patterson function on the line $v = w = 0$ within a mask excluding an area around the origin (Figs. 3.21*d* and 3.21*e*). This was performed for zero to six harmonics in expansion (113). Secondly, the original data were demodulated by dividing the intensities by the corresponding value of $\tilde{q}(h)$. Subsequently, restrained refinement using *REFMAC* was performed against each demodulated data set, starting each time from the same atomic model. The best $R = 0.162$ and $R_{\text{free}} = 0.225$ were obtained for the approximation (113) containing three harmonics. The corresponding modulation function $\tilde{q}(h)$ is shown in Fig. 3.21(*a*). The refined value of t corresponds to an obliquity angle of 0.13^o, which agrees with the values derived from the unit-cell parameters. The demodulated data gave a relatively smooth plot of $\sum_k \sum_l I(h,k,l)$ against h (Fig. 3.21*c*) and the corresponding Patterson map contained no strong non-origin peaks (Fig. 3.21*e*). The demodulated data were used in the final round of model correction and refinement.

To examine the effect of twinning on the atomic model and electron density, the model from the PDB was refined against both detwinned and original twinned data with all other refinement parameters being identical. In spite of different R-factors ($R = 0.193$ and $R_{\text{free}} = 0.258$ for twinned and $R = 0.159$ and $R_{\text{free}} = 0.220$ for detwinned data) no significant differences in the electron density could be seen and neither atomic coordinates nor B-factors were significantly different in the two refined models (the r.m.s.d. was 0.06 Å for coordinates of C^α atoms and 1.6 Å^2 for B-factors of all protein atoms). With water and two lactate molecules removed, refinement against the two data sets, original and demodulated, revealed minor differences in the two resultant maps at the positions of the removed atoms. In particular, the density for the O3-atom of the lactate of chain A was almost missing. This observation is consistent with poorly defined solvent electron density after initial model building and refinement before twinning was noticed. We therefore anticipate that detwinning in cases like this can provide a small improvement in the refinement and help manual or automated model building but will not be critical for the quality of the final model.

3.5.6 Concluding remarks

The OD structures with a large number of twin interfaces are considered as partially disordered OD structures (Dornberger-Schiff & Dunitz, 1965). They produce elongated streaky reflections on the diffraction images. Apparently, we have a case that is intermediate between a polysynthetic OD twin and a disordered OD structure, as diffuse streaks are present in some images (Fig. 3.19). Nevertheless, the demodulation procedure remains applicable to such cases (Wang *et al.*, 2005).

Macromolecular crystals are characterised by a clearly defined hierarchy of building blocks and by the different strengths of interactions between them. Because of this, protein crystals are frequently composed of symmetric layers with asymmetric interfaces between them. In some of these cases there is the potential for the formation of OD twins by reticular pseudomerohedry. The procedure described above is applicable to the majority of such twins: (i) the exact twin operation can be identified based on the organisation of the crystal and (ii) higher symmetry of OD layers can be further utilised to reduce detwinning to a simple demodulation, thereby avoiding the problem with singularity at $\alpha = 1/2$.

In the case under consideration the detection of twinning by reticular pseudomerohedry involved two steps, inspection of the Patterson map and detection of the alternative lattice. This is a quite general and practical approach. The inspection of the Patterson map is a quick test that immediately excludes irrelevant cases. The check for an alternative lattice is necessary if non-origin peaks are found in the Patterson map, as these peaks can be due to twinning or pseudotranslation. The alternative approach, prediction of twinning from unit-cell parameters and Mallard's limits (Le Page, 2002) is not sensible for growth twins as demonstrated by Hahn & Klapper (2003, p.421) and confirmed by this particular case of twinning with the twin index of ten.

4 False-origin MR-solutions

In the case of translational pseudosymmetry, the vector relating equivalent origins in the true space group also relates equivalent origins in the pseudosymmetry space group with smaller unit-cell. However, the inverse statement is not in general correct. A translation relating origins in a pseudosymmetry space group may convert the structure into a false structure, in which some of the NCS axes become crystallographic and *vice versa* and one of the pseudo-origins becomes the crystallographic origin. If the TF had picked up such a false solution, the subsequent refinement would stall at high values of R and R_{free} despite misleadingly good quality of the electron density maps. Such false structures are here referred to as false-origin structures, or false-origin MR-solutions.

The first two sections of this chapter describe two cases, in which false-origin MR-solutions were encountered in the course of structure determination. In each case, the analysis of pseudosymmetry and possible methods of resolving the false-origin problem are presented. To automatically handle the false-origin MR solutions, as well as other cases of incorrectly specified symmetry, I have developed the program *Zanuda*, which is described in the third section of this chapter. The program was successfully used to correct the symmetry assignment in a complicated case in which both NCS by translation and NCS interfering with twinning were present (§4.4). An OD-structure of type I/A with yet another type of space group ambiguity is analysed in (§4.5).

4.1 Structure solution of anti-TRAP (continued)

The structure solution of anti-TRAP from *Bacillus licheniformis* was presented in §2.2. The correct model of the dodecamer was obtained using an NCS-constrained exhaustive search and four dodecamers related by translational NCS were located in the asymmetric unit of the crystal using the conventional TF. Later analysis showed that this was a false-origin MR solution, where a pseudo-origin at $(\mathbf{a}+\mathbf{c})/4$ was incorrectly assigned as the crystallographic origin. The false structure was refined and the true structure was found using the refined dodecamer as a search model.

This section presents the comparison of the true and false-origin structures in terms of crystal packing, location of symmetry axes and refinement behaviour. Possible reasons for the MR failure to find the true solution at the first attempt and methods for correction of the false-origin solution are discussed.

4.1.1 Organisation of the crystal

This crystal structure has symmetry $P2_1$ and unit-cell parameters $a = 118.5$ Å, $b = 99.9$ Å, $c = 123.2$ Å, $\beta = 117.6^o$. The crystal asymmetric unit contains four dodecamers with pairwise differences in their orientations ranging from 1.7^o to 7.6^o. The superposition of one particular pair of dodecamers by translation $(\mathbf{a}+\mathbf{c})/2$ is shown in Fig. 4.1(*a*).

The crystal is assembled of layers, one of which is shown in Fig. 4.1(*b*). Each layer is generated by crystallographic symmetry applied to two dodecamers. Each layer is symmetric relative to the crystallographic translations $n(\mathbf{a}+\mathbf{c})+m\mathbf{b}$. All other crystallographic translations relate odd layers with odd layers and even layers with even layers. Adjacent layers are related by an NCS translation vectors $\pm 0.13\mathbf{b}+0.50\mathbf{c}$, illustrated by the Patterson map in Fig. 2.2(*b*). This NCS translation can only roughly be approximated by half of a crystallographic translation and does not cause problems with the MR. At the same time, the molecules A and B in Fig. 4.1(*b*), the individual layers and the whole structure can be well superimposed with their copies translated by $(\mathbf{a}+\mathbf{c})/2$. This superposition is mostly perturbed by small difference in the orientations of dodecamers (Fig. 4.1*a*).

The space group generated by addition of the pseudotranslation $(\mathbf{a}+\mathbf{c})/2$ to the true space group has an equivalent crystallographic origin at $(\mathbf{a}+\mathbf{c})/4$, which is not an equivalent origin in the true space group. The shift of the asymmetric unit (molecules A and B in Fig. 4.1*b* and molecules C and D with similar relative location in adjacent layer) by $(\mathbf{a}+\mathbf{c})/4$ generates the structure (Fig. 4.1*c*), which is similar but not identical to the original structure owing to altered symmetry/NCS relations between contacting molecules. The r.m.s.d. over C^α atoms between the two structures is 1.8 Å (this is half of the r.m.s.d. between C+D and A+B translated by

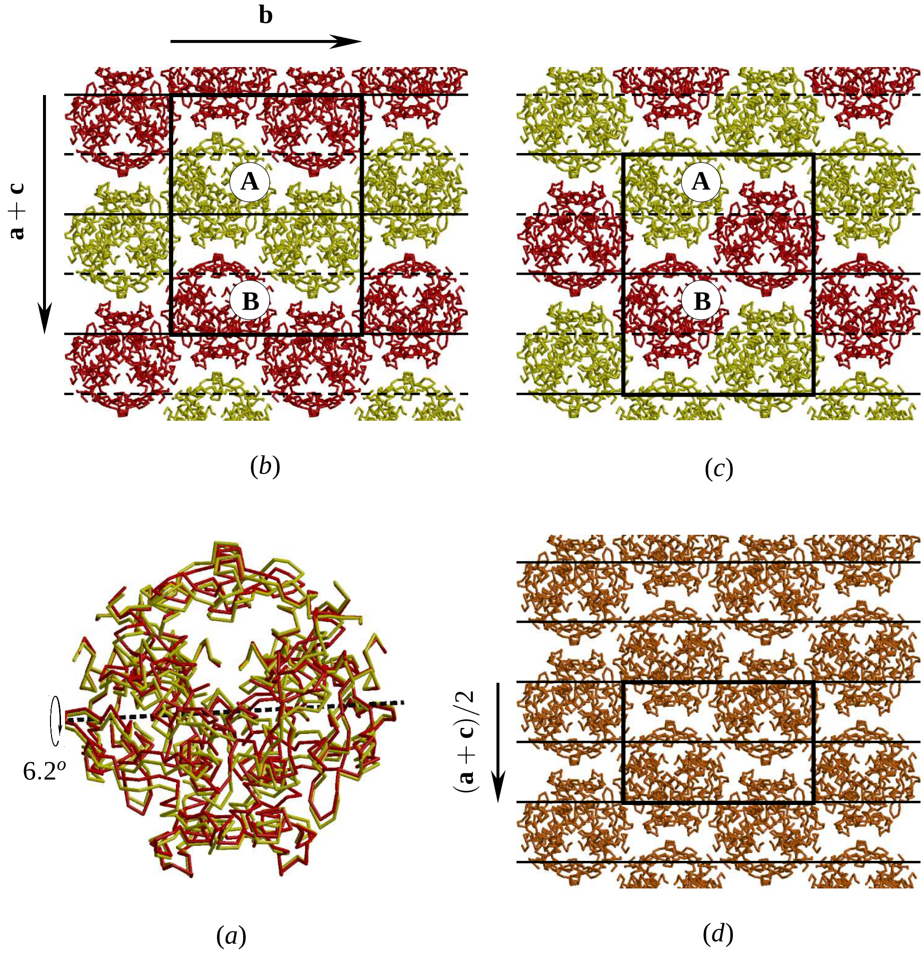

Figure 4.1. True and false-origin MR solutions of the crystal structure of anti-TRAP.

Molecules (dodecamers) are shown by C$^\alpha$ atoms. Molecules related by crystallographic symmetry are shown in the same colour. Crystallographic and NCS two-fold screw axes in (*b*, *c*,*d*) are shown by solid and dashed black lines, respectively. The unit cells are shown by thick black lines.

(*a*) Superposition of NCS related molecules A and B by translation $(\mathbf{a} + \mathbf{c})/2$. The r.m.s.d. for C$^\alpha$ atoms is 2.55 Å.

(*b*) One of two independent molecular layers of the true structure.

(*c*) A single layer of the false-origin structure. This structure belongs to the same space group and has the same unit cell parameters as (*a*), but symmetry relations between contacting dodecamers are different. Crystallographic and NCS axes are permuted in the two structures.

(*d*) A single layer of the symmetrised structure. The asymmetric unit of this layer was obtained by averaging atomic coordinates of molecule B and molecule A shifted by $(\mathbf{a}+\mathbf{c})/2$. This structure possesses higher translational symmetry and the unit cell volume is halved. All axes are crystallographic. The choice between two origins, which are equivalent in the small cell, translates into the choice between the true and false-origin structures in the large cell.

$(\mathbf{a}+\mathbf{c})/2$). The incorrect structure can also be considered as a structure in which crystallographic and NCS axes have been permuted (crystallographic symmetry became NCS and *vice versa*).

The difference between the two non-equivalent structures is small and, therefore, it is not surprising that the TF failed to select the correct one. Moreover the model of the dodecamer used in the second step of the MR (§2.2) was imperfect as it was built from the trimers aligned according to broad peaks in the SRF. The error propagated to the CRF that saw no difference between the orientations of the NCS-related dodecamers (there were no split CRF-peaks until the false-origin model had been rebuilt and refined) and further to the TF to make it insensitive to the difference between the true and false structures. The choice of the origin was in effect done when the first oligomer was positioned. The low completeness of this model further contributed to the decrease in the overall contrast in the TF. However, this is not the whole story. It may happen that a partial model, even a perfect one, gives a better correlation coefficient in a false-origin position (§4.2.5).

4.1.2 Test refinements on the two origins

A copy of the asymmetric unit of the true structure was shifted by the pseudotranslation vector $(\mathbf{a}+\mathbf{c})/2$, dodecamers A and C renamed to B and D and *vice versa*, and coordinates of corresponding atoms of the fixed and moved copies of the structure were averaged to generate the symmetrised structure presented in Fig. 4.1(*d*). The symmetrised structure belonged to the space group $P2_1$ and had a halved unit cell, as it was exactly symmetric relative to the translation $(\mathbf{a}+\mathbf{c})/2$. Accordingly, all the NCS two-fold screw axes in the true structure turned into the crystallographic axes in the symmetrised structure.

It is worth mentioning that similar symmetrised models would be in effect tested by the TF in its mode of simultaneous search for molecules related by translational NCS (§1.1.15), as long as the peaks in the Patterson map at the half of a crystallographic translation are not split (Fig. 2.2*b*). With such a search model the distinction between the two alternative structures is impossible.

Two structures with the correct unit cell were generated from the symmetrised structure, the structure with the correct origin (Fig. 4.1*b*) and the false-origin structure (Fig. 4.1*c*). The choice of the origin defines which of the two-fold screw axis is crystallographic in the large unit cell and which subsets of molecules are treated as related by crystallographic symmetry. This inevitably affects refinement: in the first case the model can converge to the correct model of the crystal structure, but in the second case such convergence is impossible.

Rigid-body refinement (22 cycles) and then restrained refinement (10 cycles) were performed for each model using *REFMAC*. Before refinements, the two structures were internally identical and effectively had a smaller unit cell. Both the true and the false symmetry constraints were satisfied in both of them. However, during the refinement, one of two sets of symmetry constraints was in effect relaxed and the two structures diverged. The *R*-factors and electron density maps of the true and false-origin structures after restrained refinements are compared in Fig. 4.2. The *R*-factors are very different and clearly indicate the correct model, whereas some

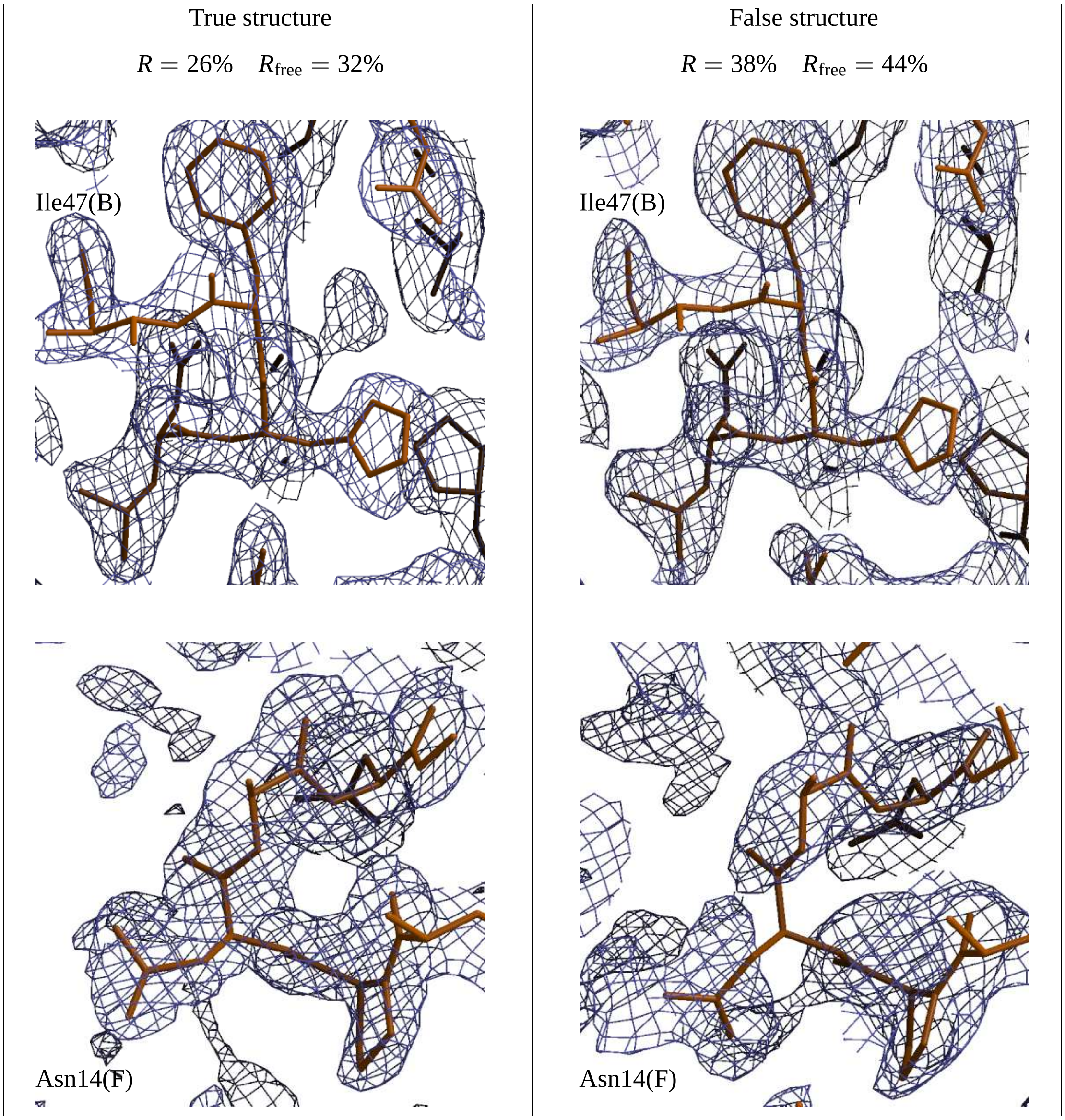

True structure
$R = 26\%$ $R_{\text{free}} = 32\%$
False structure
$R = 38\%$ $R_{\text{free}} = 44\%$
Ile47(B)
Ile47(B)
Asn14(F)
Asn14(F)

Figure 4.2. Electron density maps and *R*-factors for true and false-origin structures of anti-TRAP (Figs. 4.1*b* and 4.1*c*, respectively) after 20 cycles of rigid body refinement and 10 cycles of restrained refinement with *REFMAC* starting from the same symmetrised structure (Fig. 4.1*d*) with corresponding choice of origin. Two corresponding fragments are shown for each map at the contour level of 0.75σ. The top fragments seem to be of comparable quality, whereas there is a gap in the density for the main chain of the false-origin structure in the bottom fragment.

corresponding fragments of the two maps seem to be of a similarly good quality. However some other fragments of the electron density from the false structure are so much distorted that even the main chain atoms are not in the density. Nevertheless, the interpretable fragments of such maps can be used for partial correction of the model (§2.2.3) and may cause an impression that the model is in general correct but needs further improvement and refinement.

4.1.3 Comments on restoring the true structure

The electron density for the false structure was good enough to rebuild individual dodecamers almost to their final appearance in the actual course of structure determination. The new dodecameric search model was sufficient for the MR to distinguish between the true and false origins. However, the awareness of the possibility of false-origin solution might have simplified this work dramatically and would have saved time spent in attempts to reduce the *R*-factor by model improvement. The first step that should have been undertaken just after the MR was the comparison of two rigid-body refinements, with the MR-model and with the MR-model shifted by $(\mathbf{a} + \mathbf{c})/4$. Because of the high similarity between the search and the target proteins, it seems likely that the correct model could have been identified at this earlier stage of structure determination.

Further experiments with correction of symmetry using *Zanuda* (§4.3) showed that the series of refinements on alternative origins and space groups starting from the symmetrised model do not necessarily succeed in indicating the true structure. The same effect could be expected for a poor MR-model and, therefore, some rebuilding and refinement of false-origin structure could be a necessary step in identification of the correct structure. The experience with the anti-TRAP structure solution demonstrated that such model rebuilding and refinement are feasible. Moreover, the refinement can be performed against the reduced data corresponding to the pseudosymmetry space group with a smaller unit cell (Oksanen *et al.*, 2006, §1.1.15).

4.2 Structure solution of GAF domain of CodY

CodY protein from *Bacillus subtilis* was studied in the group of Professor Anthony Wilkinson (YSBL). The crystals of the GAF (N-terminal) domain of CodY in the apo form were grown, and the structure solved by Dr. Elena Blagova and Dr. Vladimir Levdikov (PDB code 2gx5; Levdikov *et al.*, 2009). I helped with the correction of symmetry and used this structure in further false-origin related tests.

In this case there were two possible space groups with two alternative origins in each. The correct structure was established by rigid body refinement in $P1$ followed by merging the refined structure relative to the two-fold rotations giving the smallest r.m.s.d. over C^{α} atoms. More details are given in §4.2.3.

This section presents details of the structure determination and the discussion on possible approaches to the structure correction: refinements in candidate groups and origins starting from the symmetrised structure, and MR with the dimeric and single subunit search models. The discussion is illustrated by drawings demonstrating the location of symmetry elements in four alternative structures.

4.2.1 Background

The crystal of the apo CodY GAF-domain belonged to the space group $P4_322$ with unit cell dimensions $a = 90.2$ and $c = 205.6$ Å and diffracted to 1.74 Å. The crystal had translational pseudosymmetry with translation vector $\mathbf{c}/2$ and the r.m.s.d. over the related C^{α} atoms 1.8 Å. The asymmetric unit contained four subunits.

The initial MR solution for the apo CodY GAF-domain crystal structure was found by Dr. Vladimir Levdikov. Search models were generated from the crystal structure of the CodY GAF-domain in complex with isoleucine (PDB code 2b18; Levdikov *et al.*, 2006).

The asymmetric unit of the holo-structure contained one subunit, which formed a dimer with a symmetry related molecule. After the solution of the apo-form, it was found that the dimers in the holo and apo structures were topologically identical, however, the relative orientations of subunits in the two dimers differed by 14^{o}. As a result, an attempt to solve the crystal structure of the apo form using the holo-dimer as a search model had failed.

The MR using a single subunit was successful, but it was not a trivial task because the apo and holo forms of the protein had significant conformational differences and, in addition, even the complete subunit comprised only a quarter of the asymmetric unit in the crystal of the apo form. Various options of *MOLREP* were tried with different truncated versions of the subunit. One of the MR runs in $P4_122$ gave a structure formed by dimers topologically similar to dimers in the holo structure. A significant drop of R_{free} during the initial refinement with *REFMAC* and interpretable electron density were additional evidences in favour of this solution. The electron density was good enough to partially correct the model. However the refinement stalled at an *R* factor of about 0.38 and it became clear that this was a false solution.

4.2.2 Organisation of the true and false structures

At this point of the text, it seems suitable to describe the final structure and to characterise possible false MR-solutions. A similar analysis was performed in the actual course of structure determination to understand which alternative structures were to be tested.

The molecular packing is presented in Fig 4.3(*a*). The crystal is formed by cylindrical assemblies of molecules spanning the whole crystal in the **c** direction. The approximate symmetry of a single cylinder includes an eight-fold screw axis along and a two-fold axes orthogonal to **c**. One quarter of all symmetry operations of the cylinder are crystallographic operations in the three-dimensional crystal.

Two drawings in Fig. 4.3(*b*) show two neighbouring slices of a single cylinder, such that each slice include a pair of biological dimers residing on the same NCS two-fold axis. The

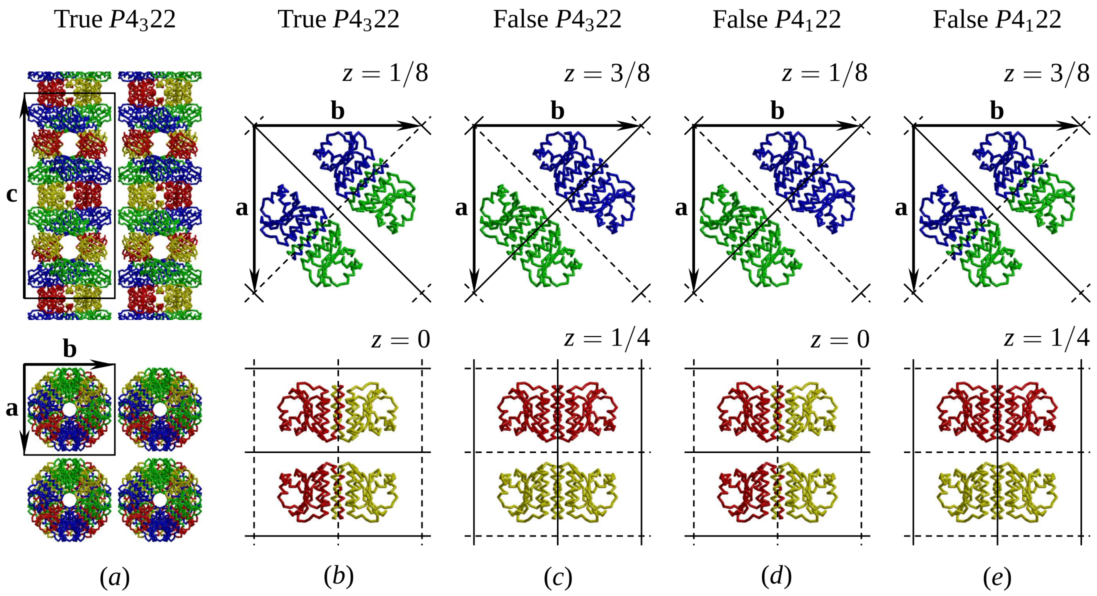

Figure 4.3. Crystal structure of GAF domain of CodY and associated false structures.
(*a*) Overall organisation of the crystal. The unit cell is shown in magenta.
(*b*) Two slices of the molecular cylindrical assembly, each slice containing a pair of dimers residing on the same NCS axis and related by a crystallographic two-fold rotation.
(*c*,*d*,*e*) Reassignments of crystallographic axes (solid black lines) and NCS axes (dashed black lines) result in three possible false structures.
In all panels of this figure, the subunits related by crystallographic symmetry are shown in the same colour and NCS translation **c**$/2$ relates red to yellow and green to blue substructures.

dimers in the pair are related by the crystallographic two-fold axis in the plane of the drawing and by the NCS two-fold axis orthogonal to this plane. The adjacent pairs of dimers are rotated relative each other by 45^o. Thus the crystallographic axis makes a half-turn by the fifth pair, so the first and the fifth pairs are related by an NCS translation of $\mathbf{c}/2$ and eight pairs span the unit cell.

Letting the axes in the bottom drawing of Fig 4.3(*b*) exchange their crystallographic nature, *i.e.* letting the crystallographic axes become NCS and *vice versa*, results in a different structure shown in Fig 4.3(*e*), which however would have the same unit cell parameters and pseudosymmetry space group as the original structure. All structures related by such permutations of the crystallographic and NCS axes can be enumerated by considering two adjacent pairs of dimers, as the crystallographic axes relating the subunits in these pairs (plus translation **a**) are generators of the space group. Two possibilities for each of two pairs result in four possible structures belonging to two different space groups $P4_122$ and $P4_322$ (Figs. 4.3*b*-*e*). The origin for a given combination of crystallographic axes is defined by the standard setting of the corresponding space group.

Therefore, similarly to the anti-TRAP case, the presence of translational pseudosymmetry in this example creates a potential for false MR-solutions. In particular, a false-origin MR-solution is possible in the true $P4_322$ space group (Fig. 4.3*c*). In addition, two false MR-solutions are possible in the enantiomorphic space group $P4_122$ (Figs. 4.3*d* and 4.3*e*). A particular solution can be identified by the crystallographic nature of the two-fold axes relating the subunits in the biological dimers. In practice this can be done by examining the four subunits forming the asymmetric unit using molecular graphics, *e.g. Coot*. The number of subunits making the biological dimer with their own symmetry equivalents and, if this number equals two, the orientations of such subunits uniquely define one of the four possible structures shown in Fig. 4.3, where this number equals zero, four, two and two in (*b*), (*c*), (*d*) and (*e*), respectively. Such an analysis was used to identify the solutions obtained in the test MR runs.

4.2.3 Structure correction using refinement in *P*1

Rigid body refinement in the *P*1 space group followed by the restoration of the higher symmetry seemed a promising technique from the point of view of automation of the false structure correction in the general case. Therefore, this method was used in the actual course of the structure solution of the CodY GAF-domain.

The $P4_122$ model and the data were transformed into a smaller unit cell ($\mathbf{c}' = \mathbf{c}/2$, space group $P4_222$) to produce a synthetic structure, in which all the axes shown in Fig. 4.3(*b*) (both crystallographic and NCS) were crystallographic. The next step was restrained refinement of the synthetic structure. This was done to eliminate influence of wrong crystallographic constraints, *i.e.* to move the structure away from the local minimum of the false solution, towards the structure, which equally well matches all four alternative structures (Figs. 4.3*b*-*e*).

The refined structure was expanded into $P1$ with correct cell dimensions and rigid body refinement was performed to drop the R-factor from 0.64 to 0.38. After that, the potential crystallographic axes (Fig. 4.3) were tested by visual inspection of the overlap between the structure and the copy rotated by the tested operation. The transformations were performed by matching two subunits using *LSQKAB* (Collaborative Computational Project, Number 4, 1994). *Coot* (Emsley & Cowtan, 2004) was used to visualise overlapping structures. The axes giving the best overlap (visually this overlap was almost exact) suggested the organisation of the crystal as illustrated in Figs. 4.3(*a*) and 4.3(*b*). The redundant molecules were removed and the new structure was transformed into and further refined in the space group $P4_322$.

In effect, the method used here allowed testing of more than the four alternative structures shown in Fig. 4.3. It also ruled out the possibility of lower symmetry and twinning, which was hard to reject with confidence from the twinning tests likely affected by pseudosymmetry. This was done at the expense of some extra manual work at the stage of testing the potential crystallographic operations, but this was an acceptable price for the confidence in the correct symmetry assignment.

4.2.4 Structure correction using the MR with a dimeric model

It is typical to start the MR trials from the available oligomeric models. In this particular case, the trials with the holo-dimer failed owing to significant conformational differences between the holo- and apo-dimers. Interestingly if these attempts were successful, the correct structure would be found and the potential problem with the false MR-solution would not be noticed. Indeed, the only configuration in which the asymmetric unit can be assembled from complete dimers is the correct one shown in Fig 4.3(*b*). Furthermore, a dimer from the refined false-origin structure could have been used as a search model. In $P4_322$ it gave a CC of 0.45 for the correct structure *vs.* the second best CC of 0.32, whereas in $P4_122$ the best CC was 0.35. Note, however, that such high contrast is only because of the packing constraints and it would have arisen even if the configuration in Fig. 4.3(*b*) were incorrect. Had the correct configuration been any other than that in Fig. 4.3(*b*), such an approach would only replace one false solution by another. Because the CodY GAF-domain structure was a particularly difficult case for refinement owing to high flexibility of the protein, it was important to have confidence in the symmetry and origin assignment, but this could not be gained with this method.

In general, the presence of translational pseudosymmetry makes any oligomeric search models vulnerable to false MR-solutions. If such model is used as a search MR-model, then space group or origin correction may need to be considered at some point of structure refinement. The crystal structure of human deoxycytidine kinase (§1.2.3, Elisabetta Sabini, personal communication) is an example of a crystal with pseudotranslation, in which two of four symmetry-independent subunits form a single dimer and two other subunits form dimers with their symmetry mates, so a configuration with two complete dimers in the asymmetric unit must be a false structure.

Note, however, that in the case of anti-TRAP (§4.1), the asymmetric unit of the pseudosymmetry space group contained two complete dodecamers and the use of dodecameric search model derived from the refined false-origin structure in the second round of the MR was a valid procedure in the sense that it did not *a priori* reject any of the possible configurations. Moreover, even if one of the two-fold axes of the dodecamer were aligned with the crystallographic two-fold axes, this procedure would remain valid, as long as the crystallographic axes were screw axes. In other words, from the point of view of origin correction, the MR-search with the dodecameric model in the case of anti-TRAP is the analogue of the MR-search with a single-subunit model in the case of CodY GAF-domain. The problems associated with the "single-subunit" search model are discussed below.

4.2.5 Structure correction using the MR with single-subunit model

Table 4.1 presents the results of the MR searches for the first copy of the CodY GAF-domain (no fixed partial model) with two search models, a single subunit from the refined false structure and subunit A from the final structure deposited in the PDB. Two runs of *MOLREP* were performed for each model and for each of two possible space group, a run in the "single model" mode and a run in the "double model" mode, which implicitly deals with the model composed of two subunits related by NCS translation (§1.1.15). The position of the first found molecule relative to the crystallographic axes defines the positions of the remaining molecules. Therefore, these data are sufficient to identify which configuration is going to be found at the end of the one-by-one MR search for four subunits.

It may seem strange that in the "single-model" search the best CC is higher in $P4_322$ (0.273) than in $P4_122$ (0.253) for the search model refined in the incorrect $P4_122$. However, these are the correlations for the first subunit found, whereas the model refined in $P4_122$ was complete and contained four subunits. Moreover, the refined model was partially rebuilt and was much closer to the final than to initial model. The best CC for the complete MR solutions was almost the same in the two space groups (0.458 in $P4_322$ *vs.* 0.457 in $P4_122$) because both solutions were incorrect, the one in the correct $P4_322$ being a false-origin solution defined by incorrect position of the first subunit found. A bias toward $P4_122$ was only revealed in the CC for the true TF solution in the "single model" mode (column *b* in Table 4.1). It ranks second among all the TF peaks shown for the final model but only fourth for the refined model.

This effect can be explained as follows. The cross-vectors between two given subunits are enhanced in the experimental Patterson map by corresponding vectors from the subunits related by NCS translation to the first pair. However, the closer the subunits are, the more consistent cross-vectors are generated. Accordingly, the most favourable (in terms of CC) position for the single subunit (among the sensible positions) is where it is closest to its symmetry mate, that is, in the symmetry-generated dimer. Indeed, the subunit in the highest-score solution was found in such a position. On the contrary, such a position did not exist in the true structure, in which all dimers were formed by independent subunits. This consideration also explains why the initial MR-solution of CodY GAF-domain was found in the incorrect space group, while the same model, or any other, gave no solution in the correct space group.

As it was mentioned in the anti-TRAP section, the "double-model" TF in the case of two-fold pseudotranslation effectively tests symmetrised structures with two times smaller cells and makes no distinction between crystallographic translation and pseudotranslation. Accordingly, it returned the same CC for all four possible configurations (Table 4.1). In effect, the "double-model" TF ignores all reflections with *l* odd and is equivalent to the "single-model" TF in two

Space group	$P4_322$			$P4_122$		
Figure	(*b*)	(*c*)	–	(*d*)	(*e*)	–
Model refined in $P4_122$						
Single-model TF CC	0.249	0.273	0.233	0.253	0.252	0.226
Double-model TF CC	0.343	0.343	0.296	0.343	0.343	0.296
Final model						
Single-model TF CC	0.277	0.297	0.228	0.274	0.276	0.224
Double-model TF CC	0.369	0.369	0.315	0.369	0.369	0.315

Table 4.1. MR with the single-subunit models of CodY GAF-domain, one taken from the refined false structure and the other from the final model (PDB code 2gx5).

For each of two search models, the MR was performed in the two enantiomorphic space groups and with two modes of the TF, the "single-model" mode and "double-model" mode.

The correlation coefficients (CC) are presented for the three top TF solutions for the first molecule to be positioned ("single-model" mode) or for the first pair of molecules ("double-model" mode). For two top peaks, entries (*a*), (*b*), (*c*) and (*d*) relate to the corresponding panels of Fig. 4.3. The third peak is the highest background peak.

times smaller cell and with reduced data set. With this mode of the TF, the choice between alternative configurations is explicitly postponed till subsequent refinement.

These tests simply underline the fact that the MR produces preliminary results that should be confirmed by subsequent refinement and it is not the MR but refinement that should be considered for making the final choice between several close structures.

4.2.6 Structure correction using refinements of alternative structures

If the possibility of twinning is ignored, then there are only four structures to test by refinement and there is no need to reduce the model and the data into $P1$ or any other space group and to change the orientation of the whole structure.

Table 4.2 presents the results of rigid-body and restrained refinements of these four structures. In all four cases, the starting R-factor in the rigid-body refinement was 0.63. The final R-factors clearly indicated the correct structure (Fig. 4.3*b*).

The starting models for the refinements were generated as follows. The “double-model” MR was completed in the $P4_122$ space group for the subunit from the refined false structure. The output model contained two pairs of subunits related by NCS-translation $\mathbf{c}/2$. Such an asymmetric unit can be “docked” into any of the four tested configurations without overlaps between symmetry related subunits (this is not so for the asymmetric unit containing, for example, a complete dimer). Therefore, the first starting model was the MR model, the second model was a copy of the first one with $P4_122$ replaced by $P4_322$ in the header of the coordinate file (an extra MR run in $P4_322$ could be performed instead), and the third and the fourth models were copies of the first two shifted by $\mathbf{c}/4$ using *LSQKAB*.

Space group	$P4_322$	$P4_322$	$P4_122$	$P4_122$
Figure	(*b*)	(*c*)	(*d*)	(*e*)
	true	false	false	false
Rigid body refinement				
R	0.44	0.52	0.48	0.48
Restrained refinement				
R	0.30	0.40	0.38	0.38
R_{free}	0.38	0.50	0.47	0.46

Table 4.2. Refinements of the crystal structure of CodY GAF-domain and three associated false-origin/enantiomorph structures. In each case, reference is made to the corresponding panel of Fig. 4.3. Rigid-body refinements started from effectively the same symmetrised structure and restrained refinements started from the models after rigid body refinements.

This protocol is easy for both manual implementation and automation, as the asymmetric unit is neither expanded nor reduced and its orientation remains the same in the tested structures. However, the automated procedure of symmetry correction may need to be more general and able to deal with pseudosymmetric twins and to restore the crystallographic symmetry of a structure refined in lower space group.

4.2.7 Concluding remarks

The cases of anti-TRAP, CodY GAF-domain and UDP-glucose 4-epimerase (PDB code 2c20; Au *et al.*, 2006, not included in this thesis), as well as the examples of incorrect space group assignment from the PDB (§3.2.4) suggested that a program that would automatically verify the symmetry and origin assignments and correct them if necessary might be useful.

The method of structure correction that involved refinement in $P1$ performed well in the cases of CodY GAF-domain and UDP-glucose 4-epimerase and seemed suitable for a variety of pseudosymmetry cases and for cases with incorrectly assigned space group. In effect, this approach allows evaluation of all possible subgroups of the pseudosymmetry space group, so, in particular, it is able to distinguish between pseudosymmetry interfering with twinning and higher symmetry, as well as between true and false origins. The automation of this approach required a program determining (pseudo)symmetry space group of the structure defined in $P1$ and evaluating potential crystallographic operations in such a structure. Such a program was written and is discussed in the next section.

4.3 *Zanuda*, a program for symmetry validation and correction

The program *Zanuda* presented in this section is designed to validate and correct symmetry and origin assignments. It was developed in the group of Dr. Murshudov (YSBL); I wrote the *FORTRAN* routines and combined them with a *tcsh*-script, and Dr. Paul Young developed a *Java*-interface for the YSBL-software web-server (http://www.ysbl.york.ac.uk/YSBLPrograms/).

Three types of target cases are characterised, then the current version of the program is demonstrated using the test cases of CodY GAF-domain (§4.2) and, finally, some technical details of the program and possible improvements are discussed.

4.3.1 Target cases

The first class of cases that *Zanuda* is designed for includes the structures with translational pseudosymmetry, such as anti-TRAP (§4.1) and the CodY GAF-domain (§4.2), in which false MR-solutions are possible with the same point group symmetry and unit cell parameters as in the true structure. The warning signs are high *R*-factor and the presence of significant peaks in the Patterson map corresponding to a rational fraction of crystallographic translation.

The untwinned cases with incorrectly assigned lower symmetry constitute the second target class. A large number of such cases were found during the search for twins in the PDB using RvR scatter plot (§3.2.4). This type of mistake does not affect significantly and may even slightly improve the refinement statistics. One of the reasons for such mistakes is that high *R*-factors from a false-origin MR solution has been erroneously interpreted as an indication of twinning.

The third class includes twinned cases with interfering NCS and with an incorrectly assigned higher symmetry. An example is presented in the next section (§4.4), the crystal structure analysis of oxidoreductase from *Thermotoga maritima*.

4.3.2 *Zanuda* run with test case

The pseudosymmetry operation is a global operation on a given structure, which matches related molecules with a high accuracy but not exactly. The pseudosymmetry space group (PSSG) of a given structure is a space group that includes all exact symmetry operations and all pseudosymmetry operations on the structure.

For example, the crystal structure of the GAF-domain of CodY (§4.2) belongs to the space group $P4_322$ with $a = 90.2$ and $c = 205.6$ Å. The PSSG is generated by pseudotranslation $\mathbf{c}/2$. Therefore the PSSG is $P4_222$ with the same a as in the true space group and c halved.

Zanuda handles a set of subgroups of the PSSG (details are in §4.3.3). Different subgroups may belong to the same abstract space group and are therefore assigned an internal reference number. In the current example, the PSSG has Ref 35 (Figs. 4.4 and 4.5).

```
Step 1.
---------------------------------------------------------------------
| Subgroup | Spacegroup | R.m.s.d. |   Refinement in tested group   |
|          |            | from the |--------------------------------|
|   Ref    |            | starting |  Rigid   |      Restrained     |
|          |            | model, A |----------|---------------------|
|          |            |          |    R     |    R     |  R-free  |
|----------|------------|----------|----------|----------|----------|
| >>  10   | P 41 2 2   |  0.0003  |    --    |  0.3808  |  0.4585  |
| <<  35   | P 42 2 2   |  0.6756  |    --    |    --    |    --    |
^^^^^^^^^^^^^^^^^^^^^^^^^^^^^^^^^^^^^^^^^^^^^^^^^^^^^^^^^^^^^^^^^^^^^
Step 2.
^^^^^^^^^^^^^^^^^^^^^^^^^^^^^^^^^^^^^^^^^^^^^^^^^^^^^^^^^^^^^^^^^^^^^
| >>  35   | P 42 2 2   |  0.6756  |    --    |    --    |    --    |
---------------------------------------------------------------------
|      1   | P 1        |  1.0868  |  0.3534  |  0.2926  |  0.3658  |
|      2   | C 1 2 1    |  1.0849  |  0.3553  |  0.2941  |  0.3692  |
|      3   | P 1 21 1   |  1.0851  |  0.3571  |  0.2944  |  0.3648  |
|      5   | C 2 2 21   |  1.0841  |  0.3600  |  0.2973  |  0.3721  |
|      6   | P 1 2 1    |  0.2069  |  0.4092  |  0.3710  |  0.4543  |
|      7   | P 41       |  0.7583  |  0.4210  |  0.3677  |  0.4399  |
|      9   | P 2 2 21   |  0.2051  |  0.4149  |  0.3754  |  0.4575  |
|     10   | P 41 2 2   |  0.1828  |  0.4181  |  0.3779  |  0.4618  |
|     11   | P 1 2 1    |  1.0865  |  0.3566  |  0.2951  |  0.3677  |
|     14   | P 1 2 1    |  0.9723  |  0.4340  |  0.3857  |  0.4711  |
|     16   | P 2 2 2    |  0.9713  |  0.4478  |  0.3938  |  0.4835  |
|     17   | C 1 2 1    |  0.9965  |  0.4215  |  0.3776  |  0.4555  |
|     19   | C 2 2 2    |  0.9753  |  0.4442  |  0.3885  |  0.4768  |
|     22   | C 2 2 21   |  0.9949  |  0.4284  |  0.3805  |  0.4615  |
|     26   | P 2 2 21   |  1.0861  |  0.3619  |  0.2989  |  0.3701  |
|     29   | P 41 2 2   |  0.9895  |  0.4305  |  0.3815  |  0.4578  |
|     31   | P 43       |  1.0844  |  0.3573  |  0.2948  |  0.3660  |
|     32   | P 43 2 2   |  1.0841  |  0.3656  |  0.3017  |  0.3771  |
|     34   | P 43 2 2   |  0.9599  |  0.4566  |  0.4007  |  0.4913  |
---------------------------------------------------------------------
| <<   3   | P 1 21 1   |  1.0851  |  0.3571  |  0.2944  |  0.3648  |
^^^^^^^^^^^^^^^^^^^^^^^^^^^^^^^^^^^^^^^^^^^^^^^^^^^^^^^^^^^^^^^^^^^^^
Step 3.
^^^^^^^^^^^^^^^^^^^^^^^^^^^^^^^^^^^^^^^^^^^^^^^^^^^^^^^^^^^^^^^^^^^^^
| >>   3   | P 1 21 1   |  1.0851  |  0.3571  |  0.2944  |  0.3648  |
---------------------------------------------------------------------
|      1   | P 1        |  1.0876  |  0.3498  |  0.2927  |  0.3659  |
|      3   | P 1 21 1   |  1.1023  |    --    |  0.2880  |  0.3699  |
|     26   | P 2 2 21   |  1.1112  |    --    |  0.2905  |  0.3750  |
|     32   | P 43 2 2   |  1.1119  |    --    |  0.2921  |  0.3783  |
---------------------------------------------------------------------
| <<  32   | P 43 2 2   |  1.1119  |    --    |  0.2921  |  0.3783  |
---------------------------------------------------------------------
```

Figure 4.4. Correction of the space group assignment for the crystal structure of GAF-domain of CodY.

This figure shows the summary file of *Zanuda*. The input structure Ref 10 was symmetrised and transformed into the PSSG, Ref 35 (Step 1), refined in candidate subgroups (Step 2) and transformed into the correct space group, Ref 32 (Step 3). The input and output for a given step are marked by “>>” and “<<”, respectively. All shown subgroups have equivalent lattices except for the PSSG, which has the parameter **c** halved.

The three steps are explained in §4.3.2 and §4.3.3 in more detail. Some of the subgroups are shown in the subgroup-supergroup graph in Fig. 4.5(*a*). Step 3 is further explained in Fig. 4.5(*b*).

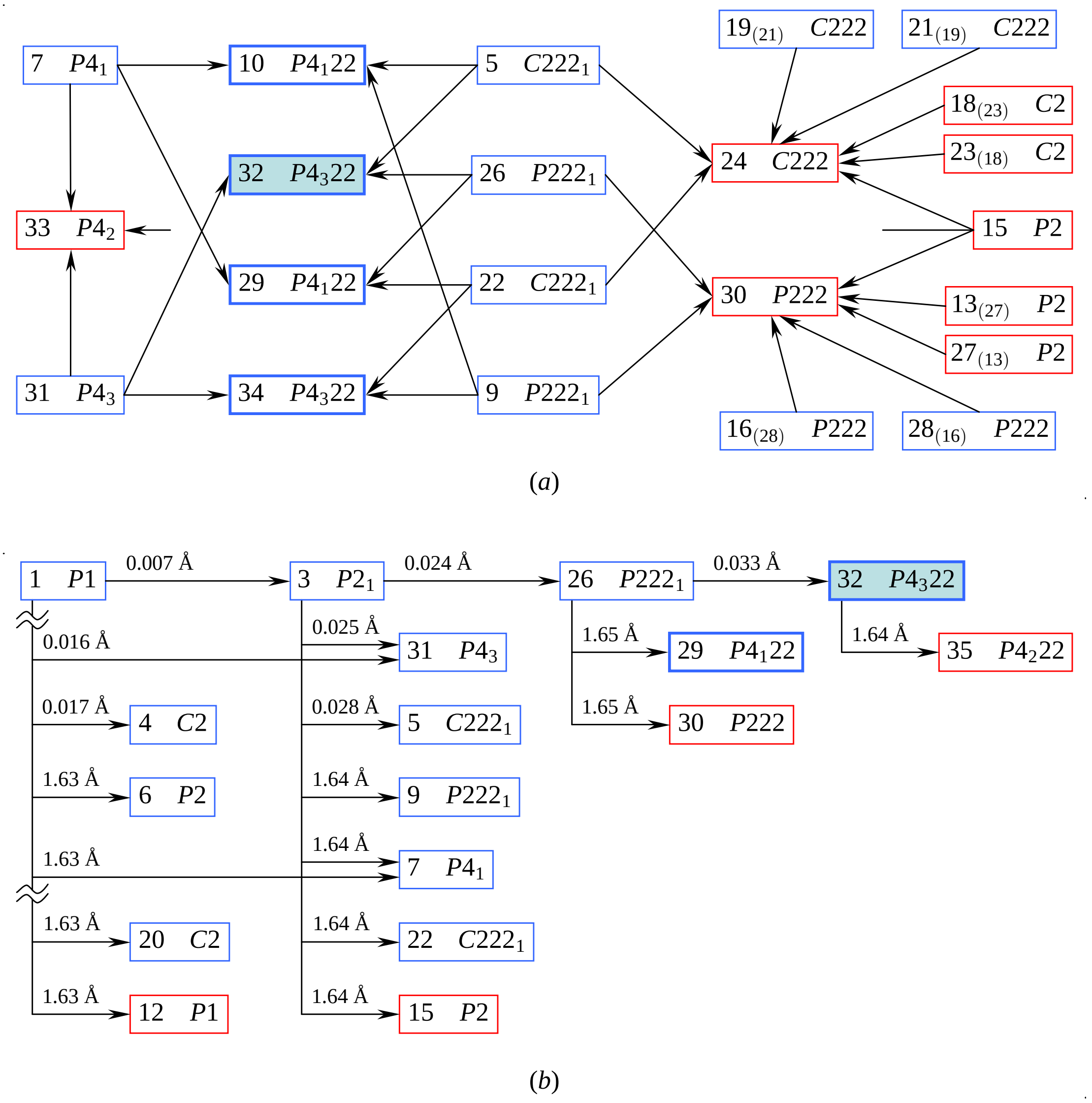

Figure 4.5. Pseudosymmetry of CodY GAF-domain crystal (§4.2).

(*a*) A fragment of the infinite subgroup-supergroup graph for pseudosymmetry $P4_222$ with translation basis $(\mathbf{a},\mathbf{b},\mathbf{c}/2)$. Only those subgroups are shown, which have (i) translation basis $(\mathbf{a},\mathbf{b},\mathbf{c}/2)$ (red frames) or translation basis $(\mathbf{a},\mathbf{b},\mathbf{c})$ (blue frames) and (ii) 4 or 8 times more operations than $P1$ with the basis $(\mathbf{a},\mathbf{b},\mathbf{c})$. Subgroups in red boxes include pseudotranslation $\mathbf{c}/2$ and disagree with experimentally observed reciprocal lattice. The basis $(\mathbf{a},\mathbf{b},\mathbf{c})$ and 8 times more operations occur in four subgroups (thick blue frames) including the true subgroup (blue background). Corresponding four structures are shown in Fig. 4.3. Arrows are directed from subgroups (4 times more operations) to their supergroups (8 times more operations). An equivalent subgroup (§4.4.4), if exists, is shown by subscript in brackets.

(*b*) Determination of the correct space group using *Zanuda*. The top row represents the path in the graph that the sequence of refinements in Step 3 in Fig. 4.4 followed. Below this row, the branches are shown, which were tested and rejected because of incorrect translation basis or higher r.m.s.d. (the numbers above the arrows) between the symmetrised structure and its precursor. Both figures were generated using the verbose output from *Zanuda*.

The protocol for correction of the space group assignment is demonstrated using the crystal structure of GAF-domain of CodY. The input model was the false-enantiomorph structure (Fig. 4.3*e*). The protocol included three steps (Figs. 4.4 and 4.5).

Several actions on the input model were performed at Step 1. In particular, the PSSG was identified and the space group of the input model was assigned (Ref 10). In this particular case the input model was not truncated as it contained identical subunits and no solvent. Manipulations with the input model in a general case are discussed in §4.3.3. The R and R_{free} for the input model (modified in a general case) were reported as a reference, to be compared with the final R-factors. The model was transformed by the operations from the PSSG and the coordinates of related atoms were averaged to generate a symmetrised model belonging to the PSSG (Ref 35). The r.m.s.d. over C^{α} atoms (these would be P-atoms for the DNA chains) between the symmetrised and input models was reported. The X-ray data were expanded into point group 1.

Step 2 was a series of refinements in selected subgroups of the PSSG. Two selection criteria were applied. A subgroup was selected, if (i) it had the same translational basis as the input model and (ii) was not equivalent to a previously selected subgroup relative to the actual point group of the data. The first criterion ensured that the translational crystallographic symmetry of the model agreed with the experimentally observed one, see Figs. 4.4 and 4.5. (Therefore the PSSG is the only subgroup shown in Figs. 4.4 that has a reduced cell.) The second selection criterion was used to reject redundant subgroups (details are in §4.4.4). In all refinements, the starting models were generated by expansion of the symmetrised model into lower-symmetry space group and therefore were internally identical. The X-ray data expanded at Step 1 were reduced into the asymmetric unit of the corresponding point group by averaging related intensities. The protocol of twelve cycles of rigid body refinement against 3 Å resolution data and 24 cycles of restrained refinement against all data had been adopted after tests with several structures selected from the PDB.

The structure with the best R_{free} in Step 2 (Ref 3) was selected for Step 3. It was expanded into $P1$, refined and symmetry elements were added one by one with a round of refinements after each addition. The symmetry operation to be added next was one of the operations unused in the last refined structure. The selection criterion was the minimum r.m.s.d. over C^{α} atoms between the refined structure and its copy transformed by the tested operation. The sequence of refinements was terminated when no symmetry element could be added without reducing the size of the unit cell. As an illustration, Step 3 for the CodY GAF-domain structure is presented in Fig. 4.5(*b*) as a path in the subgroup-supergroup graph. The result of Step 3 was a sequence of subgroups, each of them scored by R_{free} after rigid body and then restrained refinements. A large jump in R_{free} would indicate that selection of the next subgroup in the sequence was not justified and its precursor would be accepted as the likely true space group of the structure in question. If no jump in R_{free} occurred (Fig. 4.4), the last subgroup in the sequence was accepted.

There were several structures in Step 2 giving R_{free} very similar to the best value (Ref 3). However, this ambiguity is not a problem, as all these structures belonged to subgroups of the true space group (Ref 32) and any of them would have given the correct solution in Step 3. The actual problem is to have at least one structure converged to the right minimum (§4.3.4).

4.3.3 Preparation and transformations of the model

Step 1 in Fig. 4.4 includes modification of input model and definition of the PSSG, all its subgroups and transformations between the subgroups. In order to clearly define the asymmetric units of the subgroups and transformations between them, the model is truncated to a set of compact and chemically identical subunits composed of one or more polypeptide or DNA chains. These subunits are also treated as rigid groups in rigid body refinements. The PSSG is defined to include all operations of the crystal space group and the NCS operations satisfying the limit of 3 Å for the r.m.s.d. between the modified model and its pseudosymmetry-related copy. This limit was chosen based on the expected radius of convergence of rigid body refinement. These procedures are described below in more detail.

In particular, paragraphs (i) and (ii) below describe a model modification procedure which allows handling of input models comprising identical chains with different gaps, hetero-oligomers composed of two or more different chains as in the twinned pseudosymmetric PDB entry 1upp, as well as the *SHELXL* output, in which the chains are defined by gaps in residue numbering, not by chain identifiers. With minor modification, the described algorithm is suitable for handling ligands if present, but this option has not yet been implemented. Further development may include merging subunits into oligomers to define biologically sensible asymmetric units in the subgroups of the PSSG. Subsequent paragraphs explain determination of (iii) the PSSG, (iv) its subgroups and, for all of them, (v) the space group names and transformations to the standard settings. The last two paragraphs describe how the transformations between the subgroups are (vi) stored and (vii) applied to a model belonging to a particular subgroup.

(i) The solvent and hydrogen atoms are removed before the total sequence of residues constituting the asymmetric unit is aligned with itself using a slightly modified version of the algorithm by Needleman & Wunsch (1970). The large off-diagonal values in the score matrix indicate matching fragments of the total sequence. The total sequence is thus cut into segments of several types, the segments of the same type having the same sequence of residues. Atoms missing in one segment are also removed from the other segments of the same type. The atoms belonging to the segments of a given type are counted. The segment type containing maximum number of atoms is used as a reference type. If the number of segments belonging to any other type is not the same as in the reference type, then all segments of this type are removed. At this point, the numbers of segments in all the types are equal and the segments of the same type have identical chemical composition.

(ii) The segments are merged into subunits using a clustering algorithm. The entities to cluster are the types of identical segments. The reciprocal distance between two types is the number of identical interatomic contacts shorter than 3 Å made by all the pairs of corresponding segments from the two types. (The correspondence between segments is also found using clustering algorithm.) There could be more than one distance between two types owing to the contacts with symmetry related segments. The shortest distance and corresponding symmetry operations are used when two types and their segments are merged. Other distances are recalculated to include contacts with both precursors of the new joint type. At the end of this procedure, all segment types are merged into a single type or into several types with no conserved contacts between them. In the latter case, the type including the reference type is preserved, the others are removed. At this point the atomic model consists of chemically identical and spatially compact subunits, which can be used to define asymmetric unit of the PSSG and as rigid groups in rigid body refinement.

(iii) The PSSG is defined as follows. The (approximate) rotational lattice symmetry is examined using the procedure described in §3.2.1. The coset decomposition of the rotational point group of the lattice relative to the point group of the crystal is performed. The representatives of the cosets are tested to find out if they are rotational components of the operations from the PSSG. To check this, one copy of the structure is fixed and the second copy is rotated by the representative operation and translated to best fit the fixed copy. If there remain subunits in the fixed structure having no counterpart in the moved structure, or the overall match between the two structures is worse than the tolerance limit, the rotation operation is rejected. If the operation passes the test, it becomes an element of the PSSG with the translation component defined during the test. When all representatives are tested, the set of operations is assembled containing all operations of the input space group and the operations that passed the test. This set of operations is expanded to a group using multiplication, that is, if a product of two operations already belongs to the set, then it is ignored, else it is added to the set. The resultant space group is the PSSG.

(iv) The subgroup structure of the PSSG is represented as a table with rows representing subgroups and columns representing elements of the PSSG (Table 4.3). An element expands a subgroup to another subgroup. Accordingly, each table cell contains the reference to a row. If the cell refers to the row it belongs to, then the column represents an element of the subgroup represented by the row. The table is generated starting from the first row representing subgroup containing only the identity element ($P1$ with original unit cell parameters). The element and the subgroup represented by the current cell are multiplied and expanded. If the resultant subgroup is not present in the table the new row is added. The reference to the resultant subgroup is stored in the current cell. The procedure is terminated, when the last row is reached and no new rows are generated when it is scanned. The subgroups containing pure translations and therefore corresponding to a smaller unit cell are found and marked to exclude them from the series of refinements in Step 2. Also, the classes of subgroups relative to the point group of the data are found and only one from each class is tested by refinement in Step 2.

(v) At this point each subgroup is defined by its operations and requires identification. This is done using a procedure which analyses the input group of operations, calculates an identification index and defines the transformation from the current to a reference setting. Both the index and the reference setting depend only on the space group (not yet identified), to which the input group of operations is equivalent. This procedure is applied to the space group definitions in the symmetry library to produce the indices for all the space groups of interest ("biological" space groups), as well as the transformation operations X from the standard library settings to the reference settings. The procedure is also applied to a given subgroup to produce its index and transformation Y to the reference setting. The subgroup inherits its name from the library space group with the same index and the transformation to the standard library setting is defined as $Y^{-1}X$.

Subgroup reference number	Space group	Shorter basis vector	Reference to subgroup			
5	$P2_1$	$(\mathbf{a}+\mathbf{c})/2$	5	5	5	5
4	$P2_1$	–	4	5	5	4
3	$P1$	$(\mathbf{a}+\mathbf{c})/2$	3	5	3	5
2	$P2_1$	–	2	2	5	5
1	$P1$	–	1	2	3	4
Classes of operations			c_1	c_2	c_3	c_4

Table 4.3. Subgroup table for anti-TRAP crystal structure (Fig. 4.1).

The subgroup of true translations divides the operations of the PSSG into four classes, (c_1) translations $(i\mathbf{a}+j\mathbf{b}+k\mathbf{c})$, ($c_2$) screw two-fold rotations about the axes at $(i\mathbf{a}+k\mathbf{c})/2$, ($c_3$) translations $(\mathbf{a}+\mathbf{c})/2+(i\mathbf{a}+j\mathbf{b}+k\mathbf{c})$ and (c_4) screw two-fold rotations about the axes at $(\mathbf{a}+\mathbf{c})/4+(i\mathbf{a}+k\mathbf{c})/2$, where i, j and k are integer numbers. The union of a given class and a given subgroup of the PSSG expands to a subgroup of the PSSG referred to in the corresponding table cell.

(vi) The subgroups names and transformations to the standard setting are stored in an auxiliary file and can be accessed through the subgroup reference number. To simplify the transformations between subgroups, the asymmetric units of all the subgroups are also defined in advance; the PSSG operations, one per subunit, transforming the asymmetric unit of $P1$ into the asymmetric unit of given subgroup are stored in the auxiliary file. This approach also requires that the subunits are stored in the coordinate files in a particular order. In addition, the asymmetric units of all subgroups are made reasonably compact and located close to the origin to ensure convenient representations in the graphical programs.

(vii) The routine that transforms the structures from one subgroup to the other has two modes. In the first mode it reads two numbers, the "from" subgroup number and the "to" subgroup number, the coordinate file corresponding to the "from" subgroup and the auxiliary file. Using the transformations stored in the auxiliary file it expands the asymmetric unit into $P1$ and then transforms each subunit into the equivalent position in the asymmetric unit of the "to" subgroup. Coordinates of all subunits at the same position are averaged and the total r.m.s.d. is reported. New coordinates are saved. In the second mode, the "to" subgroup number is not defined, so the routine tests operations from the PSSG, which are not present in the "from" subgroup (actually it tests coset representatives), to find one giving the lowest r.m.s.d. between the input and symmetrised structures. The "from" subgroup and this operation define the "to" subgroup. If the required operation does not exist, then no output file is created. The first and the second modes are used in Step 2 and Step 3 in Fig. 4.4, respectively.

4.3.4 Starting model and refinements

In the first version of *Zanuda*, the input model was symmetrised (Step 1 in Fig. 4.4) and refined in a series of subgroups starting from $P1$, the next subgroup being generated from the previous one by the best scoring symmetry element (Step 3 in Fig. 4.4). This protocol was replicated from the protocol used for the manual correction of the CodY GAF-domain structure (§4.2.3). In the latter case, starting from a symmetrised model was indeed necessary, otherwise refinement did not escape from the local minima associated with the input false structure, even refinement with the correct space group and origin. On the other hand, the symmetrised model could, in the general case, be too far from the correct global minimum to reach the latter using refinement in $P1$. This was observed in tests with the crystal structure of the glutaminase domain of glucosamine 6-phosphate synthase (Isupov *et al.*, 1996). It was known for this structure that in the original model (PDB code 1gdo) the space group was incorrectly assigned as $P2_1$ instead of $P2_12_12_1$, and the symmetry assignment was later corrected (PDB code 1xff). Restoring the true symmetry would be very easy were it not for Step 1, in which the model was symmetrised. Because of pseudotranslation, which was present in this structure, the space group to which the model was transformed at Step 1 (*i.e.* the PSSG) was not the true space group but its supergroup with twice smaller cell. Therefore, this transformation resulted in significant shifts of molecules from their correct positions and refinement in $P1$ was unable to return them back. Thus the symmetrisation of the input model is an essential step in some instances but an additional obstacle in others. This problem was solved by adding Step 2 (Fig. 4.4) including refinements of the symmetrised structure in several subgroups of the PSSG, so the input for Step 3 was not the symmetrised structure, but the structure giving the best R_{free} in Step 2.

In addition, the table of R-factors generated in Step 2 may be useful in the cases of twinning interfering with pseudosymmetry, in which the R-factor difference between the true and false structures can be marginal, especially if the input model is an MR solution which has not yet been rebuilt. So, *Zanuda* generates the structure with currently most probable symmetry, while this table may suggest returning to the symmetry validation with the improved model.

Nevertheless, Step 2 is not a general solution for the problem of false local minima in rigid body refinement. Perhaps the starting model should not be intentionally symmetrised and the ability of the MR to find a global minimum, although approximately, should be utilised. So the current protocol is likely to be replaced by one in which the starting model is generated by the MR in $P1$. Of course, the contrast of the TF in $P1$ is small, but the advantage is that no symmetry is assumed in advance. On the other hand, the problem under consideration is to correct the structure, not to solve it. Therefore, since an approximate structure is known, the peaks in both RF and TF can be selected in accordance with this structure. In theory, the second run of TF (one molecule fixed) provides all necessary information on the relative positions of all the molecules. In practice, several molecules may need to be positioned directly using the TF to ensure clearer peaks for the remaining molecules.

4.3.5 Concluding remarks

In general, *Zanuda* is intended to close the gap between the intrinsic inaccuracy of the MR and the local character of the optimisation performed by refinement, which therefore requires the starting model with, at the least, correctly assigned symmetry.

The program has already helped to validate several structures. An example of a difficult case, in which *Zanuda* determined the symmetry of a pseudosymmetric twin, is presented in the next section.

4.4 Example of twin with double pseudosymmetry

The oxidoreductase from *Thermotoga maritima* was studied in the group of Professor Jennifer Littlechild (University of Exeter). Diffraction crystals of the holo-enzyme were obtained by Simon Willies and the crystal structure was solved by Simon Willies and Dr. Michail Isupov. I corrected the space group assignment using *Zanuda* (§4.3) and confirmed the new assignment using the MR results in $P1$ space group.

The problem with symmetry assignment was caused by the presence of both pseudosymmetry and twinning (Fig. 4.6). Moreover, the pseudosymmetry was generated by two operations, an approximate fourfold rotation and a translation by $\mathbf{c}/2$. The pseudosymmetry had a very strong effect on the intensities in the resolution range suitable for twinning tests, so the latter were hard to interpret, but the comparison of refinements in alternative space groups using *Zanuda* allowed identification of the correct space group.

In addition, this example is used to demonstrate that the structures with alternative origins may represent alternative individual crystals of a twin. This leads to an additional criterion for the selection of subgroups for test refinements.

4.4.1 Background

Oxidoreductase from *T. maritima* was co-crystallised with NAD+ to yield diffracting crystals belonging to the space group $P2_12_12_1$ with unit-cell parameters $a = b = 141.7$ Å, $c = 169.5$ Å. X-ray data were collected at Daresbury to 2.36 Å resolution and initially processed in the space group $P422$. Because of the synchrotron failure, the data set had a completeness of only 83%

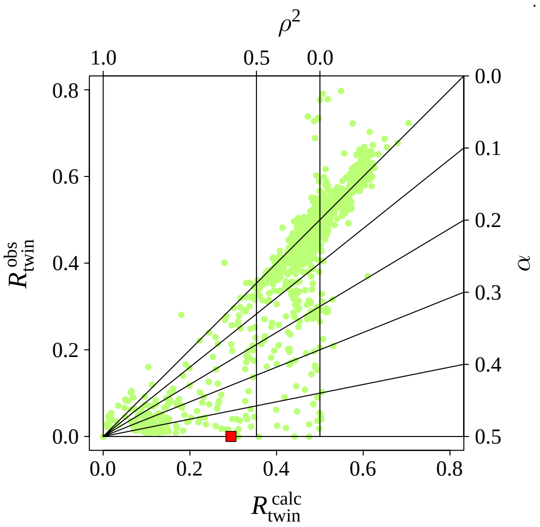

Figure 4.6. Twinning and pseudosymmetry in oxidoreductase crystal. The red point in the RvR plot (§3.2) corresponds to the correct $P2_12_12_1$ crystal structure and the X-ray data collected from the twinned crystal. Green points in the background are from Fig. 3.3(*b*).

and intensities for indices $h00$, $0k0$ and $00l$ were not measured. It was however desirable to solve the structure using this data set in order to find out whether there was substrate binding suitable for structural studies and whether this crystal form was worth pursuing for further experiments.

MR trials were performed using *MOLREP*. A single subunit of the previously solved apo-structure was used as a search model. *MOLREP* detected a pseudo-translation vector $\mathbf{c}/2$; the height of the corresponding peak in the Patterson map was 0.28 in relation to the origin peak. Therefore the TF search was conducted using two subunits related by this vector (§1.1.15). As the reflections along the crystal axes were not measured, all eight space groups with point group symmetry 422 and primitive lattice were tested. In six of them, *MOLREP* found only one pair of subunits because of packing constraints (§1.1.9). The TF-scores in the remaining two space groups as well as *R*-factors after rigid body refinements were similar, but one of them ($P42_12$, $R = 33.2\%$, $R_{\text{free}} = 39.2\%$) was much better than the other ($P4_22_12$, $R = 39.0\%$, $R_{\text{free}} = 45.9\%$) in restrained refinement (*REFMAC*).

Model correction and TLS-refinement in $P42_12$ resulted in $R = 29.9\%$ and $R_{\text{free}} = 34.3\%$. These values were still too high suggesting that an incorrect assignment of space group or origin might have happened.

4.4.2 Twinning tests

In many cases the perfect twinning tests could be used to check whether the data were processed in a higher symmetry point group. In this particular case the standard analysis was not applicable because of the pseudotranslation, which made the intensity statistics “less twinned” than the reference statistics for the untwinned case (Fig. 4.7).

The “sigmoidal” cumulative distribution of Z (the second derivative is positive at the origin) is a more universal indicator of twinning, which usually works even in the presence of pseudotranslation (Lee *et al.*, 2003) or correlated structure factors (§1.2.3, §3.1.6; Fig. 3.1*a*). The cumulative distribution of Z in this example was “sigmoidal” for all data (Fig. 4.7*a*) but not for the data in the resolution range 8–3 Å (Fig. 4.7*c*). Such behaviour could be attributed to the effect of strong pseudosymmetry by rotation, which would completely disguise twinning at low resolution. On the other hand, high values of *R*-standard in high-resolution shells (Fig. 4.7*d*) suggested that the cumulative distribution of Z for all data could also be misleading owing to the experimental errors, compare with Fig. 1.3.

The minor evidence of twinning discussed here was insufficiently convincing to exclude the originally assigned space group $P42_12$ and, therefore, the comparison of refinements in all possible space groups including $P42_12$ was necessary.

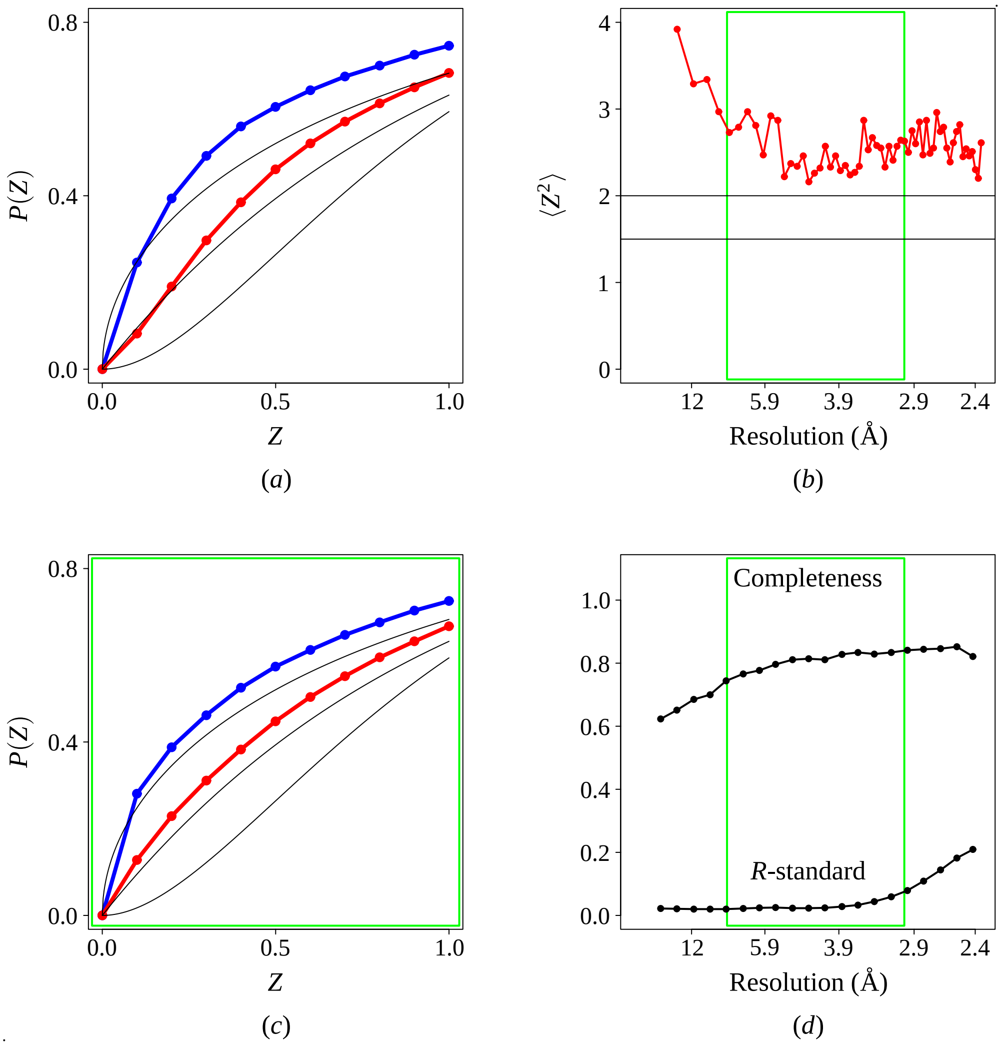

Figure 4.7. Perfect twinning tests for the twinned crystal of oxidoreductase.

The resolution range used in (*c*) is outlined by green boxes in (*b*) and (*d*).
The colour legend for (*a*) (*b*) and (*c*) is the same as for similar plots in Fig. 1.1.

(*a*) Cumulative distributions of *Z* for all the data, resolution range 26.7–2.36 Å.
(*b*) Second moment of *Z* for acentric reflections against resolution.
(*c*) Cumulative distributions of *Z* in the resolution range 8.0–3.0 Å.
(*d*) Completeness and *R*-standard against resolution.

4.4.3 Correction of symmetry

The $P42_12$ model and data were submitted to *Zanuda*. The summary of this run is shown in Fig. 4.8. The three steps of the protocol and the data presented in the summary are explained in §4.3.2. It was found that the model had pseudosymmetry $P42_12$ (subgroup S_{35}). This symmetry included the translation $\mathbf{c}/2$. The r.m.s.d. over C$^\alpha$ atoms between the input model (S_{10}) and fully symmetrised model (S_{35}) was 0.91 Å (Step 1). The series of refinements in Step 3 was terminated with the subgroup S_{27} belonging to the orthorhombic space group $P2_12_12_1$. This subgroup had no supergroup with the large cell (Fig. 4.9) and, accordingly, no further attempts were made to add symmetry elements.

The space group symmetry of the final model, $P2_12_12_1$ (S_{27}), and 422 symmetry of the data implied perfect twinning by hemihedry. Accordingly, the version of *REFMAC* allowing refinement against twinned data was used in the final round of rebuilding and refinement, which resulted in $R = 22.5\%$ and $R_{\text{free}} = 25.3\%$.

Unfortunately, no clear density for the substrate was found and this crystal form was abandoned. However, this example demonstrated that *Zanuda* is capable of correcting the space group assignment in the case of double pseudosymmetry and twinned data.

4.4.4 Additional criteria for selection of subgroups

Let S_m be the pseudosymmetry space group of the structure (in the example under consideration $S_m = S_{35}$; Step 1 in Fig. 4.8). An element $o \in S_m$ corresponds to an (approximate) (screw) rotation of the crystal. The action of $o \in S_m$ on the data d can be defined as a permutation of the elements in the data array corresponding to this rotation. The action of $o \in S_m$ on the model m can be defined as a transformation of atomic coordinates and permutation of subunits (solvent is excluded), so that the expression $om = m$ is satisfied either exactly (o is a symmetry operation) or approximately (o is a pseudosymmetry operation).

If two different subgroups are bound to produce internally identical models, then only one of them needs to be tested. The equivalence condition can be formulated as follows. If the data d are exactly invariant relative the operation o,

$$od = d, \qquad o \in S_m, \tag{114}$$

subgroups S_i and S_j are related by the o,

$$oS_io^{-1} = S_j, \qquad S_i \subset S_m, \qquad S_j \subset S_m, \tag{115}$$

and the model m optimises the target function in S_i, then the model om optimises the target function in S_j.

```
Step 1.
---------------------------------------------------------------------
| Subgroup | Spacegroup | R.m.s.d. |   Refinement in tested group   |
|          |            | from the |--------------------------------|
|   Ref    |            | starting |  Rigid   |     Restrained      |
|          |            | model, A |----------|---------------------|
|          |            |          |    R     |    R     |  R-free  |
|----------|------------|----------|----------|----------|----------|
| >>  10   | P 4 21 2   |  0.0000  |    --    |  0.4094  |  0.4478  |
| <<  35   | P 4 21 2   |  0.9050  |    --    |    --    |    --    |
^^^^^^^^^^^^^^^^^^^^^^^^^^^^^^^^^^^^^^^^^^^^^^^^^^^^^^^^^^^^^^^^^^^^^
Step 2.
^^^^^^^^^^^^^^^^^^^^^^^^^^^^^^^^^^^^^^^^^^^^^^^^^^^^^^^^^^^^^^^^^^^^^
| >>  35   | P 4 21 2   |  0.9050  |    --    |    --    |    --    |
---------------------------------------------------------------------
|       1  | P 1        |  1.5852  |  0.3904  |  0.3098  |  0.3548  |
|       2  | C 1 2 1    |  1.4912  |  0.3950  |  0.3261  |  0.3809  |
|       4  | P 1 2 1    |  1.2780  |  0.4225  |  0.3805  |  0.4341  |
|       5  | C 2 2 2    |  1.3056  |  0.4309  |  0.3950  |  0.4461  |
|       6  | P 1 21 1   |  1.5915  |  0.3941  |  0.3111  |  0.3564  |
|       7  | P 4        |  1.3526  |  0.4262  |  0.3834  |  0.4339  |
|       9  | P 21 21 2  |  1.3019  |  0.4468  |  0.4196  |  0.4699  |
|      10  | P 4 21 2   |  1.3226  |  0.4320  |  0.3989  |  0.4490  |
|      11  | C 1 2 1    |  1.5096  |  0.3966  |  0.3267  |  0.3758  |
|      12  | P 1 21 1   |  1.5926  |  0.3927  |  0.3095  |  0.3549  |
|      13  | C 2 2 21   |  1.5053  |  0.3937  |  0.3286  |  0.3789  |
|      14  | P 1 21 1   |  1.5962  |  0.3936  |  0.3104  |  0.3534  |
|      15  | P 21 21 21 |  1.5956  |  0.3960  |  0.3128  |  0.3572  |
|      16  | P 42       |  1.3780  |  0.4252  |  0.3932  |  0.4527  |
|      18  | P 21 21 2  |  1.3709  |  0.4300  |  0.3872  |  0.4420  |
|      20  | P 42 21 2  |  1.4210  |  0.4253  |  0.3915  |  0.4615  |
|      31  | C 2 2 2    |  1.3909  |  0.4205  |  0.3850  |  0.4337  |
|      32  | P 4 21 2   |  1.3917  |  0.4270  |  0.3920  |  0.4485  |
|      33  | P 42 21 2  |  1.3823  |  0.4307  |  0.4061  |  0.4657  |
---------------------------------------------------------------------
| <<  14   | P 1 21 1   |  1.5962  |  0.3936  |  0.3104  |  0.3534  |
^^^^^^^^^^^^^^^^^^^^^^^^^^^^^^^^^^^^^^^^^^^^^^^^^^^^^^^^^^^^^^^^^^^^^
Step 3.
^^^^^^^^^^^^^^^^^^^^^^^^^^^^^^^^^^^^^^^^^^^^^^^^^^^^^^^^^^^^^^^^^^^^^
| >>  14   | P 1 21 1   |  1.5962  |  0.3936  |  0.3104  |  0.3534  |
---------------------------------------------------------------------
|       1  | P 1        |  1.5942  |  0.3810  |  0.3088  |  0.3521  |
|      14  | P 1 21 1   |  1.6137  |    --    |  0.3045  |  0.3525  |
|      15  | P 21 21 21 |  1.6195  |    --    |  0.3047  |  0.3551  |
---------------------------------------------------------------------
| <<  15   | P 21 21 21 |  1.6195  |    --    |  0.3047  |  0.3551  |
---------------------------------------------------------------------
```

Figure 4.8. Correction of the space group assignment for the crystal structure of oxidoreductase.

This figure shows the summary file of *Zanuda*. The input structure Ref 10 was symmetrised and transformed into the PSSG, Ref 35 (Step 1), refined in candidate subgroups (Step 2) and transformed into the correct space group, Ref 15 (Step 3). The input and output for a given step are marked by ">>" and "<<", respectively. All shown subgroups have equivalent lattices except for the PSSG, which has the parameter **c** halved.

The three steps are explained in §4.3.2 and §4.3.3 in more detail. Some of the subgroups are shown in the subgroup/supergroup graph in Fig. 4.9.

Equation (114) is satisfied in the following three cases, the operation o is an element of the true or false-origin space group or its rotational component is the twin operation for perfectly twinned data.

The equivalence condition can be checked as follows. Simultaneous rotation of both data and crystal do not change the value of the target function. Thus, because of (114), any model m and its transformed copy om give the same value for the target function. Because of (115), any $s' \in S_j$ can be represented as $s' = oso^{-1}$, where $s \in S_i$, and, therefore, $s'om = om$ as soon as $sm = m$. This means that symmetry constraints on m in S_i are equivalent to symmetry constraints on om in S_j. Altogether, if m is an allowed model in S_i, then om is an allowed model in S_j and the two models must give the same value of the target function.

The case $o \in S_i$ is not interesting as $S_i = S_j$ and $om = m$, that is, the two solutions coincide. If $o \notin S_i$, then there are two cases, $S_i = S_j$ and $S_i \neq S_j$. In the first case there are two internally identical solutions in S_i. In the second case, there is a single solution in S_i, which is internally identical and is related by o to a single solution in S_j.

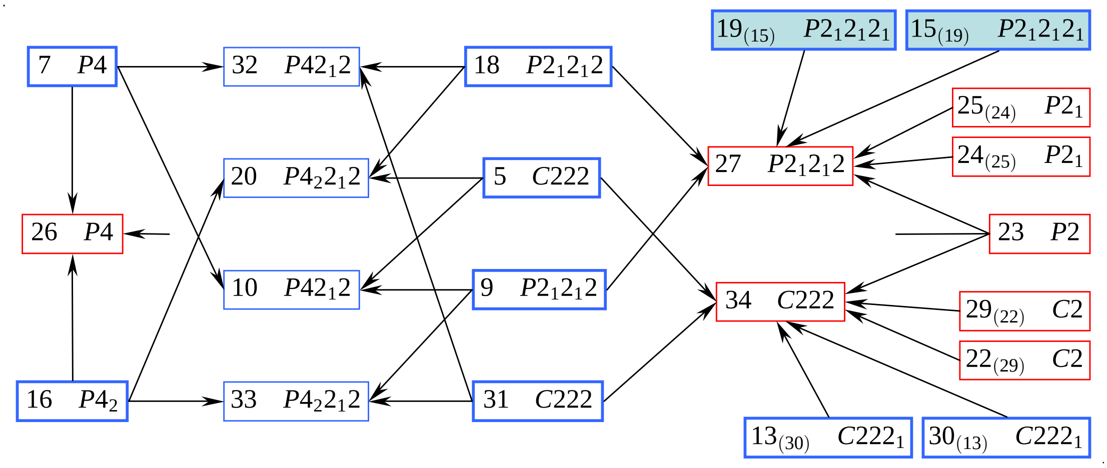

Figure 4.9. Pseudosymmetry of the oxidoreductase crystal. A fragment of (infinite) subgroup-supergroup graph for pseudosymmetry $P42_12$ with translation basis $(\mathbf{a}, \mathbf{b}, \mathbf{c}/2)$. Only those subgroups are shown, which have (i) translation basis $(\mathbf{a}, \mathbf{b}, \mathbf{c}/2)$ (red frames) or translation basis $(\mathbf{a}, \mathbf{b}, \mathbf{c})$ (blue frames) and (ii) 4 or 8 times more operations than $P1$ with the basis $(\mathbf{a}, \mathbf{b}, \mathbf{c})$. Subgroups in red boxes include pseudotranslation $\mathbf{c}/2$ and disagree with experimentally observed reciprocal lattice. Subgroups with the basis $(\mathbf{a}, \mathbf{b}, \mathbf{c})$ and 4 times more operations (thick blue frames) imply twinning by hemihedry. Two true subgroups (corresponding to two different individual crystals of the twin) are highlighted by blue background. Arrows are directed from subgroups (4 times more operations) to their supergroups (8 times more operations). An equivalent subgroup (§4.4.4), if present, is shown in brackets. Figure was generated using verbose output from *Zanuda*.

Both non-trivial cases are present in the example under consideration. Let o be a fourfold rotation about **c**. Equation (114) holds, as the data are processed in $P42_12$. Orthorhombic subgroups S_{15} *etc.* do not include o. In other words, this o, if considered as a point group operation, is the twin operation for the orthorhombic subgroups. It can be shown that

$$\begin{array}{lll} o\,S_{13}\,o^{-1} = S_{30} & o\,S_{30}\,o^{-1} = S_{13} & (C222_1) \\ o\,S_{15}\,o^{-1} = S_{19} & o\,S_{19}\,o^{-1} = S_{15} & (P2_12_12_1) \\ o\,S_5\,o^{-1} = S_5 & o\,S_{31}\,o^{-1} = S_{31} & (C222) \\ o\,S_9\,o^{-1} = S_9 & o\,S_{18}\,o^{-1} = S_{18} & (P2_12_12) \end{array} \qquad (116)$$

Therefore, pairs S_{13}, S_{30} (space group symmetry $C222_1$) and S_{15}, S_{19} (space group symmetry $P2_12_12_1$) define internally identical structures which are different individual crystals of the twin, whereas pairs S_5, S_{31} (space group symmetry $C222$) and S_9, S_{18} (space group symmetry $P2_12_12$) define internally different structures although belonging to the same space group. In the second case the structures corresponding to different individual crystals belong to the same subgroup and global optimisation would return one of the two structures by chance.

It makes sense to ignore the redundant subgroups (*e.g.* corresponding to the second individual crystal of a perfect twin by hemihedry) in order to avoid confusion with identical R-factors. This will also save some computing time. Therefore *Zanuda* implements the following selection procedure based on (114), (115). The external loop runs over $S_i \subset S_m$. If the current S_i has not been previously flagged as redundant, the internal loop runs over $o \in S_m$ satisfying (114) to find all $S_j \neq S_i$ satisfying (115) and to flag them as redundant. Because of this selection rule, S_{13} and S_{15} are tested in the second step in Fig. 4.8, whereas S_{30} and S_{19} are ignored. On the other hand, both subgroups S_5 and S_{31} with space group symmetry $C222$ and both subgroups S_9 and S_{18} with space group symmetry $P2_12_12$ were tested: if S_5 (S_9) is true, then S_{31} (S_{18}) is a false-origin solution, and *vice versa*.

Had the partial twinning been recognised and the data processed in 222, then (114) would not hold for fourfold rotation o about **c** and all orthorhombic subgroups with the large cell would be tested. This would make sense, as the individual crystal of larger size would give a lower R-factor than another individual crystal.

4.4.5 Alternative methods of structure correction

The space group $P2_12_12_1$ was confirmed using MR with the data expanded to $P1$ space group. Twelve subunits were positioned in a single run of *MOLREP* and the $P1$-model was completed using TF peaks, which had not been used in the partial model but were persistently appearing at all twelve TF steps with high scores; the subunits corresponding to these peaks were placed using *LSQKAB*. The correct symmetry was restored similarly to Step 3 in Fig. 4.8.

In manual tests involving MR searches and refinements in several space groups (an alternative to the MR in $P1$), additional refinements on the alternative origin at $\mathbf{c}/4$ would be needed in $P4_22_12$, $P42_12$, $C222$ and $P2_12_12$ (but not in $C222_1$ and $P2_12_12_1$, in which the structure with the alternative origin is the structure of the second individual crystal of the twin).

If the reflections $h00$, $0k0$ and $00l$ had been accurately measured, the assumption of twinning by hemihedry and the systematic absences would necessarily point to $P2_12_12_1$ space group. Tests of alternative origins would not be needed and straightforward MR would produce the correct solution. In this case, the comparison of refinement in $P2_12_12_1$ with two refinements in $P4_22_12$ (two non-equivalent origins) would confirm or reject the hypothesis of twinning. On the other hand, the automatic comparison of all possible subgroups gives more confidence in the final result.

Comparison of refinements in several subgroups is particularly important if there are no systematic absences along two or all three axes. For example, human deoxycytidine kinase forms $P2_12_12$ twinned crystals, in which the axis of four-fold twin operation is along **a** and maps systematic absences onto non-zero intensities (Elisabetta Sabini, personal communication).

4.5 OD-structures with enantiomorphic sequences of stacking vectors

In all three examples of this chapter, the higher space-group symmetry of the crystal was perturbed by overall, although small, displacements and rotations of biomolecules. As a result, there were appreciable differences in R-factors between the true and false structures after refinement, which made it possible to resolve the space group uncertainty.

This section presents another kind of space-group uncertainty in macromolecular crystals, which is similar to the uncertainty with the choice of enantiomorph in crystallography of small molecules and which cannot be resolved using X-ray data only. A theoretical model and an example from the PDB are discussed.

4.5.1 Theoretical model

Let **p** be a vector of structure factors representing the substructure shown in Fig. 4.10(*a*), $\hat{e}$ be the identity matrix and $\hat{o}$ be a matrix representing o, the three-fold rotation about **c**, the generator of the space group $P3$ of **p**,

$$\hat{o}\mathbf{p} = \mathbf{p}, \tag{117}$$

$$\hat{o}^3 = \hat{e}. \tag{118}$$

The matrix $\hat{o}$ is an orthogonal matrix of permutations with elements equal to either 0 or 1.

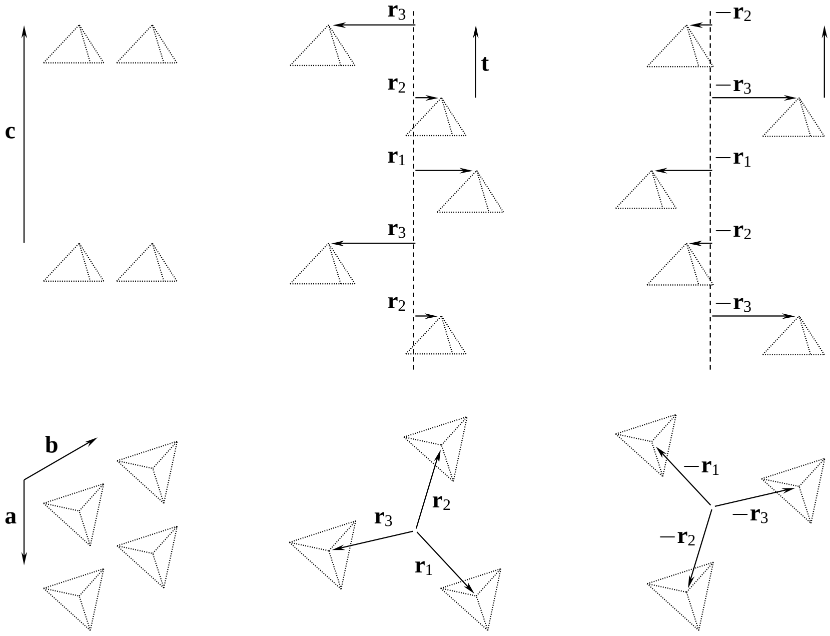

Figure 4.10. Acentric structures with equal structure amplitudes. The structures are assembled from identical layers, which are parallel to (001) plane. (*a*) Partial $P3$ structure containing every third layer. (*b*) The $P3_1$ structure. (*c*) The $P3_2$ structure. In (*b*) and (*c*), only one trimer per layer is shown.

Let $\hat{t}$ and $\hat{r}_i$ be complex diagonal matrices representing translations $\mathbf{t} = \mathbf{c}/3$ and $\mathbf{r}_i$ ($\mathbf{r}_{i+1} = o\,\mathbf{r}_i$), respectively,

$$\hat{t}^3 = \hat{e}, \tag{119}$$

$$\hat{o}\hat{t} = \hat{t}\hat{o}, \tag{120}$$

$$\hat{o}\hat{r}_i = \hat{r}_{i+1}\hat{o}. \tag{121}$$

Notations (117) to (121) are used to analyse the structures in Figs. 4.10(b) and 4.10(c). In particular, it is shown below that the two structures (i) have the same structure amplitudes, (ii) belong to different space groups but (iii) belong to the same OD family, so if one structure physically exists, another is also possible.

(i) The matrix

$$\hat{v} = \hat{r}_1 + \hat{t}\hat{r}_2 + \hat{t}^2\hat{r}_3 \tag{122}$$

represents the positions of trimers in Figs. 4.10(b). The set of trimers in Figs. 4.10(b) can be mapped into the set of trimers in Fig. 4.10(c) in such a manner that the reference points of corresponding trimers would be related by inversion. Therefore, the positions of trimers in Fig. 4.10(c) are represented by $\hat{v}^*$ and the two structures are represented by the following vectors of the structure factors,

$$\mathbf{f}_1 = \hat{v}\,\mathbf{p}, \tag{123}$$

$$\mathbf{f}_2 = \hat{v}^*\mathbf{p}. \tag{124}$$

Let $\hat{w}$ be a real diagonal matrix of weighting coefficients. Because $\hat{v}$ is also diagonal, the weighted sums of intensities for the two structures coincide,

$$\mathbf{f}_1^{*T}\hat{w}\,\mathbf{f}_1 = \mathbf{p}^{*T}\hat{v}^*\hat{w}\,\hat{v}\,\mathbf{p} = \mathbf{p}^{*T}\hat{v}\,\hat{w}\,\hat{v}^*\mathbf{p} = \mathbf{f}_2^{*T}\hat{w}\,\mathbf{f}_2. \tag{125}$$

In particular, if $\hat{w}$ contains a single non-zero element, the equation (125) means the two corresponding intensities are equal. Therefore, the structures $\mathbf{f}_1$ and $\mathbf{f}_2$ produce exactly the same structure amplitudes.

Note that the absence of anomalous signal in $\mathbf{p}$ was not assumed. Thus, in contrast to the true enantiomorphic structures, the structures with enantiomorphic sequences of stacking vectors can not be distinguished using anomalous signal.

(ii) Using equations (117) to (124), the vectors $\mathbf{f}_1$ and $\mathbf{f}_2$ are expressed as follows,

$$\mathbf{f}_1 = 3\,\hat{\pi}\,\hat{r}_1\,\mathbf{p}, \tag{126}$$

$$\mathbf{f}_2 = 3\,\hat{\pi}^*\,\hat{r}_1^*\,\mathbf{p}, \tag{127}$$

where

$$3\hat{\pi} = \hat{e} + \hat{t}\hat{o} + (\hat{t}\hat{o})^2. \tag{128}$$

Equations (123), (124) and (126), (127) represent two equivalent ways of assembling the structures $\mathbf{f}_1$ and $\mathbf{f}_2$ from layers. In (123) and (124) the two structures are assembled from translated copies of the reference layer, while in (126) and (127) the complete structures are generated from the reference layer by screw rotations. If the layers had symmetry $P11(1)$, the first procedure would result into two $P1$ structures with the same structure amplitudes and the second one would produce $P3_1$ and $P3_2$ structures with different structure amplitudes. Note however that none of the last four structures is OD because the $P11(1)$ layers can only occur in the type III (Fig. 1.5*d*), in which any two contacting layers are related via a screw two-fold axis parallel to the layers.

The symmetry of $\mathbf{f}_1$ and $\mathbf{f}_2$ can formally be identified as follow. Because of (118), (119) and (120), the matrix $\hat{\pi}$ is a projector,

$$\hat{\pi}\,\hat{\pi} = \hat{\pi}, \tag{129}$$

which commutes with own complex conjugate,

$$\hat{\pi}^*\hat{\pi} = \hat{\pi}\,\hat{\pi}^*. \tag{130}$$

Because of (130), $\hat{\pi}^*\hat{\pi}$ is a real matrix, whereas $\hat{\pi}$ itself is not. ($\hat{\pi}$ can be reduced to block diagonal form with five types of block. The blocks corresponding to reflections with $l \neq 3n$ and either $h \neq 0$ or $k \neq 0$ contain complex elements, as the elements of $\hat{t}$ for these reflections are complex numbers.) Therefore,

$$\hat{\pi}^*\hat{\pi} \neq \hat{\pi}. \tag{131}$$

Thus, (126) and (127) for a generic vector $\hat{r}_1\mathbf{p}$ result in

$$\hat{\pi}\,\mathbf{f}_1 = \mathbf{f}_1 \qquad\qquad \hat{\pi}^*\mathbf{f}_1 \neq \mathbf{f}_1 \tag{132}$$

and

$$\hat{\pi}^*\mathbf{f}_2 = \mathbf{f}_2 \qquad\qquad \hat{\pi}\,\mathbf{f}_2 \neq \mathbf{f}_2 \tag{133}$$

If a vector of structure factors is invariant relative to $\hat{\pi}$, then it is invariant relative to any matrix from the group $G_1 = \{e, \hat{t}\hat{o}, \hat{t}^2\hat{o}^2\}$ and *vice versa*. Similarly, invariance relative to $\hat{\pi}^*$ means invariance relative to $G_2 = \{e, \hat{t}^*\hat{o}, \hat{t}^{*2}\hat{o}^2\}$. The matrix groups G_1 and G_2 represent space groups $P3_1$ and $P3_2$, respectively.

Altogether, given a generic vector $\mathbf{r}_1$, the structures $\mathbf{f}_1$ and $\mathbf{f}_2$ are different and belong to different space groups although both are composed of identical layers and produce the same structure amplitudes.

(iii) In both structures $\mathbf{f}_1$ and $\mathbf{f}_2$ the consecutive pairs of adjacent layers are related by three alternating stacking vectors,

$$\mathbf{s}_i = \mathbf{r}_i - \mathbf{r}_{i-1} + \mathbf{t}, \qquad\qquad \mathbf{s}_4 = \mathbf{s}_1 \tag{134}$$

Because of (120) and (121), these vectors are equivalent relative to the symmetry $P(3)11$ of the layer and therefore the two structures are OD-structures (§1.3) from the same OD-family of type II/A, with maximum degree of order but with enantiomorphic sequences of the stacking vectors, $(\ldots, \mathbf{s}_1, \mathbf{s}_2, \mathbf{s}_3, \ldots)$ in $\mathbf{f}_1$ and $(\ldots, \mathbf{s}_3, \mathbf{s}_2, \mathbf{s}_1, \ldots)$ in $\mathbf{f}_2$.

Intermolecular contacts in two ideal OD-structures are identical and therefore both structures could in principle exist either in two separate single crystals or simultaneously in allotwin. The intensities from individual crystals of such allotwin would be equal. If, in addition, the individual crystals were large and therefore the interference term were negligible, the intensity statistics would not deviate from untwinned statistics.

Two special cases are possible, in which the structures $\mathbf{f}_1$ and $\mathbf{f}_2$ are identical. If $\mathbf{s}_1 = m\mathbf{a}+n\mathbf{b}$, then both structures belong to $P3$ space group with $\mathbf{c}' = \mathbf{t}$. If $\mathbf{s}_1 = \pm(\mathbf{a}-\mathbf{b})/3+m\mathbf{a}+n\mathbf{b}$, then both structures belong to $R3$ space group with $\mathbf{c}' = \mathbf{c}$ in hexagonal obverse or reverse settings.

4.5.2 Example

The 2.6 Å crystal structure of proliferating cell nuclear antigen (PCNA; PDB code 1axc; Gulbis *et al.*, 1996) belongs to the space group $P3_221$ with unit-cell parameters $a = 83.5$ Å, $c = 233.9$ Å. The structure possesses $R32$ pseudosymmetry (C^α r.m.s.d. from the symmetrised structure is 0.83 Å) and therefore it was selected as a test case for *Zanuda*. Surprisingly, the refinement in two different space groups, $P3_221$ (symmetry of the PDB model) and $P3_121$ gave very similar *R*-factors. The pseudosymmetry could not be a reason for this space group uncertainty. Therefore further analysis has been performed. A comparison of the two alternative structures with the symmetrised $R32$-structure showed that these were OD-structures from the same OD-family of type I/A with $P(3)21$ symmetry of the OD-layers. Compared to the theoretical model above, the symmetries of both the single layer and the complete structure include additional operations, two-fold rotations. Therefore, the orthogonal projection of stacking vector on the plane (001) is necessarily orthogonal to one of the two-fold axes. Except for this constraint, the theoretical model remains valid and explains the space group uncertainty in the crystal structure under consideration.

Validation of the space group assignment was performed as follows. The solvent was removed and the protein trimer constituting the asymmetric unit of the PDB model was symmetrised to generate a structure in which the OD-layers were exactly symmetric relative to the plane space group $P(3)21$. This model was refined in $P3_221$ space group. The symmetrised trimer was shifted by $0.7053(\mathbf{a}+\mathbf{b})$ to generate the starting model for refinement in space group

$P3_121$. The results of the two refinements are presented in Table 4.4. The symmetrised starting models were assumed not to be biased toward the original space group $P3_221$. Nevertheless, the R-factors in this space group were lower and the difference were not negligible, especially the difference in R_{free}. Refinement in $P3_221$ persistently produced lower R-factors even when the starting model was generated from the structure refined in $P3_121$.

Nevertheless, the results of refinements could not be interpreted unambiguously. One possibility was that the crystal was indeed a single $P3_221$ crystal, in which small asymmetric deformations in a given layer induced by contacts with one neighbouring layer defined the position of another neighbour. However, the asymmetry of the OD-layer was very small (C^{α} r.m.s.d. from the symmetrised layer was only 0.182 Å) and was not associated with overall shifts or rotations of the subunits. It seemed therefore also possible that the crystal was a polysynthetic allotwin or partially disordered crystal with the $P3_221$ fraction predominating. The latter hypothesis was consistent with the large difference between R and R_{free}, poor electron density at the interfaces between adjacent OD-layers and large structure amplitudes for some of the axial reflections with $h = k = 0$ and $l \neq 3n$, which had to be extinct in both $P3_221$ and $P3_121$. All these could be signs of partial disorder and could be due to the small sizes of individual crystals in the putative allotwin.

4.5.3 Concluding remarks

The space group uncertainty discussed in this section is quite general for OD-structures. If the plane space group of the OD-layer contains symmetry elements of order 3, 4 or 6, then the OD-family contains the members with inverted sequences of stacking vectors. The OD-structures with the opposite order of stacking vectors belong to different space groups, but, similarly to the

Space group	$P3_221$	$P3_121$
R (%)	22.094	22.345
R_{free} (%)	29.148	30.016
R.m.s.d. from ideal values		
bond lengths (Å)	0.016	0.016
bond angles (^{o})	1.70	1.65

Table 4.4. Refinements of OD-structures with enantiomorphic sets of stacking vectors. Two models of the PCNA crystal with symmetrised OD-layers and opposite order of stacking vectors were generated from the PDB entry 1axc. The models belonged to different space groups, $P3_221$ and $P3_121$, but produced equal structure amplitudes. Refinements of these models were performed to identify better symmetry assignment.

structures with inverted atomic coordinates, produce the same structure amplitudes. Moreover, the OD-family contains allotwins and partially disordered structures, in which domains with opposite sequences of stacking vectors coexist.

In all these cases, the X-ray data and especially macromolecular X-ray data of limited resolution are insufficient for an unambiguous characterisation of the actual crystal structure. Nevertheless, a simple approach, in which the macromolecular crystal is considered as a single crystal belonging to the space group producing better *R*-factor, is sufficient for model building and structure analysis. Locally, the electron density maps and intermolecular contacts are almost identical in the alternative space groups and therefore allotwins and partially disordered structures would be handled with reasonable accuracy. Simultaneous refinement of two individual crystals for better treatment of allotwin is unlikely to be possible because of too many correlated parameters. However, it seems feasible to account for the interference between domains of a partially disordered structure.

5 Conclusions

NCS is a feature of macromolecular structures, which, if present, typically raises extra problems with the structure solution. For example, the presence of NCS implies the use of multi-body MR complicated by low signal-to-noise ratio. In special cases of translational pseudosymmetry or twinning interfering with NCS, the space group assignment can be a problem. Accordingly, the two particular issues raised in this work are the use of NCS-guided MR for structure solution and the validation of symmetry assignment.

5.1 Non-standard MR protocols

Several examples of structures that could not have been solved routinely using MR are presented in this thesis. The methods that have facilitated the structure solutions are summarised below.

5.1.1 NCS-constrained exhaustive search

Three methods that can be generally classified as NCS-constrained exhaustive searches are presented in this thesis. They differ in whether all available NCS constraints are used for structure solution or only some of them. These methods are applicable to crystal structures of oligomeric proteins, oligomers possessing hierarchical structure and being “oligomers of oligomers”. Three relevant examples are presented in which smaller oligomers were known from homologous structures, but larger oligomers were either unknown or very different from those formed by homologues,

(i) Thioredoxin peroxidase B from human erythrocytes (§2.1, PDB code 1qmv),

(ii) Anti-TRAP protein from *Bacillus licheniformis* (§2.2),

(iii) Hydroxycinnamoyl-CoA hydratase-lyase from *Pseudomonas fluorescens* (§2.3, PDB code 2j5i).

In the method used for solving (ii), only one of two unknown parameters was scanned and another was found by subsequent TF searches. Therefore this method is

- faster;
- applicable to oligomers with only one symmetry axis and is therefore more general;
- is easier for manual use and for general implementation, as the search models for the TF do not need to be generated explicitly.
- delivers an additional validation criterion, the integrity of the larger oligomer.

Therefore this method is recommended as the next option to try after the standard one-by-one search and is worthy of implementing in MR pipelines.

The other two methods are useful in specific circumstances. Method (i) uses all NCS constraints and provides the highest possible contrast in the TF search, so it was used for the structure determination of a large non-spherical oligomer with relatively low sequence identity to the search model. Method (iii) was used in the presence of translational NCS to avoid the effect of long cross-vectors on the TF search.

5.1.2 Substructure solution using NCS-constrained exhaustive search

Another variation of the general method was used in the course of structure solution of the tridecameric portal protein from phage SPP1 (§2.6, PDB code 2jes). Here the substructure of thirteen Hg atoms was not found using direct methods but was found using NCS-constrained exhaustive search against isomorphous differences. This example shows that the MR method, which is usually less efficient for substructure solution than direct methods, can nevertheless be the best choice if information on NCS is available and the whole substructure is therefore defined by a small number of variable parameters.

5.1.3 Refinement of partial structures

Refinement of a partial structure was a critical step of the MR solution of

(i) E1-helicase from bovine papillomavirus-1 (§2.4, PDB code 2v9p) and

(ii) Hypothetical protein MTH685 from *M. thermautotrophicus* (§2.5).

Two different approaches were used: (i) NCS-constrained refinement of four internal parameters of a hexamer, the maximum value of the CRF being the target function and (ii) restrained refinements of partial structures and the use of refined domains as search models in subsequent rounds of MR.

The idea of method (i) is to increase the radius of convergence by reducing both spatial and angular resolution. An implementation of this method for a general oligomeric or multidomain model may use the spherical harmonic representation of the data and model generated at the RF step of the MR to refine a composition model before the TF step.

Method (ii) requires the presence of two or more identical molecules in the asymmetric unit, but does not require a point group symmetry relation between them. Restrained refinement used in this method allows utilisation of high resolution data, which otherwise are useless for MR. It was found that the completeness of a partial model of about 30% is sufficient for its efficient refinement and for substantial improvement of the search models derived from it.

5.2 Symmetry validation and correction

Several issues concerning crystal symmetry and twinning are discussed in this thesis and summarised below. These include the effect of twinning on the atomic model, the interference of twinning with NCS and pseudosymmetry, data processing and detwinning in the case of twinning by reticular merohedry and a program for symmetry validation and correction.

5.2.1 Twinning by (pseudo)merohedry

In this type of twin, all reflections from one individual crystal overlap with the reflection from any other individual crystal. This is the most frequent, or, at least, most frequently reported case of twinning in macromolecular crystals. An analysis of the PDB was performed using R-factors between twin related intensities, observed and calculated, to generate a comprehensive collection of such twins. The examples found were used for testing twinned refinement implemented in the new version of *REFMAC* (Garib Murshudov, personal communication).

An atomic model represents only one individual crystal and no phases can be ascribed to a contribution from other individuals into the observed intensities. The atomic model cannot be significantly affected by the latter contribution as the refinement program will treat it as noise provided reasonably strong stereochemical restraints. However, the analysis of the PDB revealed several models refined against twinned data, which were significantly corrupted. It seemed likely that in these cases an unnoticed twinning and too high R-factors may have lead to an incorrect assessment of model quality and resulted in further refinement, likely with weaker restraints, involving overfitting of the models towards the twinned data. One such model was rebuilt and refined to show that untwinned refinement as such cannot be responsible for any significant changes in the model or electron density map. It was therefore concluded that the main role of twinned refinement is to produce more usual low values of R-factors and thus exclude overfitting, and that the main problem associated with twinning is an awareness of its presence.

The analysis of the PDB showed that in about a half of all twins the twin axis was approximately parallel to an NCS axis. In such circumstances the structure factors related by twin operation correlate and therefore the contrast of twinning tests decreases. The high occurrence of this special case of twinning and additional complications that it causes simulated a theoretical analysis resulting in a simple analytical expression for the distributions of Z and H for variable twinning fraction and correlation. These distributions can be used as references in the perfect and partial twinning tests, respectively, in the presence of correlation.

In addition, three examples with different correlation of twin-related structure factors were analysed in detail:

(i) a twin with NCS but without correlation (C-terminal domain of large terminase subunit from phage SPP1, §3.3);

(ii) an OD-twin with a significant correlation, in which the symmetry of OD-layers induced both twinning and NCS (Ferrochelatase-1 from *Bacillus anthracis*, §3.4, PDB code 2c8j);

(iii) a twin with a very strong correlation caused by interference of twinning and pseudosymmetry (Oxidoreductase from *Thermotoga maritima*, §4.4).

The presence of twinning caused no problems with the space group assignment in (i). The twinning tests had not been performed until refinement in (ii) as the MR gave a solution with a great contrast in one of the higher symmetry space groups. In addition, this space group could not be rejected with certainty because of pseudo-absences induced by the symmetry of OD-layers. The twinning tests were not conclusive in (iii) and the lower symmetry space group and twinning could only be confirmed using refinements in a series of space groups consistent with the cell parameters.

Case (iii) highlights a problem of distinguishing pseudosymmetry interfering with twinning in a lower symmetry space group from a higher symmetry. The analysis of the PDB showed that the lower symmetry space group was incorrectly assigned in many cases and that some of these models were significantly corrupted because of refinements with some of the symmetry constraints being in effect ignored. It was therefore concluded that a specialised program is needed that could validate or correct symmetry assignment during or after refinement and model building.

5.2.2 Twinning by reticular pseudomerohedry

This type of twinning is characterised by overlap of only a fraction of all the reflections. It is either very rare in macromolecular crystals or usually remain unnoticed, as it creates less problems with symmetry assignment, structure solution and refinement compared to twinning by (pseudo)merohedry. Two cases were discussed in this thesis,

(i) the twinned crystal of lipase B from *Candida antarctica* (§1.3.4, §3.2.5, PDB code 1lbs) with a very small obliquity angle and a low twin index of three;

(ii) the twinned crystal of L-2-haloacid dehalogenase from *Sulfolobus tokodaii* (§3.5, PDB code 2w11) with a small but appreciable obliquity angle and a large twin index of ten.

The two cases differ in how the diffraction data were processed and in potential mistakes that could have been made.

The twinned data (i) with low obliquity angle and twin index were indexed and processed in the large unit cell (of the twin lattice) and therefore twinning could have been mistaken for pseudotranslation. The integrated data were reindexed to remove non-overlapping reflections from the smaller individual crystal and to detwin overlapping reflections.

The autoindexing of the data (ii) with larger obliquity angle and twin index resulted in the correct cell dimension so the twinning could have remained unnoticed. As the spots from one of the individual crystals were not integrated, the data correction only involved the detwinning of overlapping reflections, which, however, was more sophisticated in this case because of equal sizes of individual crystals and significant obliquity angle.

The raw data were available in example (ii) and therefore two refinements of the complete final model were compared, against twinned and detwinned data. No significant differences between the two resultant models were found although the difference between R-factors was about 5%. However, the difference map from an incomplete model was more distorted for twinned than for detwinned data. This difference can be of some importance for model building, which, as in the case of twinning by (pseudo)merohedry, could lead to a misinterpretation of a weak density and a corrupted model if twinning were ignored. This may be especially relevant to poorly ordered segments with low electron density.

An additional problem associated with cases like (i) is to distinguish between twinning and pseudotranslation. From the general point of view, this is again a problem of identification of the correct symmetry, but a possible mistake is an assignment of incorrect translational symmetry (i.e. unit cell parameters), not the point group symmetry as it was for twinning by (pseudo)merohedry.

The two twins by reticular pseudomerohedry presented in this thesis are OD-twins, as are the twins encountered by Ian Tickle and Gleb Bourenkov (personal communications). Both twining and NCS in all these structures are due to the symmetry of OD-layers and, therefore, twin-related structure factors of overlapped reflections strongly correlate and detwinning can be replaced by demodulation (§3.5).

5.2.3 False origin solutions

A new class of false solutions, which can occur in the presence of pseudotranslation, is characterised in this thesis. In some crystals, there exist equivalent origins in a pseudosymmetry space group (PSSG) with a smaller unit cell, which are not equivalent in the true space group with a larger unit cell. Assignment of a false origin during MR structure solution leads to a false model which differ from the true model by

- a large overall shift of the while crystal structure relative to fixed crystallographic axes

- small translations, rotations and distortion of individual molecules to accommodate new symmetry constraints.

The large overall shift of the whole structure does not affect the structure amplitudes but it cannot be corrected by local optimisation, rigid body or restrained refinements. Small differences between the true and false structures owing to changed symmetry constraints introduce significant errors even in the relative coordinates of atoms in any particular molecule, corrupt some fragments of electron density and increase R-factors.

Three examples of false origin MR solutions are presented in this thesis, which were encountered in the actual courses of structure determination. This are the structures of Anti-TRAP protein from *Bacillus licheniformis* (§4.1), GAF (N-terminal) domain of apo CodY protein from *Bacillus subtilis* (§4.2, PDB code 2gx5) and Oxidoreductase from *Thermotoga maritima* (§4.4). Three approaches to the origin correction are discussed,

(i) MR with oligomeric models,

(ii) Refinements in alternative origins,

(iii) Refinement in *P*1 followed by restoring the correct space group.

It was found that approach (i) can be misleading. Approach (ii) appeared to have a larger radius of convergence than (iii). However, approach (iii) is more general as it in effect tests all relevant subgroups of the PSSG and can in principle handle both false origin solutions and cases of twinning interfering with pseudosymmetry mistaken for higher crystallographic symmetry.

The analysis of twinning interfering with pseudosymmetry and false origin solutions simulated development of *Zanuda*, a specialised program for symmetry validation and correction.

5.2.4 Program for symmetry validation and correction

Three cases are outlined above, in which an incorrect symmetry assignment is hard or impossible to correct using the experimental data only. These are

- erroneous higher symmetry assigned to a pseudosymmetric twin,
- erroneous lower symmetry and twinning, whereas the higher symmetry space group is a correct assignment,
- assignment of a false origin.

All these errors can in principle be corrected by refinement in *P*1 followed by the determination of the space group symmetry of the refined model. Because of possible bias of the input model toward incorrect space group and because of poor convergence of refinement in $P1$ a more sophisticated protocol was implemented, which includes

- merging the model into the PSSG,
- refinements in subgroups of the PSSG,
- expanding the structure with the lowest R_{free} into $P1$,
- restoring higher symmetry by adding symmetry elements one after another and refinement after each addition.

In future development of *Zanuda* the following issues need to be addressed,

- Better refinement protocol with larger radius of convergence,
- Better than R_{free} criterion for comparing the space groups,
- NCS-guided detection of twinning by reticular merohedry mistaken for pseudotranslation.

5.3 Outline on symmetry assignment

Very generally, the problem of symmetry assignment can be divided into crystallographic and statistical parts. The first include an accumulation of knowledge on the possible organisation of crystalline matter and the use of this knowledge for characterisation of particular structures. Point and space group symmetry of a single crystal are only a small and indeed simplest part of the whole subject. Even for protein crystallography, in which the crystal is only a tool for determination of protein structure, a more detailed knowledge of the organisation of crystal twins and partially disordered structures may be important for utilisation of experimental diffraction data. This thesis concerned only this aspect of the subject and provides several examples either interesting from structural point of view or difficult for interpretation, and describes the program *Zanuda* for symmetry validation.

However the statistical part of the subject is no less important. For example, a simple criterion of smaller R_{free} does not work for comparison of refinements in different space groups, and an *ad hoc* tolerance limit for differences between two R_{free} values is used in *Zanuda* for this purpose. This approach needs to be replaced by proper hypothesis testing. This could be, for example, a likelihood test, or the linear model analysis of the quadratic approximation to the likelihood function. Further development of the symmetry validation program may require the use of unmerged intensities, as the radiation damage to a crystal may be a reason for its apparent lower symmetry. Advanced statistical methods will be absolutely necessary for approaching this problem.

5.4 Impact on structure refinement and the resulting model

This thesis is dedicated to rather unusual crystal structures and methods for their solution. However some useful experience on structure refinement emerged during these analyses.

It was noticed that the complete atomic model well and properly refined against twinned data does not suffer in a major way if subjected to untwinned refinement, nor indeed does the electron density corresponding to this model. However, while is true for the major features of the structure, those for which the density is weak may be better defined after twinned refinement. Accordingly, there are two valid ways to build a model using twinned data: (i) to use untwinned refinement in the beginning of the model building and switch to twinned refinement for the final model correction or (ii) to use twinned refinement from the very beginning. Either approach has disadvantages although both, if refinements are done carefully, will result in correct models with the differences in their atomic parameters within experimental uncertainties. The things to care about are strong restraints, validation of main- and side-chain torsion angles and avoiding any over-interpretation of the density, *e.g.* postponing the building of alternative conformations and poorly ordered loops and solvent molecules till the very last moment.

These common practices are especially important for (i), as weak restraints and hasty modelling combined with untwinned refinement against twinned data can lead to a substantially corrupted model, which would not be possible to revert to the correct one by any refinement without rebuilding. The model building follows path (i) if twinning is unnoticed, and this possibility means that the above rules need always to be obeyed. Path (ii) can cause troubles if an untwinned structure belonging to a higher symmetry space group has been mistaken for twinned structure and is refined in lower symmetry as if it were a pseudosymmetric twin. In this case the corruption of the model is revealed in large differences between molecules which are in fact related by crystallographic symmetry. Here, NCS restraints can be a possible precaution. However it is always better to handle the model in the correct space group, to carry out the twinning test at an early stage, and to validate the model symmetry after some rebuilding if there were any uncertainties with the symmetry assignment or twinning detection.

All above relates only to refinement in the correct space group or any of its subgroups, whether or not the data are twinned. The major errors in symmetry assignment, such as assignment of supergroup or false origin, would inevitably lead to significant coordinate errors and corrupted electron density, in at least some of its regions. Both unnoticed twinning and major errors in symmetry assignment are monitored by R_{free}, so a large value with no clear hints in the density for further steps of model correction may well indicate a need for symmetry validation.

For real confidence in obtaining the best set of coordinates in crystals which are twinned, procedures such as those described in this thesis provide useful insights.

References

Afonine, P. V., Grosse-Kunstleve, R. W. & Adams, P. D. (2005). The *Phenix* refinement framework. *CCP4 Newslett.* **42**, contribution 8.

Allpress, J. D. & Gowland, P. C. (1998). Dehalogenases: environmental defence mechanism and model of enzyme evolution. *Biochem. Educ.* **26**, 267–276.

Álvarez-Rúa, C., Borge, J. & García-Granda, S. (2000). *OVIONE*: a new vector-search rotation-function program for macromolecular crystallography. *J. Appl. Cryst.* **33**, 1436–1444.

Antson, A. A., Dodson, E. J., Dodson, G., Greaves, R. B., Chen, X. & Gollnick, P. (1999). Structure of the *trp* RNA-binding attenuation protein, TRAP, bound to RNA. *Nature (London)*, **401**, 235–242.

Antson, A. A., Otridge, J., Brzozowski, A. M., Dodson, E. J., Dodson, G. G., Wilson, K. S., Smith, T. M., Yang, M., Kurecki, T. & Gollnick, P. (1995). The structure of *trp* RNA-binding attenuation protein. *Nature (London)*, **374**, 693–700.

Arai, R., Kukimoto-Niino, M., Kuroishi, C., Bessho, Y., Shirouzu, M. & Yokoyama, S. (2006). Crystal structure of the probable haloacid dehalogenase PH0459 from *Pyrococcus horikoshii* OT3. *Prot. Sci.* **15**, 373–377.

Argos, P., Ford, G. C. & Rossmann, M. G. (1975). An application of the molecular replacement technique in direct space to a known protein structure. *Acta Cryst.* A**31**, 499–506.

Asojo, O. A., Boulègue, C., Hoover, D. M., Lu, W. & Lubkowski, J. (2003). Structures of thymus and activation-regulated chemokine (TARC). *Acta Cryst.* D**59**, 1165–1173.

Au, K., Berrow, N. S., Blagova, E., Boucher, I. W., Boyle, M. P., Brannigan, J. A., Carter, L. G., Dierks, T., Folkers, G., Grenha, R., Harlos, K., Kaptein, R., Kalliomaa, A. K., Levdikov, V. M., Meier, C., Milioti, N., Moroz, O., Müller, A., Owens, R. J., Rzechorzek, N., Sainsbury, S., Stuart, D. I., Walter, T. S., Waterman, D. G., Wilkinson, A. J., Wilson, K. S., Zaccai, N., Esnouf, R. M. & Fogg, M. J. (2006). Application of high-throughput technologies to a structural proteomics-type analysis of *Bacillus anthracis*. *Acta Cryst.* D**62**, 1267–1275.

Bahnson, B. J., Anderson, V. E. & Petsko, G. A. (2002). structural mechanism of enoyl-CoA hydratase: three atoms from a single water are added in either an E1cb stepwise or concerted fashion. *Biochemistry*, **41**, 2621–2629.

Bailey, S. W., Frank-Kamenetskii, V. A., Goldsztaub, S., Kato, A., Pabst, A., Schulz, H., Taylor, H. F. W., Fleischer, M. & Wilson, A. J. C. (1977). Report of the International Mineralogical Association (IMA)–International Union of Crystallography (IUCr) Joint Committee on Nomenclature. *Acta Cryst.* A**33**, 681–684.

Bamford, D. H., Grimes, J. M. & Stuart, D. I. (2005). What does structure tell us about virus evolution? *Curr. Opin. Struct. Biol.* **15**, 655–663.

Benning, M. M., Taylor, K. L., Liu, R.-Q., Yang, G., Xiang, H., Wesenberg, G., Dunaway-Mariano, D. & Holden, H. M. (1996). Structure of 4-chlorobenzoyl coenzyme A dehalogenase determined to 1.8 Å resolution: an enzyme catalyst generated via adaptive mutation. *Biochemistry*, **35**, 8103–8109.

Bentley, G. A. & Houdusse, A. (1992). Some applications of the phased translation function in macromolecular structure determination. *Acta Cryst.* A**48**, 312–322.

Berman, H. M., Battistuz, T., Bhat, T. N., Bluhm, W. F., Bourne, P. E., Burkhardt, K., Feng, Z., Gilliland, G. L., Iype, L., Jain, S., Fagan, P., Marvin, J., Padilla, D., Ravichandran, V., Schneider, B., Thanki, N., Weissig, H., Westbrook, J. D. & Zardecki, C. (2002). The Protein Data Bank. *Acta Cryst.* D**58**, 899–907.

Bonev, I. (1972). On the terminology of the phenomena of mutual crystal orientation. *Acta Cryst.* A**28**, 508–512.

Borge, J., Álvarez-Rúa, C. & García-Granda, S. (2000). A new vector-search rotation function: image-seeking functions revisited in macromolecular crystallography. *Acta Cryst.* D**56**, 735–746.

Bragg, W. L. & Howells, E. R. (1954). X-ray diffraction by imidazole methaemoglobin. *Acta Cryst.* **7**, 409–411.

Bricogne, G. (1974). Geometric sources of redundancy in intensity data and their use for phase determination. *Acta Cryst.* A**30**, 395–405.

Britton, D. (1972). Estimation of twinning parameter for twins with exactly superimposed reciprocal lattices. *Acta Cryst.* A**28**, 296–297.

Brooks, B. R., Bruccoleri, R. E., Olafson, B. D., States, D. J., Swaminathan, S. & Karplus, M. (1983). *CHARMM*: a program for macromolecular energy, minimization, and dynamics calculations. *J. Comput. Chem.* **4**, 187–217.

Brünger, A. T. (1990). Extension of molecular replacement: a new search strategy based on Patterson correlation refinement. *Acta Cryst.* A**46**, 46–57.

Brünger, A. T., (1992). *X-PLOR. Version 3.1. A system for X-ray Crystallography and NMR*. Yale Univ. Press, New Haven, CT.

Brünger, A. T., Adams, P. D., Clore, G. M., DeLano, W. L., Gros, P., Grosse-Kunstleve, R. W., Jiang, J.-S., Kuszewski, J., Nilges, M., Pannu, N. S., Read, R. J., Rice, L. M., Simonson, T. & Warren, G. L. (1998). *Crystallography & NMR System*: a new software suite for macromolecular structure determination. *Acta Cryst.* D**54**, 905–921.

Buerger, M. J. (1959). *Vector Space*. New York: John Wiley.

Camacho, A. G., Gual, A., Lurz, R., Tavares, P. & Alonso, J. C. (2003). *Bacillus subtilis* bacteriophage SPP1 DNA packaging motor requires terminase and portal proteins. *J. Biol. Chem.* **278**, 23251–23259.

Chapman, M. S., Tsao, J. & Rossmann, M. G. (1992). *Ab initio* phase determination for spherical viruses: parameter determination for spherical-shell models. *Acta Cryst.* A**48**, 301–312.

Choi, H. J., Kang, S. W., Yang, C. H., Rhee, S. G. & Ryu, S. E. (1998). Crystal structure of a novel human peroxidase enzyme at 2.0 Å resolution. *Nat. Struct. Biol.* **5**, 400–406.

Cianci, M., Antonyuk, S., Bliss, N., Bailey, M. W., Buffey, S. G., Cheung, K. C., Clarke, J. A., Derbyshire, G. E., Ellis, M. J., Enderby, M. J., Grant, A. F., Holbourn, M. P., Laundy, D., Nave, C., Ryder, R., Stephenson, P., Helliwell, J. R. & Hasnain, S. S. (2005). A high-throughput structural biology/proteomics beamline at the SRS on a new multipole wiggler. *J. Synchrotron Rad.* **12**, 455–466.

Cochran, W. & Howells, E. R. (1954). X-ray diffraction by a layer structure containing random displacements. *Acta Cryst.* **7**, 412–415.

Collaborative Computational Project, Number 4 (1994). The *CCP*4 suite: programs for protein crystallography. *Acta Cryst.* D**50**, 760–763.

Cowtan, K. D. & Main, P. (1993). Improvement of macromolecular electron-density maps by the simultaneous application of real and reciprocal space constraints. *Acta Cryst.* D**49**, 148–157.

Crowther, R. A. (1972). The fast rotation function. In *The Molecular Replacement Method*, edited by M. G. Rossmann, pp. 173–178. New York: Gordon & Breach.

Crowther, R. A. & Blow, D. M. (1967). A method of positioning a known molecule in an unknown crystal structure. *Acta Cryst.* **23**, 544–548.

Cygler, M. & Desrochers, M. (1989). A full-symmetry translation function based on electron density. *Acta Cryst.* A**45**, 563–572.

Czjzek, M., Arnoux, P., Haser, R. & Shepard, W. (2001). Structure of cytochrome c_7 from *Desulfuromonas acetoxidans* at 1.9 Å resolution. *Acta Cryst.* D**57**, 670–678.

Dauter, Z., Botos, I., LaRonde-LeBlanc, N. & Wlodawer, A. (2005). Pathological crystallography: case studies of several unusual macromolecular crystals. *Acta Cryst.* D**61**, 967–975.

DeLano, W. L. & Brünger, A. T. (1995). The direct rotation function: rotational Patterson correlation search applied to molecular replacement. *Acta Cryst.* D**51**, 740–748.

Dornberger-Schiff, K. (1956). On order–disorder structures (OD-structures). *Acta Cryst.* **9**, 593–601.

Dornberger-Schiff, K. & Dunitz, J. D. (1965). Pseudo-orthorhombic diffraction patterns and OD structures. *Acta Cryst.* **19**, 471–472.

Dornberger-Schiff, K. & Grell-Niemann, H. (1961). On the theory of order–disorder (OD) structures. *Acta Cryst.* **14**, 167–177.

Dornberger-Schiff, K. & Schmittler, H. (1971). The determination of cyclicity, hexagonality and other properties of polytypes. *Acta Cryst.* A**27**, 216–219.

Dube, P., Tavares, P., Lurz, R. & van Heel, M. (1993). The portal protein of bacteriophage SPP1: a DNA pump with 13-fold symmetry. *EMBO J.* **12**, 1303–1309.

Eberhard, E. D. & Gerlt, J. A. (2004). Evolution of function in the crotonase superfamily: the stereochemical course of the reaction catalyzed by 2-ketocyclohexanecarboxyl-CoA hydrolase. *J. Am. Chem. Soc.* **126**, 7188–7189.

Emsley, P. & Cowtan, K. (2004). *Coot*: model-building tools for molecular graphics. *Acta Cryst.* D**60**, 2126–2132.

Enemark, E. J. & Joshua-Tor, L. (2006). Mechanism of DNA translocation in a replicative hexameric helicase. *Nature (London)*, **442**, 270–275.

Engel, C. K., Mathieu, M., Zeelen, J. P., Hiltunen, J. K. & Wierenga, R. K. (1996). Crystal structure of enoyl-coenzyme A (CoA) hydratase at 2.5 angstroms resolution: a spiral fold defines the CoA-binding pocket. *EMBO J.* **15**, 5135–5145.

Esnouf, R. M. (1999). Further additions to *MolScript* version 1.4, including reading and contouring of electron-density maps. *Acta Cryst.* D**55**, 938–940.

Evans, P. (2006). Scaling and assessment of data quality. *Acta Cryst.* D**62**, 72–82.

Evans, P. R. (1997). Scala. *Jnt CCP4/ESF-EACMB Newslett. Protein Crystallogr.* **33**, 22–24.

Fiser, A. & Sali, A. (2003). *Modeller*: generation and refinement of homology-based protein structure models. *Methods Enzymol.* **374**, 461–491.

Flack, H. D. (1983). On enantiomorph-polarity estimation. *Acta Cryst.* A**39**, 876–881.

Flack, H. D. (1987). The derivation of twin laws for (pseudo-)merohedry by coset decomposition. *Acta Cryst.* A**43**, 564–568.

Franken, S. M., Rozeboom, H. J., Kalk, K. H. & Dijkstra, B. W. (1991). Crystal structure of haloalkane dehalogenase: an enzyme to detoxify halogenated alkanes. *EMBO J.* **10**, 1297–1302.

Friedel, G. (1926). *Leçons de Cristallographie*. Paris: Blanchard.

Fujinaga, M. & Read, R. J. (1987). Experiences with a new translation-function program. *J. Appl. Cryst.* **20**, 517–521.

Gerlt, J. A. & Babbitt, P. C. (2001). Divergent evolution of enzymatic function: mechanistically diverse superfamilies and functionally distinct suprafamilies. *Annu. Rev. Biochem.* **70**, 209–246.

Giacovazzo, H. L., Monaco, H. L., Viterbo, D., Scordari, F., Gilli, G., Zanotti, G. & Catti, M. (1992). *Fundamentals of Crystallography*. Oxford: Oxford University Press.

Glykos, N. M. & Kokkinidis, M. (2003). Structure determination of a small protein through a 23-dimensional molecular-replacement search. *Acta Cryst.* D**59**, 709–718.

Grell, H. & Dornberger-Schiff, K. (1982). Symbols for OD groupoid families referring to OD structures (polytypes) consisting of more than one kind of layer. *Acta Cryst.* A**38**, 49–54.

Grimmer, H. (2003). Determination of all misorientations of tetragonal lattices with low multiplicity; connection with Mallard’s rule of twinning. *Acta Cryst.* A**59**, 287–296.

Grininger, M., Ravelli, R. B. G., Heider, U. & Zeth, K. (2004). Expression, crystallization and crystallographic analysis of DegS, a stress sensor of the bacterial periplasm. *Acta Cryst.* D**60**, 1429–1431.

Grosse-Kunstleve, R. W. & Adams, P. D. (2001). Patterson correlation methods: a review of molecular replacement with *CNS*. *Acta Cryst.* D**57**, 1390–1396.

Guasch, A., Pous, J., Ibarra, B., Gomis-Ruth, F. X., Valpuesta, J. M., Sousa, N., Carrascosa, J. L. & Coll, M. (2002). Detailed architecture of a DNA translocating machine: the high-resolution structure of the bacteriophage phi29 connector particle. *J. Mol. Biol.* **315**, 663–676.

Guillet, V., Lapthorn, A., Fourniat, J., Benoit, J.-P., Hartley, R. W. & Mauguen, Y. (1993). Crystallization and prelilminary X-ray investigation of barster, the intracellular inhibitor of barnase. *Proteins Struct. Funct. Genet.* **17**, 325–328.

Gulbis, J. M., Kelman, Z., Hurwitz, J., O'Donnell, M. & Kuriyan, J. (1996). Structure of the C-terminal region of p21WAF1/CIP1 complexed with human PCNA. *Cell*, **87**(2), 297–306.

Guo, P., Peterson, C. & Anderson, D. (1987). Prohead and DNA-gp3-dependent ATPase activity of the DNA packaging protein gp16 of bacteriophage phi29. *J. Mol. Biol.* **197**, 229–236.

Hahn, T. & Klapper, H. (2003). Twinning of crystals. In *Physical Properties of Crystals*, edited by A. Authier, vol. D of *International Tables for Crystallography*, chap. 3.3. Dordrecht: Kluwer Academic Publishers.

Hao, Q. (2006). Macromolecular envelope determination and envelope-based phasing. *Acta Cryst.* D**62**, 909–914.

Harada, Y., Lifchitz, A., Berthou, J. & Jolles, P. (1981). A translation function combining packing and diffraction information: an application to lysozyme (high-temperature form). *Acta Cryst.* A**37**, 398–406.

Hendrix, R. W. (1978). Symmetry mismatch and DNA packaging in large bacteriophages. *Proc. Natl Acad. Sci. USA*, **75**, 4779–4783.

Herbst-Irmer, R. & Sheldrick, G. M. (1998). Refinement of twinned structures with *SHELXL*97. *Acta Cryst.* B**54**, 443–449.

Herbst-Irmer, R. & Sheldrick, G. M. (2002). Refinement of obverse/reverse twins. *Acta Cryst.* B**58**, 477–481.

Hill, K. E., Marchesi, J. R. & Weightman, A. J. (1999). Investigation of two evolutionarily unrelated halocarboxylic acid dehalogenase gene families. *J. Bacteriol.* **181**, 2535–2547.

Hisano, T., Hata, Y., Fujii, T., Liu, J. Q., Kurihara, T., Esaki, N. & Soda, K. (1996). Crystal structure of L-2-haloacid dehalogenase from *Pseudomonas sp.* YL. An α/β hydrolase structure that is different from the α/β hydrolase fold. *J. Biol. Chem.* **271**, 20322–20330.

Hubbard, P. A., Yu, W., Schulz, H. & Kim, J.-J. P. (2005). Domain swapping in the low-similarity isomerase/hydratase superfamily: The crystal structure of rat mitochondrial Δ^3, Δ^2-enoyl-CoA isomerase. *Prot. Sci.* **14**, 1545–1555.

Huber, R. (1965). Die automatisierte Faltmolekülmethode. *Acta Cryst.* **19**, 353–356.

Isidro, A., Santos, M. A., Henriques, A. O. & Tavares, P. (2004). The high-resolution functional map of bacteriophage SPP1 portal protein. *Mol. Microbiol.* **51**, 949–962.

Isupov, M. N. & Lebedev, A. A. (2008). NCS-constrained exhaustive search using oligomeric models. *Acta Cryst.* D**64**, 90–98.

Isupov, M. N., Obmolova, G., Butterworth, S., Badet-Denisot, M.-A., Badet, B., Polikarpov, I., Littlechild, J. A. & Teplyakov, A. (1996). Substrate binding is required for assembly of the active conformation of the catalytic site in Ntn amidotransferases: evidence from the 1.8 Å crystal structure of the glutaminase domain of glucosamine 6-phosphate synthase. *Structure*, **4**, 801–810.

Jamrog, D. C., Zhang, Y. & Phillips Jr, G. N. (2003). *SOMoRe*: a multi-dimensional search and optimization approach to molecular replacement. *Acta Cryst.* D**59**, 304–314.

Jekow, P., Schaper, S., Günther, D., Tavares, P. & Hinrichs, W. (1998). Crystallization and preliminary X-ray crystallographic studies of the 13-fold symmetric portal protein of bacteriophage SPP1. *Acta Cryst.* D**54**, 1008–1011.

Jeong, J. I., Lattman, E. E. & Chirikjian, G. S. (2006). A method for finding candidate conformations for molecular replacement using relative rotation between domains of a known structure. *Acta Cryst.* D**62**, 398–409.

Jones, T. A., Zou, J.-Y., Cowan, S. W. & Kjeldgaard, M. (1991). Improved methods for building protein models in electron density maps and the location of errors in these models. *Acta Cryst.* A**47**, 110–119.

Kawarabayasi, Y., Hino, Y., Horikawa, H., Jin-no, K., Takahashi, M., Sekine, M., Baba, S., Ankai, A., Kosugi, H., Hosoyama, A., Fukui, S., Nagai, Y., Nishijima, K., Otsuka, R., Nakazawa, H., Takamiya, M., Kato, Y., Yoshizawa, T., Tanaka, T., Kudoh, Y., Yamazaki, J., Kushida, N., Oguchi, A., Aoki, K., Masuda, S., Yanagii, M., Nishimura, M., Yamagishi, A., Oshima, T. & Kikuchi, H. (2001). Complete genome sequence of an aerobic thermoacidophilic crenarchaeon, *Sulfolobus tokodaii* strain 7. *DNA Res.* **8**, 123–140.

Keegan, R. M. & Winn, M. D. (2008). *MrBUMP*: an automated pipeline for molecular replacement. *Acta Cryst.* D**64**, 119–124.

Keillor, J. W., Lherbet, C., Castonguay, R., Lapierre, D., Martinez-Oyanedel, J., Fothergill-Gilmore, L. A. & Walkinshaw, M. D. (2003). Expression, purification, crystallization and preliminary crystallographic analysis of *Trypanosoma brucei* phosphofructokinase. *Acta Cryst.* D**59**, 532–534.

Kissinger, C. R., Gehlhaar, D. K. & Fogel, D. B. (1999). Rapid automated molecular replacement by evolutionary search. *Acta Cryst.* D**55**, 484–491.

Kovacs, J. A. & Wriggers, W. (2002). Fast rotational matching. *Acta Cryst.* D**58**, 1282–1286.

Krissinel, E. & Henrick, K. (2004). Secondary-structure matching (SSM), a new tool for fast protein structure alignment in three dimensions. *Acta Cryst.* D**60**, 2256–2268.

Krissinel, E. & Henrick, K. (2005). Detection of protein assemblies in crystals. In *First International Symposium CompLife 2005, Konstanz, Germany, September 25–27, 2005, Proceedings*, edited by M. R. Berthold, R. Glen, K. Diederichs, O. Kohlbacher & I. Fischer, pp. 163–174. Berlin, Heidelberg: Springer-Verlag.

Ladner, R. C., Heidner, E. J. & Perutz, M. F. (1977). The structure of horse methaemoglobin at 2.0 Å resolution. *J. Mol. Biol.* **114**, 385–413.

Langs, D. A. (1975). Translation vector functions based on a deconvolution of the Patterson function provided by transform methods. *Acta Cryst.* A**31**, 543–550.

Laskowski, R. A., MacArthur, M. W., Moss, D. S. & Thornton, J. M. (1993). *PROCHECK*: a program to check the stereochemical quality of protein structures. *J. Appl. Cryst.* **26**, 283–291.

Le Page, Y. (2002). Mallard's law recast as a Diophantine system: fast and complete enumeration of possible twin laws by [reticular] [pseudo] merohedry. *J. Appl. Cryst.* **35**, 175–181.

Lebedev, A. A., Krause, M. H., Isidro, A. L., Vagin, A. A., Orlova, E. V., Turner, J., Dodson, E. J., Tavares, P. & Antson, A. A. (2007). Structural framework for DNA translocation via the viral portal protein. *EMBO J.* **26**, 1984–1994.

Lebedev, A. A., Vagin, A. A. & Murshudov, G. N. (2006). Intensity statistics in twinned crystals with examples from the PDB. *Acta Cryst.* D**62**, 83–95.

Lebedev, A. A., Vagin, A. A. & Murshudov, G. N. (2008). Model preparation in *MOLREP* and examples of model improvement using X-ray data. *Acta Cryst.* D**64**, 33–39.

Lee, S., Sawaya, M. R. & Eisenberg, D. (2003). Structure of superoxide dismutase from *Pyrobaculum aerophilum* presents a challenging case in molecular replacement with multiple molecules, pseudo-symmetry and twinning. *Acta Cryst.* D**59**, 2191–2199.

Leonard, P. M., Brzozowski, A. M., Lebedev, A., Marshall, C. M., Smith, D. J., Verma, C. S., Walton, N. J. & Grogan, G. (2006). The 1.8 Å resolution structure of hydroxycinnamoyl-coenzyme A hydratase-lyase (HCHL) from *Pseudomonas fluorescens*, an enzyme that catalyses the transformation of feruloyl-coenzyme A to vanillin. *Acta Cryst.* D**62**, 1494–1501.

Leonard, P. M., Marshall, C. M., Dodson, E. J., Walton, N. J. & Grogan, G. (2004). Purification, crystallization and preliminary X-ray crystallographic analysis of hydroxycinnamoyl-coenzyme A hydratase-lyase (HCHL), a crotonase homologue active in phenylpropanoid metabolism. *Acta Cryst.* D**60**, 2343–2345.

Leslie, A. G. W. (1992). *Jnt CCP4/ESF-EACMB Newslett. Protein Crystallogr.* **26**.

Leslie, A. G. W. (2006). The integration of macromolecular diffraction data. *Acta Cryst.* D**62**, 48–57.

Levdikov, V. M., Blagova, E., Colledge, V. L., Lebedev, A. A., Williamson, D. C., Sonenshein, A. L. & Wilkinson, A. J. (2009). Structural rearrangement accompanying ligand binding in the GAF domain of CodY from *Bacillus subtilis*. *J. Mol. Biol.* **390**, 1007–1018.

Levdikov, V. M., Blagova, E., Joseph, P., Sonenshein, A. L. & Wilkinson, A. J. (2006). The structure of CodY, a GTP- and isoleucine-responsive regulator of stationary phase and virulence in gram-positive bacteria. *J. Biol. Chem.* **281**, 11366–11373.

Li, T., Ji, X., Sun, F., Gao, R., Cao, S., Feng, Y. & Rao, Z. (2002). Crystallization and preliminary X-ray analysis of recombinant histone HPhA from the hyperthermophilic archaeon *Pyrococcus horikoshii* OT3. *Acta Cryst.* D**58**, 870–871.

Lilien, R. H., Bailey-Kellogg, C., Anderson, A. C. & Donald, B. R. (2004). A subgroup algorithm to identify cross-rotation peaks consistent with non-crystallographic symmetry. *Acta Cryst.* D**60**, 1057–1067.

Litvin, D. B. (1977). The molecular replacement method. II. The translation function problem; a new translation function. *Acta Cryst.* A**33**, 62–70.

Liu, Q., Weaver, A. J., Xiang, T., Thiel, D. J. & Hao, Q. (2003). Low-resolution molecular replacement using a six-dimensional search. *Acta Cryst.* D**59**, 1016–1019.

Long, F., Vagin, A. A., Young, P. & Murshudov, G. N. (2008). *BALBES*: a molecular-replacement pipeline. *Acta Cryst.* D**64**, 125–132.

Lougheed, J. C., Holton, J. M., Alber, T., Bazan, J. F. & Handel, T. M. (2001). Structure of melanoma inhibitory activity protein, a member of a recently identified family of secreted proteins. *Proc. Natl Acad. Sci. USA*, **98**, 5515–5520.

Lunin, V. Y., Lunina, N. L. & Baumstark, M. W. (2007). Estimates of the twinning fraction for macromolecular crystals using statistical models accounting for experimental errors. *Acta Cryst.* D**63**, 1129–1138.

Lurz, R., Orlova, E. V., Gunther, D., Dube, P., Droge, A., Weise, F., van Heel, M. & Tavares, P. (2001). Structural organisation of the head-to-tail interface of a bacterial virus. *J. Mol. Biol.* **310**, 1027–1037.

Main, P. & Rossmann, M. G. (1966). Relationship among structure factors due to identical molecules in different crystallographic environments. *Acta Cryst.* **21**, 67–72.

Makino, D. L., Henschen-Edman, A. H., Larson, S. B. & McPherson, A. (2007). Bence Jones KWR protein structures determined by X-ray crystallography. *Acta Cryst.* D**63**, 780–792.

Makino, D. L., Henschen-Edman, A. H. & McPherson, A. (2005*a*). Four crystal forms of a Bence-Jones protein. *Acta Cryst.* F**61**, 79–82.

Makino, D. L., Larson, S. B. & McPherson, A. (2005*b*). Preliminary analysis of crystals of panicum mosaic virus (PMV) by X-ray diffraction and atomic force microscopy. *Acta Cryst.* D**61**, 173–179.

Mancheno, J. M., Martin-Benito, J., Martinez-Ripoll, M., Gavilanes, J. G. & Hermoso, J. A. (2003). Crsytal and electron microscopy structures of sticholysin II actinoporin refeal insights into the mechanism of membrane pore formation. *Structure*, **11**, 1319–1328.

Matthews, B. W. (1968). Solvent content of protein crystals. *J. Mol. Biol.* **33**, 491–497.

McCoy, A. J., Grosse-Kunstleve, R. W., Adams, P. D., Winn, M. D., Storoni, L. C. & Read, R. J. (2007). *Phaser* crystallographic software. *J. Appl. Cryst.* **40**, 658–674.

Mighell, A. D. & Rodgers, J. R. (1980). Lattice symmetry determination. *Acta Cryst.* A**36**, 321–326.

Millward, G. R., Ramdas, S., Thomas, J. M. & Barlow, M. T. (1983). Evidence for semi-regularly ordered sequences of mirror and inversion symmetry planes in ZSM-5/ZSM-11 shape-selective zeolitic catalysts. *J. Chem. Soc. Faraday Trans. 2*, **79**, 1075–1082.

Modis, Y., Filppula, S. A., Novikov, D. K., Norledge, B., Hiltunen, J. K. & Wierenga, R. K. (1998). The crystal structure of dienoyl-CoA isomerase at 1.5 Å resolution reveals the importance of aspartate and glutamate sidechains for catalysis. *Structure*, **6**, 957–970.

Morais, M. C., Choi, K. H., Koti, J. S., Chipman, P. R., Anderson, D. L. & Rossmann, M. G. (2005). Conservation of the capsid structure in tailed dsDNA bacteriophages: the pseudoatomic structure of phi29. *Mol. Cell*, **18**, 149–159.

Morales, R., Kachalova, G., Vellieux, F., Charon, M.-H. & Frey, M. (2000). Crystallographic studies of the interaction between the ferredoxin-NADP$^+$ reductase and ferredoxin from the cyanobacterium *Anabaena*: looking for the elusive ferredoxin molecule. *Acta Cryst.* D**56**, 1408–1412.

Morgan, N., Pereira, I. A. C., Andersson, I., Adlington, R. M., Baldwin, J. E., Cole, S. E., Crouch, N. P. & Sutherland, J. D. (1994). Substrate specificity of recombinant streptomyces clabuligerus deacetoxycepalosporin C synthase. *Bioorg. Med. Chem. Lett.* **4**, 1595–1600.

Morita, M., Tasaka, M. & Fujisawa, H. (1993). DNA packaging ATPase of bacteriophage T3. *Virology*, **193**, 748–752.

Muirhead, H., Cox, J. M., Mazzarella, L. & Perutz, M. F. (1967). Structure and function of haemoglobin: III. A three-dimensional fourier synthesis of human deoxyhaemoglbin at 5.5 Å resolution. *J. Mol. Biol.* **28**, 117–150.

Müller, P., Herbst-Irmer, R., Spek, A. L. & Schneider, T. R. (2006). *Crystal Structure Refinement: A Crystallographer's Guide to SHELXL*. Oxford: Oxford University Press.

Muraki, M., Ishimura, M. & Harata, K. (2002). Interactions of wheat-germ agglutinin with GlcNAcβ1,6Gal sequence. *Biochim. Biophys. Acta*, **1569**, 10–20.

Murshudov, G. N., Vagin, A. A. & Dodson, E. J. (1997). Refinement of macromolecular structures by the maximum-likelihood method. *Acta Cryst.* D**53**, 240–255.

Mursula, A. M., van Aalten, D. M. F., Hiltunen, J. K. & Wierenga, R. K. (2001). The crystal structure of 3-2-enoyl-CoA isomerase. *J. Mol. Biol.* **309**, 845–853.

Murzin, A. G., Brenner, S. E., Hubbard, T. & Chothia, C. (1995). *SCOP*: a structural classification of proteins database for the investigation of sequences and structures. *J. Mol. Biol.* **247**, 536–540.

Nakai, T., Ishijima, J., Masui, R., Kuramitsu, S. & Kamiya, N. (2003). Structure of *Thermus thermophilus* HB8 H-protein of the glycine-cleavage system, resolved by a six-dimensional molecular-replacement method. *Acta Cryst.* D**59**, 1610–1618.

Narbad, A. & Gasson, M. J. (1998). Metabolism of ferulic acid via vanillin using a novel CoA-dependent pathway in a newly isolated strain of *Pseudomonas fluorescens*. *Microbiology*, **144**, 1397–1405.

Navaza, J. (1987). On the fast rotation function. *Acta Cryst.* A**43**, 645–653.

Navaza, J. (1990). Accurate computation of the rotation matrices. *Acta Cryst.* A**46**, 619–620.

Navaza, J. (1993). On the computation of the fast rotation function. *Acta Cryst.* D**49**, 588–591.

Navaza, J. (2001). Implementation of molecular replacement in *AMoRe*. *Acta Cryst.* D**57**, 1367–1372.

Navaza, J., Panepucci, E. H. & Martin, C. (1998). On the use of strong Patterson function signals in many-body molecular replacement. *Acta Cryst.* D**54**, 817–821.

Navaza, J. & Vernoslova, E. (1995). On the fast translation functions for molecular replacement. *Acta Cryst.* A**51**, 445–449.

Needleman, S. B. & Wunsch, C. D. (1970). A general method applicable to the search for similarities in the amino acid sequence of two proteins. *J. Mol. Biol.* **48**, 443–453.

Nespolo, M. & Ferraris, G. (2004). Applied geminography – symmetry analysis of twinned crystals and definition of twinning by reticular polyholohedry. *Acta Cryst.* A**60**, 89–95.

Nespolo, M., Ferraris, G., Durovic, S. & Takeuchi, Y. (2004). Twins vs. modular crystal structures. *Z. Kristallogr.* **219**, 773–778.

Nordman, C. E. & Nakatsu, K. (1963). Interpretation of the Patterson function of crystals containing a known molecular fragment. The structure of an alstonia alkaloid. *J. Am. Chem. Soc.* **85**, 353–354.

Oksanen, E., Jaakola, V.-P., Tolonen, T., Valkonen, K., Åkerstróm, B., Kalkkinen, N., Virtanen, V. & Goldman, A. (2006). Reindeer β-lactoglobulin crystal structure with pseudo-body-centred non-crystallographic symmetry. *Acta Cryst.* D**62**, 1369–1374.

Oliveira, L., Alonso, J. C. & Tavares, P. (2005). A defined in vitro system for DNA packaging by the bacteriophage SPP1: insights into the headful packaging mechanism. *J. Mol. Biol.* **353**, 529–539.

Oliveira, L., Henriques, A. O. & Tavares, P. (2006). Modulation of the viral ATPase activity by the portal protein correlates with DNA packaging efficiency. *J. Biol. Chem.* **281**, 21914–21923.

Orlova, E. V., Dube, P., Beckmann, E., Zemlin, F., Lurz, R., Trautner, T. A., Tavares, P. & van Heel, M. (1999). Structure of the 13-fold symmetric portal protein of bacteriophage SPP1. *Nat. Struct. Biol.* **6**, 842–846.

Orlova, E. V., Gowen, B., Droge, A., Stiege, A., Weise, F., Lurz, R., van Heel, M. & Tavares, P. (2003). Structure of a viral DNA gatekeeper at 10 Å resolution by cryo-electron microscopy. *EMBO J.* **22**, 1255–1262.

Otwinowski, Z. & Minor, W. (1997). Processing of X-ray diffraction data collected in oscillation mode. *Methods Enzymol.* **276**, 307–326.

Pavelcik, F. (2006). Phased rotation, conformation and translation function: theory and computer program. *J. Appl. Cryst.* **39**, 483–486.

Pena, V., Liu, S., Bujnicki, J. M., Lührmann, R. & Wahl, M. C. (2007). Structure of a multipartite protein-protein interaction domain in splicing factor Prp8 and its link to *Retinitis Pigmentosa*. *Mol. Cell*, **25**, 615–624.

Perrakis, A., Morris, R. M. & Lamzin, V. S. (1999). Automated protein model building combined with iterative structure refinement. *Nat. Struct. Biol.* **6**, 458–463.

Potterton, L., McNicholas, S., Krissinel, E., Gruber, J., Cowtan, K., Emsley, P., Murshudov, G. N., Cohen, S., Perrakis, A. & Noble, M. (2004). Developments in the *CCP*4 molecular-graphics project. *Acta Cryst.* D**60**, 2288–2294.

R Development Core Team, (2005). *R: A Language and Environment for Statistical Computing*. R Foundation for Statistical Computing, Vienna, Austria. http://www.R-project.org.

Rees, D. C. (1980). The influence of twinning by merohedry on intensity statistics. *Acta Cryst.* A**36**, 578–581.

Rossmann, M. G. & Blow, D. M. (1962). The detection of sub-units within the crystallographic asymmetric unit. *Acta Cryst.* **15**, 24–31.

Rossmann, M. G. & Blow, D. M. (1963). Determination of phases by the conditions of non-crystallographic symmetry. *Acta Cryst.* **16**, 39–45.

Rossmann, M. G. & Blow, D. M. (1964). Solution of the phase equations representing non-crystallographic symmetry. *Acta Cryst.* **17**, 1474–1475.

Rossmann, M. G., Blow, D. M., Harding, M. M. & Coller, E. (1964). The relative positions of independent molecules within the same asymmetric unit. *Acta Cryst.* **17**, 338–342.

Rudolph, M. G., Kelker, M. S., Schneider, T. R., Yeates, T. O., Oseroff, V., Heidary, D. K., Jennings, P. A. & Wilson, I. A. (2003). Use of multiple anomalous dispersion to phase highly merohedrally twinned crystals of interleukin-1β. *Acta Cryst.* D**59**, 290–298.

Rye, C. A., Isupov, M. N., Lebedev, A. A. & Littlechild, J. A. (2007). An order–disorder twin crystal of L-2-haloacid dehalogenase from *Sulfolobus tokodaii*. *Acta Cryst.* D**63**, 926–930.

Rye, C. A., Isupov, M. N., Lebedev, A. A. & Littlechild, J. A. (2009). Biochemical and structural studies of a L-haloacid dehalogenase from the thermophilic archaeon *Sulfolobus tokodaii*. *Extremophiles*, **13**, 179–190.

Sanders, C. M., Kovalevskiy, O. V., Sizov, D., Lebedev, A. A., Isupov, M. N. & Antson, A. A. (2007). Papillomavirus E1 helicase assembly maintains an asymmetric state in the absence of DNA and nucleotide cofactors. *Nucleic Acids Res.* **35**, 6451–6457.

Schröder, E., Littlechild, J. A., Lebedev, A. A., Errington, N., Vagin, A. A. & Isupov, M. N. (2000). Crystal structure of decameric 2-Cys peroxiredoxin from human erythrocytes at 1.7 Å resolution. *Structure*, **8**, 605–615.

Schuermann, J. P. & Tanner, J. J. (2003). MRSAD: using anomalous dispersion from S atoms collected at Cu $K\alpha$ wavelength in molecular-replacement structure determination. *Acta Cryst.* D**59**, 1731–1736.

Schwarzenbacher, R., Godzik, A., Grzechnik, S. K. & Jaroszewski, L. (2004). The importance of alignment accuracy for molecular replacement. *Acta Cryst.* D**60**, 1229–1236.

Schwarzenbacher, R., Godzik, A. & Jaroszewski, L. (2008). The JCSG MR pipeline: optimized alignments, multiple models and parallel searches. *Acta Cryst.* D**64**, 133–140.

Schwede, T., Kopp, J., Guex, N. & Peitsch, M. C. (2003). *SWISS-MODEL*: an automated protein homology-modeling server. *Nucleic Acids Res.* **31**, 3381–3385.

Scouloudi, H. (1960). The crystal structure of myoglobin. VI. Seal myoglobin. *Proc. R. Soc.* A**258**, 181–201.

Shan, L., Lu, J.-X., Gan, J.-H., Wang, Y.-H., Huang, Z.-X. & Xia, Z.-X. (2005). Structure of the F58W mutant of cytochrome b_5: the mutation leads to multiple conformations and weakens stacking interactions. *Acta Cryst.* D**61**, 180–189.

Sheldrick, G. M. (2008). A short history of *SHELX*. *Acta Cryst.* A**64**, 112–122.

Sheriff, S., Klei, H. E. & Davis, M. E. (1999). Implementation of a six-dimensional search using the *AMoRe* translation function for difficult molecular-replacement problems. *J. Appl. Cryst.* **32**, 98–101.

Shevtsov, M. B., Chen, Y., Gollnick, P. & Antson, A. A. (2005). Crystal structure of *Bacillus subtilis* anti-TRAP protein, an antagonist of TRAP/RNA interaction. *Proc. Natl Acad. Sci. USA*, **102**, 17600–17605.

Simpson, A. A., Tao, Y., Leiman, P. G., Badasso, M. O., He, Y., Jardine, P. J., Olson, N. H., Morais, M. C., Grimes, S., Anderson, D. L., Baker, T. S. & Rossmann, M. G. (2000). Structure of the bacteriophage phi29 DNA packaging motor. *Nature (London)*, **408**, 745–750.

Slater, J. H. (1982). New microbes to tackle toxic compounds. *S. Afr. J. Sci.* **78**, 101–104.

Slater, J. H., Bull, A. T. & Hardman, D. J. (1997). Microbial dehalogenation of halogenated alkanoic acids, alcohols and alkanes. *Adv. Microb. Physiol.* **38**, 133–176.

Smith, D. E., Tans, S. J., Smith, S. B., Grimes, S., Anderson, D. L. & Bustamante, C. (2001). The bacteriophage phi29 portal motor can package DNA against a large internal force. *Nature (London)*, **413**, 748–752.

Strokopytov, B. V., Fedorov, A., Mahoney, N. M., Kessels, M., Drubin, D. G. & Almo, S. C. (2005). Phased translation function revisited: structure solution of the cofilin-homology domain from yeast actin-binding protein 1 using six-dimensional searches. *Acta Cryst.* D**61**, 285–293.

Strop, P., Brzustowicz, M. R. & Brünger, A. T. (2007). *Ab initio* molecular-replacement phasing for symmetric helical membrane proteins. *Acta Cryst.* D**63**, 188–196.

Stuart, A. & Ord, J. K. (1994). *Distribution Theory*, vol. 1 of *Kendall's Advanced Theory of Statistics*, chap. 3. London: Edward Arnold.

Stuart, A., Ord, J. K. & Arnold, S. (1999). *Classical Inference and the Linear Model*, vol. 2A of *Kendall's Advanced Theory of Statistics*, chap. 17. Oxford: Oxford University Press.

Stubbs, M. T. & Huber, R. (1991). An analytical packing function employing Fourier transforms. *Acta Cryst.* A**47**, 521–526.

Sugishima, M., Sakamoto, H., Kakuta, Y., Omata, Y., Hayashi, S., Noguchi, M. & Fukuyama, K. (2002). Crystal structure of rat apo-heme oxygenase-1 (HO-1): mechanism of heme binding in HO-1 inferred from structural comparison of the apo and heme complex forms. *Biochemistry*, **41**, 7293–7300.

Suhre, K. & Sanejouand, Y. H. (2004). *ElNemo*: a normal mode web-server for protein movement analysis and the generation of templates for molecular replacement. *Nucleic Acids Res.* **32**, W610–W614.

Tavares, P., Santos, M. A., Lurz, R., Morelli, G., de Lencastre, H. & Trautner, T. A. (1992). Identification of a gene in *Bacillus subtilis* bacteriophage SPP1 determining the amount of packaged DNA. *J. Mol. Biol.* **225**, 81–92.

Ten Eyck, L. F. (1977). Efficient structure-factor calculation for large molecules by the fast Fourier transform. *Acta Cryst.* A**33**, 486–492.

Tollin, P. (1966). On the determination of molecular location. *Acta Cryst.* **21**, 613–614.

Tollin, P. & Rossmann, M. G. (1966). A description of various rotation function programs. *Acta Cryst.* **21**, 872–876.

Tong, L. (2001). How to take advantage of non-crystallographic symmetry in molecular replacement: 'locked' rotation and translation functions. *Acta Cryst.* D**57**, 1383–1389.

Tong, L. & Rossmann, M. G. (1990). The locked rotation function. *Acta Cryst.* A**46**, 783–792.

Trame, C. B. & McKay, D. B. (2001). Structure of *Haemophilus influenzae* HslU protein in crystals with one-dimensional disorder twinning. *Acta Cryst.* D**57**, 1079–1090.

Trapani, S., Abergel, C., Gutsche, I., Horcajada, C., Fita, I. & Navaza, J. (2006). Combining experimental data for structure determination of flexible multimeric macromolecules by molecular replacement. *Acta Cryst.* D**62**, 467–475.

Trapani, S. & Navaza, J. (2006). Calculation of spherical harmonics and Wigner *d* functions by FFT. Applications to fast rotational matching in molecular replacement and implementation into *AMoRe*. *Acta Cryst.* A**62**, 262–269.

Trapani, S., Siebert, X. & Navaza, J. (2007). The concept of resolution in the domain of rotations. *Acta Cryst.* A**63**, 126–130.

Truglio, J. J., Theis, K., Feng, Y., Gajda, R., Machutta, C., Tonge, P. J. & Kisker, C. (2003). Crystal structure of *Mycobacterium tuberculosis* MenB, a key enzyme in vitamin K2 biosynthesis. *J. Biol. Chem.* **278**, 42352–42360.

Trus, B. L., Cheng, N., Newcomb, W. W., Homa, F. L., Brown, J. C. & Steven, A. C. (2004). Structure and polymorphism of the UL6 portal protein of herpes simplex virus type 1. *J. Virol.* **78**, 12668–12671.

Tsao, J., Chapman, M. S. & Rossmann, M. G. (1992). *Ab initio* phase determination for viruses with high symmetry: a feasibility study. *Acta Cryst.* A**48**, 293–301.

Uppenberg, J., Oehrner, N., Norin, M., Hult, K., Kleywegt, G. J., Patkar, S., Waagen, V., Anthonsen, T. & Jones, T. A. (1995). Crystallographic and molecular-modeling studies of lipase B from *Candida antarctica* reveal a stereospecificity pocket for secondary alcohols. *Biochemistry,* **34**, 16838–16851.

Vagin, A. & Teplyakov, A. (1997). *MOLREP*: an automated program for molecular replacement. *J. Appl. Cryst.* **30**, 1022–1025.

Vagin, A. & Teplyakov, A. (1998). A translation-function approach for heavy-atom location in macromolecular crystallography. *Acta Cryst.* D**54**, 400–402.

Vagin, A. & Teplyakov, A. (2000). An approach to multi-copy search in molecular replacement. *Acta Cryst.* D**56**, 1622–1624.

Vagin, A. A. (1983). Ph.D. thesis, Institute of Crystallography, Moscow.

Vagin, A. A. & Isupov, M. N. (2001). Spherically averaged phased translation function and its application to the search for molecules and fragments in electron-density maps. *Acta Cryst.* D**57**, 1451–1456.

Vaguine, A. A., Richelle, J. & Wodak, S. J. (1999). *SFCHECK*: a unified set of procedures for evaluating the quality of macromolecular structure-factor data and their agreement with the atomic model. *Acta Cryst.* D**55**, 191–205.

Valpuesta, J. M. & Carrascosa, J. L. (1994). Structure of viral connectors and their function in bacteriophage assembly and DNA packaging. *Q. Rev. Biophys.* **27**, 107–155.

Wang, J., Kamtekar, S., Berman, A. J. & Steitz, T. A. (2005). Correction of X-ray intensities from single crystals containing lattice-translocation defects. *Acta Cryst.* D**61**, 67–74.

Wilson, A. J. C. (1949). The probability distribution of X-ray intensities. *Acta Cryst.* **2**, 318–321.

Winn, M. D., Isupov, M. N. & Murshudov, G. N. (2001). Use of TLS parameters to model anisotropic displacements in macromolecular refinement. *Acta Cryst.* D**57**, 122–133.

Yeates, T. O. (1988). Simple statistics for intensity data from twinned specimens. *Acta Cryst.* A**44**, 142–144.

Yeates, T. O. & Fam, B. C. (1999). Protein crystals and their evil twins. *Structure,* **7**, R25–R29.

Yeates, T. O. & Rini, J. M. (1990). Intensity-based domain refinement of oriented but unpositioned molecular replacement models. *Acta Cryst.* A**46**, 352–359.

Zhang, X.-J. & Matthews, B. W. (1994). Enhancement of the method of molecular replacement by incorporation of known structural information. *Acta Cryst.* D**50**, 675–686.

Zhou, Z. & Gong, W. (2004). Co-crystallization of *Leptospira interrogans* peptide deformylase with a potent inhibitor and molecular-replacement schemes with eight subunits in an asymmetric unit. *Acta Cryst.* D**60**, 137–139.